

Simulation and modelling of the aerodynamic impact of sensor setups on autonomous road vehicles

Simulation und Modellierung des aerodynamischen Einflusses von Sensoraufbauten auf autonome Straßenfahrzeuge

Scientific work for obtaining the academic degree

Master of Science (M.Sc.)

at the Department of Mechanical Engineering of Technical University of Munich

Supervised by Prof. Dr.-Ing. Markus Lienkamp
Philipp Hafemann, M.Sc.
Chair of Automotive Technology

Submitted by Aleix Lazaro Prat, B.Sc.
Schleissheimerstr 222
80797 München

Submitted on October 8, 2021

Aufgabenstellung

Simulation und Modellierung des aerodynamischen Einflusses von Sensoraufbauten auf autonome Straßenfahrzeuge

Die Mobilität der Zukunft ist elektrisch, vernetzt und automatisiert. Dies wird zu einer umfassenden Umgestaltung des motorisierten Straßenverkehrs führen und auch das Fahrzeug selbst betreffen. Heutige Fahrzeuge sind bereits mit einer Vielzahl von unterschiedlichen Sensoren ausgestattet, die Informationen über die Umgebung liefern. Für die Realisierung vollautonomer Fahrzeuge wird in Zukunft eine Vielzahl von Sensoren in den Fahrzeugen zum Einsatz kommen, die alle an der Karosserie angebracht werden müssen. Diese Aufbauten wirken sich nicht nur auf das Außendesign aus, sondern erhöhen auch den aerodynamischen Widerstand des Basisfahrzeugs.

Im Rahmen dieser Masterarbeit sollen die Auswirkungen verschiedener Sensoraufbauten auf die Aerodynamik eines autonomen Fahrzeugs untersucht werden. Dazu soll ein Simulationsmodell zur aerodynamischen Simulation entwickelt werden. Mit Hilfe der Simulationsumgebung sollen verschiedene Sensorausstattungen an autonomen Fahrzeugen evaluiert werden. Es soll quantifiziert werden, inwieweit die Sensorausstattungen die Aerodynamik und damit die Energieeffizienz eines autonomen Fahrzeugs beeinflussen.

Folgende Punkte sind durch Herrn Aleix Lazaro Prat zu bearbeiten:

- Literaturübersicht über die aerodynamischen Auswirkungen von Sensoren auf autonome Fahrzeuge.
- Entwicklung einer Simulationsumgebung für die Aerodynamik von autonomen Fahrzeugen
- Modellierung von Fahrzeugen und Sensoraufbau
- Definition von Testszenarien und Randbedingungen
- Simulation von AVs mit verschiedenen Sensoraufbauten und Integrationstechniken
- Erstellung eines Modells zur Abschätzung des aerodynamischen Einflusses von Sensorausstattungen

Die Ausarbeitung soll die einzelnen Arbeitsschritte in übersichtlicher Form dokumentieren. Der Kandidat/Die Kandidatin verpflichtet sich, die Masterarbeit selbstständig durchzuführen und die von ihm verwendeten wissenschaftlichen Hilfsmittel anzugeben.

Die eingereichte Arbeit verbleibt als Prüfungsunterlage im Eigentum des Lehrstuhls.

Announcement date: April 10, 2021

Submission date: October 8, 2021

Prof. Dr.-Ing. Markus Lienkamp

Philipp Hafemann

Geheimhaltungsverpflichtung

Herr: **Lazaro Prat, Aleix**

Gegenstand der Geheimhaltungsverpflichtung sind alle mündlichen, schriftlichen und digitalen Informationen und Materialien die der Unterzeichner vom Lehrstuhl oder von Dritten im Rahmen seiner Tätigkeit am Lehrstuhl erhält. Dazu zählen vor allem Daten, Simulationswerkzeuge und Programmcode sowie Informationen zu Projekten, Prototypen und Produkten.

Der Unterzeichner verpflichtet sich, alle derartigen Informationen und Unterlagen, die ihm während seiner Tätigkeit am Lehrstuhl für Fahrzeugtechnik zugänglich werden, strikt vertraulich zu behandeln.

Er verpflichtet sich insbesondere:

- derartige Informationen betriebsintern zum Zwecke der Diskussion nur dann zu verwenden, wenn ein ihm erteilter Auftrag dies erfordert,
- keine derartigen Informationen ohne die vorherige schriftliche Zustimmung des Betreuers an Dritte weiterzuleiten,
- ohne Zustimmung eines Mitarbeiters keine Fotografien, Zeichnungen oder sonstige Darstellungen von Prototypen oder technischen Unterlagen hierzu anzufertigen,
- auf Anforderung des Lehrstuhls für Fahrzeugtechnik oder unaufgefordert spätestens bei seinem Ausscheiden aus dem Lehrstuhl für Fahrzeugtechnik alle Dokumente und Datenträger, die derartige Informationen enthalten, an den Lehrstuhl für Fahrzeugtechnik zurückzugeben.

Eine besondere Sorgfalt gilt im Umgang mit digitalen Daten:

- Für den Dateiaustausch dürfen keine Dienste verwendet werden, bei denen die Daten über einen Server im Ausland geleitet oder gespeichert werden (Es dürfen nur Dienste des LRZ genutzt werden (Lehrstuhlaufwerke, Sync&Share, GigaMove).
- Vertrauliche Informationen dürfen nur in verschlüsselter Form per E-Mail versendet werden.
- Nachrichten des geschäftlichen E-Mail Kontos, die vertrauliche Informationen enthalten, dürfen nicht an einen externen E-Mail Anbieter weitergeleitet werden.
- Die Kommunikation sollte nach Möglichkeit über die (my)TUM-Mailadresse erfolgen.

Die Verpflichtung zur Geheimhaltung endet nicht mit dem Ausscheiden aus dem Lehrstuhl für Fahrzeugtechnik, sondern bleibt 5 Jahre nach dem Zeitpunkt des Ausscheidens in vollem Umfang bestehen. Die eingereichte schriftliche Ausarbeitung darf der Unterzeichner nach Bekanntgabe der Note frei veröffentlichen.

Der Unterzeichner willigt ein, dass die Inhalte seiner Studienarbeit in darauf aufbauenden Studienarbeiten und Dissertationen mit der nötigen Kennzeichnung verwendet werden dürfen.

Datum: 8. Oktober 2021

Unterschrift: _____



Erklärung

Ich versichere hiermit, dass ich die von mir eingereichte Abschlussarbeit selbstständig verfasst und keine anderen als die angegebenen Quellen und Hilfsmittel benutzt habe.

Garching, den 8. Oktober 2021



Aleix Lazaro Prat ,B.Sc.

Declaration of Consent, Open Source

Hereby I, Lazaro Prat, Aleix, born on August 17, 1995, make the software I developed during my Semester Thesis available to the Institute of Automotive Technology under the terms of the license below.

Garching, October 8, 2021



Aleix Lazaro Prat ,B.Sc.

Copyright 2021 Lazaro Prat, Aleix

Permission is hereby granted, free of charge, to any person obtaining a copy of this software and associated documentation files (the "Software"), to deal in the Software without restriction, including without limitation the rights to use, copy, modify, merge, publish, distribute, sublicense, and/or sell copies of the Software, and to permit persons to whom the Software is furnished to do so.

THE SOFTWARE IS PROVIDED "AS IS", WITHOUT WARRANTY OF ANY KIND, EXPRESS OR IMPLIED, INCLUDING BUT NOT LIMITED TO THE WARRANTIES OF MERCHANTABILITY, FITNESS FOR A PARTICULAR PURPOSE AND NONINFRINGEMENT. IN NO EVENT SHALL THE AUTHORS OR COPYRIGHT HOLDERS BE LIABLE FOR ANY CLAIM, DAMAGES OR OTHER LIABILITY, WHETHER IN AN ACTION OF CONTRACT, TORT OR OTHERWISE, ARISING FROM, OUT OF OR IN CONNECTION WITH THE SOFTWARE OR THE USE OR OTHER DEALINGS IN THE SOFTWARE.

Contents

| | |
|--|------------|
| List of Abbreviations | III |
| Formula Symbols | V |
| 1 Introduction | 1 |
| 2 State of the Science and Technology | 3 |
| 2.1 Introduction to aerodynamics | 4 |
| 2.1.1 Fundamentals of aerodynamics | 4 |
| 2.1.2 Road vehicle aerodynamics | 19 |
| 2.1.3 DrivAer | 23 |
| 2.1.4 Autonomous shuttle and sensor aerodynamics..... | 24 |
| 2.2 Current autonomous shuttle data | 29 |
| 2.3 Introduction to <i>Pacefish</i>[®] | 29 |
| 3 Method | 33 |
| 3.1 Aerodynamic analysis methodology | 35 |
| 3.2 Analysis of current autonomous shuttle data and derivation of the simulation conditions | 37 |
| 3.2.1 Analysis of current autonomous shuttle data | 37 |
| 3.2.2 Derivation of the simulation conditions | 39 |
| 3.3 Validation of the simulation software (<i>Pacefish</i>[®]) | 40 |
| 3.3.1 DrivAer geometry selection | 40 |
| 3.3.2 Setup of the DrivAer simulations | 41 |
| 3.3.3 Evaluation of the DrivAer simulations..... | 44 |
| 3.4 Generic autonomous shuttle | 46 |
| 3.4.1 Design of the generic shuttle | 47 |
| 3.4.2 Setup of the generic autonomous shuttle simulation..... | 49 |
| 3.5 Design influence on the generic shuttle | 50 |
| 3.5.1 Derivation of the study-relevant design variables | 50 |
| 3.5.2 Setup of simulations | 51 |
| 3.6 Single sensor influence on the generic shuttle | 52 |

| | | |
|------------|--|--------------|
| 3.6.1 | Derivation of the study-relevant sensor single positions | 52 |
| 3.6.2 | Setup of simulations | 61 |
| 3.7 | Multi-sensor setup influence on the generic shuttle | 61 |
| 3.7.1 | Derivation of the study-relevant sensor layouts | 61 |
| 3.7.2 | Setup of the simulations | 62 |
| 4 | Results | 65 |
| 4.1 | Evaluation of generic shuttle simulation..... | 65 |
| 4.2 | Evaluation of design influence on the generic shuttle | 69 |
| 4.2.1 | Windshield angle..... | 69 |
| 4.2.2 | Edge rounding | 70 |
| 4.2.3 | Covered wheel..... | 71 |
| 4.3 | Evaluation of single sensor on the generic shuttle | 71 |
| 4.3.1 | Sensor impact evaluation: functional approach..... | 78 |
| 4.4 | Evaluation of sensor setup on the generic shuttle..... | 79 |
| 4.4.1 | Sensor setup b_S_d_B | 80 |
| 4.4.2 | Sensor setup c_S_i_S | 80 |
| 4.4.3 | Sensor setup a_S_b_S_k_S | 80 |
| 4.4.4 | Sensor setup a_S_g_S_i_S | 81 |
| 4.4.5 | Sensor setup b_B_c_S_l_S | 81 |
| 4.4.6 | Sensor setup a_boxB_c_B_g_S_i_S | 81 |
| 4.4.7 | Sensor setup a_S_c_S_h_S_i_S | 82 |
| 4.5 | Creation of the mathematical model to assess the impact of sensor setups | 82 |
| 4.5.1 | Model..... | 83 |
| 5 | Discussion | 87 |
| 6 | Summary | 91 |
| | List of Figures | i |
| | List of Tables | xvii |
| | Bibliography..... | xix |
| | Appendix | xxiii |

List of Abbreviations

| | |
|-------|--|
| AAWK | Audi Aeroacoustic Wind Tunnel |
| BGK | Bahattnagar-Gross-Krook |
| CAD | Computational Aided Design |
| CAV | Connected and Automated Vehicle |
| CFD | Computational Fluid Dynamics |
| CPU | Central Processing Unit |
| DDES | Delayed Detached Eddy Simulation |
| DES | Detached Eddy Simulation |
| DNS | Direct Numerical Simulation |
| FKFS | Research Institute for Road Vehicles and Engines |
| GPU | Graphics Processing Unit |
| GS | Ground Simulation |
| ICE | Internal Combustion Engine |
| IDDES | Improved Delayed Detached Eddy Simulation |
| LBE | Lattice Boltzmann Equation |
| LBGK | Lattice Bahattnagar-Gross-Krook |
| LBM | Lattice Boltzmann Method |
| LES | Large Eddy Simulation |
| LGA | Lattice Gas Automaton |
| NEDC | New European Driving Cycle |
| NS | Navier Stokes |
| OEM | Original Equipment Manufacturer |
| PVT | Volvo Cars Slotted Walls Wind Tunnel |
| RANS | Reynolds Averaged Navier Stokes |
| RST | Reynolds Stress Tensor |
| SST | Shear Stress Transport |
| TCO | Total Cost of Ownership |
| TUM | Technical University of Munich |
| uRANS | Unsteady Reynolds Averaged Navier Stokes |
| VLES | Very Large Eddy Simulation |
| WT | Wind Tunnel |

Formula Symbols

| Formula Symbols | Unit | Description |
|--|-------------------|--|
| $\alpha, \beta, \gamma, \delta, \zeta$ | - | Identified turbulent structures in the generic shuttle simulation |
| ΔC_d | - | Drag coefficient increment |
| Δt | s | Time increment between timesteps |
| Δx | m | Dimension/length of the cell |
| ϵ | J/kg s | Dissipation rate |
| η | m | Kolmogorov length-scale |
| θ | ° | Road slope angle |
| κ | J/kg | Turulent kinetic energy |
| μ | kg/m s | Dynamic viscosity |
| μ_R | - | Rolling resistance coefficient |
| ν | m ² /s | Kinematic viscosity |
| ν_t | m ² /s | Turbulent viscosity |
| ρ | kg/m ³ | Density |
| τ | N/m ² | Shear stress |
| τ_{wall} | - | Wall shear vector |
| $ \tau_{wall} $ | N/m ² | Wall shear magnitude |
| ω | - | Vorticity vector |
| $ \omega $ | s ⁻¹ | Vorticity magnitude |
| $\bar{\Omega}$ | - | Vorticity tensor |
| $\Omega_i(f(x, t))$ | - | Collision operator which represents the rate of change of f_i resulting from the collision |
| A | m ² | Frontal area |
| a | ° | Windshield angle |
| ac | m/s ² | Acceleration in the longitudinal movement of the vehicle |
| A_{in}, A_{out} | m ² | Inflow/Outflow cross-section area |
| b | mm | Vehicle width |
| c | m/s | Speed of sound in air medium |
| C_d | - | Drag coefficient |
| $C_{d,f}$ | - | Friction drag coefficient |
| $C_{d,p}$ | - | Pressure drag coefficient |
| C_l | - | Lift coefficient |
| C_p | - | Pressure coefficient |
| D | - | Velocity gradient tensor |
| e_i | - | Local particle velocity direction vector |
| F_A | N | Acceleration resistance |
| F_D | N | Drag force |
| F_H | N | Grade resistance |
| f_i | - | Single-particle velocity distribution function along the i-th direction |
| F_R | N | Rolling resistance |
| g | m/s ² | Gravity |

| | | |
|-----------------------|----------|--|
| H | mm | Vehicle height |
| i | - | Feasible directions of the particle velocities at each of the lattice |
| l | m | Characteristic length |
| M | - | Total number of feasible directions of the particle velocities at each position of the lattice |
| Ma | - | Mach number |
| m | - | Number of sensors multiple of 4 |
| \dot{m} | kg/s | Mass flow |
| m_{res} | kg | Resistance mass |
| m_v | kg | Vehicle mass |
| n | - | Odd number of sensors |
| n_{cells} | - | Number of cells |
| N | % | Incline |
| P | Pa | Pressure |
| $\langle P \rangle$ | Pa | Time averaged pressure |
| P_{amb} | Pa | Ambient pressure |
| P_{dyn} | Pa | Dynamic pressure |
| $P_{dyn,\infty}$ | Pa | Dynamic pressure at freestream conditions |
| P_{stat} | Pa | Static pressure |
| P_x | Pa | Pressure in the x direction |
| P_z | Pa | Elevation pressure |
| q | s^{-2} | Q-value |
| r | mm | Edge radius |
| Re | - | Reynolds number |
| Re_η | - | Kolmogorov Reynolds number |
| Re_{crit} | - | Critical Reynolds number |
| Re_R | - | Radius Reynolds number |
| S | m^2 | Body's surface |
| \bar{S} | - | Rate-of-strain tensor |
| t | s | Time |
| t_m | s | Molecular mixing timescale |
| t_t | s | Turbulent mixing timescale |
| Tu | % | Turbulence intensity |
| U | m/s | Velocity magnitude |
| \bar{U} | m/s | Surface averaged velocity magnitude |
| u | - | Velocity vector |
| U_τ | m/s | Shear velocity magnitude |
| u_τ | - | Shear velocity vector |
| $u_{\tau,x}$ | m/s | Velocity component in direction x |
| U_c | m/s | Characteristic velocity magnitude |
| u_i | m/s | Velocity component i |
| u'_i | m/s | Time fluctuations of the velocity in direction i |
| $\langle u_i \rangle$ | m/s | Time averaged value value of the velocity in direction i |
| U_∞ | m/s | Freestream velocity magnitude |
| x | - | Space vector |
| x_i | m | Space component i |
| y | m | Perpendicular distance from the surface |
| z | m | Elevation |

Acknowledgment

Foremost, I would like to thank Mr. Prof. Dr.-Ing. Markus Lienkamp for allowing me to write my thesis in the field that I love the most, vehicle aerodynamics.

I would like to thank my mentor M. Sc. Philipp Hafemann, for the constant support, interest, feedback and encouragement during the entire 6 months. His excellent guidance and advice help me shape this thesis into something that I'm proud of. I'm absolutely thanked for his mentorship.

Also, my sincere appreciations to my current boss Eugen Riegel for giving me access to the *Pacefish*[®] and the GPU cluster. It gave me the chance to perform this study at a level of accuracy that I would have never accomplished otherwise. Moreover, I'm honestly thanked for his unconditional support when I had any aerodynamic or technical doubt. He was always willing to give me a hand.

Finally, I want to express my most profound gratitude to my beloved ones, that during these last months helped me face the challenges that I encountered. Without their help, even from the distance, I would have never made it.

Munich, October 2021.

1 Introduction

Nowadays, the road transportation paradigm is changing after many years of stagnation in small iterations of the same vehicle shapes and propulsion methods. The rapid evolution of battery technology and machine learning, the lowering price of sensors and other electric components, together with the constant increase in density of urban areas, brings the opportunity to develop a new vehicle concept that not only adapts to the urban transportation needs, but that does it in an efficient and environmentally friendly way. For that reason, several companies started to develop an electric autonomous driving shuttle-like vehicle/taxi in the last few years. This vehicle concept seems to check all the boxes to redefine the future of urban mobility:

- It is electric. Therefore does not produce "tank-to-wheel" emissions. This is not only beneficial in terms of the global environment, but it directly impacts the air quality in the cities, where most of the population of the world lives.
- It embraces the concept of car-sharing or taxi mobility, which reduces the number of vehicles on the road and therefore allows almost invariable and faster transportation times between two points. Moreover, this vehicle sharing concept aims to ultimately substitute owning a car, which is economically beneficial for many drivers due to the high Total Cost of Ownership (TCO) of most current cars.
- It uses autonomous driving capabilities to increase transportation efficiency (number of users per vehicle), minimize road accidents and reduce costs.
- It is designed for urban environments and, for that reason, the driving is predictably more efficient than in highway conditions. Thus, it can use compact batteries that take less space; hence it has higher package efficiency in terms of cabin space.
- It has the potential to belong in a network of connected vehicles, which optimizes the global mobility of the cities even further.

Given the characteristics of this vehicle, it is highly desirable to achieve low energy consumption. Therefore, it is crucial to analyze and possibly optimize all components that produce a loss in the energy chain that connects the chemical energy from the battery to the car's kinetic energy. From those, the aerodynamic resistance is noticeably influential. In urban conditions, it represents approximately 21% of the total energetic loss in electric vehicles [1], while at highway speed, this share rises substantially. This increase is caused by the velocity-quadratic behavior of the drag force. This highlights the relevance of the aerodynamic force at high speeds in case this vehicle concept transitions from urban to highway mobility. For that reason, this project focuses on the impact of sensor layouts in the drag coefficient C_d of autonomous shuttles quantified as the ΔC_d in comparison with a reference geometry. A mathematical model is developed based on the simulated results to estimate the ΔC_d impact of sensor setups.

This study opens the topic of autonomous shuttle aerodynamics, which has not been explored before due to the novelty of this vehicle concept.

This thesis is structured in the following parts:

- Chapter 2 is an introduction to general aerodynamics and vehicle aerodynamics, it collects current autonomous shuttle published data and introduces the Computational Fluid Dynamics (CFD) simulation software *Pacefish*[®].
- Chapter 3 describes the methodology, workflow and steps followed to perform the aerodynamic analysis. Additionally, it includes the evaluation of the current autonomous shuttle design space and the derivation of the relevant geometries to study.
- Chapter 4 analyzes the simulation results and proposes a mathematical model to approximate the aerodynamic impact of sensor setups on autonomous shuttles.
- Chapter 5 exposes the conclusions of this study.

2 State of the Science and Technology

Nowadays, road vehicles with autonomous driving capabilities have a range of shapes that go from a "stock-design cars" shape to "box concepts" and all the spectrum in between (as depicted in Figure 2.1).

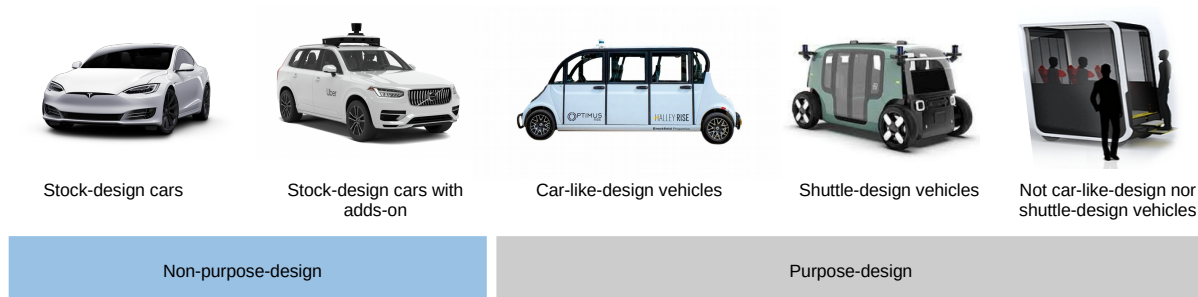


Figure 2.1: Current spectrum of autonomous driving road vehicles (in production or under development) in terms of external design

The stock-design cars take the conservative approach of blending/incorporating autonomous driving capabilities with/in "traditional-shaped" cars. This take has various potential limitations and technical difficulties, besides the intrinsic complexity of autonomous driving functionalities. The adaptation of regular cars to drive autonomously requires the addition of multiple data-collection components in the bodywork. These have a significant impact on the vehicle at all levels (electrical requirements, packaging, aerodynamics, costs, and others), inevitably leading to compromises in some areas. On top of that, the adoption of autonomous driving capabilities of traditionally shaped cars does not have a transcendent impact on urban mobility. They are personal-owned vehicles for personal use.

On the other side of the spectrum, there are the purpose-design autonomous road vehicles. These are new concepts that do not follow any design heritage or socially embedded conception of vehicle aesthetics. They are inevitably design-disruptive given their different take on their usage and their role in urban mobility. Unlike autonomous driving stock-design cars, purpose-design vehicles are conceptualized for efficient urban shared mobility. This is translated to two main shared technical specifications of the vehicles categorized within this group:

- Electric-powered
- High package efficiency in terms of effective cabin volume¹

The aim of maximizing the effective cabin volume and its focus on urban mobility influences the overall shape/proportions of this vehicle concept.

This thesis focuses on the aerodynamic influence of sensor setups in shuttle-design vehicles (the second vehicle starting from the right in Figure 2.1). They represent a significant proportion of all

¹Maximum number of possible transported people per surface unit of cabin floor

current purpose-design autonomous road vehicles. Moreover, their similar design language (in terms of proportions) slightly facilitates the aerodynamic study. For that purpose, it is essential to define the concept of the autonomous shuttle. There is no official definition of such a vehicle. In this thesis, it is considered as the vehicle that meets the following characteristics:

- Purpose-designed road vehicle.
- Autonomous driving level 4 or above.
- Possibility to easily access all sitting/standing positions once inside the vehicle.
- Recognizable length of the car in terms of dimensions (significantly bigger than the width).
- Side-mounted door/s to access the cabin.

These conditions exclude:

- Car-like purpose-design vehicles (the third vehicle starting from the right in Figure 2.1) with rows of seats facing exclusively one direction without possibility to access all seats once inside the vehicle.
- Differently shaped purpose-design vehicles (the first vehicle starting from the right in Figure 2.1).

For this study, literature research on the aerodynamics of shuttle vehicles has been conducted with the intent to obtain reference data for comparability/validation purposes. Additionally, technical and dimensional characteristics of existing autonomous shuttles have been gathered. These define the reference geometry on which the aerodynamic study is based.

The following two sections expound, assemble and analyze the knowledge and data required for the target of this thesis: *Simulation and modeling of the aerodynamic impact of sensor setups on autonomous road vehicles*. Section 2.1 is an introduction to the fundamentals of aerodynamics, road vehicle aerodynamics and autonomous shuttle aerodynamics. Section 2.2 summarizes the collected information regarding geometrical and technical specifications of currently active/under development autonomous shuttles.

2.1 Introduction to aerodynamics

This section briefly introduces aerodynamics and related literature, essential for understanding the simulation framework and the corresponding aerodynamic evaluation.

2.1.1 Fundamentals of aerodynamics

Aerodynamics is the part of fluid dynamics that studies the properties and effects of moving air around solids.

Classification of flows

There are multiple ways to classify a flow. The following are the most relevant:

- By its dimension: 1-dimensional, 2-dimensional or 3-dimensional.

- By its temporal response: steady and unsteady.
- By its viscosity: Newtonian or non-newtonian.
- By its density: compressible or incompressible.
- By its Reynolds number: laminar or turbulent.

In the framework of this study (external car aerodynamics), the most interesting classification is Reynolds-related. The properties used for the other classification methods remain invariable throughout the simulation time in the spatial domain. Air at normal road vehicle driving conditions is:

- 3-dimensional: The air in the three dimensions of the space around the vehicle.
- Unsteady: The properties of the air fluctuate in the time domain. Thus, a simulation software that approaches the study of the fluid properties in the time domain is preferred. Even though the temporal approach of the software does not define the accuracy of the simulated scenario, an unsteady simulation can potentially provide information filtered out otherwise. This study employs the CFD software *Pacefish*[®].
- Newtonian: The shear stresses are linearly correlated to the shear velocity in the perpendicular direction of the flowing air. This correlation constant is defined as the dynamic viscosity. Equation 2.1 expresses the interaction of these three factors:

$$\tau = \mu \frac{du}{dy} \quad (2.1)$$

where:

- τ = Shear stress
- μ = Dynamic viscosity
- y = Perpendicular distance from the surface
- u = Flow velocity along the boundary

- Incompressible: The air density is considered invariable. This assumption presumes that no air particle of the simulation domain reaches $U \sim 367$ km/h (Mach number is below 0.3), which is a safe consideration in external car aerodynamics at normal road conditions.

$$Ma = \frac{U}{c} \quad (2.2)$$

where:

- U = Speed magnitude of air
- c = Speed of sound in air medium

The speed of sound can be calculated with a specific formula that contemplates the medium's particle state. Nonetheless, the approximation of $c = 340$ m/s is considered valid in the aerodynamic framework of this study. The used value for the density is $\rho = 1.23$ kg/m³.

The Reynolds number is an unsteady flow characteristic in the simulation time and spatial domain, unlike the previous properties. For that reason, it is of particular interest.

Reynolds number

The Reynolds number is a dimensionless parameter that defines the regime of turbulence of the fluid. It characterizes the state of the fluid in terms of its viscous-to-inertial forces. The formula of the Reynolds number is the following:

$$Re = \frac{Ul}{\nu} \quad (2.3)$$

where:

U = Speed magnitude of the flowing air

l = Characteristic length

ν = Kinematic viscosity

Under the studied conditions and at the same conditions with assume $\rho = 1.23 \text{ kg/m}^3$, the kinematic viscosity is approximated as:

$$\nu = \frac{\mu}{\rho} \approx 1,5 \times 10^{-5} \frac{\text{m}^2}{\text{s}} \quad (2.4)$$

The characteristic length (l) from the Reynolds number equation Equation 2.3 is normally considered as the length of the object in the freestream direction. However, this value describes the flow state at the end of such length. The first interaction of the fluid with the body occurs at $l = 0 \text{ m}$. At that point, $Re = 0$. As the fluid particles move along the solid surface, the characteristic length, and proportionally the Reynolds number, increase.

At low Re numbers, the viscous forces prevail over the inertial forces. The fluid does not significantly mix, such that its particles can transfer momentum to one another. This effect is known as molecular diffusion. The timescale of the mixing by molecular diffusion can be expressed as follows:

$$t_m \sim \frac{l^2}{\nu} [\text{s}] \quad (2.5)$$

where:

l = Given length-scale

ν = Kinematic viscosity

This timescale contemplates the viscosity, which characterizes the fluid at such low Re numbers. This type of flow is denominated: laminar flow.

At high Re numbers, the inertial forces prevail over the viscous forces. The particles of the fluid mix with each other. This effect is known as advection or turbulent diffusion, and its timescale can be expressed as follows:

$$t_t \sim \frac{l}{U_c} [\text{s}] \quad (2.6)$$

where:

l = Given length-scale

U_c = Characteristic velocity magnitude

In the timescale of the turbulent mixing, the viscosity does not appear. Instead, the velocity represents the inertial forces that predominate in the fluid at these Re numbers. This type of flow is denominated: turbulent flow.

The Reynolds number is the rate of the two timescales:

$$\frac{t_m}{t_t} \sim \frac{u'l}{\nu} \sim Re_t \quad (2.7)$$

From the Equation 2.7, it can be discerned that high Re values translate to $t_m > t_t$. Hence, the turbulent mixing timescale (t_t) is smaller. Thus, it appears in a higher frequency. This means that the turbulent mixing prevails over the molecular diffusion.

The division between laminar flows (low Re) and turbulent flows (high Re) occurs at a critical Reynolds value (or range of values). There is no universal critical Re number that clearly defines the transition point between laminar and turbulent flows. Multiple variables affect this phenomenon, the most relevant ones being the geometry topology and the surface roughness of the solid. The accepted critical Re number has been updated to adapt to renewed standards during the years, most of which are based on experimental data. Nowadays, the accepted value for the transition from laminar to turbulent lay around $Re_{crit} \simeq 5 \times 10^5$ [2]. Nonetheless, the particular value depends on the air properties and the solid characteristics of the specific situation.

The appearance of the laminar-to-turbulent transition (if that is the case) during the fluid-solid interaction influences the detachment of the boundary layer, and subsequently, it can considerably impact the body's drag coefficient. Figure 2.2 depicts the Reynolds number influence over the total drag coefficient C_d of a sphere. Note that the transition to turbulent flow causes the substantial decrease in C_d of the sphere around $Re = 3 \times 10^5$. In such conditions, the air stays attached to the solid for a longer distance. This causes a reduction of the wake behind the sphere, which decreases the drag.

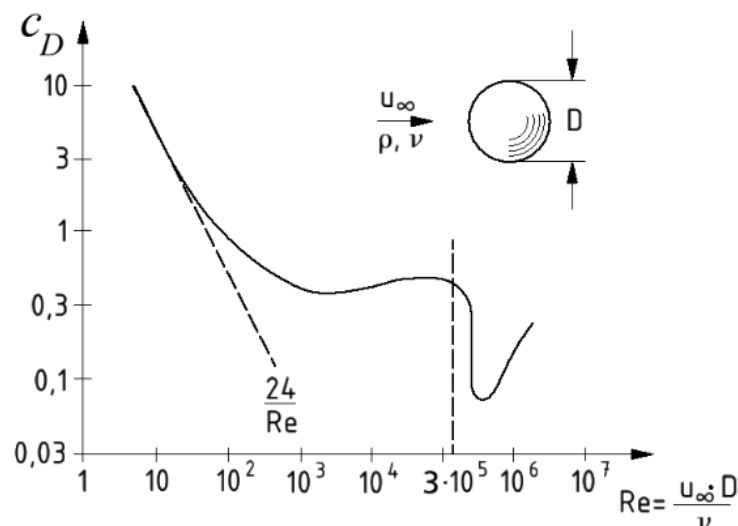


Figure 2.2: Drag coefficient C_d function of Reynolds number of a sphere (Dillmann, 2016, p. 127, Fig 2.43) [2]

As mentioned before, various variables influence the Re_{crit} value, which at the same time, influences the C_d . Figure 2.3 depicts the typical example of a golf ball, in which the influence of

the surface roughness on the drag (chart (a)) and influence of the turbulence intensity (Tu) on the critical Re number (chart (b)) are represented. The turbulence intensity or turbulence level (Tu in %) assesses the relative importance of the fluctuation of the velocity components relative to the mean velocity of the fluid. The surface roughness is a measure of microscopic surface topology. On the chart (a) of Figure 2.3, the surface roughness is measured in sand-grain roughness relative to the diameter of the sphere.

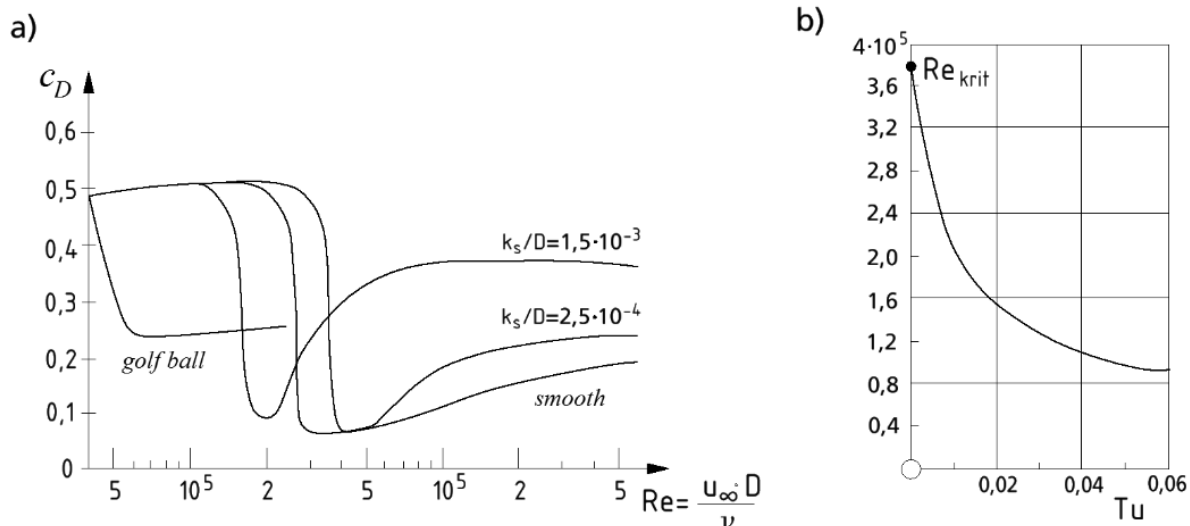


Figure 2.3: Influence of the surface roughness on the drag (chart (a)) and influence of the turbulence intensity (Tu) on the critical Re number (chart (b)) (Dillmann, 2016, p. 128, Fig 2.44) [2]

The examples presented in Figures 2.2 and 2.3 depict the critical Reynolds impact on the drag coefficient of spheres, which are blunt bodies. On these types of bodies, the pressure contribution on the drag prevails over the friction contribution. Nonetheless, not all bodies behave in such a manner. At the other extreme of the spectrum, there are the streamlined bodies. These geometries have virtually no pressure drag. Their C_d vs. Re characteristic line is horizontal or with minimal positive constant slope at low drag coefficient values. Further information about the drag and the boundary layer is explained in pages 15 and 17, respectively.

Governing equations

There are two main (equivalent) approaches for the characterization of a fluid volume:

- Consideration of the fluid as a continuum medium (macroscopic): Navier Stokes equations.
- Consideration of the fluid as a group of particles (microscopic): Lattice Boltzmann equation.

Navier Stokes The Navier Stokes (NS) equations apply Newton's second law over a differential volume of fluid. They are derived from the two following assumptions:

1. Continuity equation:

$$\Delta u = \frac{\partial u_i}{\partial x_i} = 0 \quad (2.8)$$

where:

u_i = Velocity component i

x_i = Space component i

This implies constant density: $\rho = cte$. The continuity equation (Equation 2.8) is sometimes referred to as the mass conservation law. In an enclosed volume with inflow and outflow surfaces, like the one depicted in Figure 2.4, the continuity law indicates constant mass flow between the inflow and the outflow is $\dot{m}_{in} = \dot{m}_{out}$. This can be reformulated as:

$$\rho \overline{U}_{in} A_{in} = \rho \overline{U}_{out} A_{out} \quad (2.9)$$

where:

ρ = Density

\overline{U}_{in} = Inflow surface averaged velocity magnitude

A_{in} = Inflow cross-section area

\overline{U}_{out} = Outflow surface averaged velocity magnitude

A_{out} = Outflow cross-section area

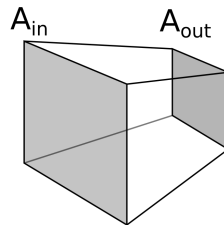


Figure 2.4: Defined volume with single inflow and outflow surfaces

As depicted in Figure 2.4, $A_{in} > A_{out}$. If this condition is added to Equation 2.8, it results: $\overline{U}_{in} < \overline{U}_{out}$. This simple example represents the acceleration/deceleration effect of the fluid due to the reduction/enlargement of cross-section area. In automotive external aerodynamics this event is frequently observable.

2. Conservation of momentum:

$$\frac{\partial u_i}{\partial t} + \frac{\partial (u_i u_j)}{\partial x_j} = -\frac{1}{\rho} \frac{\partial P}{\partial x_i} + \frac{\partial^2 u_i}{\partial x_j^2} \quad (2.10)$$

where:

u_i = Velocity component i

u_j = Velocity component $j, j \neq i$

t = Time

x_i = Space component i

ρ = Density

P = Pressure

The combination of both assumptions (Equations 2.8 and 2.10) leads to the NS equations:

$$\frac{\partial u_i}{\partial t} + u_j \frac{\partial u_i}{\partial x_j} = -\frac{1}{\rho} \frac{\partial P}{\partial x_i} + \nu \frac{\partial^2 u_i}{\partial x_j^2} \quad (2.11)$$

where:

- u_i = Velocity component i
- u_j = Velocity component j , $j \neq i$
- t = Time
- x_i = Space component i
- ρ = Density
- P = Pressure
- ν = Kinematic viscosity

Lattice Boltzmann This approach considers the fluid differential as a discrete collection of particles. This perspective is implemented in the CFD software *Pacefish*[®], which has been used to perform the aerodynamic simulations.

The upcoming introduction to Lattice Boltzmann Method (LBM) is based on the publications of Chen [3] and Yu [4].

This method assumes that the macroscopic dynamics of a fluid can be expressed as the collection of particle behaviors. The Lattice Boltzmann Equation (LBE), which the LBM solves, describes the kinetics of the constituent particles. This equation is derived from the Lattice Gas Automaton (LGA), which is constructed as a simplified, fictitious molecular dynamic in which space, time and particle velocities are all discrete. Therefore, particles can only be placed in discrete positions defined by a lattice and move in a discrete manner to the immediate surroundings at each point in time. The exclusion principle remains valid at every timestep and position: no more than one particle is allowed at a given time. The LBE is the discrete kinetic equation for the particles distribution function:

$$f_i(x + e_i \Delta x, t + \Delta t) = f_i(x, t) + \Omega_i(f(x, t)) \quad i = 0, 1, \dots, M \quad (2.12)$$

where:

- x = Position vector
- t = Time
- Δx = Dimension/length of the cell
- Δt = Time increment between timesteps
- i = Feasible directions of the particle velocities at each of the lattice
- M = Total number of feasible directions of the particle velocities at each position of the lattice
- e_i = Local particle velocity direction vector
- f_i = Single-particle velocity distribution function along the i -th direction
- $\Omega_i(f(x, t))$ = Collision operator which represents the rate of change of f_i resulting from the collision

The number of feasible directions from which a particle can move in consecutive time points i , and consequently their respective velocity direction vectors (e_i), are defined by the lattice dimension and the user preference.

The evolution between consecutive timesteps is composed of two sub-steps: streaming and collision. The streaming sub-step describes the propagation of the particles to the arrival lattice positions covering the advection of the fluid. Many approaches exist for the collision term ($\Omega_i(n(x, t))$), which describes the particle interaction covering the friction of the fluid. One of the most known approaches assumes a linearly stable collision operator, which uses a relaxation term known as Bahattnagar-Gross-Krook (BGK). Qian [5] further developed various models in three dimensions based on the Lattice Bahattnagar-Gross-Krook (LBGK) concept.

From the LBE (Equation 2.12), the macroscopic fluid variables can be derived.

In order to derive the NS equations from LBE, the Chapman-Enskog expansion is used. In essence, it is a standard multi-scale expansion of the LBE in the nearly incompressible limit. Yu [4] further develops this topic.

CFD solving methods and turbulence modeling

The working principle of CFD software is the application of the fluid's governing equations in a delimited spatial and temporal domain up to a particular scale and defined error.

The Direct Numerical Simulation (DNS) solving method resolves all flow structures up to the Kolmogorov scale (η). This length-scale defines the threshold for smaller flow structures to dissipate their energy in viscosity (ν) through a dissipation rate (ϵ). This assumption is based on the Kolmogorov Hypothesis of energy transfer in turbulent flows, depicted in Figure 2.5. Kolmogorov theorized that turbulent fluctuations consist of different length and time scales. Large length (long-wave) and large time-scales (low-frequency), which he observed to be the source of turbulence, decay to shorter-scale and higher-frequency fluctuations until they become so small that they dissipate into heat, which occurs at $Re_\eta = 1$. This theory has been empirically confirmed, evidencing the existence of universal laws for the inertial and dissipation sub-ranges (from Figure 2.5).

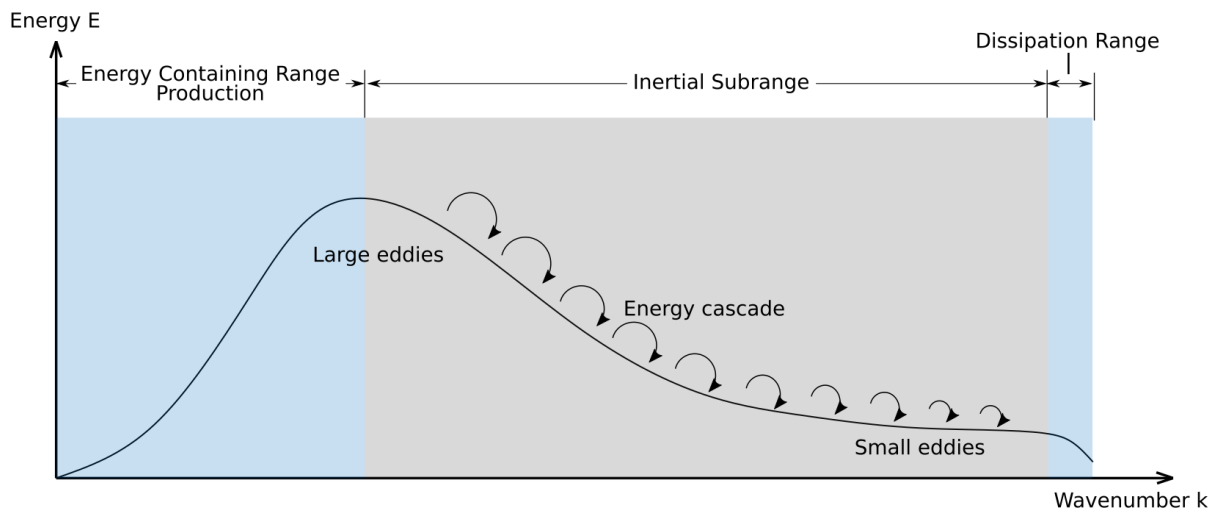


Figure 2.5: Kolmogorov energy transfer theory

The Kolmogorov Reynolds (Re_η), together with the simulation space and the simulated velocity, define the total number of cells. An example of external car aerodynamics follows. It considers a simulation domain of $15 \times 6 \times 3$ (measured in reference length), a reference length of 4.5 m and three grid points to represent a Kolmogorov length-scale (η).

$$Re_\eta = 1 = \frac{u\eta}{\nu} \Rightarrow \eta = \frac{\nu}{u} = \frac{1.5 \times 10^{-5}}{13.8} = 1.09 \times 10^{-6} m \quad (2.13)$$

Hence:

$$n_{cells} = 15 \times 6 \times 3 \times \left(\frac{l}{\eta} \times 3 \right) = 15 \times 6 \times 3 \times \left(\frac{4.5}{1.09 \times 10^{-6}} \times 3 \right) = 5,17 \times 10^{23} cells \quad (2.14)$$

where:

- Re_η = Kolmogorov Reynolds
- u = Simulation velocity
- η = Kolmogorov length-scale
- ν = Kinematic viscosity
- n_{cells} = Number of cells
- l = Characteristic length

As seen in the previous calculation (Equation 2.14), the resulting number of cells is immensely high, such that it is not feasible to perform a simulation with that solving method.

Note that the solving method does not define the approach considered for the treatment of the fluid. It can use either Navier Stokes or the Lattice Boltzmann fluid governing equations.

The Large Eddy Simulation (LES) approach resolves the turbulent structures until a defined length-scale. Smaller structures can not be captured in the grid (their size is inferior to the cell length), and therefore, a modeling technique is required to account for their effect. This is usually performed with the addition of a Turbulent Viscosity (ν_t). The concept of Turbulent Viscosity is derived from the Reynolds Averaged Navier Stokes (RANS) solving method (later explained in this section). The LES approach works very well in the far-field, but using it close to solid walls requires high resolution, which is not for industrial-scale applications. Like the DNS, this solving method can use either the NS or the LBE even though the concept of ν_t is derived from the RANS equation.

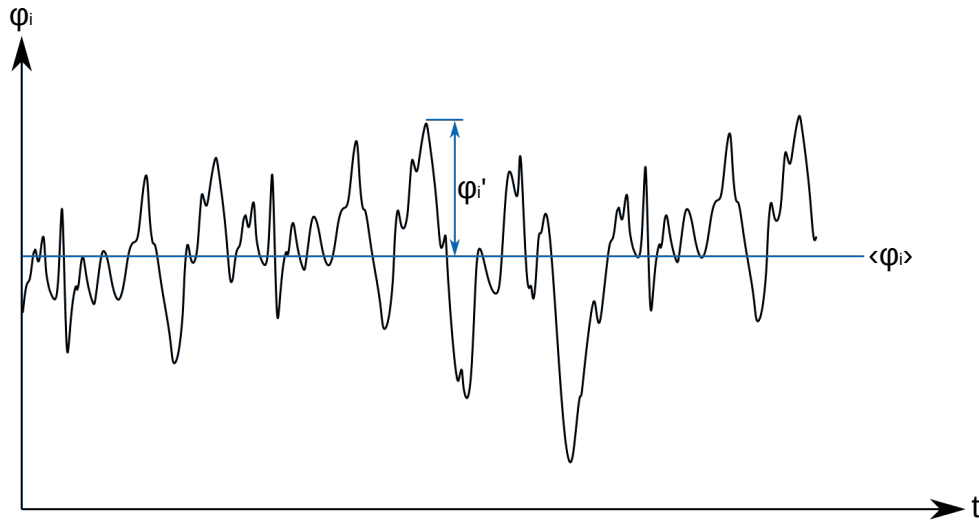
The RANS solving method applies Reynolds decomposition to the NS equation (Equation 2.11). This decomposition considers the fluid properties as a sum of a time averaged value and a fluctuation component for each of the three space dimensions (i). See below:

$$\varphi_i = \langle \varphi_i \rangle + \varphi'_i \quad (2.15)$$

where:

- φ_i = Property in direction i
- $\langle \varphi_i \rangle$ = Time averaged value of the property in direction i
- φ'_i = Time fluctuations of the property in direction i

Visual representation of the Reynolds averaging/decomposition is depicted in Figure 2.6.

Figure 2.6: Reynolds decomposition applied to property φ

The application of the Reynolds decomposition (Equation 2.15) to the Navier Stokes equations (Equation 2.11), brings the RANS equation:

$$\frac{\partial \langle u_i \rangle}{\partial t} + \langle u_j \rangle \frac{\partial \langle u_i \rangle}{\partial x_j} = -\frac{1}{\rho} \frac{\partial \langle p \rangle}{\partial x_i} + \frac{\partial}{\partial x_j} \left(\nu \frac{\partial \langle u_i \rangle}{\partial x_j} - \langle u_i' u_j' \rangle \right) \quad (2.16)$$

where:

t = time

$\langle u_i \rangle$ = Time averaged value value of the velocity in direction i

$\langle u_j \rangle$ = Time averaged value value of the velocity in direction j , $j \neq i$

u_i' = Time fluctuations of the velocity in direction i

u_j' = Time fluctuations of the velocity in direction j , $j \neq i$

x_i = Displacement in direction i

x_j = Displacement in direction j , $j \neq i$

$\langle p \rangle$ = Time averaged Pressure

ν = Kinematic viscosity

ρ = Density

The so-known Reynolds Stress Tensor (RST) appears on the RANS equation (Equation 2.16): $\langle u_i' u_j' \rangle$. This component has no clear physical interpretation. For that reason, multiple approximations exist to model it. These are known as turbulence models. The mainstream turbulence models are depicted in Figure 2.7.

The most used models account for the effects of the turbulent fluctuations at all scales, large, medium and small, by an additional local Turbulent Viscosity ν_t . From those, the most used is the $\kappa - \omega$ Shear Stress Transport (SST). This combines both descriptions of the ν_t with $\kappa - \omega$ near the walls and $\kappa - \epsilon$ in the far-field. Despite the fact that the artificial Turbulent Viscosity concept is discovered using RANS, it can be applied within the LBM in similar way. This is depicted in Figure 2.8. The Unsteady Reynolds Averaged Navier Stokes (uRANS) denomination refers to applying the RANS equations in the time domain.

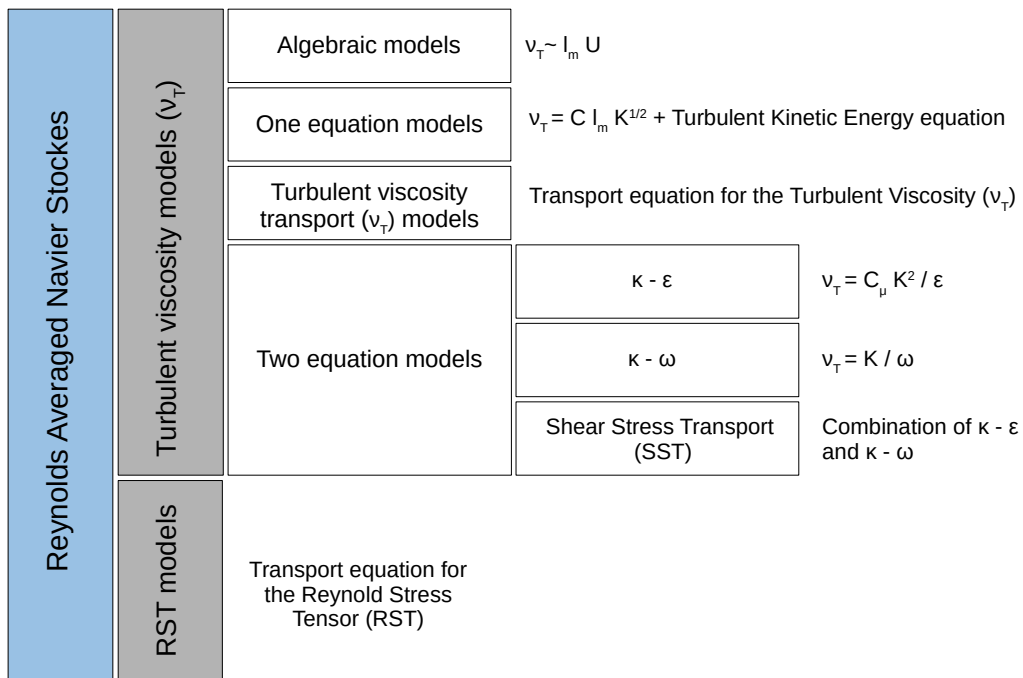


Figure 2.7: Overview of the mainstream turbulence models

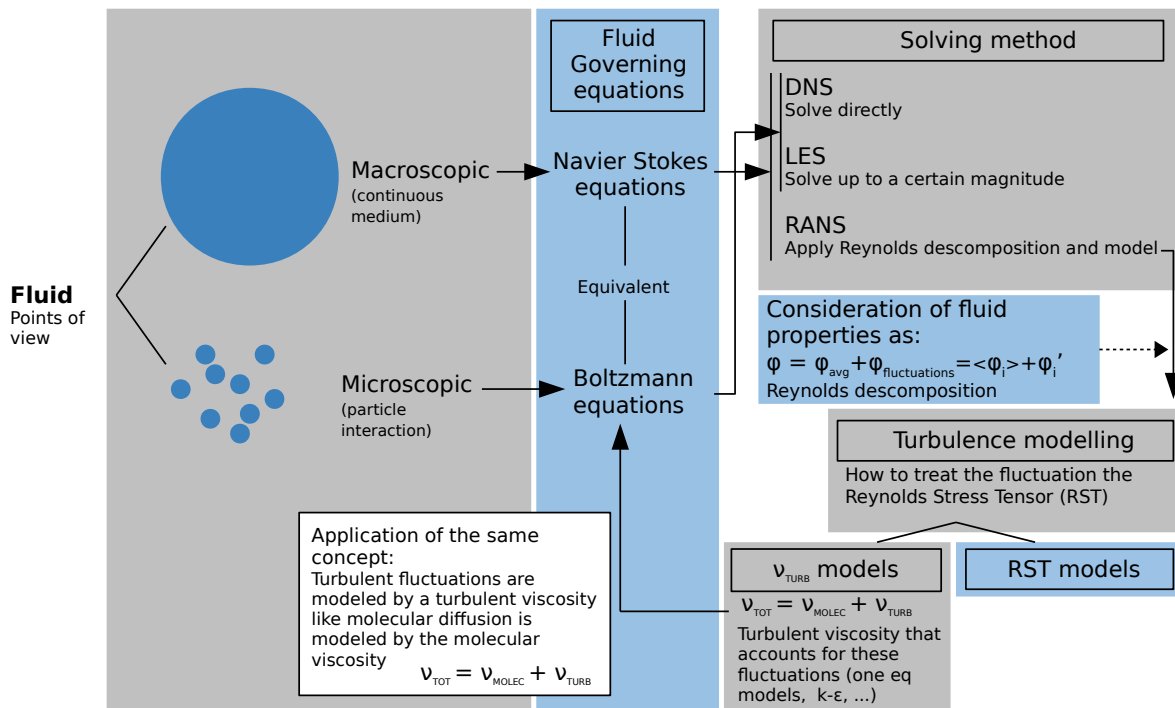


Figure 2.8: Overview of the turbulent viscosity concept applied to LBM

The Detached Eddy Simulation (DES) approach uses a hybrid RANS-LES turbulence modeling. Depending on the blending point between the RANS and LES, two turbulence models are used: SST-Delayed Detached Eddy Simulation (DDES) and SST-Improved Delayed Detached Eddy Simulation (IDDES), both from the $\kappa - \omega$ SST family. Figure 2.9 depicts the blending point between RANS and LES of the two turbulence models. Close to solid walls, the SST-DDES and SST-IDDES use the uRANS approach, enabling a robust solution for under-resolved walls. Approaching the far-field (freestream conditions), both turbulence models blend over to LES to

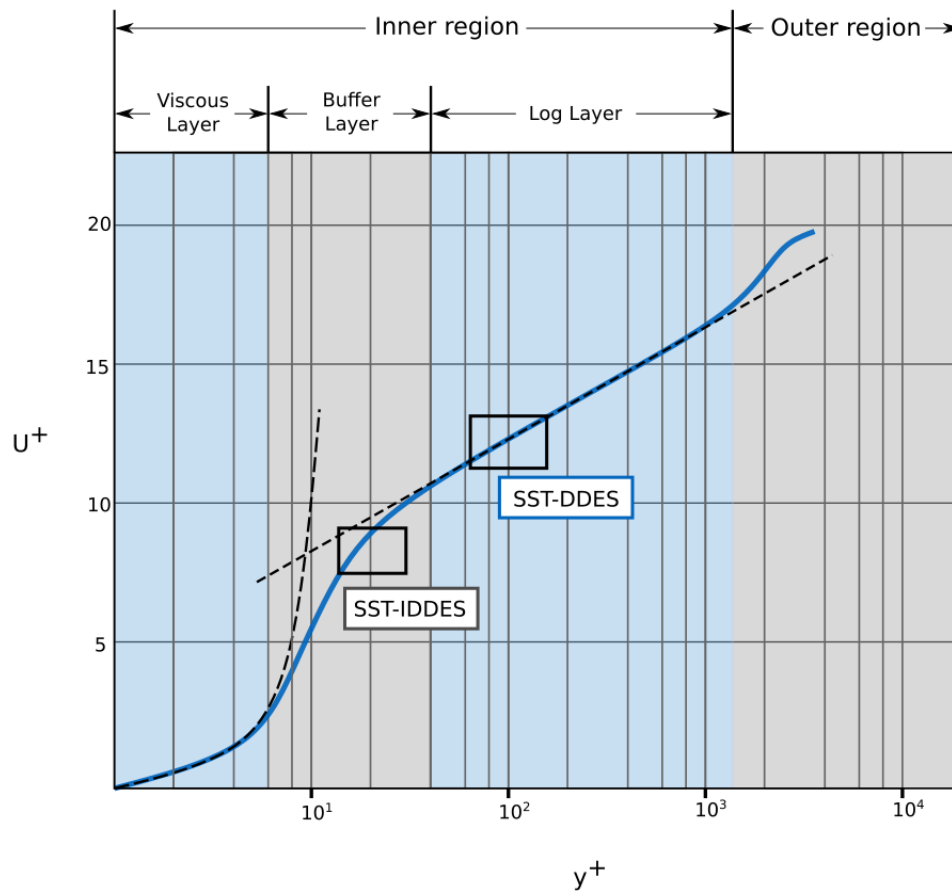


Figure 2.9: Blending y^+ positions of the SST-DDES and SST-IDDES in the turbulent boundary layer

resolve the large-scale fluctuations and fluid dynamics directly in the transient velocity vector and pressure states. Nonetheless, the blending point differs between the two models. As depicted in Figure 2.9, the SST-IDDES method transitions from uRANS to LES in the Buffer Layer. This region has been found not to follow any universal mathematical expression. Differently, the Viscous Layer and the Log Layer are governed by universal laws. For that reason, the SST-DDES is a more robust turbulence model. The simulations performed in this thesis use this solving method.

Note that the y^+ is a "dimensionless length" parameter that can be interpreted as a local Reynolds number. It characterizes the fluid behavior close to the walls and enables the detection of universal laws. The U^+ is the mean fluid velocity normalized with the shear velocity.

Drag force and drag coefficient

In aerodynamics, the drag force is the force produced by the flowing air over a body (in the freestream direction) by the fact that it exists relative movement between the two. From the physical point of view, there are two types of drag force:

- Pressure drag force: It is produced by the pressure impact generated by the volume placement in the flow stream. It is calculated as the integration of the pressure in the freestream direction over the surface.

- Friction drag force: It is produced by the friction forces generated in the interface fluid-surface. It is calculated as the integration of the shear wall stresses in the freestream direction over the surface.

From the drag force, the drag coefficient (C_d) can be derived. This dimensionless parameter assesses the magnitude of the drag force over the body under specific flow conditions and independently of its frontal area. The formula that maps this relation follows:

$$F_D = \frac{1}{2} \rho A C_d U_\infty^2 \quad (2.17)$$

where:

- F_D = Drag force
- ρ = Density
- A = Frontal area
- C_d = Drag coefficient
- U_∞ = Free stream velocity magnitude

(Equation 2.17) is valid for each of the three space dimensions. Nonetheless, the *drag* naming refers to the component of the force in the freestream direction.

As described previously, the drag force is divided into pressure and friction effects. Analogously, the total drag coefficient is the contribution of the pressure drag and the friction drag coefficients. Their formulas follow:

$$C_{d,p} = \int_S \frac{P_x}{\frac{1}{2} \rho A U_\infty^2} dS \quad (2.18)$$

and

$$C_{d,f} = \int_S 2 \frac{u_{\tau,x}^2}{U_\infty^2} dS \quad (2.19)$$

where:

- $C_{d,p}$ = Pressure drag coefficient
- $C_{d,f}$ = Friction drag coefficient
- S = Body's surface
- P_x = Pressure in the x direction (fluid free streaming direction)
- ρ = Density
- A = Body's frontal area
- U_∞ = Free stream velocity magnitude
- $u_{\tau,x}$ = Shear velocity in the x direction

The x subindex denotes the freestream direction, which is generally the x -axis of the simulation domain.

The shear velocity (or friction velocity) is defined as:

$$u_\tau = \sqrt{\frac{\tau_{wall}}{\rho}} \quad (2.20)$$

where:

$$\begin{aligned} u_\tau &= \text{Shear velocity vector} \\ \tau_{wall} &= \text{Wall shear vector} \\ \rho &= \text{Density} \end{aligned}$$

The surface representation of this fluid property identifies the detachment of the boundary layer. The detachment is followed by the appearance of turbulent structures, which induce pressure drag.

Pressure coefficient

The pressure coefficient (C_p) is the dimensionless expression of the pressure. It is calculated as the normalization of the static pressure with the dynamic pressure at freestream conditions:

$$C_p = \frac{P_{stat}}{P_{dyn,\infty}} = \frac{P_{stat}}{\frac{1}{2}\rho U_\infty^2} \leq 1 \quad (2.21)$$

where:

$$\begin{aligned} P_{stat} &= \text{Static pressure considering an ambient pressure } P_{amb} = 101,325 \text{ Pa} \\ P_{dyn,\infty} &= \text{Dynamic pressure at freestream conditions} \\ \rho &= \text{Density} \\ U_\infty &= \text{Freestream velocity} \end{aligned}$$

The C_p is highly used in the aerodynamic analysis. Its maximum value is 1, which indicates a stagnation area. These are regions of high pressure commonly seen in front of bluff objects.

Boundary layer

The boundary layer is the part of the fluid that is closer to a body's surface. It is generated by the contact of fluid particles with the solid surface, which produces a velocity gradient between the solid surface (particles at velocity zero) and the positions away from the wall (particles at freestream velocity). This region of space contains laminar flow when the first air particle encounters the geometry. In the measure that the fluid travels along the surface (x), the Reynolds number proportionally increases ($Re = \frac{Ux}{\nu}$). When the Reynolds number reaches its critical value (Re_{crit}), the flow turns into a turbulent state. Figure 2.10 depicts this transition.

Note that the velocity profiles of the fluid in the two types of boundary layers are different. The laminar boundary layer contains essentially laminar flow, where the viscous forces prevail. Whereas inside the turbulent boundary layer, there are four identifiable regions called sub-layers. They are distinguished by the y^+ , a dimensionless height representing the flow state. It can be thought of as a local Reynolds number. The four regions are called: Viscous layer, Buffer layer, Log layer and Outer region. Figure 2.9 depicts the u^+ profile of the turbulent boundary layer. Universal laws rule the Viscous layer and the Log layer.

The concept of boundary layer detachment alludes to the separation of the streamlines from the body surface due to geometrical surface features. This generally induces an area of chaotic fluid particle movement with a negative pressure drag impact.

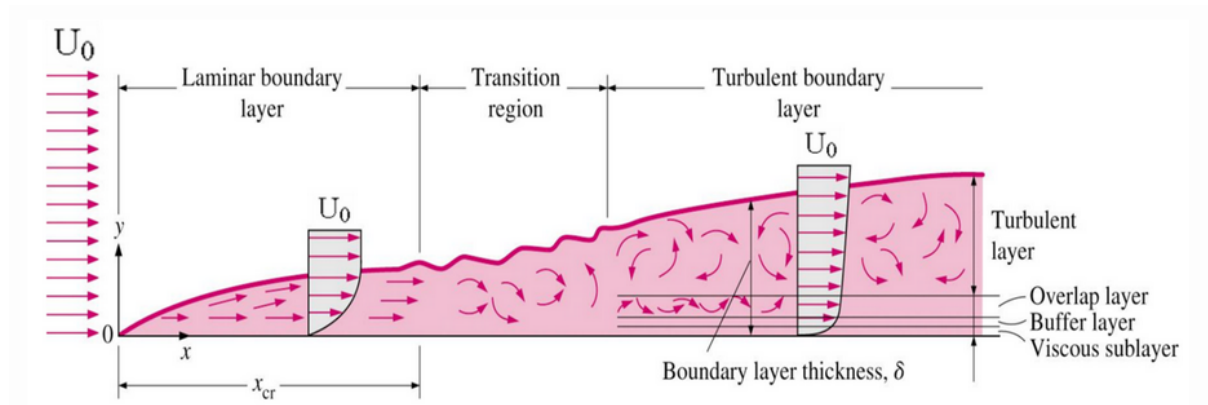


Figure 2.10: Boundary layer evolution over a flat plate (Cengel, 2006, p. 579, Fig. 11-25) [6]

Bernoulli equation

The Bernoulli equation characterizes the relation between pressure, speed and elevation of two points in space connected by a streamline. Hence, static pressure (P_{stat}), dynamic pressure (P_{dyn}) and elevation pressure (P_z). Neglecting the viscosity losses by friction, the Bernoulli equation is written as follows:

$$P_{stat} + P_{dyn} + P_z = P_{stat} + \frac{1}{2}\rho U^2 + g\rho z = cte \quad (2.22)$$

where:

- P_{stat} = Static pressure
- P_{dyn} = Dynamic pressure
- P_z = Elevation pressure
- ρ = Density
- U = Particle velocity magnitude
- g = Gravity
- z = Elevation

Together with the continuity equation (Equation 2.8), the Bernoulli's equation (Equation 2.22) constitutes the basics of the velocity-pressure interaction.

Turbulence identification

Turbulent flows ($Re > Re_{crit}$) contain somehow-patterned and -rotational flow structures named vortices. These are primarily originated from the interaction of laminar flow with external elements or from the influence of the own fluid state. Those first alterations trigger a chain of instabilities that lead to the generation of vortices. These flow structures transport and dissipate their contained energy, a fact observed and theorized by Kolmogorov with the energy transfer in turbulent flows hypothesis (principle depicted in Figure 2.5).

Turbulence/vortex identification facilitates the understanding of the fluid state and its characteristics around a solid, such that they can be considered mechanisms of drag generation. For that reason, the identification and control of these structures play a significant role in external aerodynamics.

Holmen [7] summarizes the state of the art of vortex identification's methods. In it, those are classified in the following categories:

- Methods based on the velocity gradient
- Methods that rely on vorticity
- Lagrangian methods
- Other methods

The top four currently used vortex identification methods in the automotive industry are the Q-criterion, the λ_2 -criterion, the total pressure and the vorticity magnitude (in no particular order). The first two methods are based on the velocity gradient. The total pressure is a measurement of particle energy. It is more used to visualize wakes or identify high energetic regions coarsely. The last method, as the name describes, relies on vorticity.

Two vortex identification methods have been used for the aerodynamic analysis of this thesis' simulations: Q-criterion and vorticity magnitude. A short introduction of both topics follows.

Q-criterion The Q-value is the second invariant of the velocity gradient tensor ($\bar{D} = \nabla u$). It assesses the difference between the vorticity tensor ($\bar{\Omega}$) and the rate-of-strain tensor (\bar{S}). These two correspond to the skew-symmetric and the symmetric parts of the velocity gradient tensor, such that:

$$\bar{D} = \bar{\Omega} + \bar{S} \quad (2.23)$$

where:

- \bar{D} = Velocity gradient tensor
- $\bar{\Omega}$ = Vorticity tensor
- \bar{S} = Rate-of-strain tensor

This decomposition is valid given the square property of the tensor \bar{D} . The eigenvalues (named P, Q and R) of the velocity gradient equal:

$$P = -tr(\bar{D}) \quad Q = \frac{1}{2}(tr(\bar{D})^2 - tr(\bar{D}^2)) = \frac{1}{2}(\|\bar{\Omega}\|^2 - \|\bar{S}\|^2) \quad R = -det(\bar{D}) \quad (2.24)$$

The Q-criterion considers the vortex as the part of the linked volume of the fluid with $Q > 0$ and $P < P_{amb}$. The higher the Q-value, the higher the relevance of the vorticity magnitude over the rate-of-strain of the fluid.

Vorticity Magnitude This method uses the magnitude of the vorticity ($|\omega|$) as the vortex identification method. This property is defined as the curl of the velocity and it represents the local spinning of the fluid around a point. Mathematically:

$$\omega \equiv \nabla \times u \quad (2.25)$$

2.1.2 Road vehicle aerodynamics

Road vehicle aerodynamics is the study of flowing air around and through a road vehicle. From those, external aerodynamics has been a topic of interest for the last few years. Progressively

more strict emissions restrictions have pushed to pay special attention to the total vehicle efficiency, especially aerodynamic drag. This tendency is depicted in Figure 2.11.

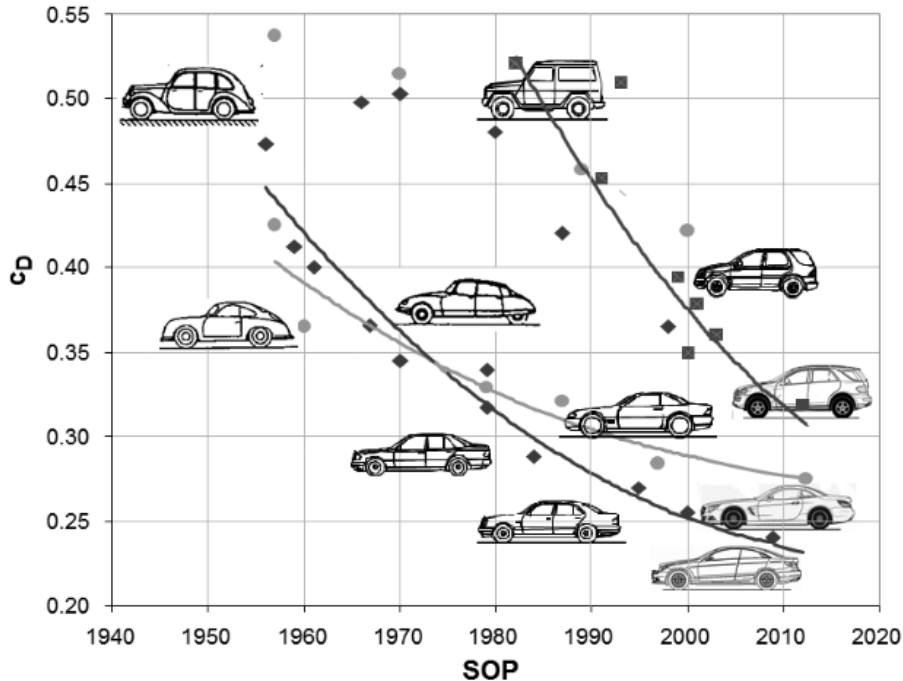


Figure 2.11: C_d evolution during the years across vehicle categories (Woll, 2017, p. 153, Fig 3.3) [1]

In the last decade, the electric car market has grown significantly. Still, nowadays, this vehicle concept has no comparable range to equivalent Internal Combustion Engine (ICE) cars. For that reason, it requires minimal driving resistance to account for the current battery technological limitations. Nevertheless, the driving resistance reduction (for any car type) depends on the Original Equipment Manufacturer (OEM) philosophy and the company design language since the aerodynamic resistance and the vehicle's design are connected. Additionally, the cultural legacy around car designs still defines what an appealing car is. These facts, including the driving dynamics, manufacturing, costs, safety, packaging and regulations, determine the balance between reducing the driving resistance and designing a desirable, economically profitable vehicle.

The driving resistance in the longitudinal movement of the vehicle has four components: Rolling resistance (F_R), Aerodynamic drag (F_D), Acceleration (F_A) and Grade resistance (F_H). They are depicted in Figure 2.12 and are calculated with the following formula:

$$F_{tot} = F_R + F_D + F_A + F_H = \mu_R(m_v g - \frac{1}{2} \rho A C_l U_\infty^2) + \frac{1}{2} \rho A C_d U_\infty^2 + m_{res} a c + m_v g \sin \theta \quad (2.26)$$

where:

- μ_R = Rolling resistance coefficient
- m_v = Vehicle mass
- g = Gravity
- ρ = Density
- A = Vehicle frontal area
- C_l = Lift coefficient
- U_∞ = Vehicle velocity magnitude
- C_d = Drag coefficient
- θ = Road slope angle
- m_{res} = Resistance mass
- ac = Acceleration in the longitudinal movement of the vehicle

From Equation 2.26, consider the following:

- The resistance mass (m_{res}) includes the mass of the vehicle and the mass moment of inertia of the rotating element, like the wheels and the engine.
- Grade resistance can be given in incline N in % or slope angle θ in $^\circ$. The relation between the two is: $\theta = \arctan N$.
- The Rolling resistance (F_R) includes the contribution of the lift force, which is the aerodynamic force defined in the orthogonal direction to the longitudinal movement of the vehicle located in the longitudinal plane of symmetry of the car and pointing away from the ground.

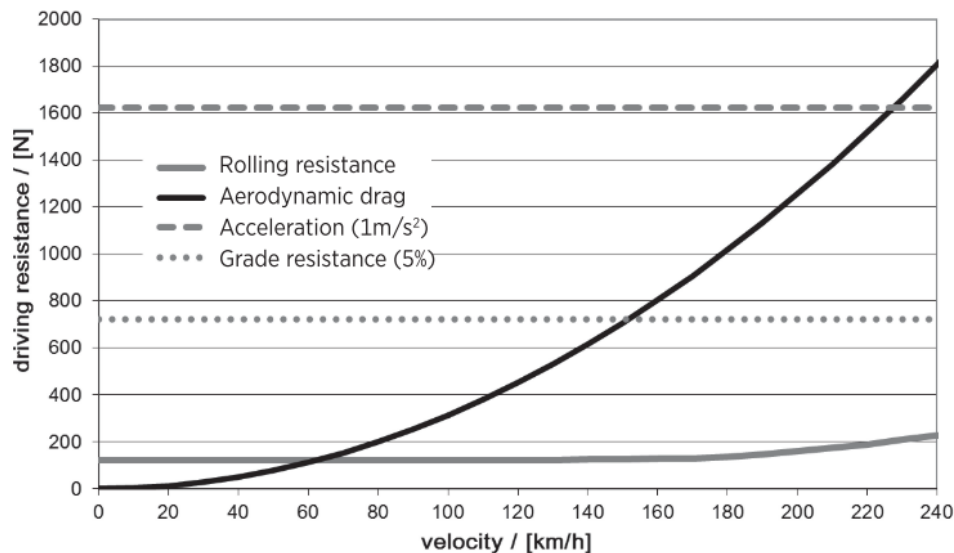


Figure 2.12: Driving resistance (Woll, 2017, p. 10, Fig 3.9) [1]

From the four components of the driving resistance, only the Rolling resistance and the Aerodynamic drag are always present for non-zero velocity. The other two components depend on the driving/road conditions. Figure 2.12 depicts an example of the disassembled total driving resistance. It is observed, as well as in Equation 2.26, the quadratic behavior of the Aerodynamic drag in comparison to the quasi-linear velocity dependency of the Rolling resistance. At usual highway speed (120 km/h) the aerodynamic drag force is noticeably more prominent than the

Rolling resistance: $F_D > F_R$. This difference intensifies at higher speeds. Hucho [8] states that for a medium-sized car, the aerodynamic drag usually represents 75%-80% of the driving resistance at 100 km/h. Whereas at highway speeds this share rises to almost 90% [1].

From the physical point of view, total drag is divided into pressure drag and friction drag. Nevertheless, there are other ways to classify a road vehicle's drag. Schuetz [9] breaks down the total drag into five components: Basic form drag, induced drag, cooling drag, roughness drag of add-on parts drag and interference drag. A brief explanation of each drag element follows:

- Basic form drag: Drag contribution from the basic vehicle's shape, without wheels and internal flow and considering smooth underbody and closed wheelhouses. Hence, the smooth flying primary shape of the car.
- Induced drag: Drag contribution induced by the correlation drag-lift caused by the attack angle of the vehicle's basic form.
- Cooling drag: Drag contribution from the open cooling system of the vehicle: radiators, condensers, air cooler, engine air for combustion, brakes and more.
- Roughness drag of add-on parts drag: Drag contribution from the detailed underbody, the suspension, the wheels and all the exterior add-ons like: mirrors, antennas, aerodynamic elements and roof racks. Given the distinctive influence of the rotating wheels, these are usually considered separately as a new drag component.
- Interference drag: Drag contribution of the interaction between all the previous drag components.

In passenger cars, the share of the drag components over the total is estimated by Schuetz [9] as: basic form ($\sim 50\%$), cooling drag ($\sim 5\%$), roughness drag ($\sim 22\%$), wheel drag ($\sim 20\%$) and interference drag ($\sim 3\%$).

Even though aerodynamic drag is the most influential driving resistance component starting from 60 km/h, the improvements in that area do not significantly affect ICE vehicles' consumption. In the case of electric cars, this influence is considerably more notable. The consumption is strictly related to energetic efficiency, including thermal losses, mechanical losses, driving resistance and more. Therefore, it is conditioned by the entire energy chain: from the tank/battery to the car movement. Woll [1] found out that the aerodynamic drag produces 6.5% of the energetic losses on the New European Driving Cycle (NEDC) cycle [10] for an ICE car, which used a 10.6% of the combustion energy as kinetic energy. For an electric vehicle, the drag was found to produce an energetic loss of 21.1% on the NEDC cycle and a total of 37% of the electric energy transformed into kinetic energy (without considering brake regeneration).

The roughly $\simeq 3.2$ times higher influence of the drag in electric cars highlights the relevance of optimizing the aerodynamics of such vehicles like autonomous shuttles. At the same time, it is important to remark that the drag impacts the efficiency with the square of the velocity, like the aerodynamic force itself. This means that the influence is more noticeable at highway speeds. Woll [1] states that a drag coefficient reduction of $\Delta C_d = -0.010$ brings a consumption decrease in a city cycle of 0.01 l/100 km and a reduction of 0.05 l/100 km, 0.09 l/100 km and 0.15 l/100 km at constant speeds of 90 km/h, 120 km/h and 150 km/h respectively. This is approximately equal to CO₂ decrements of 0.23 g CO₂/km, 1.17 g CO₂/km, 2.11 g CO₂/km and 3.51 g CO₂/km respectively in a petrol car (using the equivalence: 1 gasoline l/100 km \equiv 23.4 g CO₂/km [1]).

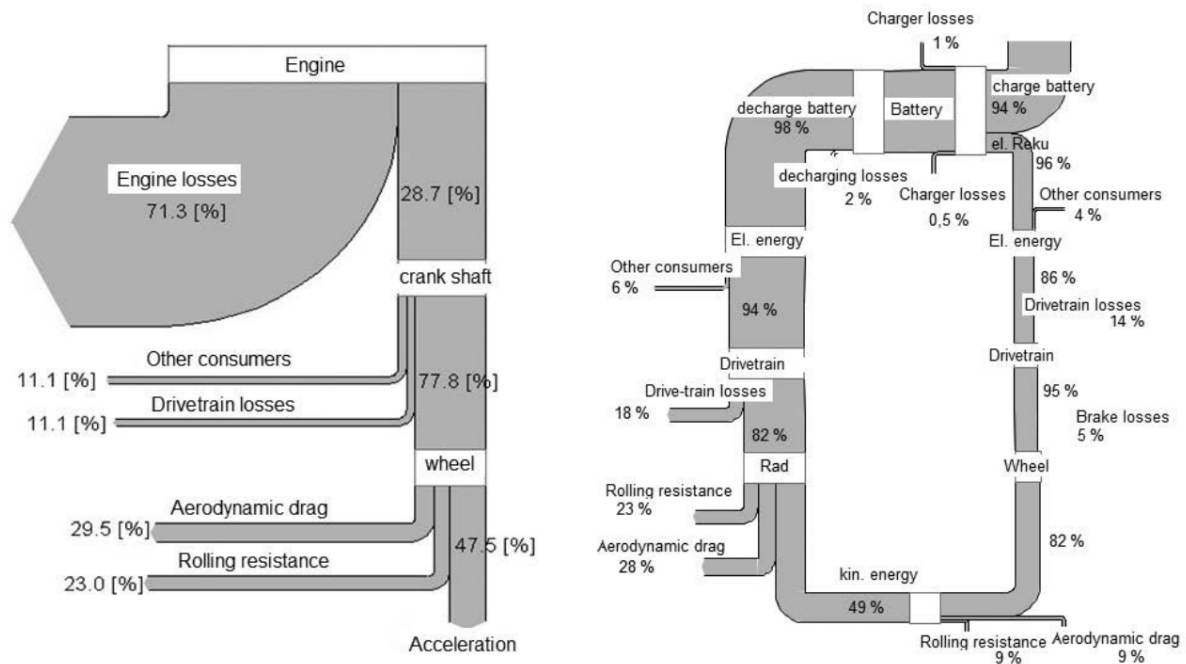


Figure 2.13: Energy flows in the NEDC: To the left, for a vehicle with a combustion engine; to the right, for a vehicle with a battery-electric drive (Woll, 2017, p. 178, Fig 3.20) [1]

2.1.3 DrivAer

The DrivAer is a set of car geometries (notchback, fastback and estate) that were introduced and validated in the Technical University of Munich (TUM)'s wind tunnel by Heft [11] in 2012 to establish a realistic generic car model for aerodynamic research purposes (depicted in Figure 2.14).

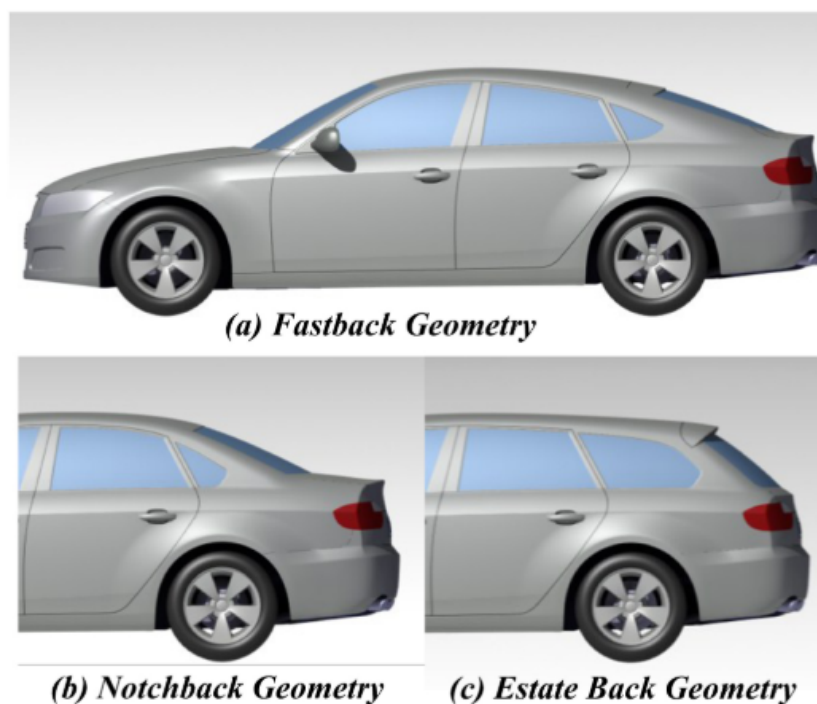


Figure 2.14: DrivAer body with different tops (Heft, 2012, p. 3, Fig 4) [11]

The notchback, fastback and estate car variants, coded N, F and E respectively, have additional coded features considered as study variables: underbody (smooth: S, detailed: D), wheels (with: wW, without: woW), mirrors (with: wM, without: woM) and ground simulation (with: with Ground Simulation (GS), without: w/o GS). Hence, all the possible spectrum of geometries have a unique tag that combines the previous codes. For example, an estate model with mirrors, wheels, smooth underbody and ground simulated is identified as E_S_wM_wW with GS or ESwMwW with GS. Note that the order of the features inside the tag is usually similar in different published articles. Sometimes the positions of the mirror code and the wheel code can be switched.

Given the wide acceptance of the DrivAer in the field of automotive aerodynamics, multiple studies, articles and theses from both simulation and experimental sides have been published. They provide a solid base for validating CFD software, comparing wind tunnel data and evaluating turbulence models. In this study, specific published DrivAer data [12–20] has been used to validate *Pacefish*[®]. This topic is extended in Section 3.3.

2.1.4 Autonomous shuttle and sensor aerodynamics

After deep research, no published data has been found on autonomous shuttle aerodynamics due to the novelty of this vehicle concept. The research has been performed under the consideration that the following characteristics define an autonomous shuttle:

- Purpose-designed road vehicle.
- Autonomous driving level 4 or above.
- Possibility to easily access all sitting/standing positions once inside the vehicle.
- Recognizable length of the car in terms of dimensions (significantly bigger than the width).
- Side-mounted door/s to access the cabin.

In terms of external geometry, the autonomous shuttle is similar to a bus, minibus or van. This association provides some reference data for comparability. Nonetheless, these vehicles' geometries differ from the autonomous shuttles in two features that might substantially affect their aerodynamics. Buses usually have substantially higher length than autonomous shuttles, which influences on the Re . Furthermore, regular buses, minibusses and vans do not incorporate the sensors and cameras' add-on geometries that autonomous shuttles require for the self-driving capabilities. Nevertheless, and given the lack of data on this vehicle concept, the following sections collect aerodynamic studies of:

- Bus, minibus and van: Used to evaluate the basic form's aerodynamics and the design sensitivity.
- Add-on parts: Used for comparison of the aerodynamic impact of add-on geometries.

Bus, minibus and van aerodynamics

Commercial vehicle aerodynamics are not less relevant than passenger car aerodynamics. Already in the early 1980s, multiple studies investigated their C_d and aerodynamic optimization.

McDonald [21] performed a study to optimize the aerodynamics of intercity buses, in which he investigated the drag coefficient impact of the side and top edge radii under multiple conditions. Figure 2.15 depicts the C_d for different radius / vehicle height (r/H) values at 0° and 10° yaw angles and $Re = 4.4 \times 10^5$. He observed a stabilization of the drag coefficient at $r/H = 0.2$ under study conditions. The maximum reduction values were $\sim 45\%$ for the side edge and a $\sim 25\%$ for the top edge. The research was performed using wind tunnel scale models and validated with full-scale road tests.

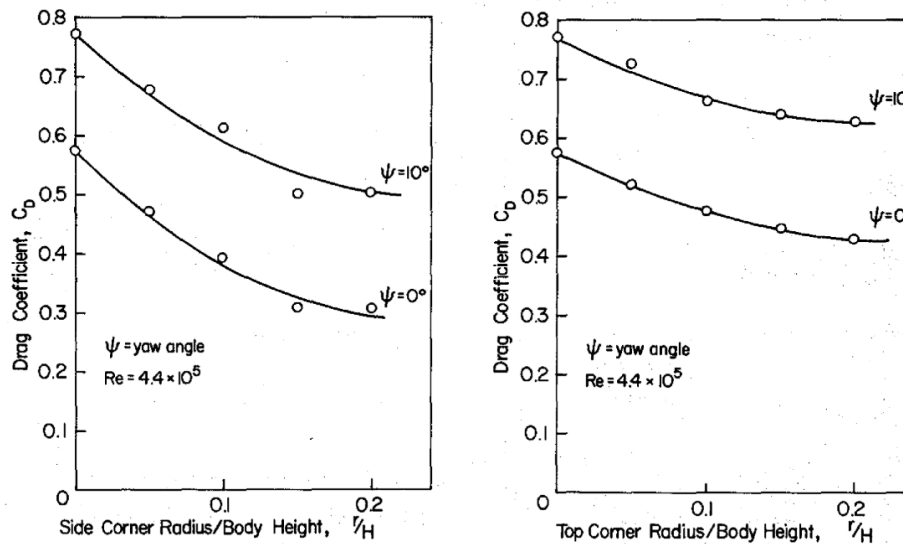


Figure 2.15: Effect of the side corner radius (left-hand side) and top corner radius (right-hand side) on the C_d (McDonald, 1980, p. 4473, Fig 6 and 7) [21]

Gilhaus [22] studied the influence of cab shape on air drag trucks, in which the study of the front edge radii was analyzed at different Reynolds numbers (left-hand side of Figure 2.16). In order to compute the change in radius, he used the parameter Re_R , which is a Reynolds value that considers the radius as reference length. The maximum reduction values were $\sim 30\%$ for the side edge and $\sim 17\%$ for the top edge. Furthermore, he analyzed the drag coefficient function of the Reynolds numbers, which he found out to have a substantial decrease tendency for increasing Re (right-hand side of Figure 2.16).

Gotz [23] and Hucho [8] published the influence of the front entire edge radius on the C_d of a bus (Figure 2.17) and the influence of the front side-edge radius on a van (Figure 2.18) respectively. Both findings had similar trends: The C_d decreases until it stabilizes around $r/b = 0.05$ (radius to vehicle width ratio). At that point, maximum drag coefficient reduction, the C_d is $\sim 55\%$ lower for buses [23] and $\sim 15\%$ lower for vans [8] in comparison their reference geometry, which have sharp edges.

The studies of McDonald [21], Gilhaus [22], Gotz [23] and Hucho [8] highlight the importance of the rounding of the front edges for such vehicle types. It defines the detachment of the boundary layer from the body, and therefore, it directly impacts the C_d . Rounded front edges can reduce between 15% and 55% the C_d , depending on the vehicle type and the edge selected for rounding (side-edge, top-edge or both). For the visualization of the impact of these geometrical features, Hucho [8] used small threads for both sharp and round front edge vans to visualize the flow at the vehicle's surface (Figure 2.19).

Besides studying the impact of the front edge radius of buses, Gotz [23] states various features and aerodynamic characteristics in *Commercial vehicles*. Findings concluded that the front of

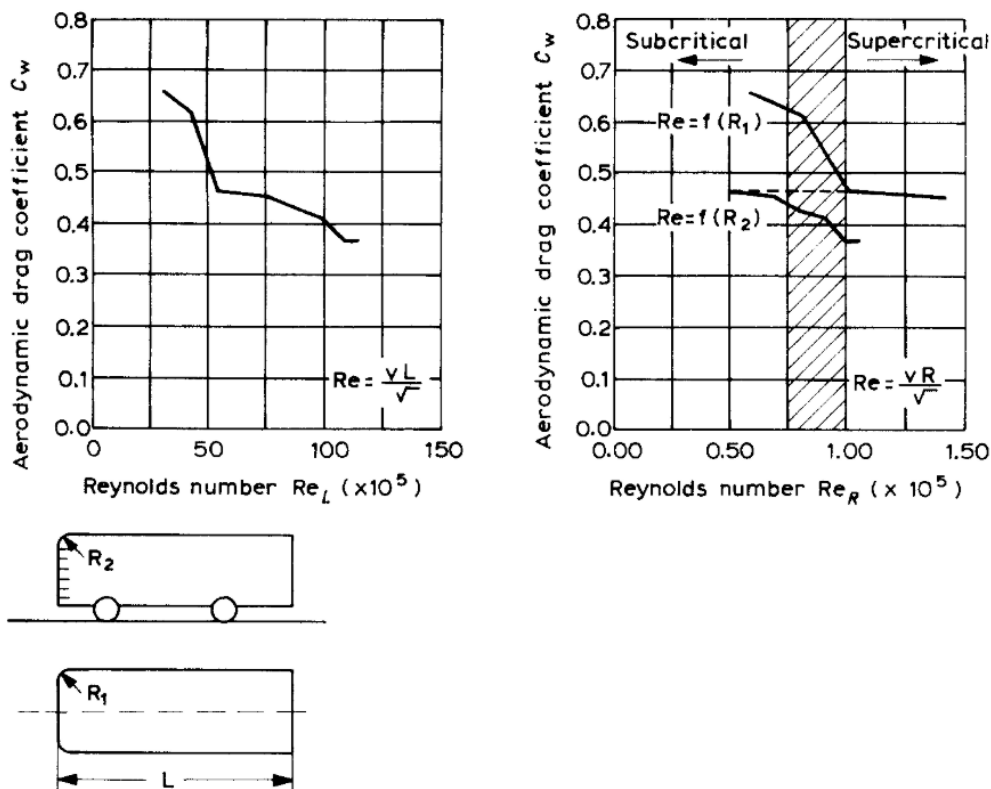


Figure 2.16: Influence of the Reynolds number on the drag of rounded front edges vehicle (Gilhaus, 1981, p. 80, Fig 3) [22]

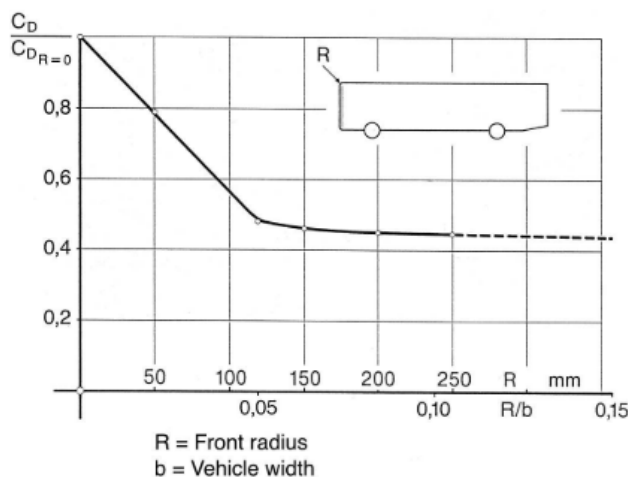


Figure 2.17: Effect of the leading-edge radius on drag of a bus (Gotz, 1987, p. 773, Fig 10.82) [23]

the vehicle accounts for approximately 70% of the total drag. This remarks even more relevance of the front edges. Additionally, Gotz [23] found that lowering the rear top edge of a commercial vehicle reduces C_d by 8%.

Rodrigues [24] analyzed the drag impact on body variations of a minibus vehicle, with a max reduction of the C_d of 18.6%, which was estimated to translate to a fuel consumption reduction of 2%, 6% and 10% in urban, intercity and highway scenarios respectively. This improvement was obtained with a closed profile rim, housing the protruding geometry of the roof using rounded shapes and separating the mirrors from the A-pillars.

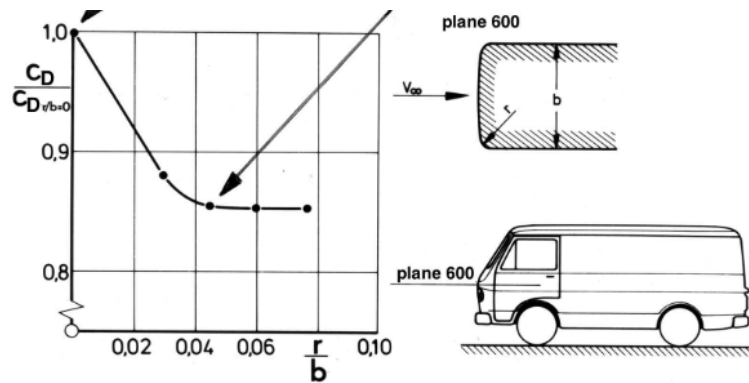


Figure 2.18: Effect of the side-edge radius on drag of a van (Hucho, 1987, p. 45, Fig 1.48) [8]

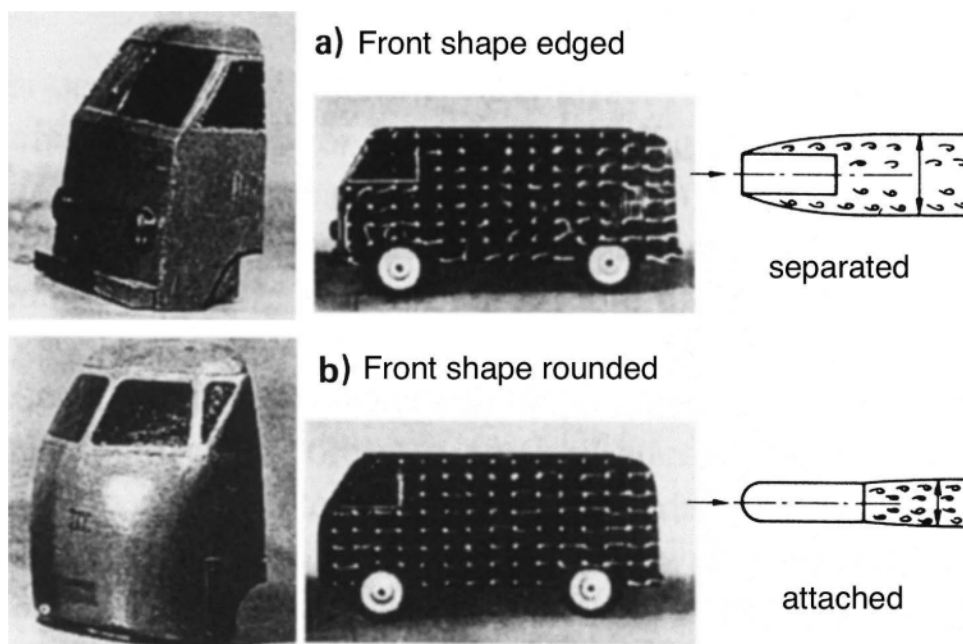


Figure 2.19: Boundary layer detachment in the front edge of a van (Hucho, 1987, p. 44, Fig 1.47) [8]

Kim [25] investigated the drag benefits of installing a rear spoiler in a bus. Results concluded an average C_d reduction of 13.4% between speeds of 80 km/h and 120 km/s, with increasing tendency with the velocity. Jiang [26] studied some variations of detail drag optimization of a van, all found to be in the range of 2.8% - 8.9% C_d reduction. The maximum improvement was obtained with the addition of a rear edge spoiler. A similar value (8%) is stated by Gotz [23].

Add-on parts aerodynamics

Several studies analyze the aerodynamic impact of add-on elements in road vehicles. These focus mainly on mirrors and roof racks, which could have a similar effect as sensor geometries added on the vehicle surface. Even though the mirror and roof rack geometries differ substantially from the sensors, the found data is used as an orientation of magnitude of add-on components' ΔC_d .

Schuetz [9] observes the following effects:

- The contribution of a pair of external mirrors is approximately of 4% (C_d).

- The impact of the roof rack approximately 10% (C_d).
- The impact of the ski carrier up to 40% (C_d).

Figure 2.20 depicts different studied geometries and their ΔC_d [%].

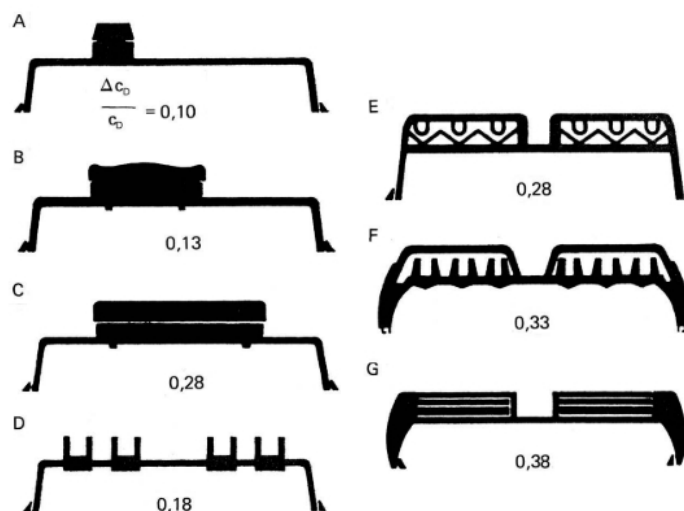


Figure 2.20: Drag impact of different sky carriers (Schuetz, 2016, p. 365, Fig 4.170) [9]

Hirose [27] studied as well the impact on the drag of the mirrors using simulation and wind tunnel data.

Gotz [23] states that the integrated (optimized) mirrors reduce a 2% the fuel consumption in buses at 100 km/h.

Lenner [28] performed an on-road study to determine the consumption and emissions impact. The following were his findings:

- The impact of the roof rack on the consumption was between 1% and 3% at speeds between 70 km/h and 90 km/h.
- The impact of the ski-box on the consumption was around 10% at speeds between 70 km/h and 90 km/h.

Chowdhury [29] and Alam [30] in two different studies experimentally analyzed the energy consumption and greenhouse gas emissions impact of vehicle add-on geometries. The findings were the following:

- The impact of the roof rack is 20.4% (C_d) between 40 km/h and 120 km/h [29] and 6.7% (C_d) between 60 km/h and 120 km/h [30].
- The impact of the taxi sign is 5.1% (C_d) between 40 km/h and 120 km/h [29] and 11.3% (C_d) between 60 km/h and 120 km/h [30].

Taiebat [31] and Gawron [32] study the total energetic impact of transforming a regular passenger car into a Connected and Automated Vehicle (CAV)s. They conclude that the aerodynamic influence of the total energy delta ranges between 10% and 68%, depending on the size of the sensor layout. Nonetheless, they do not state absolute values. Moreover, they did not simulate nor experimentally test the aerodynamic change induced by the sensor layout. They used the published data from Chen [33] to approximate such impact.

2.2 Current autonomous shuttle data

Three sources [34–36] defined the starting point of the state of the technology’s analysis of autonomous shuttles. They allowed the exploration of this vehicle concept design space and permitted gathering relevant information for this study’s goal.

Unfortunately, there is a significant lack of data regarding the published list of existing companies and vehicle specifications. This lack of transparency is caused by the companies’ small size and poor visibility and the fact that most of the vehicles are still concept cars in the early stages of development. Consequently, the analysis is performed on 21 vehicles. Nonetheless, these 21 data points constitute the total representation of the segment autonomous driving shuttles on the 15th of May 2021. Shuttles with no technical specification or dimension have been dismissed.

The autonomous vehicles have been clustered by design and functionality in the groups depicted in Figure 2.21. Highlighted in blue are the vehicles of interest for this thesis. The shuttles used for the transportation of objects are as well considered for the derivation of some study-relevant parameters.

For the purpose of this study, the relevant characteristics of the autonomous shuttles are design parameters and maximum speed. The first ones are used to define and design a generic shuttle vehicle that constitutes the reference shape for the aerodynamic analysis. The maximum speed, together with the length of the generic shuttle, characterizes the Reynolds number of the simulation. The collected values of these relevant characteristics are depicted in Table 2.1. The windshield angles of all vehicles have been approximated through visual inspection². If the value is not displayed in Table 2.1, the geometry of the shuttle is such that it is not feasible to define a windshield angle.

In Table 2.1 the vehicles are presented in no particular order. Nonetheless, that the last three are separated from the rest due to their scope of transporting objects.

The extended analysis of the collected data of Table 2.1 is performed in Section 3.2.

2.3 Introduction to *Pacefish*[®]

Pacefish[®] is a CFD software from the company Numeric Systems GmbH based on the LBM that runs on Graphics Processing Unit (GPU). It combines the discretization approach of the LBM and the efficient parallel data treatment of GPUs to provide radically shorter simulation times. *Pacefish*[®] uses a novel proprietary mathematical discretization scheme allowing accurate consideration of strong local gradients as well as a proprietary collision operator. Further LBM information can be found on Section 2.1.1.

²Derivation of properties by looking at images





























| | | Transportation of people | | | Transportation of objects | |
|--|---|--|--|---|---|--|
| Non-purpose-design | Stock-design cars |  Tesla ... | | | | |
| | Stock-design cars with add-on |  Cruise av |  Waymo |  Uber ... | | |
| Purpose-design | Car-like-design vehicles |  Navya Autonom Cab |  Optimus Ride | ... | | |
| | Shuttle-design vehicles |  Milla pod |  HEAT |  i-Cristal, Lohr | |  Westfield pod |
| | |  Sango, NEVS |  Kamaz, Nami |  2GetThere | |  Nuro |
|  Zoox | |  UnicarAgil |  Navya Autonom Shuttle |  e-Palette, Toyota | | |
|  Apollo, Baidu | |  Olli, Local Motors |  Coast Autonomous |  Ohmio Lift | | |
|  e.Go | |  Yutong autonomous shuttle |  EasyMile |  Sensible 4 | | |
| Not car-like-design nor shuttle-design vehicles |  Next Modular Vehicle | | | ... |  Cleveron ... | |

Figure 2.21: Cluster of current autonomous driving road vehicles

Table 2.1: Summary of the collected data of the current autonomous shuttles

| | Design parameters | | | | | | | |
|--------------------------------|-------------------|-----------|------------|----------------------|---------------|------------|----------------------|------------------|
| | Length [m] | Width [m] | Height [m] | Ground clearance [m] | Wheelbase [m] | Wheel size | Slope windshield [°] | Max speed [km/h] |
| Milla Pod [37] | | | | | | | | 30 |
| Sango [38] | 4.270 | 2.020 | | | | | | 50 |
| Zoox [39] | 3.630 | | 1.936 | | | 175/60 R22 | 76 | 120 |
| Navya Autonom Shuttle Evo [40] | 4.780 | 2.100 | 2.670 | 0.17 | | 215/60 R17 | 68 | 25 |
| UnicarAgil [41] | | | | | | | 70 | 72 |
| Kamaz [42] | 4.600 | 2.000 | | | | | 64 | 25 |
| 2getThere GTR [43] | 6.044 | 2.104 | 2.784 | | 3.7 | | 67 | 60 |
| E-Palette [44] | 5.255 | 2.065 | 2.760 | | 4.00 | | 86 | 19 |
| Apollo [45] | 4.330 | 2.150 | 2.715 | | | | 67 | 40 |
| Olli [46] | 3.920 | 2.041 | 2.637 | | 2.57 | 225/50 R18 | 90 | 40 |
| Coast Autonomous [47] | | | | | | | 90 | 40 |
| Ohmio Lift [48] | | | | | | | 90 | 25 |
| Yutong Autonomous Shuttle | | | | | | | 78 | |
| EasyMile [49] | 4.050 | 1.892 | 2.871 | | | | 85 | 40 |
| I-Cristal [50] | 4.300 | 1.870 | 2.530 | | | | 90 | 50 |
| Sensible4 [51] | 4.500 | 2.400 | 2.800 | | | | 78 | 40 |
| Westfield Pod [52] | 3.700 | 1.650 | 2.115 | | | 135/70R13 | | 40 |
| HEAT [53] | 5.100 | 2.050 | 2.710 | | | | 90 | 40 |
| Nuro R2 [54] | 2.740 | 1.100 | 1.860 | | | | 70 | 40 |
| Neolix [55] | | 1.000 | | | | | 88 | 50 |
| Udelv [56] | | | | | | | 90 | 104 |

3 Method

With the purpose to assess the C_d impact of sensor layouts on autonomous shuttles , the resulting detailed steps are defined:

1. Data collection:
 - (a) Analysis of current autonomous shuttle data.
 - (b) Derivation of the generic shuttle geometry.
 - (c) Derivation of the simulation conditions.
2. Setup validation (Validation of the CFD software, mesh parameters and simulation parameters):
 - (a) Comparison of the ΔC_d of the two literature DrivAer geometries with their respective simulations in *Pacefish*[®].
 - (b) Assessment of the pressure distribution along the top and bottom of one DrivAer vehicle's simulation.
3. Reference simulation:
 - (a) Simulation of the generic shuttle.
 - (b) Particular attention on the surrounding flow topology and structures.
4. Design influence:
 - (a) Derivation and design of the features to evaluate.
 - (b) Simulation of the defined geometries.
 - (c) Evaluation of the design influence.
 - (d) Comparison of the results with literature data if possible.
5. Single sensor influence:
 - (a) Derivation and design of the geometries to evaluate.
 - (b) Simulation of the defined geometries.
 - (c) Evaluation of the single sensor influence.
6. Sensor setup influence:
 - (a) Derivation and design of the geometries to evaluate.
 - (b) Simulation of the defined geometries.
 - (c) Evaluation of the sensor setup influence.

7. Model to assess the C_d impact of sensor setups

- (a) Generation of a mathematical model to approximate the drag impact of the sensor setups based on the prevailing drag mechanisms.

Figure 3.1 visually represents the seven steps followed in this study.

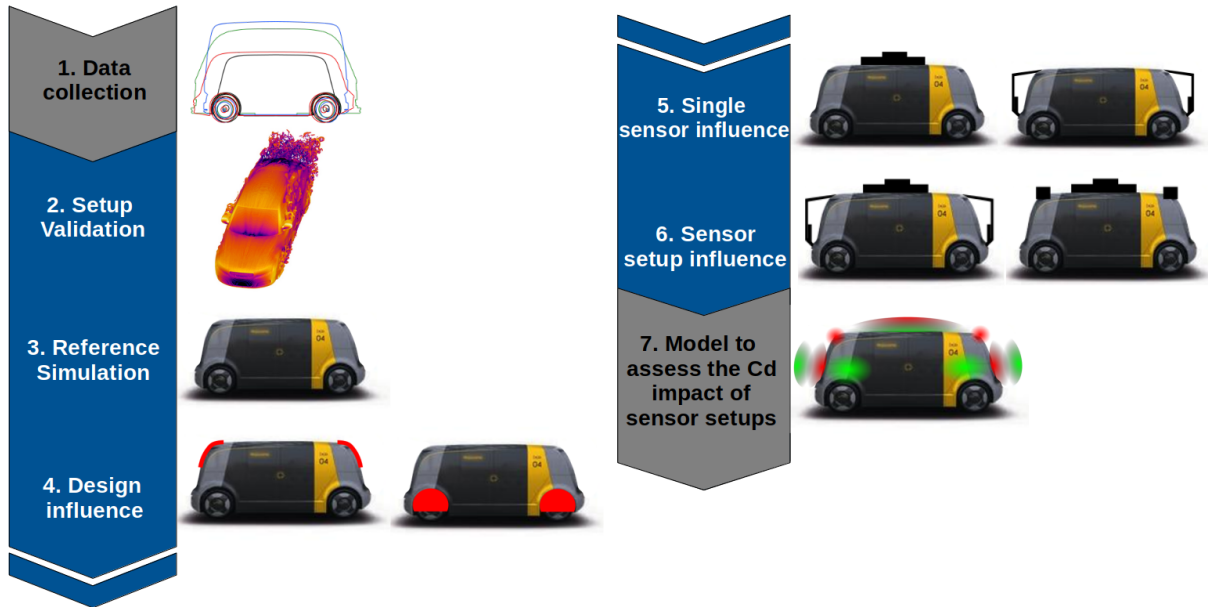


Figure 3.1: Study process by steps

The steps 2 to 6 are similar: there is the Computational Aided Design (CAD) design, the CFD simulation and the aerodynamic analysis of a specific geometry. In the setup validation (step 2), the geometry of the DrivAer vehicles is given, so the design substep is not required. Nonetheless, generally, there is a clear workflow of information through different software. It begins with the analysis in LibreOffice of the current data on shuttle vehicles, which is performed only once. From the extracted geometrical specifications, a geometry is designed in Catia V5. The .stp file is imported to ANSA, where it is cleaned up and transformed into .stl format. This tessellation file is imported to Pacefish® Workbench, where the simulation is set up. Afterwards, Pacefish® Backend executes the simulation file and generates the defined outputs in .case extension. These can be read by Paraview, which enables the aerodynamic analysis. Finally, LibreOffice collects all the data from all the defined simulated geometries. The last software facilitates the generation of a model to approximate the sensor setup C_d impact. Figure 3.2 depicts this global workflow. Highlighted in blue are the actions that are performed multiple times.

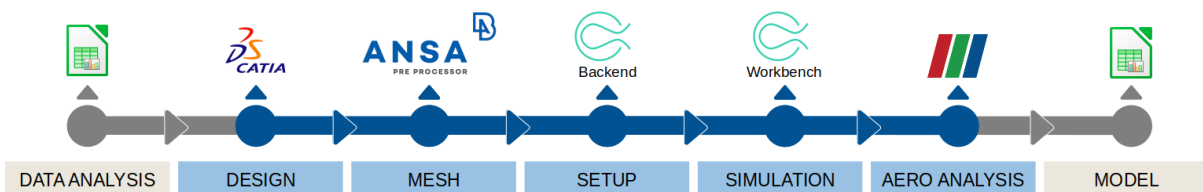


Figure 3.2: Data workflow

3.1 Aerodynamic analysis methodology

In order to assess the impact in C_d of sensor setups, a specific methodology has been developed.

First, the simulation software with which the study is performed must be validated under the study conditions. Hence, the defined simulation parameters (including the mesh) must correctly identify the changes in C_d of the tested geometries. This parameter is taken as the primary evaluation factor over the absolute value of the drag coefficient. The reason is to avoid the account of possibly appearing non-physical inaccuracies in all simulations due to the resolution or the own fluid treatment of *Pacefish*[®]. In other words, *Pacefish*[®] more precisely identifies ΔC_d rather than C_d .

To confirm the software's accuracy under those setup conditions, the extensively studied and validated geometry DrivAer has been used, more specifically, the geometries E_D_wW_wM with GS and E_S_wW_wM with GS. The choice of this car shape (Estate) is based on the rear-end geometrical similarity to the autonomous shuttle. Therefore, the flow is expected to have comparable detachment behavior. In order to confirm the correct identification of ΔC_d , the simulated DrivAer geometries must have similar drag delta to the one found in the literature. Figure 3.3 depicts the validation methodology.

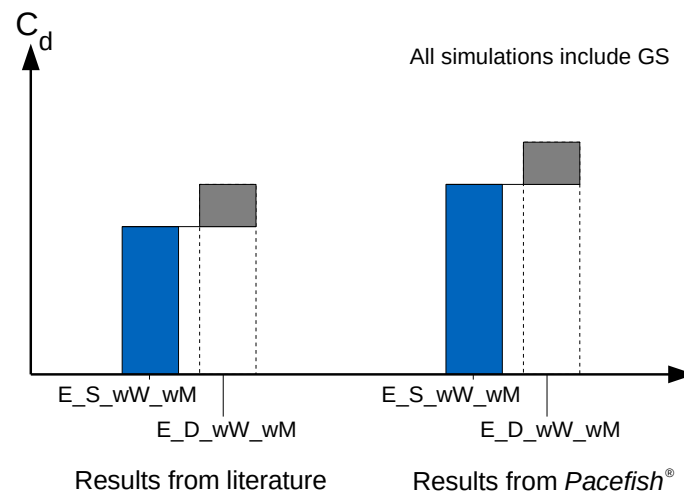


Figure 3.3: Approach considered for the validation of the CFD software *Pacefish*[®]

With the DrivAer geometries, the aim is to obtain identifiable drag coefficient increments at the same or similar Reynolds number as the one used for the rest of the simulations and using a specific mesh and simulation parameters. Figure 3.4 depicts this validation of the setup.

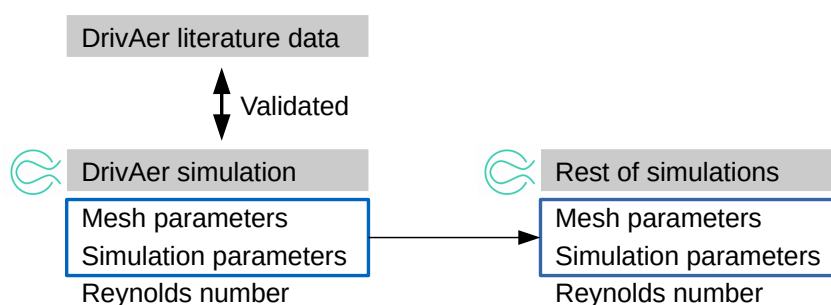


Figure 3.4: Derivation of simulation setup from the software validation step

Once the mesh and the simulation parameters are correctly validated, that same (or comparable) setup is used to proceed with the aerodynamic analysis of the sensor setups. For that purpose, a generic autonomous shuttle is designed, which defines the aerodynamic reference data. Afterward, some relevant design changes are simulated. These analyses aim to create a wider perception of the impact of sensors in the generic shuttle geometry. Finally, the single sensor positions and the sensor layouts are analyzed. The idea behind this distinction is first to isolate the effect of each isolated sensor and then analyze the interaction between them. Furthermore, this approach facilitates the possible derivation of a mathematical model to approximate the C_d of sensor setups considering each component's contribution. Figure 3.3 depicts this aerodynamic analysis methodology.

The drag evaluation of all the simulations is performed in relation to the reference simulation (generic shuttle geometry), hence not considering the absolute drag coefficient result. This ΔC_d -analysis method aligns with the validation procedure used for the CFD software.

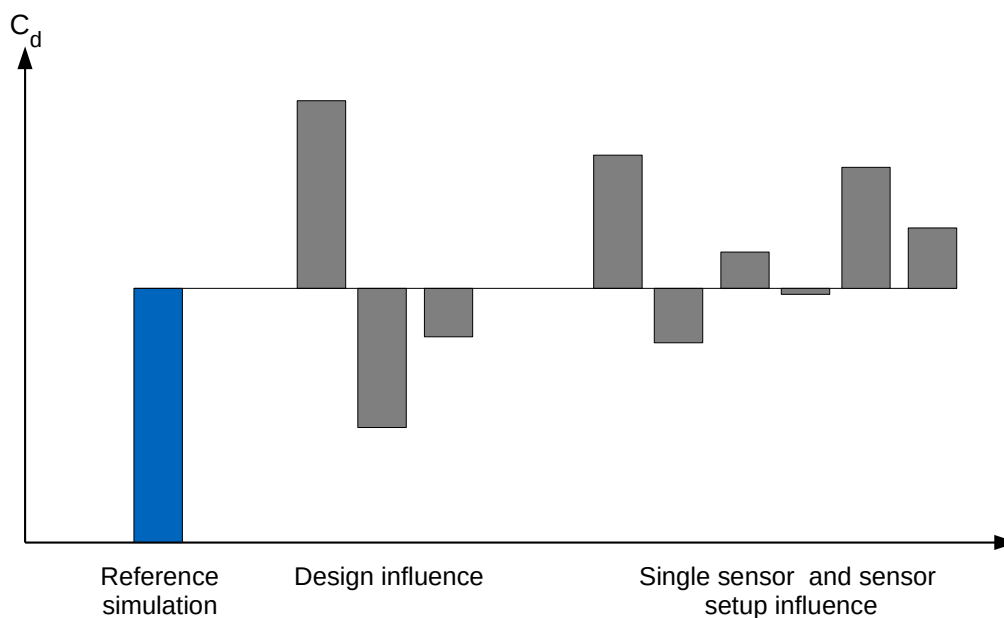


Figure 3.5: Approach considered for the analysis of design and sensor aerodynamic influence

If the study considers all the possible design variables, single sensor positions and shapes and sensor layouts, the required number of simulations to represent the entire design space is immense. For that reason, the geometry selection (and hence the extent of the analysis) is based on the following factors:

- Reference simulation: Based on the design of a generic autonomous shuttle derived from current vehicle data and aerodynamic features extracted from literature.
- Design influence: Based on aerodynamic design-relevant features extracted from literature.
- Single sensor and sensor setup influence: Based on geometries derived from current vehicle data.

3.2 Analysis of current autonomous shuttle data and derivation of the simulation conditions

3.2.1 Analysis of current autonomous shuttle data

Table 3.1 collects the study-relevant parameters.

Table 3.1: Summary of the collected data of the current autonomous shuttles with derived parameters

| | Design parameters | | | | | | | |
|--------------------------------|-------------------|--------------|--------------|----------------------|---------------|------------|----------------------|------------------|
| | Length [m] | Width [m] | Height [m] | Ground clearance [m] | Wheelbase [m] | Wheel size | Slope windshield [°] | Max speed [km/h] |
| Milla Pod [37] | | | | | | | | 30 |
| Sango [38] | 4.270 | 2.020 | 1.970 | | | | | 50 |
| Zoox [39] | 3.630 | 1.936 | 1.936 | | | 175/60 R22 | 76 | 120 |
| Navya Autonom Shuttle Evo [40] | 4.780 | 2.100 | 2.670 | 0.17 | | 215/60 R17 | 68 | 25 |
| UnicarAgil [41] | 4.428 | 2.096 | 1.957 | | | | 70 | 72 |
| Kamaz [42] | 4.600 | 2.000 | 2.390 | | | | 64 | 25 |
| 2getThere GTR [43] | 6.044 | 2.104 | 2.784 | | 3.7 | | 67 | 60 |
| E-Palette [44] | 5.255 | 2.065 | 2.760 | | 4.00 | | 86 | 19 |
| Apollo [45] | 4.330 | 2.150 | 2.715 | | | | 67 | 40 |
| Olli [46] | 3.920 | 2.041 | 2.637 | | 2.57 | 225/50 R18 | 90 | 40 |
| Coast Autonomous [47] | | | | | | | 90 | 40 |
| Ohmio Lift [48] | | | | | | | 90 | 25 |
| Yutong Autonomous Shuttle | | | | | | | 78 | |
| EasyMile [49] | 4.050 | 1.892 | 2.871 | | | | 85 | 40 |
| I-Cristal [50] | 4.300 | 1.870 | 2.530 | | | | 90 | 50 |
| Sensible4 [51] | 4.500 | 2.400 | 2.800 | | | | 78 | 40 |
| Westfield Pod [52] | 3.700 | 1.650 | 2.115 | | | 135/70R13 | | 40 |
| HEAT [53] | 5.100 | 2.050 | 2.710 | | | | 90 | 40 |
| Nuro R2 [54] | 2.740 | 1.100 | 1.860 | | | | 70 | 40 |
| Neolix [55] | 3.000 | 1.000 | 1.800 | | | | 88 | 50 |
| Udelv [56] | | | | | | | 90 | 104 |

Given the shortage of information regarding vehicle specifications, some dimensions (highlighted in bold font) of Table 3.1 are derived by visual inspection. This approximation is performed using a known measurement of the vehicle and a side or top picture of it. The inherently induced error results insignificant. Considering an error of 10% for each approximated measurement (highlighted in bold font in Table 3.1), the worst-case induced error of any calculated dimension (length, width or height) of the generic shuttle is $\sim 2.48\%$. This value is extracted from the guidelines used to derive the generic shuttle's length, width, and height (see upcoming section). Such error in a vehicle with a simple box form is insignificant in terms of aerodynamics.

Similarly, the windshield angles are derived by visual inspection. This is the only possible option, given that the manufacturer does not provide this geometrical parameter. The evaluation of the

influence of the design features in the generic shuttle will consider the windshield slope as a variable. Therefore, its possible induced error in the visual derivation is not assessed.

From the Table 3.1, the following is observed:

- There is a clear separation between passenger shuttles and object-transportation shuttles in terms of dimensions. Nonetheless, the ratios width/length and height/length are quite similar for all vehicles. This is depicted in Figure 3.6.

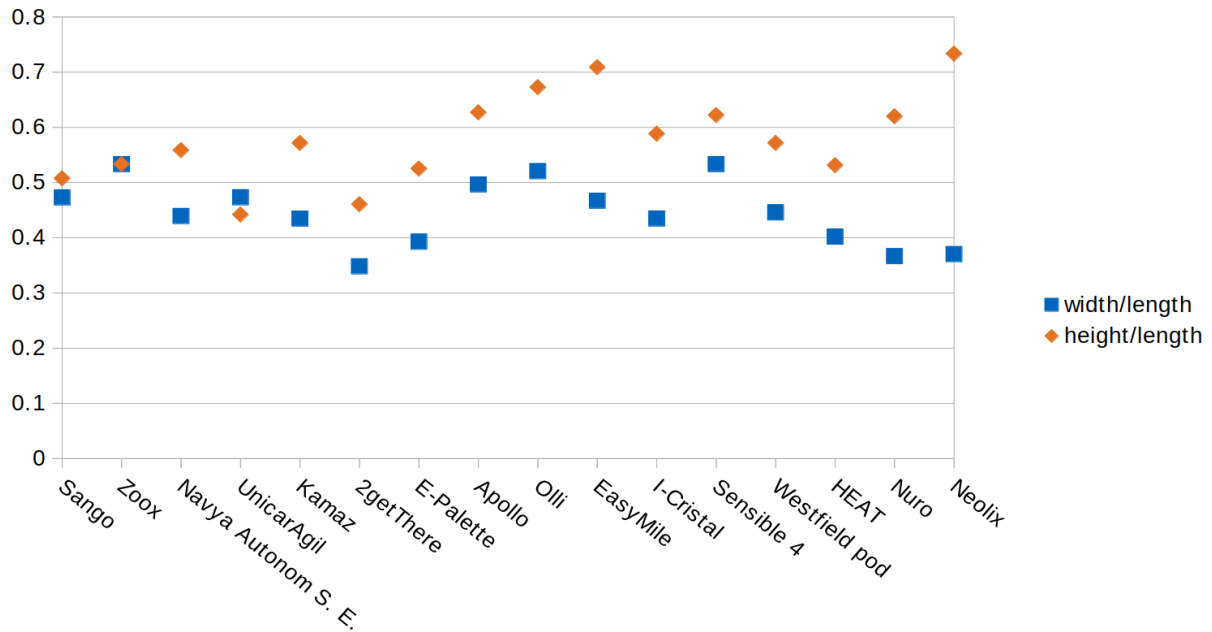


Figure 3.6: Width/length and height/length of current autonomous shuttles

- There is a noticeable height difference in passenger shuttles. They are clustered into two categories: Standing (ST) and sitting (SI). As the name describes, the ceiling height is designed to accommodate people in standing positions (ST) or exclusively sitting (SI). Figure 3.7 depicts such analysis.

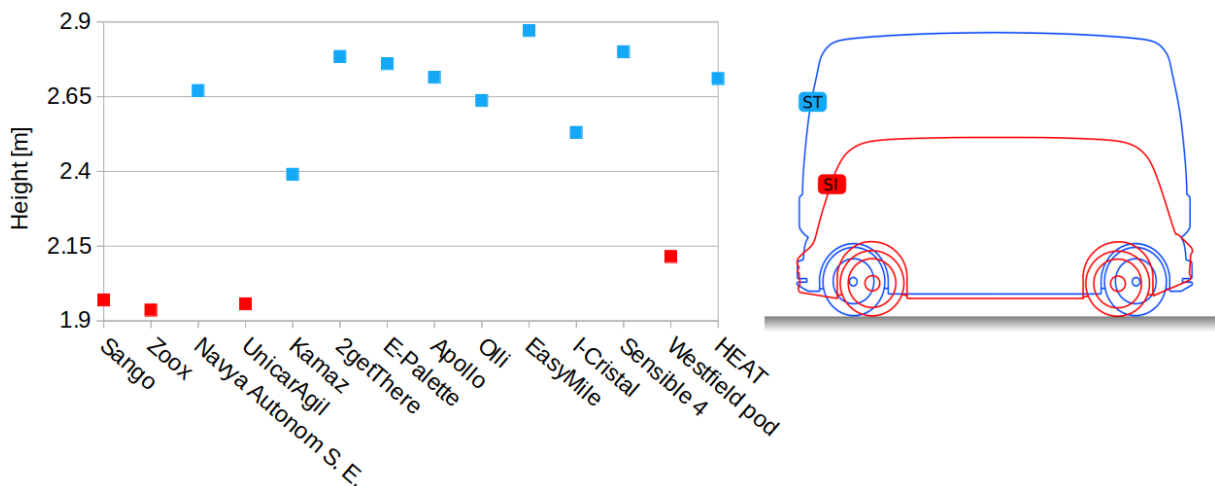


Figure 3.7: Clustered height of the shuttles (excluding the object transportation vehicles)

- Data on ground clearance, wheelbase and wheel size is hardly ever provided by the manufacturer. Only one value of ground clearance has been gathered. Wheelbase and wheel size data points are slightly more numerous, but they contain significant scattering.
- The windshield angle (α) (measured from the horizontal) of autonomous shuttles is clustered in 3 main groups. Figure 3.8 depicts such classification. The derivation of this geometrical feature for the Milla Pod, the Sango and the Westfield Pod was not feasible due to their curvy character.

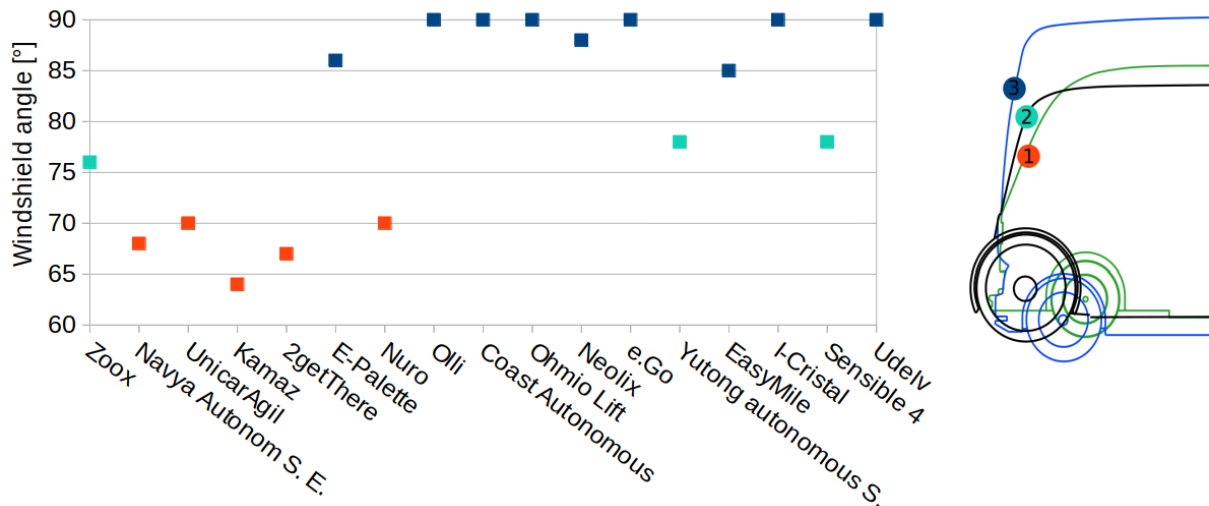


Figure 3.8: Clustered windshield angle

- Maximum velocities confirm the urban character of this vehicle concept. Only 2 data points (out of 20) are clearly highway capable.

3.2.2 Derivation of the simulation conditions

From the analyzed data of the previous section, a representative geometry and velocity are derived. From those, the relevant fields are the generic car length and the simulation velocity. They define the Reynolds number of the reference simulation.

The **length** of the generic shuttle is defined as the average of the passenger shuttle's length, which for simplification is **4.5 m** (instead of the exact value 4.493 m).

The **simulation velocity** is defined as the permitted maximum urban speed in the majority of the countries: **50 km/h**, which is the rounding of the average of the calculated max shuttle speed: 49.6 km/h.

These two parameters define the **Reynolds** number:

$$Re = \frac{Ul}{\nu} = \frac{\frac{50}{3.6} [m/s] 4.5 [m]}{1.5 \times 10^{-5} [m^2/s]} = 4.17 \times 10^6 \quad (3.1)$$

This value is used as a reference value to identify similar DrivAer studies for validation purposes.

The Reynolds number provides information on the flow regimen under simulation conditions. Gilhaus [22] studied the C_d characterization depending on the drag of similar types of vehicles. The chart on the top left corner of Figure 2.16 depicts such analysis. This behavior is relevant

to understand the effects of increasing/decreasing the length of the shuttle or the simulation speed. From Figure 2.16, the C_d is expected to decrease for rising values of Reynolds. Moreover, $Re = 4.17 \times 10^6$ indicates that only the first 12% of the vehicle's length is surrounded by laminar flow. From that point on ($Re = 5 \times 10^5$), the turbulent regimen appears.

3.3 Validation of the simulation software (*Pacefish*[®])

The lack of aerodynamic studies of this vehicle type eliminates the possibility to accurately validate the simulation software and the results with existing data. For that reason, the validation of the CFD software under study conditions has been performed with the extensively investigated and validated DrivAer geometries.

3.3.1 DrivAer geometry selection

The DrivAer is a set of 3 base shape cars (notchback, fastback and estate) with interchangeable geometrical features developed by Heft [11] to establish a realistic generic car model for aerodynamic research purposes. From the multiple DrivAer geometries, E_D_wW_wM with GS and E_S_wW_wM with GS were selected for the validation of *Pacefish*[®]. These vehicle codes represent:

- E_D_wW_wM with GS: Estate car, Detailed underbody, with Wheels, with Mirrors and including Ground Simulation.
- E_S_wW_wM with GS: Estate car, Smooth underbody, with Wheels, with Mirrors and including Ground Simulation.

The choice of these geometries is based on the geometrical similarity in the rear-end (Estate vehicle) with comparable flow detachment to the autonomous shuttle. The selection of Detailed and Smooth underbodies as the two geometries to derive a ΔC_d is due to the extensive literature evaluation of these combinations. Figure 3.9 depicts the selected geometries.

The collected data from these the E_S_wW_wM with GS and E_D_wW_wM with GS is listed in Table 3.2. The nomenclature used for Table 3.2 is:

- Wind Tunnel (WT) experimental data: WT (*institution (author)*).
- Simulation data: CFD (*turbulence model(author)*).

From the Table 3.2, the data selected for the validation is highlighted in blue. This choice is based on the following reasons:

- The Reynolds number of these reference data (4.87×10^6) is similar to the study-simulation Reynolds number: 4.17×10^6 .
- They are the only data obtained in the same study [11] and under the exact same conditions. No other study found analyzes both geometries.

Therefore, the reference literature value employed to validate the CFD software is $\Delta C_d = 0.027$.

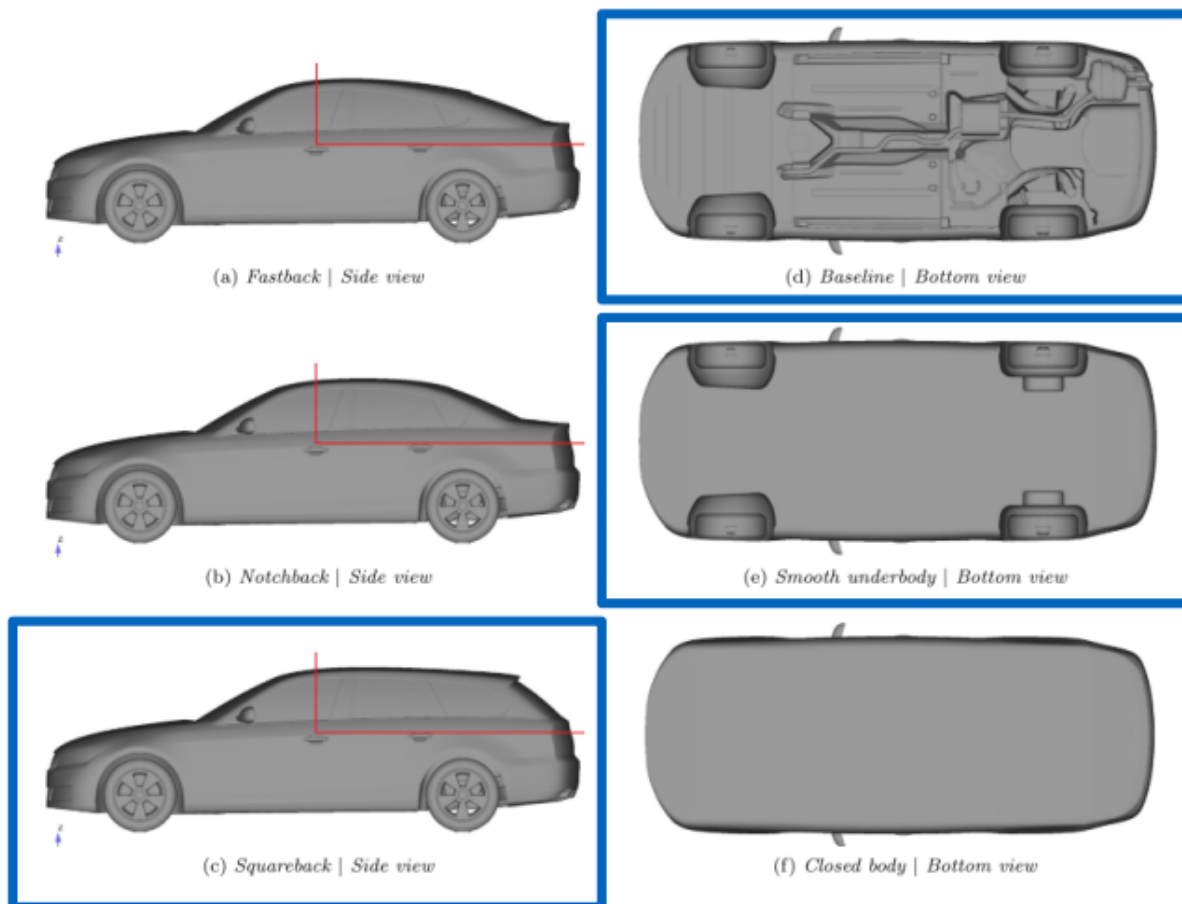


Figure 3.9: Selected DrivAer state geometries. Bottom-left image depicts the Estate (or Squareback) car. Right-hand side highlighted images depict the detailed (top) and smooth (bottom) underbodies (Yazdani R., 2015, p. 4, Fig 3.1) [20]

Table 3.2: Collected literature C_d E_S_wW_wM with GS and E_D_wW_wM with GS data

| E_S_wW_wM with GS | C_d | Re (10^6) |
|---|-------|-----------------|
| WT (TUM (Heft)) [11] | 0.292 | 4.87 |
| WT (TUM (Collin)) [14] | 0.299 | 5.2 |
| WT (Audi Aeroacoustic Wind Tunnel (AAWK) (Collin)) [14] | 0.298 | 5.2 |
| CFD (DDES (Collin)) [14] | 0.295 | 11 |
| WT (TUM (Miao)) [13] | 0.291 | 5.2 |
| CFD (RANS kwSST (Miao)) [13] | 0.259 | 5.06 |
| CFD (SST-IDDES (Wang)) [19] | 0.298 | 8 |
| WT (Volvo Cars Slotted Walls Wind Tunnel (PVT) (Yazdani)) [20] | 0.276 | 8.54 |
| CFD (SA-DDES (Yazdani)) [20] | 0.296 | 8.54 |
| E_D_wW_wM with GS | C_d | Re (10^6) |
| WT (TUM (Heft)) [11] | 0.319 | 4.87 |
| CFD (LBM-Very Large Eddy Simulation (VLES) (Maier)) [17] | 0.301 | 3.82 |
| WT (Research Institute for Road Vehicles and Engines (FKFS) (Maier)) [17] | 0.309 | 3.82 |
| CFD (SST-IDDES (Ashton)) [18] | 0.306 | 4.87 |

3.3.2 Setup of the DrivAer simulations

The main parameters of the validation setup are depicted in Figure 3.10. Framed in blue are the common parameters aimed to be used in the rest of the simulations performed in this study.

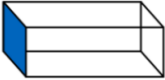
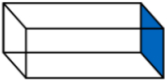
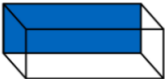



| Setup report: DrivAer simulations | | | | | | | | | | | | | | | | | | | | | | | | | | | | | | | | | | | | | | | | | | | |
|--|---|------------------------------|----------|------|-------|----------------------|-------|----------------------------|-------|----------------------|---------|-------------------|---------------|-----------------------|--------------|-----------------|------------|-------------------|----------|-----------------------|--|---------------|---------------------------|-------------------|---------|---------------------|--------|-----------------------|----|-------------------------|-----|------------------|--|------------------|--------|-----------------------|-------|-----------|---------------------------------|--------------------|------------------------|------------------------------------|-----|
| Domain size: 15.00 x 6.00 x 3.00 [dimless] | | | | | | | | | | | | | | | | | | | | | | | | | | | | | | | | | | | | | | | | | | | |
|  | Inlet Inflow turbulence: 0% | | | | | | | | | | | | | | | | | | | | | | | | | | | | | | | | | | | | | | | | | | |
|  | Outlet | | | | | | | | | | | | | | | | | | | | | | | | | | | | | | | | | | | | | | | | | | |
|  | Cyclic boundary | | | | | | | | | | | | | | | | | | | | | | | | | | | | | | | | | | | | | | | | | | |
|  | Cyclic boundary | | | | | | | | | | | | | | | | | | | | | | | | | | | | | | | | | | | | | | | | | | |
|  | Slip wall | | | | | | | | | | | | | | | | | | | | | | | | | | | | | | | | | | | | | | | | | | |
|  | Wall with no slip Translation velocity: 16 m/s | | | | | | | | | | | | | | | | | | | | | | | | | | | | | | | | | | | | | | | | | | |
| <table border="1"> <tbody> <tr> <td>Number of refinement levels:</td> <td>Up to R7</td> </tr> <tr> <td>Car:</td> <td>R1-R7</td> </tr> <tr> <td>Floor under the car:</td> <td>R1-R6</td> </tr> <tr> <td>Floor in front of the car:</td> <td>R1-R4</td> </tr> <tr> <td>Base mesh cell size:</td> <td>0.288 m</td> </tr> <tr> <td>Finest cell size:</td> <td>2.252 mm (R7)</td> </tr> <tr> <td>Total number of cells</td> <td>81.7 million</td> </tr> <tr> <td>Wheel rotation:</td> <td>Only tires</td> </tr> <tr> <td>Turbulence Model:</td> <td>SST-DDES</td> </tr> <tr> <td colspan="2">Simulation parameters</td> </tr> <tr> <td>Duration LBM:</td> <td>4,800 timesteps (8.650 s)</td> </tr> <tr> <td>Reference length:</td> <td>4.613 m</td> </tr> <tr> <td>Reference velocity:</td> <td>16 m/s</td> </tr> <tr> <td>Reference length LBM:</td> <td>16</td> </tr> <tr> <td>Reference velocity LBM:</td> <td>0.1</td> </tr> <tr> <td colspan="2">Model indicators</td> </tr> <tr> <td>Reynolds number:</td> <td>4.88e6</td> </tr> <tr> <td>Grid Reynolds number:</td> <td>4,769</td> </tr> <tr> <td>Exporter:</td> <td>Statistical (steady state-like)</td> </tr> <tr> <td>Sampling interval:</td> <td>32 timesteps (0.057 s)</td> </tr> <tr> <td>Averaging time share from the end:</td> <td>70%</td> </tr> </tbody> </table> | | Number of refinement levels: | Up to R7 | Car: | R1-R7 | Floor under the car: | R1-R6 | Floor in front of the car: | R1-R4 | Base mesh cell size: | 0.288 m | Finest cell size: | 2.252 mm (R7) | Total number of cells | 81.7 million | Wheel rotation: | Only tires | Turbulence Model: | SST-DDES | Simulation parameters | | Duration LBM: | 4,800 timesteps (8.650 s) | Reference length: | 4.613 m | Reference velocity: | 16 m/s | Reference length LBM: | 16 | Reference velocity LBM: | 0.1 | Model indicators | | Reynolds number: | 4.88e6 | Grid Reynolds number: | 4,769 | Exporter: | Statistical (steady state-like) | Sampling interval: | 32 timesteps (0.057 s) | Averaging time share from the end: | 70% |
| Number of refinement levels: | Up to R7 | | | | | | | | | | | | | | | | | | | | | | | | | | | | | | | | | | | | | | | | | | |
| Car: | R1-R7 | | | | | | | | | | | | | | | | | | | | | | | | | | | | | | | | | | | | | | | | | | |
| Floor under the car: | R1-R6 | | | | | | | | | | | | | | | | | | | | | | | | | | | | | | | | | | | | | | | | | | |
| Floor in front of the car: | R1-R4 | | | | | | | | | | | | | | | | | | | | | | | | | | | | | | | | | | | | | | | | | | |
| Base mesh cell size: | 0.288 m | | | | | | | | | | | | | | | | | | | | | | | | | | | | | | | | | | | | | | | | | | |
| Finest cell size: | 2.252 mm (R7) | | | | | | | | | | | | | | | | | | | | | | | | | | | | | | | | | | | | | | | | | | |
| Total number of cells | 81.7 million | | | | | | | | | | | | | | | | | | | | | | | | | | | | | | | | | | | | | | | | | | |
| Wheel rotation: | Only tires | | | | | | | | | | | | | | | | | | | | | | | | | | | | | | | | | | | | | | | | | | |
| Turbulence Model: | SST-DDES | | | | | | | | | | | | | | | | | | | | | | | | | | | | | | | | | | | | | | | | | | |
| Simulation parameters | | | | | | | | | | | | | | | | | | | | | | | | | | | | | | | | | | | | | | | | | | | |
| Duration LBM: | 4,800 timesteps (8.650 s) | | | | | | | | | | | | | | | | | | | | | | | | | | | | | | | | | | | | | | | | | | |
| Reference length: | 4.613 m | | | | | | | | | | | | | | | | | | | | | | | | | | | | | | | | | | | | | | | | | | |
| Reference velocity: | 16 m/s | | | | | | | | | | | | | | | | | | | | | | | | | | | | | | | | | | | | | | | | | | |
| Reference length LBM: | 16 | | | | | | | | | | | | | | | | | | | | | | | | | | | | | | | | | | | | | | | | | | |
| Reference velocity LBM: | 0.1 | | | | | | | | | | | | | | | | | | | | | | | | | | | | | | | | | | | | | | | | | | |
| Model indicators | | | | | | | | | | | | | | | | | | | | | | | | | | | | | | | | | | | | | | | | | | | |
| Reynolds number: | 4.88e6 | | | | | | | | | | | | | | | | | | | | | | | | | | | | | | | | | | | | | | | | | | |
| Grid Reynolds number: | 4,769 | | | | | | | | | | | | | | | | | | | | | | | | | | | | | | | | | | | | | | | | | | |
| Exporter: | Statistical (steady state-like) | | | | | | | | | | | | | | | | | | | | | | | | | | | | | | | | | | | | | | | | | | |
| Sampling interval: | 32 timesteps (0.057 s) | | | | | | | | | | | | | | | | | | | | | | | | | | | | | | | | | | | | | | | | | | |
| Averaging time share from the end: | 70% | | | | | | | | | | | | | | | | | | | | | | | | | | | | | | | | | | | | | | | | | | |

Figure 3.10: Setup report of the DrivAer simulations

The dimensions of the simulation domain are 15.00 x 6.00 x 3.00 dimensionless length units, which is equivalent to 15, 6 and 3 times the reference length (car length [m]). These measurements try to replicate an open-air condition. The vehicle is positioned such that there are four car lengths in front of it in the x-direction, its center of gravity is located at $y = 3$ and it lays on top of the plane $z = 0$. Considering the DrivAer frontal area of $A = 2.17125 \text{ m}^2$, this spatial configuration produces a blockage of:

$$\text{Blockage} = \frac{2.17125 \text{ m}^2}{6 \times 3 \times (4.613 \text{ m})^2} 100 = 0.57\% \quad (3.2)$$

The calculated blockage indicates a shallow impact of the walls surrounding the vehicle. Gleason [57] found that already starting at blockages upwards from 0.5%, the drag coefficient is substantially influenced by pressure generated by the walls. The increment between blockages of 0.5% and 2% induce a variation of $\Delta C_d = 0.007$ on the studied vehicle [57]. Hence, this layout is assumed to be close to represent of an open-air situation. Lower blockage values require larger simulation domain, and hence, more simulation cells to achieve the same accuracy. This fact is not desired.

Inflow Turbulence is defined as 0%. Generally, wind tunnels have values $Tu \leq 0.4\%$. This is the case of the experimental setup selected for validation [11]. Nonetheless, Heft [11] does not state the exact value of such property. Therefore, a value contained within the normal range is defined. Even though a $Tu = 0\%$ might seem unrealistic and the known influence of this property on the Re_{crit} (Figure 2.3), the approach taken in the observation of the ΔC_d as a validation parameter annuls the relevance Tu . Nonetheless, this fact should be considered in the analysis of single DrivAer geometries.

The mesh is focused on three regions: surrounding the shuttle, the floor section underneath the vehicle and in front of it. All mesh regions use a geometry-adapted technique. The mesh around the car contains seven refinement levels created with a combination of uniform and

wake-directional expansion cells. The red carpet region (floor area underneath and in front of the vehicle) is refined up to refinement levels 4 and 6, respectively.

The base mesh cell size and the finest cell size vary from this simulation to the other because of how these parameters are calculated:

$$\text{Base mesh cell size} = \frac{\text{Reference length}}{\text{Reference length LBM}} \quad (3.3)$$

$$\text{Finest cell size} = \frac{\text{Reference length}}{\text{Reference length LBM}} \frac{1}{2^{\text{highest refinement level}}} \quad (3.4)$$

The duration of the simulation, which is 4,800 timesteps, corresponds to 2 flow passes. Thus, a particle travelling at reference velocity takes 4,800 timesteps to cover the simulation domain length twice. During the first 400 timesteps *Pacefish*[®] accelerates the fluid particles with a virtual force. This process takes less than 10% of the total time. The settle face is considered as 20% of the 4,800 timesteps. The averaging of the fluid variables is performed in the last 70%. Increasing the total simulation duration and the averaging share (in %) could potentially identify slower fluctuations in the time domain. Nonetheless, this would increase the running time, which is already considerably high.

The *reference length LBM* and *reference velocity LBM* are intrinsic Lattice Boltzmann parameters. The first one controls the base grid dimensions. The second one is related to the execution time and simulation accuracy of the physical problem's representation.

Figure 3.11 depicts the car position in the simulation domain and the representation of the refinement levels.

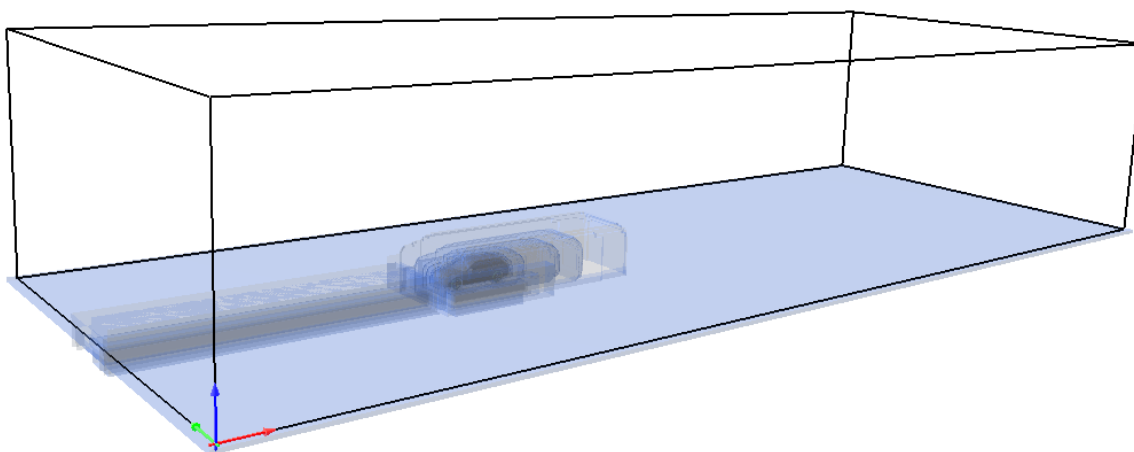


Figure 3.11: Simulation domain and refinement levels representation of the DrivAer simulations

In LBM, a mesh with 81.7 million cells is considered to have medium-high complexity. This value offers a good trade-off between simulation time and accuracy. A simulation with the setup depicted in Figure 3.10 takes between 7 hours and 9 hours (depending on the different factors) in a system with specifications:

Table 3.3: Description of the system used for the simulations

| System Information | Data |
|--|---------------------------------------|
| Total GPU Memory | 48 Gb |
| GPU Components | 4 x Titan V |
| Total Central Processing Unit (CPU) Memory | 264 Gb |
| CPU Components | 12 x Intel® Xeon® E5-2630 0 @ 2.30GHz |

In *Pacefish*[®], the approximated accuracy of a simulation is diagnosed with a parameter called *Grid Reynolds number*. It describes the wall resolution, which approximates the error performed in the shear forces. For values under 30,000, the error in the shear forces is lower than 10%. Ideally, the *Grid Reynolds number* should be below 3,000 (corresponding to an estimated error in the shear forces below 1%). In the described setup, this parameter is 4,769. This value directly influences the y^+ , which defines the "application window" of the wall model used by *Pacefish*[®]. This range of values and the equivalent estimated error in shear forces is calibrated with empirical data. However, the error in the drag coefficient can not be estimated.

The described setup finds the optimal balance between accuracy and simulation time, given that more than 30 simulations are required to achieve the study objective.

3.3.3 Evaluation of the DrivAer simulations

The simulations in the frame of the setup depicted in Figure 3.10 are correctly performed due to the observation of the following health variables:

- The maximum LBM velocity at any cell and timestep of the simulation does not exceed 0.25, which is the warning threshold. This variable is related to the Ma , and this one to the compressibility and the error of the LBE.
- The maximum y^+ at any cell and timestep of the simulation is contained within the "application window" of the wall model.

The assessment of the setup and software validation is performed with the analysis and comparison of the C_p distribution of the E_D_wM_wW with GS DrivAer vehicle [11] and the evaluation of the similarities between the experimental ΔC_d [11] and the simulated value.

Figure 3.12 and 3.13 depict the comparison of the C_p distribution in the longitudinal symmetry plane of the E_D_wM_wW with GS DrivAer vehicle on the top and bottom respectively, between the obtained simulation data and the findings of Heft [11]. These last ones are linear interpolations of point data (pressure sensors in a wind tunnel), whereas the simulation results are described with a continuous function. This comparison aims to visualize a correct pressure distribution under the conditions of the defined simulation setup.

Both figures (3.12 and 3.13) characterize the C_p over the dimensionless x-coordinate of the simulation domain. The abscissa of the chart represents the length of the car [dimensionless] in the global reference system ($x \in [4,5]$).

The simulated C_p response over the top of the DrivAer vehicle (Figure 3.12) has a very similar trend as the wind tunnel data [11]. There are slight discrepancies between $4.45 < x < 4.6$. However, out of this segment, the lines match accurately. Most importantly, the critical rear-end region ($x > 4.9$), where the flow detaches, is appropriately characterized.

The positioning of the sensors that capture the pressure coefficient (C_p) along the bottom of the vehicle [11] is more spaced than along the top. Therefore, the linear interpolation between points

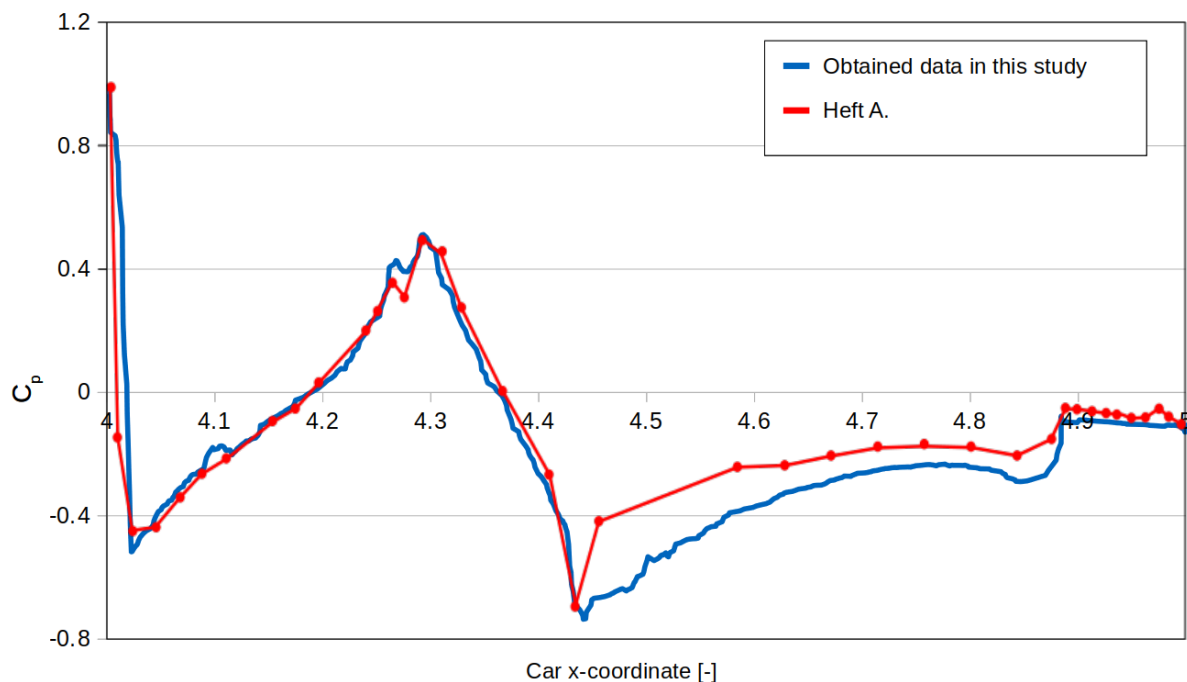


Figure 3.12: Comparison of the distribution of the pressure coefficient in the $y = 0$ mm plane at the top of the vehicle configuration E_D_wM_wW with GS with literature data

is coarser. Nonetheless, the match with the obtained data is substantial. The only discrepancy is located at $x \sim 4.38$. Similar to the Figure 3.12, the critical rear-end region ($x > 4.8$) is properly characterized.

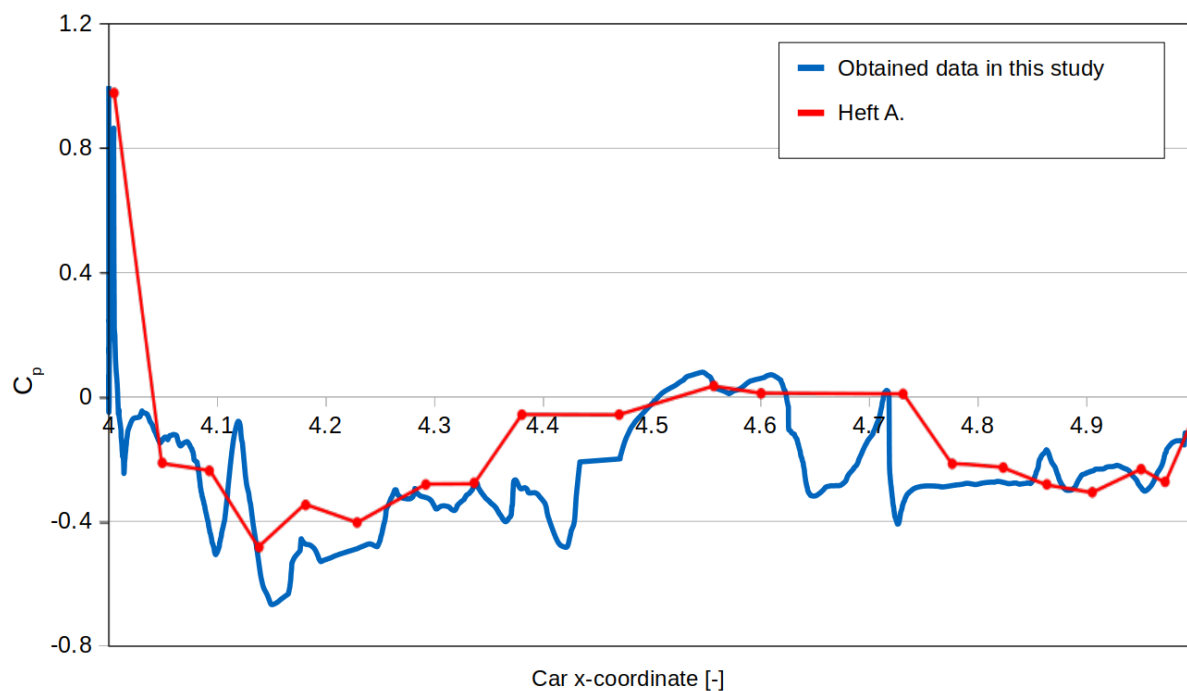


Figure 3.13: Comparison of the distribution of the pressure coefficient in the $y = 0$ mm plane at the bottom of the vehicle configuration E_D_wM_wW with GS with literature data

The obtained difference in C_d between E_D_wM_wW with GS and E_S_wM_wW with GS is $\Delta C_d = 0.019$. This value is not far from the observed experimental increment $\Delta C_d = 0.027$ [11]. Karniadakis [58] defines a range of values to assess the accuracy between experimental and simulated data. This is depicted in Table 3.4.

Table 3.4: Rating of the Difference Between Numerical and Experimental Data (Karniadakis, 2019, p. 1081, Table 14.2) [58]

| Rating | Drag coefficient |
|------------|-------------------------|
| Good | $\Delta C_d \leq 0.005$ |
| Acceptable | $\Delta C_d \leq 0.010$ |
| Bad | $\Delta C_d > 0.010$ |

Karniadakis [58] considers as accurate a simulation that differs less than 0.005 in C_d to the equivalent experimental result. Therefore, $|C_{d,experimental} - C_{d,simulation}| \leq 0.005$, which extrapolated to difference between two studied geometries results in $|\Delta C_{d,experimental} - \Delta C_{d,simulation}| \leq 0.010$. This corroborates the accuracy of the validation process of the software and setup conditions, given that $|\Delta C_{d,Heft A.} - \Delta C_{d,Pacefish}| = 0.008 \leq 0.010$.

The observed disparity in ΔC_d is assumed to be caused by the following factors:

- The simulation accuracy has been defined such that there is a trade-off between results and simulation time. Under those setup conditions, the *Grid Reynolds number* indicates an error in the shear forces of $\simeq 1.6\%$.
- The experimental averaging is performed over three sets of 10 seconds with data collection intervals of 0.05 seconds. Due to the execution time limitations, the analogous simulated parameters are 6.055 seconds and 0.057 seconds.
- The wheel rotation in *Pacefish*[®] is only applied to the rotation-symmetric geometries, which in this case are the tires (excluding the rims). In the experimental setup [11], this is not the case.

However, from the obtained findings the following is assumed:

- The C_p characterization along the top and bottom of the vehicle matches the experimental data [11].
- The difference in drag coefficient is assessed as accurate by the standards of Karniadakis [58].

Thus, it is assumed that *Pacefish*[®] is capable to accurately identify drag variations under the used mesh and setup conditions.

3.4 Generic autonomous shuttle

After validating the CFD software, a base geometry defined as the aerodynamic reference data is required. The design choices for the derivation of this generic shuttle follow.

3.4.1 Design of the generic shuttle

The derivation of the generic shuttle is based on the data analysis performed in Section 3.2.1. The following is a description of the necessary dimensions and design features for the CAD representation of such geometry:

- Length: **4.50 m** (instead of the exact value 4.493 m). Derived in Section 3.2.2. Use of the passenger shuttle length average.
- Width (b): **2.00 m** (instead of the exact value 1.996 m). Use of the ratio width/length average of all shuttles (passenger and object transportation) and the derived length.
- Height (H): **2.64 m** (instead of the exact value 2.638 m). Use of the ratio height/length average of standing-clustered passenger shuttles and the derived length.
- Wheelbase: **2.95 m**. Use of the ratio length/wheelbase of the Olli vehicle and the derived generic shuttle length. The wheelbase values of the E-Palette and the 2get-ThereGTR were obtained after the generic geometry was designed. Considering these new parameters and using the length/wheelbase average, the generic shuttle wheelbase would be 3.04 m. The difference in the values does not significantly impact the aerodynamic outcome due to the nature of the parameter.
- Wheel size: **215/60 R17**. Use of a representative wheel size from the four available. There is no mathematical derivation to obtain this design variable. The selected wheel size was the one from the Navya Autonom Shuttle Evo. Figure 3.14 depicts the dimensions of the rim and the tire.

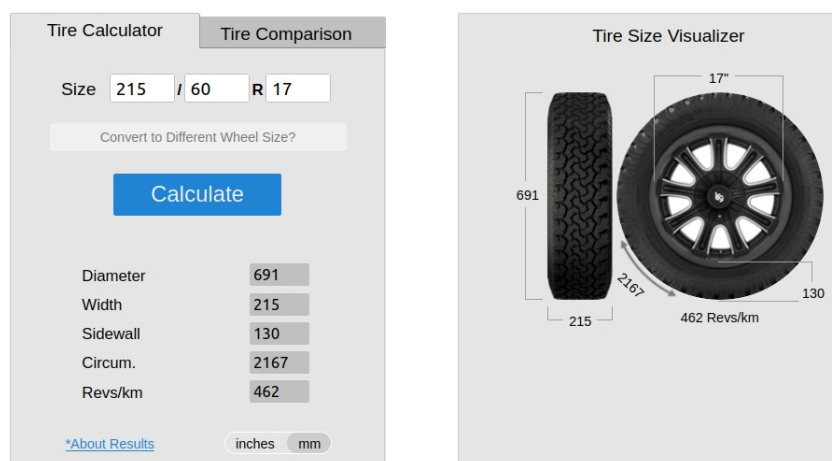


Figure 3.14: Tire and rim dimensions of a wheel 215/60 R17 (<https://tiresize.com/calculator/>)

- Ground clearance: **0.17 m**. Use of the only available data-point.
- Edge radius (r): **99.8 mm**. Use of experimental data obtained by Gotz [23] and Hucho [8]. Their findings, depicted in Figure 2.17 and 2.18, define a big C_d reduction at $r/b = 0.05$ (edge radius/vehicle width). This is equivalent to the selected edge rounding. This condition is applied to the four front and rear edges and the two longitudinal top edges.
- Windshield angle (a): **77.33°**. Use of the clustered windshield angles. From the analyzed data in Figure 3.8, an averaged windshield angle has been extracted from each cluster: $a = 67.80^\circ$, $a = 77.33^\circ$ and $a = 88.63^\circ$. These values correspond

to cluster 1, cluster 2 and cluster 3, respectively. The value used for the generic geometry belongs to the averaged value of the second cluster, which at the same time is not far away from the total average ($\alpha = 80.59^\circ$).

- Height at which the windshield starts: **25% of the height**. Use of only height share studied by Gotz [23], depicted in Figure 3.15. It provides a base for comparison between the front angled "windshield" starting at 25% of the height and the flat front: $\Delta C_d = 0.010$.

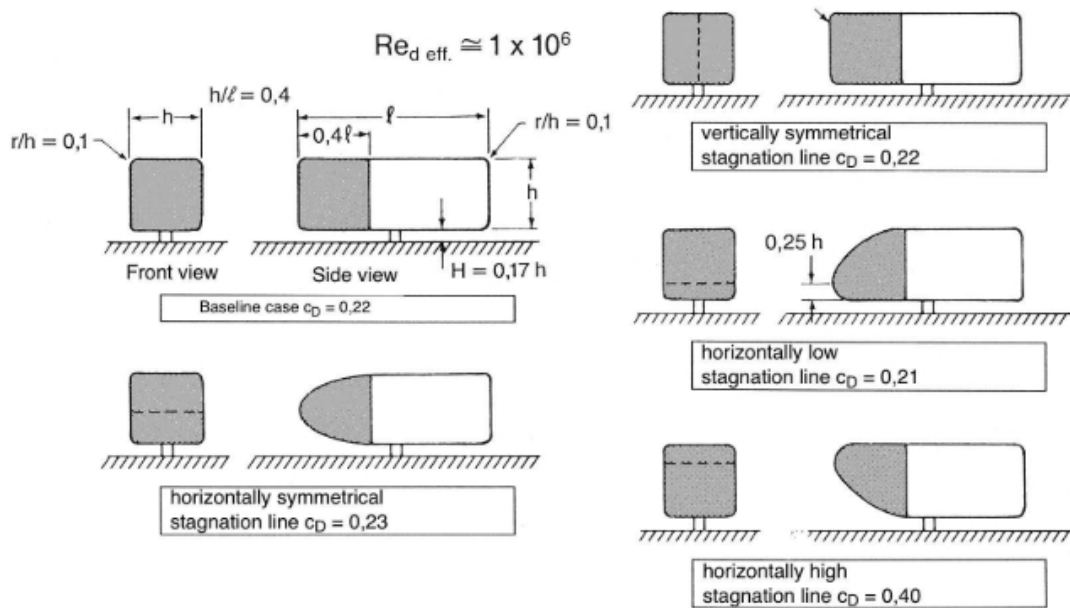


Figure 3.15: Impact of streamlined front-mounted structures on cuboids on the c_D value at ground level (Gotz, 1987, p. 774, Fig 10.83) [23]

The generic shuttle considers all above listed variables in a symmetric design. The render is depicted in Figure 3.16.

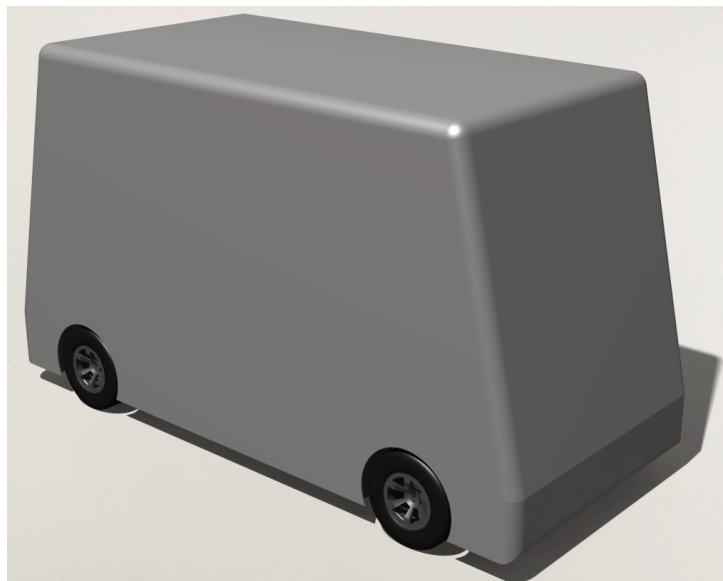


Figure 3.16: Generic shuttle design

3.4.2 Setup of the generic autonomous shuttle simulation

The setup of the generic shuttle geometry defines the base setup that is used by upcoming simulations.

For the geometrical representation of a solid inside the simulation, *Pacefish*[®] requires an .stl format file. The format transformation from CAD file to .stl is done in ANSA. This software enables custom meshing of surfaces and volumes. The process followed for surface meshing of each geometry component is:

1. Save CAD component in Catia V5 with format .stp.
2. Import .stp.
3. Set the global resolution of 3 mm. This value defines the segment distance to represent the edges of the geometry.
4. Fix geometry.
5. Mesh as .stl with the automatic feature.
6. Run mesh check control and fix problematic cells if needed.
7. Export as .stl.

The setup summary of the generic shuttle simulation is depicted in Figure 3.17.

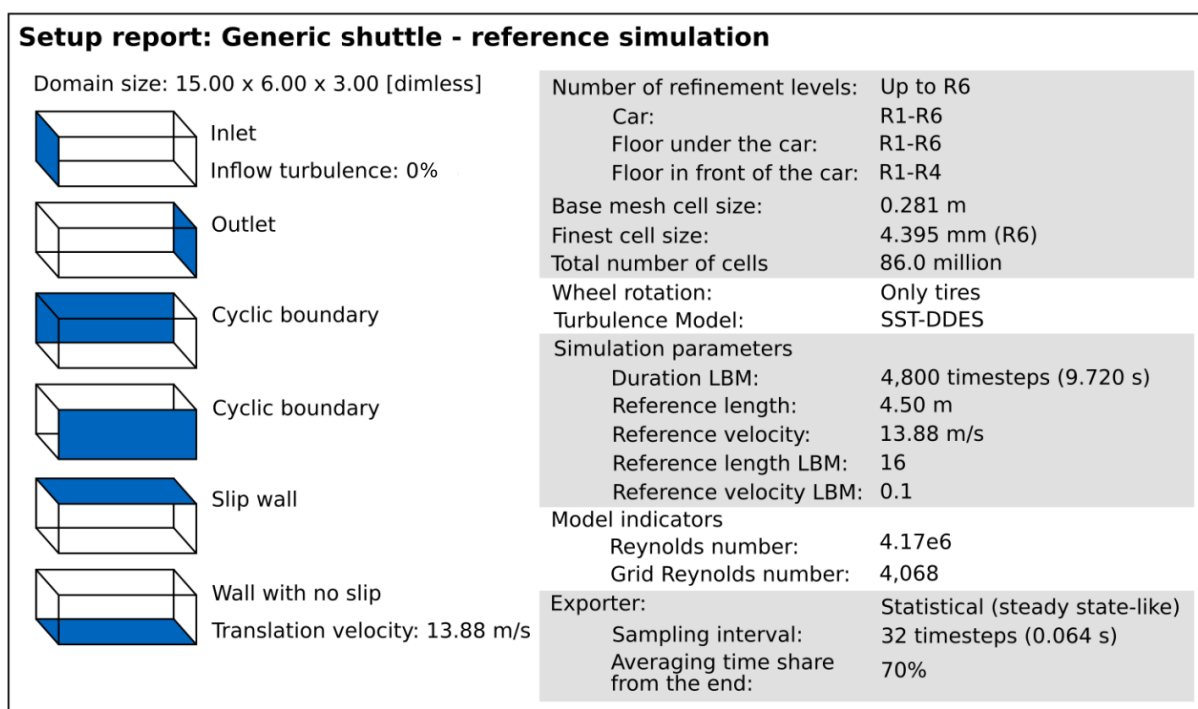


Figure 3.17: Setup report of the generic shuttle simulation

Unlike the setup of the validation simulations, this has the highest refinement level: 6 (instead of 7). This change affects the smallest cell size, which raises to 4.395 mm. Nonetheless, this modification maintains a similar number of total cells (related to the execution time) and Grid Reynolds number (which controls the accuracy). These two parameters are indicators of the equivalence of simulations. Since the refinement levels are geometry-based, the change in the body topology affects them. Hence, the mesh is slightly different. However, the setup of the

generic shuttle has higher accuracy since the Grid Reynolds number is lower. The rest of the parameters are the same as the DrivAer setup (Section 3.3.2).

In order to ensure the correct setup of the wheel rotation, a short simulation is performed. Figure 3.18 depicts the obtained surface velocity, which validates the correct definition of that parameter.

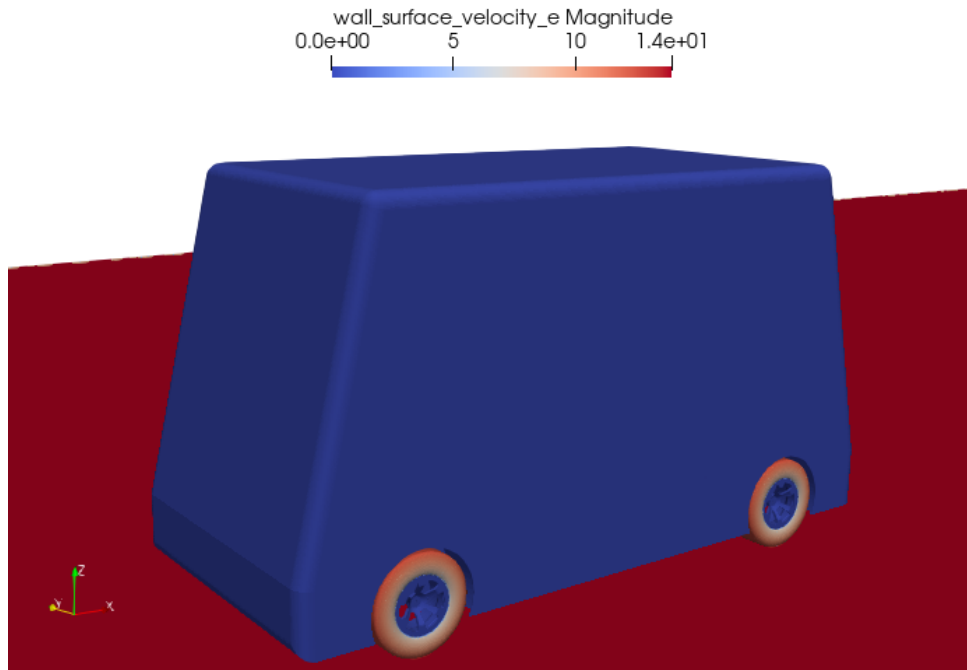


Figure 3.18: Visualization of the rotation ground and tires in the generic shuttle simulation

Figure 3.18 depicts the approach used by *Pacefish*[®] to treat rotation of geometries. As illustrated, only the tires allocate rotation. The rims do not. This restriction is required due to the non-rotation-symmetry of these elements.

3.5 Design influence on the generic shuttle

The analysis of the sensor setup's impact on the aerodynamics raises the question of how significant is that influence relative to other geometrical modifications of the vehicle (Figure 3.5). For that reason, a few design variables are studied.

3.5.1 Derivation of the study-relevant design variables

This analysis aims to study in a simplified way the fundamentals of shuttle aerodynamics, without sensors and at constant Reynolds number. For that reason, the vehicle dimensions (length, width and height) are not considered in the study-relevant design variables.

Previous studies from McDonald [21], Gilhaus [22], Gotz [23] and Hucho [8], identify the radius of the front edges as highly influential in the C_d of similar vehicle shapes. The last two authors use the parameter r/b (edge radius / vehicle width) to characterize the drag change. Both studies describe a pronounced C_d decrease from $r/b = 0$ until $r/b = 0.05$, followed by an insignificant reduction of the drag at $r/b > 0.05$. For that reason, this threshold value is used in design of

the generic shuttle. Furthermore, this studied r/b influence brings the chance to evaluate and compare its effect on this different vehicle shape. Therefore, the selected values are: $r/b = 0$ and $r/b = 0.1$.

During the analysis of the dimensions of the current autonomous shuttles, 3 clusters of windshield angles have been derived (Figure 3.8). The identified angles (average of each cluster) are $a = 67.80^\circ$, $a = 77.30^\circ$ and $a = 88.63^\circ$. The average of the second cluster is used to design the generic shuttle. The other two are considered study-relevant design variables due to the noticeable and representative use of those angles in current autonomous shuttles.

Additionally, the wheel (rim) design is considered a variable of interest, given the importance of wheel drag in current car aerodynamics. For simplification, only a fully-closed flat design is analyzed.

In order to keep the design-influence study compact, the simulations performed consider only a single variable factor change. Hence, no combination of design variables is analyzed. With that approach, the effect of the factor is isolated and the design space of the study is reduced. Table 3.5 breaks down the design influence simulations by variables, including their designated simulation code.

Table 3.5: Break down of the features selection of the design-influence simulations

| code | Windshield angle (a) | | | Radius (r) | | | Wheel design | |
|------|----------------------|--------|--------|------------|---------|----------|--------------|--------|
| | 67.8° | 77.33° | 88.65° | 0 mm | 98.9 mm | 197.8 mm | normal | closed |
| a68 | ■ | ■ | ■ | ■ | ■ | ■ | ■ | ■ |
| a89 | ■ | ■ | ■ | ■ | ■ | ■ | ■ | ■ |
| r0 | ■ | ■ | ■ | ■ | ■ | ■ | ■ | ■ |
| r198 | ■ | ■ | ■ | ■ | ■ | ■ | ■ | ■ |
| wC | ■ | ■ | ■ | ■ | ■ | ■ | ■ | ■ |

Where:

- a68: Generic shuttle geometry with windshield angle at $a = 67.8^\circ$.
- a89: Generic shuttle geometry with windshield angle at $a = 88.65^\circ$.
- r0: Generic shuttle geometry with edge rounding of $r = 0$ mm.
- r198: Generic shuttle geometry with edge rounding of $r = 197.8$ mm.
- wC: Generic shuttle geometry with closed rims.

The following images depict the renders of the geometries (Figure 3.19).

3.5.2 Setup of simulations

The setup of the simulations is the same as the one used in the generic shuttle (Section 3.4.2).

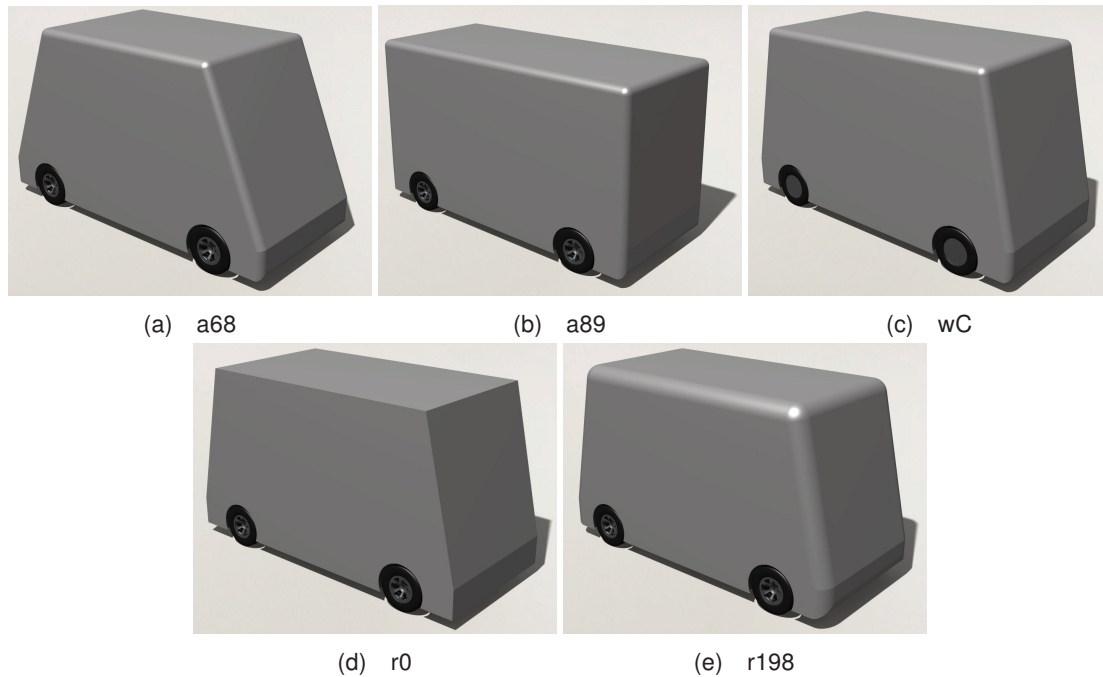


Figure 3.19: Design-influence simulation geometries

3.6 Single sensor influence on the generic shuttle

The approach taken for the analysis of the aerodynamic influence of sensor setups includes the study of individual sensor positions.

3.6.1 Derivation of the study-relevant sensor single positions

Derivation of relevant sensor positions

Due to the lack of information provided by the manufacturer, the derivation of relevant sensor positions is performed through visual inspection. Nonetheless, the possible induced error on the exact positioning is irrelevant due to the high variability of these locations present in current autonomous shuttles. The only condition for the correctness of this derivation is the selection of representative configurations and their clear documentation.

The aerodynamic analysis only considers the sensors that protrude from the bodywork, easily identifiable in the images of the vehicles. The bodywork-embedded sensors do not influence the C_d .

All identified protruding sensors have been labeled by their position (depicted in Figure 3.20). Only the front right quarter of the vehicle is represented.

Even though the positions depicted in Figure 3.20 are laid out on a quarter of the car's volume, the arranging of sensors is always symmetric relative to the longitudinal symmetry plane of the vehicle. Hence, the left side and the right side of the shuttle have the same sensors. This does not always apply to front and back.

This thesis defines the concept of *sensor position* or *single sensor position* as a combination of sensors located in the same letter code (from Figure 3.20), considering a maximum of 1 sensor per quarter of vehicle.

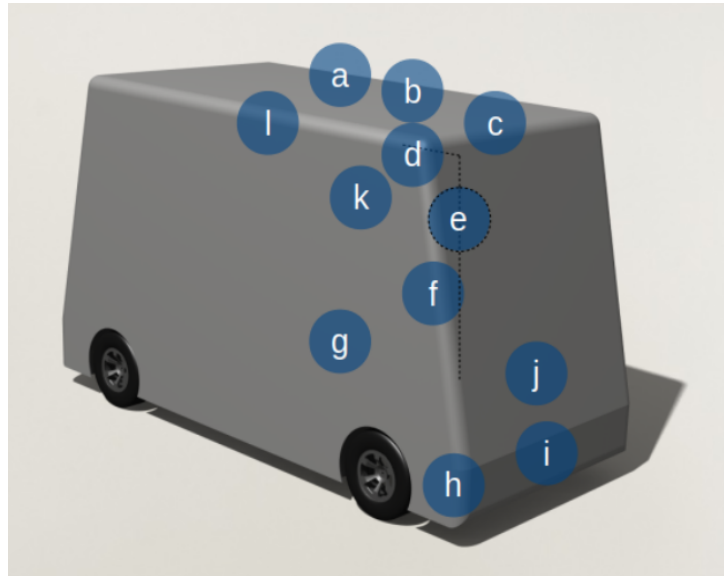


Figure 3.20: Identification of all sensor placements in current autonomous shuttles

The collected absolute number of sensors at each sensor position is gathered in Table 3.6.

Table 3.6: Sensor classification of current autonomous vehicles

| | a | b | c | d | e | f | g | h | i | j | k | l | total |
|---------------------------|---|----|----|----|---|----|----|----|----|----|----|---|-------|
| Milla Pod | 1 | | | | | | | | 1* | | | | 2 |
| Sango | | 1* | | | | 6* | | | | 2 | | | 9 |
| Zoox | | 2 | | 4 | | | | | | | | | 6 |
| Navya Autonom Shuttle Evo | 1 | | 2 | | | | 2* | | 2 | | | | 7 |
| UnicarAgil | | | | | 4 | | | | | | | | 4 |
| Kamaz | | | | | | | | | | | | | 0 |
| 2getThere GTR | | | | | | | | | | | | | 0 |
| E-Palette | 1 | | | | | | 2* | | | 2 | | | 5 |
| Apollo | | 2 | 2 | 2* | | | | 2* | | | | | 8 |
| Olli | 1 | | 2 | | | | | 6* | | 2 | | | 11 |
| Coast Autonomous | | | 2 | | | | | | | | | | 2 |
| Ohmio Lift | | 2 | | | | | | | | | | | 2 |
| Yutong Autonomous Shuttle | | | 1* | | | 2* | | | | | | | 3 |
| EasyMile | 1 | | | | | | | 4 | | 2 | 4 | | 11 |
| I-Cristal | | | 1* | | | | | | | | | | 1 |
| Sensible4 | | | 2 | | | | | | | 2 | | | 4 |
| Westfield Pod | 1 | 2 | | | | | | | | | 2* | | 5 |
| HEAT | | 4 | 2 | | | | | | | | | 2 | 8 |
| Nuro R2 | 1 | | | | | 2* | | | | | | 2 | 5 |
| Neolix | 2 | | 2 | | | 2* | | | | | | | 6 |
| Udelv | | | 2 | | | | | | | | | | 2 |
| | 9 | 13 | 18 | 6 | 4 | 12 | 4 | 12 | 3 | 10 | 6 | 4 | 101 |

From Table 3.6, the following observations are made:

- There are two vehicles which do not contain protruding sensors: Kamaz and 2getThere GTR.
- The UnicarAgil only has sensors in the position e. Moreover, no other vehicle has sensors in that location.

- In terms of location, the position i and j are quite similar. This makes it difficult to define a clear distinction.
- Considering that all shuttles have a sensor layout symmetric to longitudinal's vehicle plane:
 - Position a: 1 means one sensor and 2 means one sensor on top of the other. This rare arrangement is only present in the Neolix shuttle.
 - Position b, c, i and j (located in the longitudinal symmetry plane of the car): Even number of sensors means that sensors are positioned symmetrically in the front and back of the car. Odd number of sensors (n) means that the extra sensor is positioned in the front half of the vehicle and the remaining $n - 1$ (even number) sensors are positioned symmetrically front and back. This situation describes an asymmetric distribution (highlighted in Table 3.6 with an asterisk: *). An example of symmetric and asymmetric distributions for a single position of the longitudinal symmetry plane of the car are depicted in Figure 3.21.

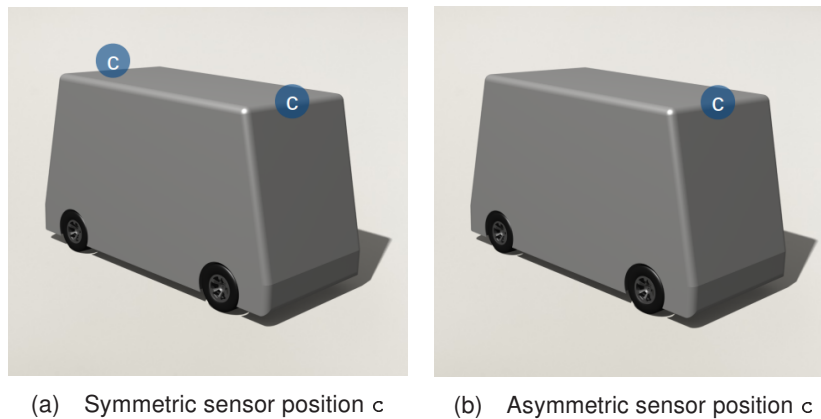
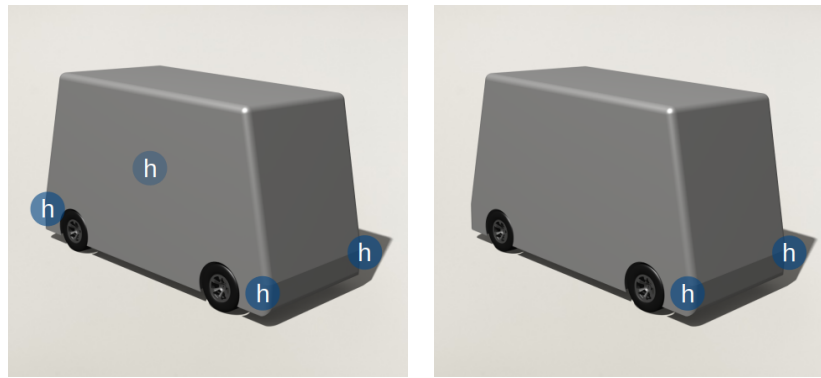


Figure 3.21: Symmetric and asymmetric sensor position c

- Positions d, e, f, g, h and k: Number of sensors multiple of 4 (m) means that the sensors are laid out symmetrically in the four quadrants of the vehicle. Even number of sensors not multiple of 4 have 2 extra sensors that are arranged in the front half of the car, besides the other ($m - 2$) which are distributed in the 4 quarters of the shuttle. This second case describes an asymmetric distribution (highlighted in Table 3.6 with an asterisk: *). Example of symmetric and asymmetric distributions for a single d, e, f, g, h or k positions are depicted in Figure 3.22.
- Position l: Always allocates an even number of sensors, arranged equally: left and right.

Figure 3.23 depicts the absolute number of times that a sensor appears in every of the labeled positions.

Differently from Figure 3.23, Figure 3.24 depicts the number of shuttles that contain at least one sensor in each defined sensor position. This differs from the first since, for example, position a has generally 1 sensor whereas h contains usually 2 or 4.



(a) Symmetric sensor position h (b) Asymmetric sensor position h

Figure 3.22: Symmetric and asymmetric sensor position h

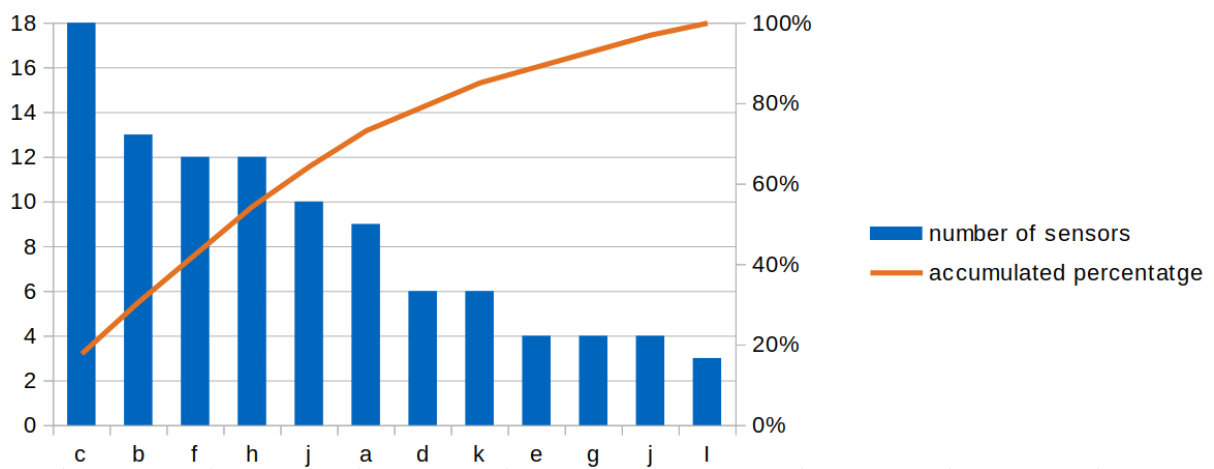


Figure 3.23: Histogram of sensor positions by number of single sensors

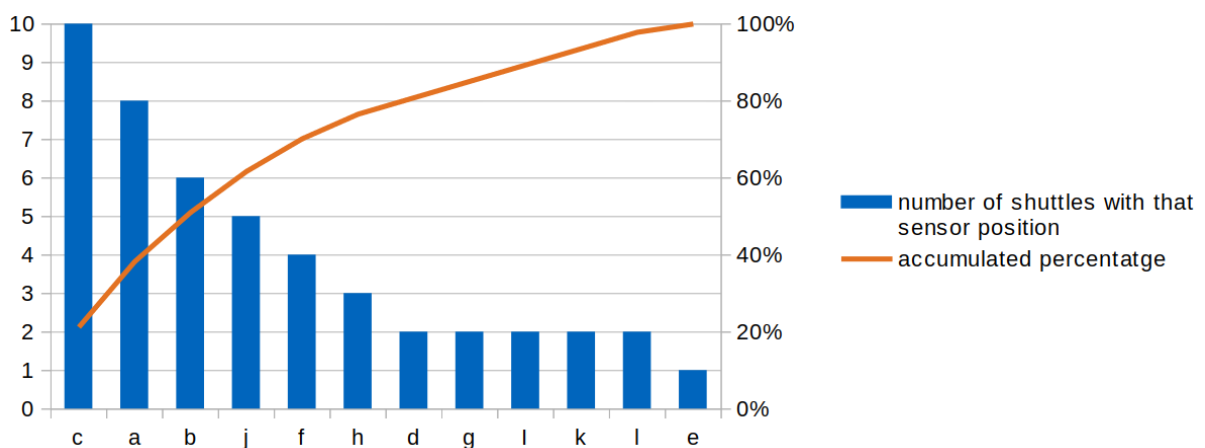


Figure 3.24: Histogram of number of cars with sensor position

Both Figure 3.23 and 3.24 show that there is no clear dominance of specific sensor position over the others. Therefore, the following simplifications have been applied in order to reduce the design space:

- Position e is considered non-relevant. Only one vehicle has sensors in that location. It is not representative of the design space.

- Given the proximity of positions *i* and *j*, they are both considered as position *i*.

Besides these two simplifications, the rest of the sensor positions are considered study-relevant. Nonetheless, to further reduce the number of simulations, only a single arrangement of sensors (symmetric or asymmetric) per each position has been considered. Figure 3.25 depicts this distribution of sensors in each position.

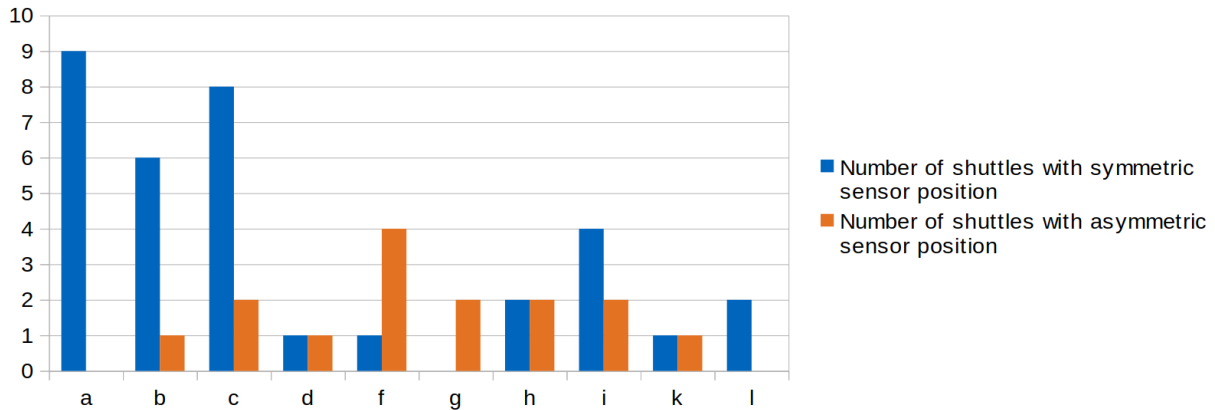


Figure 3.25: Histogram of symmetric and asymmetric distributions per sensor position

The selected sensor distributions in each position are:

- Position *a* and *l*: Symmetric, since it is the only feasible geometrical distribution.
- Positions *b*, *c* and *i*: Symmetric, since these distributions prevail over the others.
- Positions *f* and *g*: Asymmetric, since these distributions prevail over the others.
- Positions *d*, *h* and *k*: They have same number of symmetric and asymmetric sets. The sensor distribution of positions *d* and *h* has been chosen as symmetric since it is of interest to evaluate the aerodynamic impact of sensors in each of the four lower and upper corners of the vehicle. In position *k*, the selected arrangement is asymmetric, like in position *g*. This enables the observation of the height's C_d impact in side-located sensors under the same conditions of sensor position distribution.

Figure 3.26 depicts the extracted relevant position distributions. Even with the considered simplifications, the representation of the selected single sensor layouts over the total is $\sim 80\%$.

Derivation of sensor dimensions

The assessment of the sensor dimensions is quite complex. Their geometry includes the outer measurements of the component itself (defined by the sensor type and technical specifications) and the housing that attaches it to the bodywork. This last element is strictly vehicle-dependent. Nonetheless, some geometrical similarities have been used for the derivation of such housing structures.

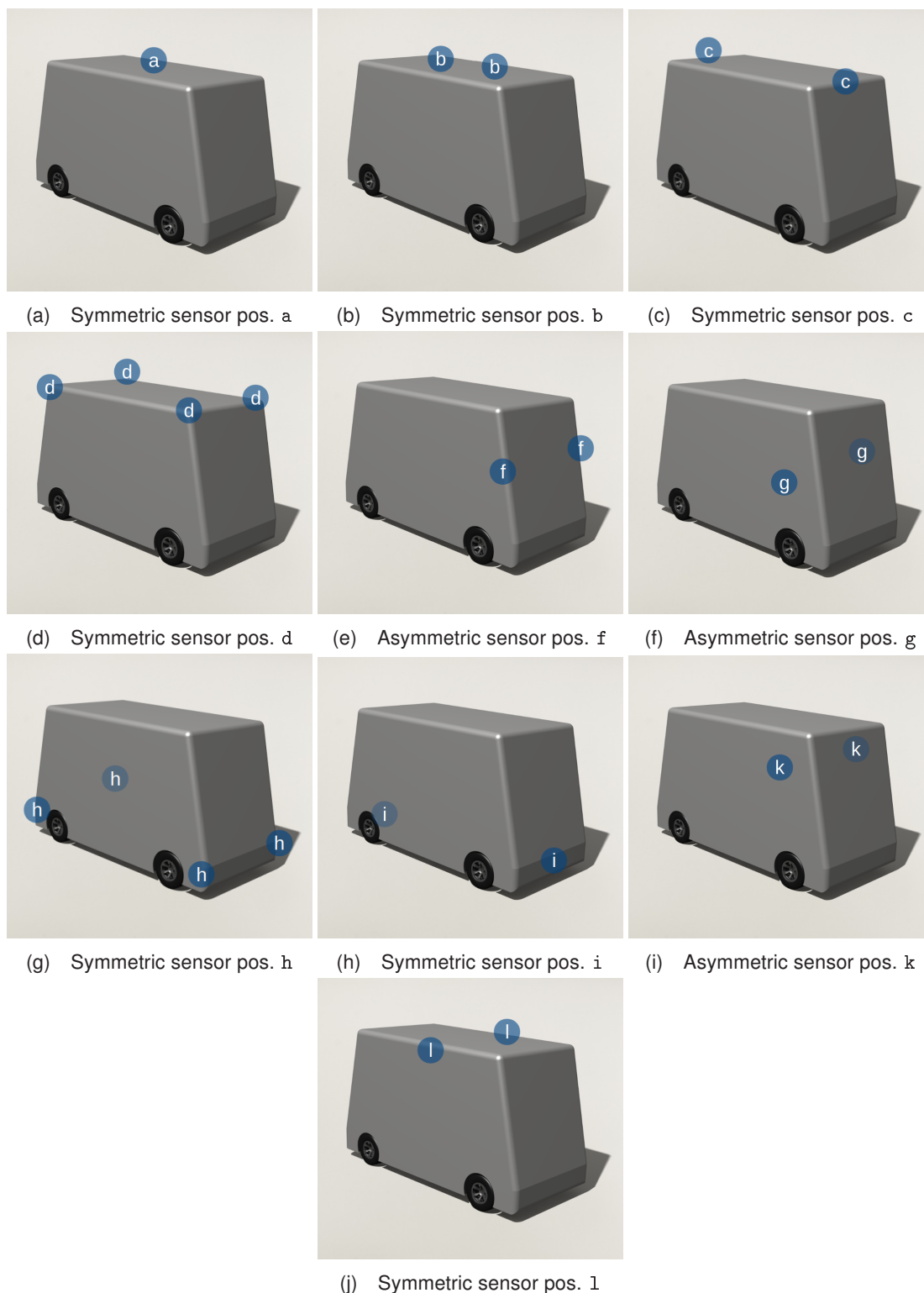


Figure 3.26: Position locations for the simulations of the single sensor case

The following are observations extracted from the visual inspection of the protruding sensors of the shuttles listed in Table 3.6:

- Generally, they are lidars with puck-like geometry.
- Generally, the lidars have two sizes. Therefore, it can not be simplified to a single sensor dimension. This increases the number of simulations but simultaneously

describes the current state of the art of autonomous shuttles more accurately. Furthermore, studying two different sizes enables the observation (simplified) of the dimensions' sensibility on the C_d .

- The housing of sensors uses curvy shapes to blend the component (fully protruding from the original bodywork surface) with the vehicle. Each sensor position and vehicle has unique housing structures.
- In position a, besides the typical puck-like geometries, some shuttles use a big box to house several sensors.

Regarding the above-described observations, the study of the single sensors is defined to include two different puck sizes at each sensor position, with unique housing structures that mimic the observed current shuttles. Additionally, sensor position a incorporates the study of two box-shaped geometries. The derivation of the dimensions is described in the upcoming sections.

Puck-like sensors For the representation of the puck-like sensors, two different *Velodyne Lidar*¹ products have been selected: The Ultra Puck and the Alpha Prime. These lidars are frequently observed in autonomous shuttles. Their measurements are depicted in Figure 3.27.

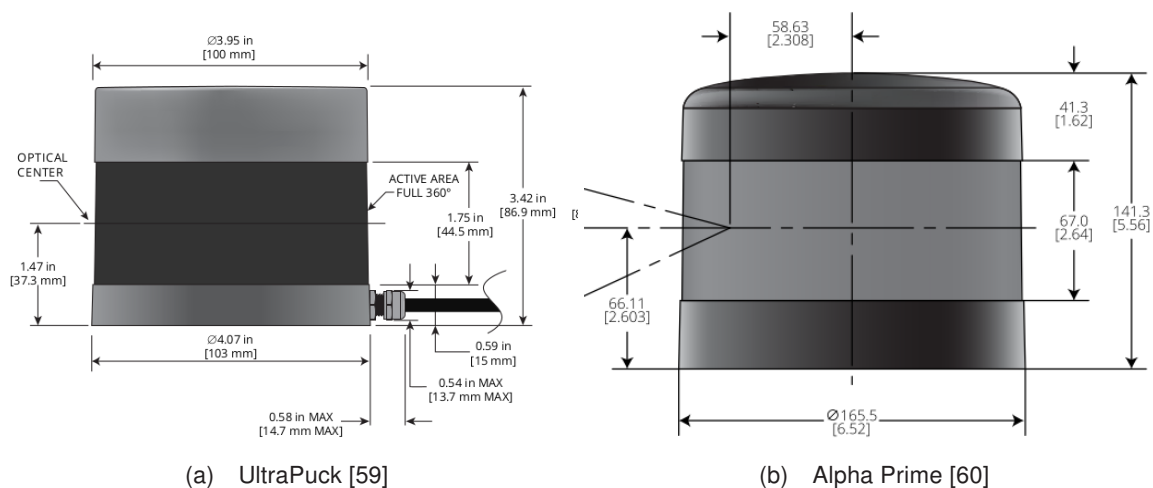


Figure 3.27: Puck sensor dimensions

Box sensors In position a, box-shaped sensor-housing geometries are employed. They constitute a representative percentage of the sensors placed in that position, and therefore they are considered in the aerodynamic study. Following the approach of the puck-like sensors, two sizes of boxes are derived:

- Big box: Dimensions 1600 mm x 1246 mm x 270 mm with 62.3 mm rounding on the four top and vertical edges. The dimensions are approximated by visual inspection from the vehicles that include this geometry. They mimic the ones found in the Milla Pod, the Navya Autonom Shuttle Evo and the EasyMile. The edges' radius is calculated with the condition $r/b = 0.05$ (radius/box width), the same aspect ratio used for the generic vehicle edge rounding.

¹<https://velodynelidar.com/>

- Small box: Same footprint, but different height and rounding. The dimensions are 1600 mm x 1246 mm x 90 mm and rounding of 20.8 mm. The box's height is derived as the smallest value to house a small puck-type lidar.

Housing The puck-like sensor supporting structures have been self-developed, mimicking existing geometries. The following grouped design guidelines have been considered:

- Housing of positions a and b: They do not require any structure. They pucks lay on top of the surface (depicted in Figure 3.28)

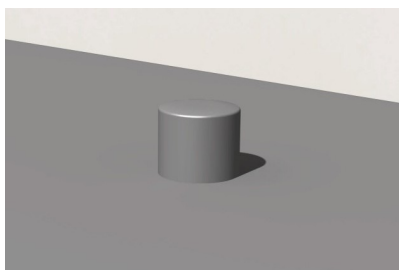
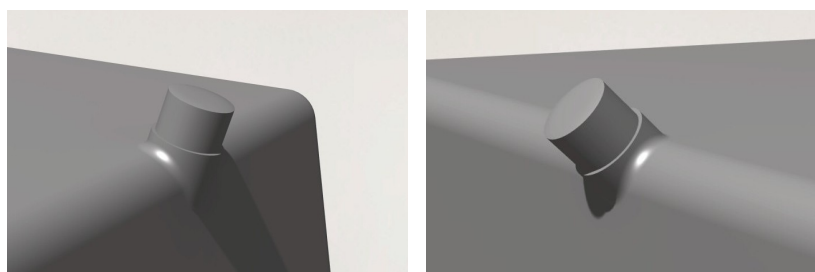


Figure 3.28: Puck sensor over top surface without supporting structure (positions a and b)

- Housing of positions c and 1: Curvy under-support structure that joins the tilted puck geometry with the bodywork. It covers a third of the puck height. Sensors in position c are angled 15° (Figure 3.29a) and in position 1 45° (Figure 3.29b). These inclinations replicate observed currently used sensors.



(a) Big puck sensor in position c (b) Big puck sensor in position 1

Figure 3.29: Puck sensors on top edge with underneath supporting structure

- Housing of position d: Special case of sensor location. In order to replicate the Zoox shuttle (only observed vehicle with comparable geometry), two pucks connected by a flat rounded structure are used (depicted in Figure 3.30).

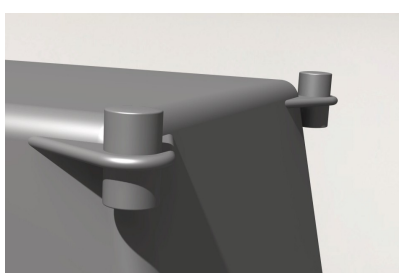


Figure 3.30: Big puck sensor in position d with supporting structure

- Housing of positions g and k: Covers exclusively the top and bottom 25% of the puck. Has small rounded top and bottom edges and curvy blending on the interface with the bodywork. This is depicted in Figure 3.31



Figure 3.31: Puck sensor on lateral surfaces with supporting structure

- Housing of positions h and f: Extruded triangular structure that covers the top and bottom 25% of the puck, enabling a visibility of 240°. Has small rounded top and bottom edges and pronounced curvy blending on the interface with the bodywork (depicted in Figure 3.32).

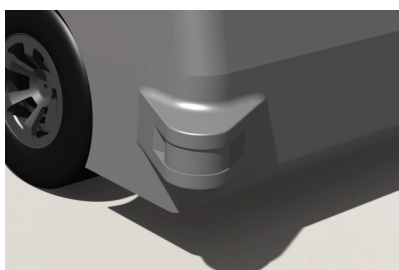


Figure 3.32: Puck sensor on lateral edges with supporting structure

- Housing of position i: Crossover structure between the last two housing structures. Covers the top and bottom 25% of the puck, enabling a visibility of 180°. Has small rounded top and bottom edges and pronounced curvy blending on the interface with the bodywork (depicted in Figure 3.33).

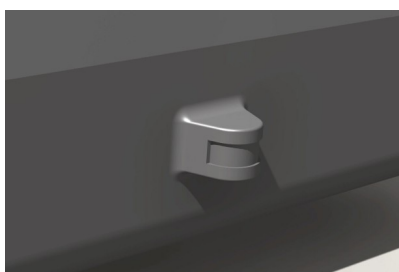


Figure 3.33: Puck sensor on front and rear surfaces with supporting structure

The final number of defined simulations to analyze the aerodynamic behavior of single sensor positions is 22. These are a combination of the 10 position layouts (depicted in Figure 3.26), considering 2 sizes of sensor and 2 extra simulations that contemplate the box-shape sensors. All these combinations try to accurately represent currently used sensor geometries in autonomous shuttles.

To more easily reference the simulations, a code is assigned to each geometry. It uses a feasible combination of two parts joined with an underscore symbol:

<sensor position>_<sensor type>

The <sensor position> is one of the following: a, b, c, d, f, g, h, i, k or l. The sensor type's code is one of the following: puckSMALL, puckBIG, boxSMALL or boxBIG.

3.6.2 Setup of simulations

The setup of the simulations is the same as the one used in the generic shuttle (Section 3.4.2).

3.7 Multi-sensor setup influence on the generic shuttle

3.7.1 Derivation of the study-relevant sensor layouts

The sensor setups are classified by the number of sensor positions that they contain. Table 3.7 contains 5 groups of rows (divided by an horizontal line) that indicate 0, 1, 2, 3 and 4 sensor positions.

Table 3.7: Classification of current autonomous shuttles by number of sensor positions and highlighting of geometries simulated (in blue) and to simulate (in gray)

| | a | b | c | d | f | g | h | i | k | l | code |
|--------------------------------|---|----|----|----|----|----|----|----|----|---|--------------------|
| Kamaz 2getThere GTR | | | | | | | | | | | |
| Coast Autonomous Ohmio Lift | | 2 | 2 | | | | | | | | |
| I-Cristal | | | 1* | | | | | | | | |
| Udelv | | | 2 | | | | | | | | |
| Milla Pod | 1 | | | | | | | 1* | | | |
| Zoox | | 2 | | 4 | | | | | | | b_S_d_B |
| Yutong Autonomous Shuttle | | | 1* | | 2* | | | | | | |
| Sensible4 | | | 2 | | | | | 2 | | | c_S_i_S |
| Sango | | 1* | | | 6* | | | 2 | | | |
| E-Palette | 1 | | | | | 2* | | 2 | | | a_S_g_S_i_S |
| Westfield Pod | 1 | 2 | | | | | | | 2* | | a_S_b_S_k_S |
| HEAT | | 4 | 2 | | | | | | | 2 | b_B_c_S_l_S |
| Navya Autonom Shuttle Evo | 1 | | 2 | | | 2* | | 2 | | | a_boxB_c_B_g_S_i_S |
| Apollo | | 2 | 2 | 2* | | | 2* | | | | |
| Olli | 1 | | 2 | | | | 6* | 2 | | | a_S_c_S_h_S_i_S |
| EasyMile | 1 | | | | | | 4 | 2 | 4 | | |

In Table 3.7, the sensor positions e and j are not included. These simplifications are derived in Section 3.6.1. At the same time, the following shuttles have been dismissed:

- UnicarAgil: Shuttle with sensors exclusively in position e. Considered as not representative.

- Nuro R2 and Neolix: They have shorter lengths, meaning that their surrounding flow state (defined by the Reynolds number) is substantially different from the one observed in the generic shuttle.

Highlighted in blue in Table 3.7 are the shuttles represented by geometries simulated in previous sections. For instance, the Kamaz and the 2getThere GTR do not have any protruding sensors. Hence, they are covered as the generic shuttle model. Whereas from the shuttles with only one sensor position, 3 out of 4 are modeled with previously selected in the study of the single sensor position.

Highlighted in gray in Table 3.7 are the shuttles that contain a combination of studied single sensor locations. Each has an associated code, defined as combinations of the following block units: <sensor position>_<sensor type2>. The positions' codes correspond to the letter depicted on top of Table 3.7. The sensor type code is one of the following: S (small puck), B (big puck), boxS (small box) and boxB (big box). These code block units are connected to others with an underscore.

The identification of the sensor type for each shuttle is performed by visual inspection. From those, two shuttles do not match exactly with a combination of previously selected single sensor position distributions:

- HEAT: Instead of having the regular number (symmetric arrangement) of sensors in position b, it has the double. Those components are represented as two big puck sensors.
- Olli: At position h, this shuttle has four sensors in symmetric distribution and two sensors in asymmetric. However, their total dimensions are approximated with a symmetric distribution of small pucks.

The renders of the selected sensor setup geometries are depicted in Figure 3.34.

The studied sensor setups (highlighted in gray and blue in Table 3.7) over the total number of considered shuttles (Table 3.6) represents $\sim 57\%$. Dismissing the Nuro R2 and the Neolix, due to its substantial difference in dimensions, the representation raises to $\sim 63\%$. This value might not seem high. Nonetheless, the goal of this study is not exclusively to simulate sensor setups on autonomous shuttles but to model the change in C_d induced by those. The approach selected to derive such impact requires studying individual components and the consequent analysis of the total and interaction drag. The selection of the meaningful individual sensor locations restricts the total number of simulated sensor setups, but at the same time, reduces the design space. The time limitations induced by the simulation's duration condition the extent of this analysis.

3.7.2 Setup of the simulations

The setup of the simulations is the same as the one used in the generic shuttle (Section 3.4.2).

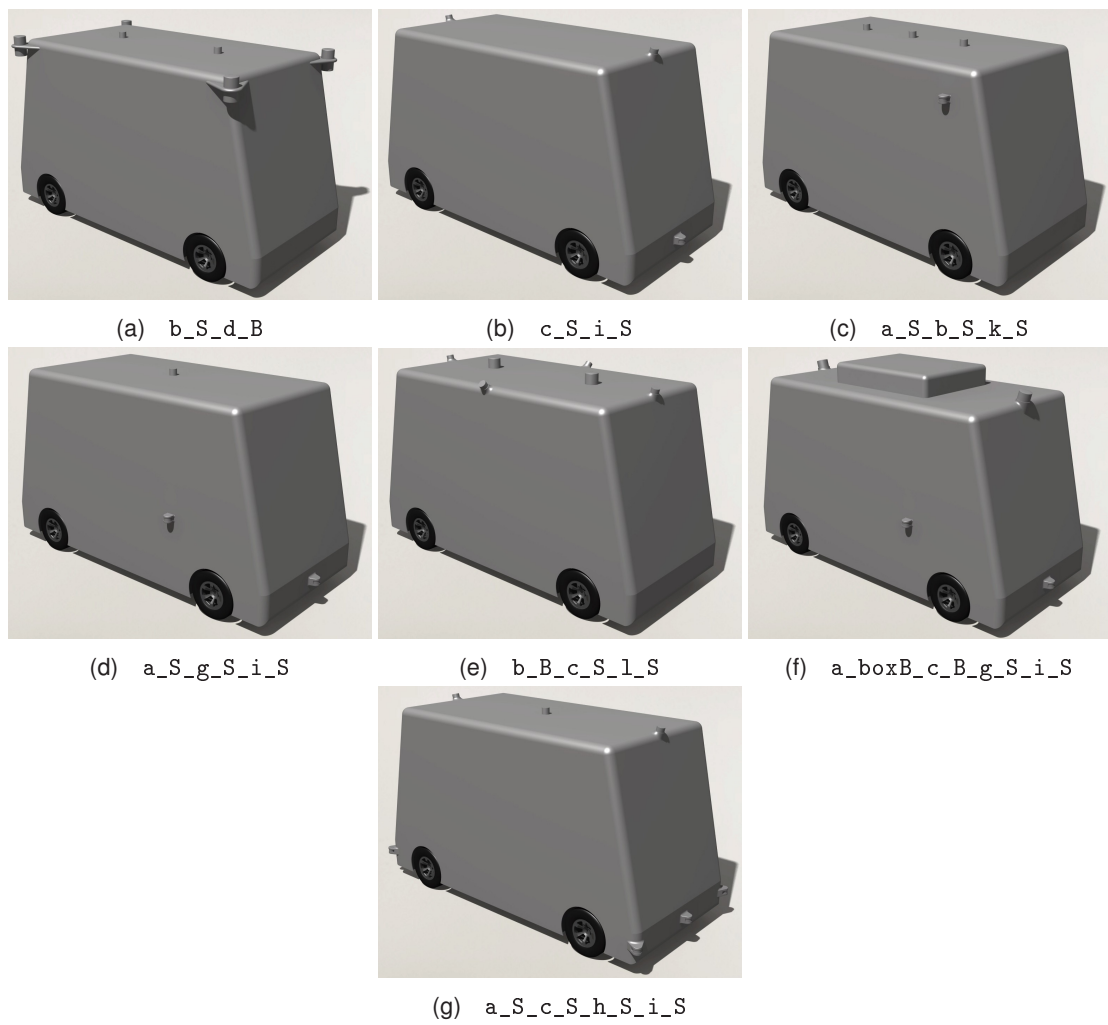


Figure 3.34: Sensor setups

4 Results

The analysis of the results is divided into two sequential steps performed in different software:

1. Post-processing of the fluid data (Paraview).
2. Collection, comparison and modeling of the C_d (LibreOffice).

These steps apply to all executed simulations, following the approach described in Chapter 3 and depicted in Figure 3.5.

Automatic reports of each individual simulation, generated by means of a Paraview macro, are collected in the Appendix (Chapters A, B, C and D). The description of the results uses the figures gathered in the reports.

The images used for the post-processing of all simulations contain a reference axis on the bottom left corner. The red arrow points to the positive x-direction, the yellow arrow the positive y-direction and the green arrow the positive z-direction. The movement of the vehicle is in the negative x-direction. Therefore, when talking about drag, this is referred to as the negative red arrow direction.

All the simulations of this section, which use the setup depicted in Figure 3.17, are correctly performed due to the correctness of the observed health variables.

4.1 Evaluation of generic shuttle simulation

The generic shuttle simulation defines the reference data from which the other simulations are compared. The flow structures surrounding the geometry characterize the drag distribution and the possible increase/decrease by adding external components.

From the physical point of view, drag force is defined as the contribution of the pressure and friction forces on the body's surface. Expressed in dimensionless coefficients: $C_d = C_{d,p} + C_{d,f}$. Generally, in road cars, the pressure contribution predominates over the friction. In this aspect, the generic shuttle is no different. Its contribution of the $C_{d,p}$ constitutes $\sim 97\%$ of the total drag coefficient (Figure 4.1).

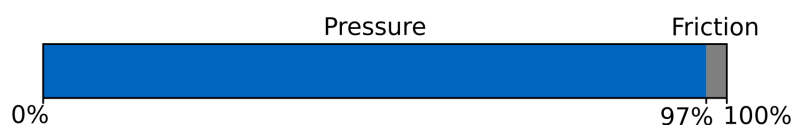


Figure 4.1: Pressure-Friction drag ratio over the total C_d for the generic shuttle

In terms of aerodynamics, cars are bluff bodies. Unlike trains, which have large side surfaces compared to front and rear ones, cars a big area normal to the flowing air and relatively similar

surface in the other orthogonal directions. Those are the contributing regions, by definition, where the pressure drag and the friction drag, respectively. This effect is exaggerated and more easily identifiable by the box-like shape of the generic shuttle. Due to the definition of the surface normals, pressure drag is only possible in the front and rear panels of the vehicle and the wheels. The pressure coefficient C_p on the side surfaces does not contribute to the $C_{d,p}$, given that their normal does not point to the x-direction. In this case, from the feasible pressure drag areas, the front surface is the most relevant (Figure 4.2). The representations in 4.2a and 4.2b depict the C_p , not the $C_{d,p}$. The d from the $C_{d,p}$ indicates the "drag direction". Hence, this value considers the pressure in each surface differential multiplied by the longitudinal component ("drag direction") of its normal vector.

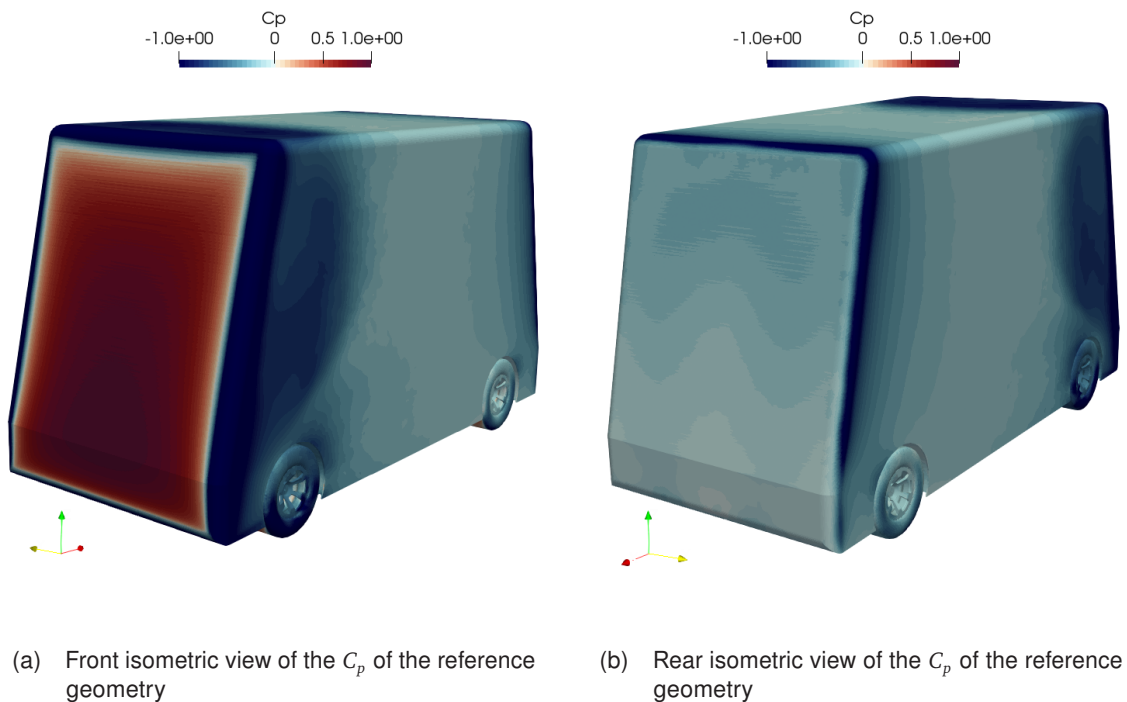
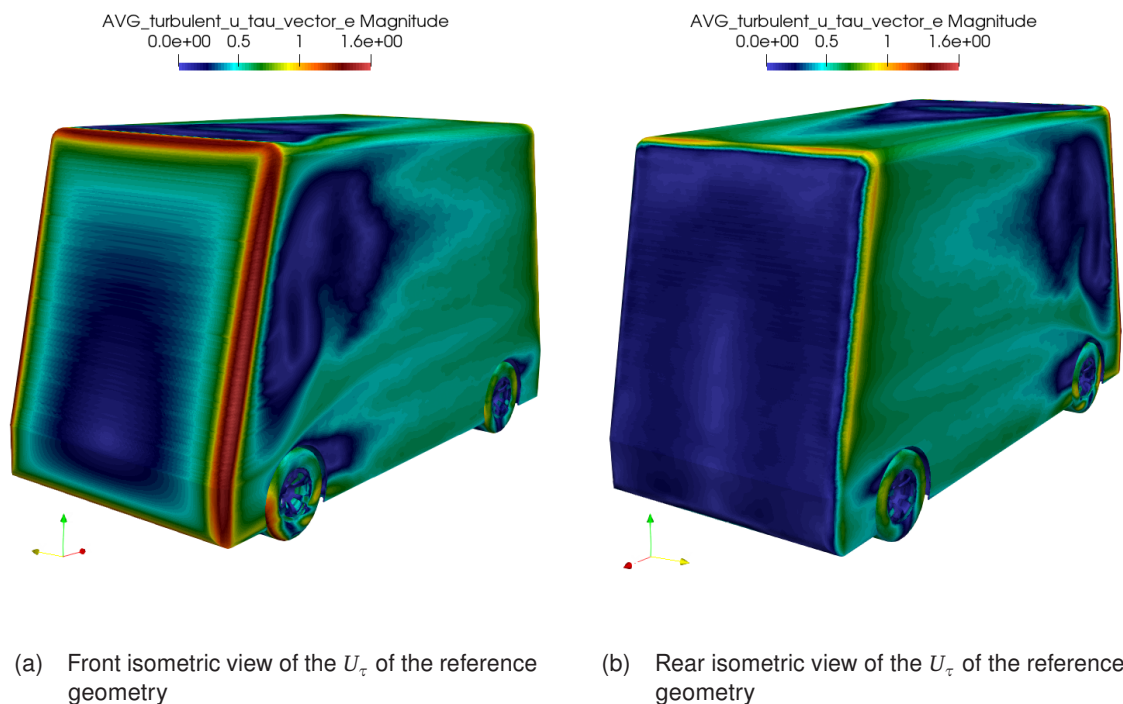


Figure 4.2: C_p surface distribution of the reference geometry

Figure 4.2 depicts low surface pressure in the front and rear rounded edges produced by the acceleration of the fluid in those regions. This effect is stronger in the front. The friction contribution in the drag ($C_{d,f}$) is not plotted in the vehicle surface. Instead, Figure 4.3 depicts the shear velocity magnitude U_τ .

The shear velocity indicates the friction areas (in all directions), stagnation points and fluid detachment areas. High friction zones have high shear velocity, like in the front edges, where surrounding fluid accelerates. The stagnation point is located in the front surface and distinguished by high pressure and very low U_τ . Figure 4.3a depicts a big area with that behavior. Additionally, this fluid property provides information on the detachment regions observed in the top, the side and the rear surface of the shuttle and behind the wheels. The front edge radius (98.9 mm) generates detachment of the flow almost in the entire edge perimeter. This effect is not visible on the front corners. Due to the slope of the windshield, the $U_\tau = 0$ m/s region of the side panel is wider at z-coordinates closer to the full vehicle height. Instead, the bottom section of the side surface has no flow detachment induced by the edge rounding. However, the wheel jets (flow structure created by the wheel movement) produce flow detachment behind them. Figure 4.3 depicts a larger low shear velocity region behind the front wheel compared to

Figure 4.3: U_τ surface distribution of the reference geometry

the rear one. Furthermore, Figure 4.3a depicts an abrupt detachment area in the rear section of the shuttle generated by the box shape of the geometry.

Even though the shear velocity is an indicator of friction drag ($C_{d,f}$), its surface representation is highly relevant for the perception of the total drag, which is mainly ($C_{d,p}$). This paradox is caused by the capacity to identify pressure drag-inducing flow structures employing the U_τ visualization. The detachment areas spot regions of turbulence that enlarge the wake of the vehicle. A good representation of this interaction is depicted in Figures 4.4 and 4.5.

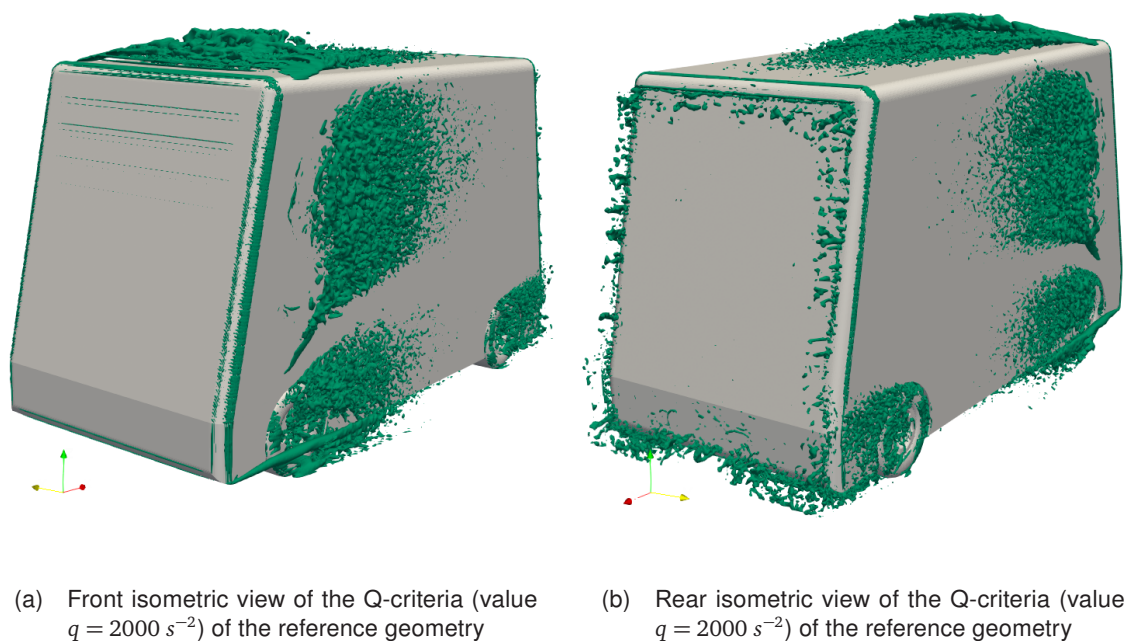
Figure 4.4: Q-criteria (value $q = 2000 \text{ s}^{-2}$) isosurface representation around the reference geometry

Figure 4.4 depicts the vortex structures with the Q-criterion turbulence identification method, at $q = 2,000 \text{ s}^{-1}$. This is a high value, meaning that only extremely turbulent regions are displayed. Those are located right after the flow detachment and match with the $U_\tau = 0 \text{ m/s}$ areas of the side and top surfaces of the vehicle (Figure 4.3). Unlike in Figure 4.3, the isosurfaces of q value depict a turbulent structure generated by the bottom front corner that moves along the exterior of the front wheel. Additionally, slight evidence of turbulent structures is observed at the perimeter of the rear surface, where the abrupt flow detachment occurs. On the bottom edge, this effect is more evident.

Figure 4.5 depicts the vortex structures with the vorticity magnitude turbulence identification method, at $|\omega| = 10 \text{ s}^{-1}$. This less restrictive value is used to identify bigger turbulent structures, intuitively describes the car's wake. This representation permits the coarse visual assessment of the C_d . Bodies with detached flow structures create a "pressure shield" that the air surrounds instead of moving along the slimmer body surface. This can be understood as a virtual enlargement of the geometry, which ultimately increases the pressure drag. This effect is partly observable in Figure 4.6. Sharper front edges should produce a more visible effect.

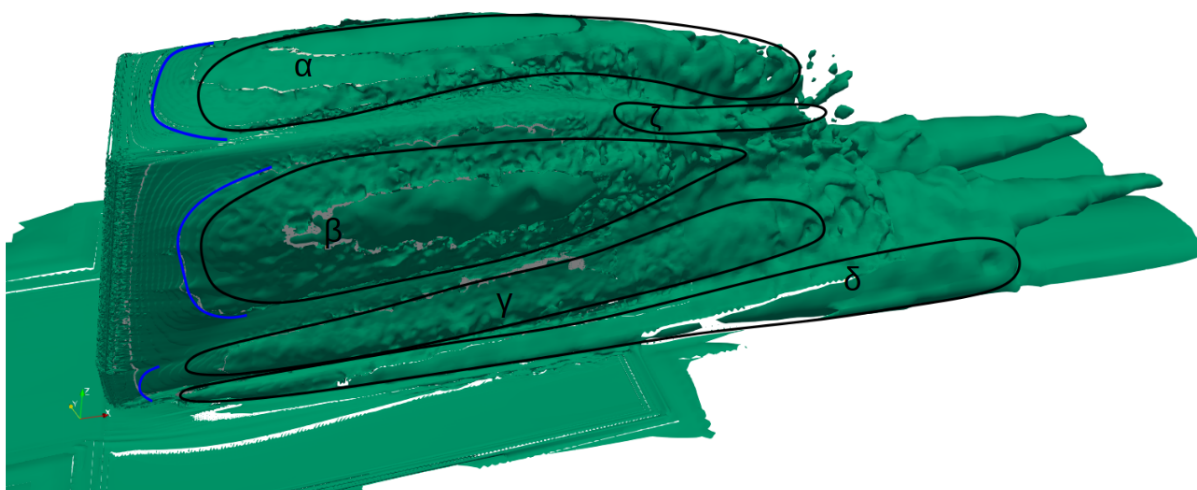


Figure 4.5: Side view of the vorticity (value $|\omega| = 10 \text{ s}^{-1}$) of the reference geometry with identified flow structures α , β , γ , δ and ζ

In Figure 4.5, five observed predominant turbulent structures are highlighted with a black surrounding line: α , β , γ , δ and ζ . The first two flow structures are on the top and side vehicle's panels, respectively. γ and δ are originated from the bottom front corner and the wheel jet. ζ is the prolongation of the top rear corners. This last one is not as noticeable as the other identified vortices. Additionally, the observed flow detachment fronts are highlighted in blue, which have this layered appearance in the vorticity representation. They reaffirm the pattern identified in Figure 4.3.

As in Figure 4.5, Figure 4.6 depicts the flow detachment and the subsequent car wake using a different representation. It displays the velocity magnitude in the longitudinal symmetry plane of the shuttle. Given the box-like shape of the vehicle, there is a large stagnation area in the front panel represented with low velocity. The rounding of the top and bottom front edges facilitates the flow acceleration. Nonetheless, on the top, the flow detaches, creating a low-velocity bubble. This plays a big role in the impact of sensors in this area.

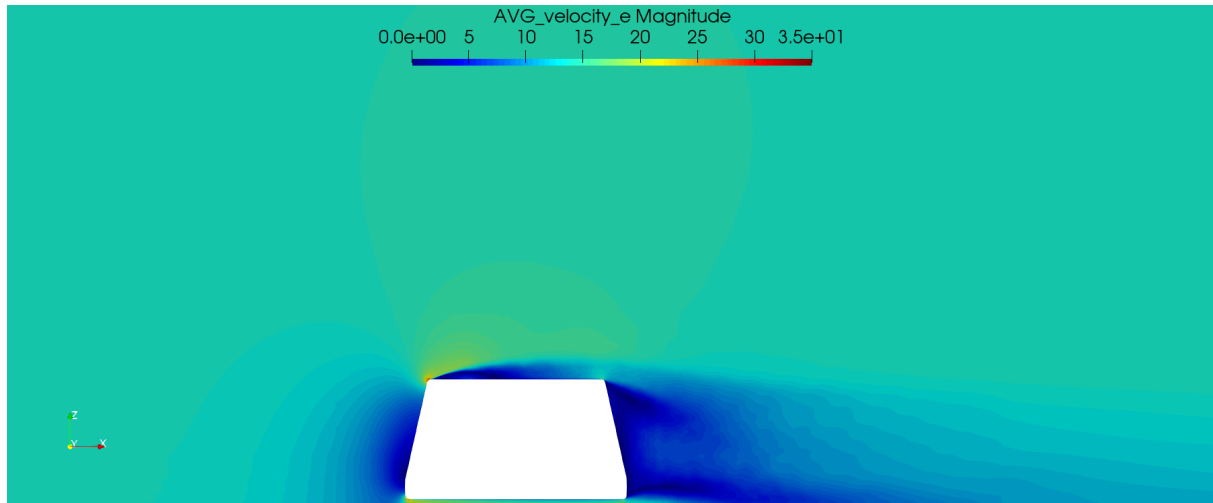


Figure 4.6: Side view symmetry plane of the velocity magnitude of the reference geometry

4.2 Evaluation of design influence on the generic shuttle

The obtained results of the design modifications are depicted in Figure 4.7. From the three variables (windshield angle, edge rounding and wheel cover), the second one clearly predominates.

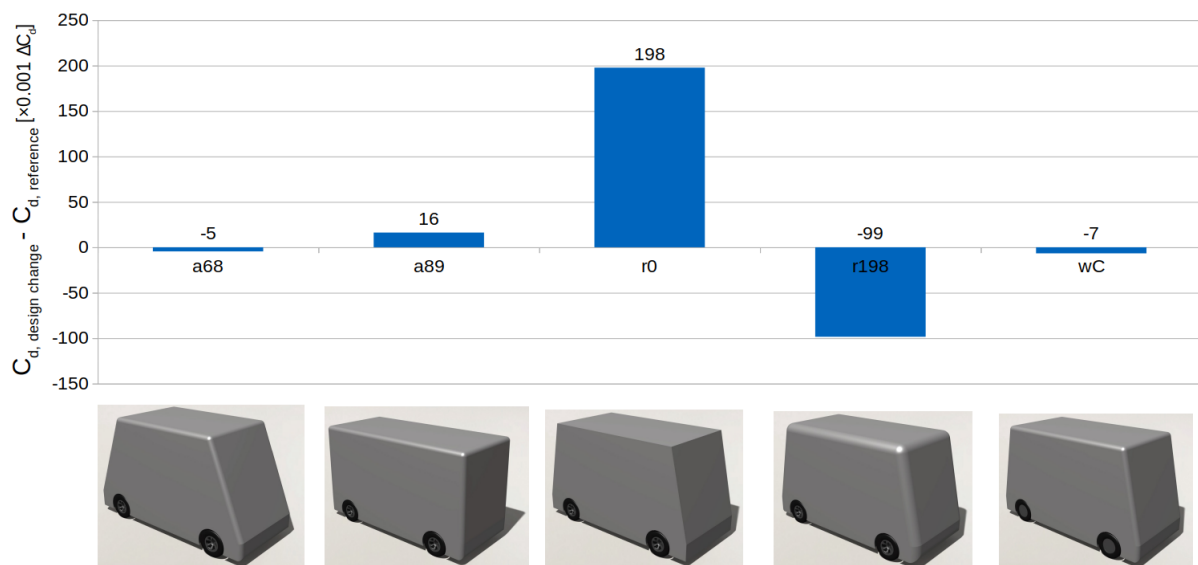


Figure 4.7: Design features ΔC_d

The upcoming subsections analyze each isolated design variable.

4.2.1 Windshield angle

The influence of the windshield slope is intuitive. Steeper front and back surfaces increase the drag. Lower angles allow the flow that moves along the side panels to roll towards the back surface. This effect is strongly observable in Figure B.8. However, this is not particularly good for drag. The rear-end, including behind the rear wheels, is still very turbulent (Figure B.6). Instead,

the geometry with bigger windshield angle has detached flow behind the vehicle (Figures B.15 and B.17) and a bigger stagnation area in front of it (Figure B.12). This last is probably the major cause of the drag increase. The normal vector of the windshield's surface has a larger x-component at higher angles. This translates to higher pressure drag compared to lower angles. As in the generic shuttle, $\sim 98\%$ of the total C_d is contributed by $C_{d,p}$. Therefore, variation of that component dominates the trend of the ΔC_d .

The windshield slope characterizes the shape of the detachment area on the vehicle's side panels. Figures B.7 and B.16 depict the shear velocity for $\alpha = 67.8^\circ$ and $\alpha = 88.65^\circ$ respectively. This effect is very noticeable when comparing both extreme cases. The geometry with the highest slope has a very uniform detachment region along the longitudinal direction. Differently, the incoming flow with the windshield angle of $\alpha = 67.8^\circ$ rolls along the leading-edge at different x coordinates. This translates to the presence of turbulent structures towards the top half of the shuttle.

4.2.2 Edge rounding

The edge radius is observed to be the most influential design parameter of the three studied. The shuttle with sharp edges ($r/b = 0$, $r = 0$ mm) has $\Delta C_d = 0.198$, which is an increase almost equivalent to the full drag coefficient of a passenger car. This pronounced positive delta is caused by the immediate and abrupt detachment of the flow at the four leading edges of the shuttle. It creates a bubble of high pressure that virtually enlarges the vehicle's geometry and consequently raises the pressure drag. This component constitutes the $\simeq 99\%$ of the total drag. This detachment effect is clearly observed in Figures B.25 to B.28. Contrary to that, the radius of $r/b = 0.1$ ($r = 197.8$ mm) allows the incoming air to surround the curved front perimeter and follow the side panels without any visible detachment (Figures B.30 to B.37). This decreases the drag by $\Delta C_d = -0.099$. In both cases, the wheels create vortex structures, given their rotational nature.

From the observed fluid data representations, the drag reduction at $r/b = 0.1$ probably constitutes the 95% - 100% of the asymptotic limit of the C_d reduction of that design variable. The three studied radius are collected and compared with literature data [8] [23] in Figure 4.8. These are $r = 0$ mm, $r = 98.9$ mm and $r = 197.8$ mm, which are equivalent to a radius/vehicle width ratio of $r/b = 0$, $r/b = 0.05$ and $r/b = 0.1$, respectively. A quadratic interpolation connects the points.

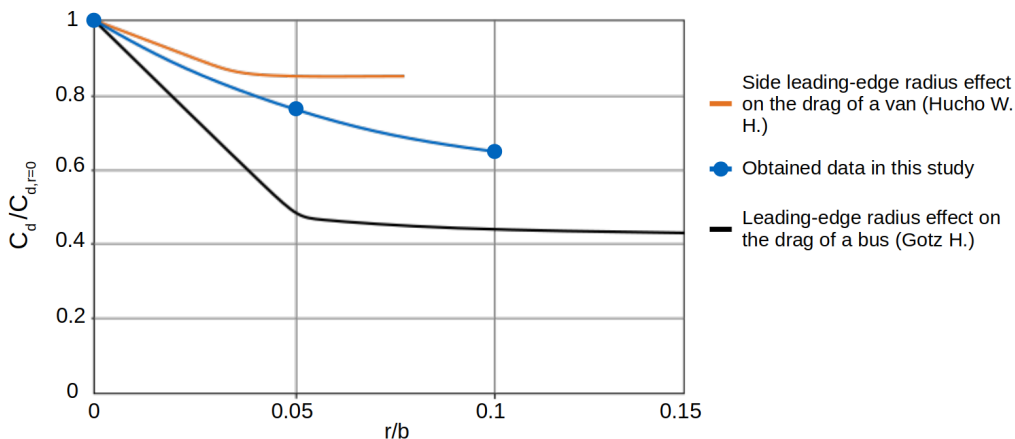


Figure 4.8: Observed radius effect of the leading-edge compared to literature results [8] [23]

Figure 4.8 depicts the trends of $C_d/C_{d,r=0}$ over the quotient r/b . The three lines behave similarly. Nonetheless, in the geometries studied by Hucho [8] and Gotz [23] there is a pronounced observable change of slope between $0.04 \leq r/b \leq 0.05$, whereas, in the simulated results, this effect seems to appear at $r/b = 0.1$. These differences might be caused by:

- The selected edges with rounding: front leading edge, front side leading edge, or all edges.
- The geometry itself of the vehicle.
- The flow regiment (Reynolds number) at which the vehicle is evaluated.

At the same time, this symmetrical basic-form vehicle concept could have a different edge rounding response than van and bus geometries.

4.2.3 Covered wheel

The effect of the rim styling modification is only $\Delta C_d = -0.007$, which is not a lot. Even though the wheels have a closed profile, they still create turbulence structures behind them. This can be observed in Figures B.41 and B.42.

4.3 Evaluation of single sensor on the generic shuttle

Figure 4.9 depicts the obtained results from the single sensor position simulations. They are clustered by colors, indicating the similar effect on the identified flow structures (α , β , γ , δ and ζ) of the reference simulation (Figure 4.5). The following sections discuss the effect of each group of sensor positions.

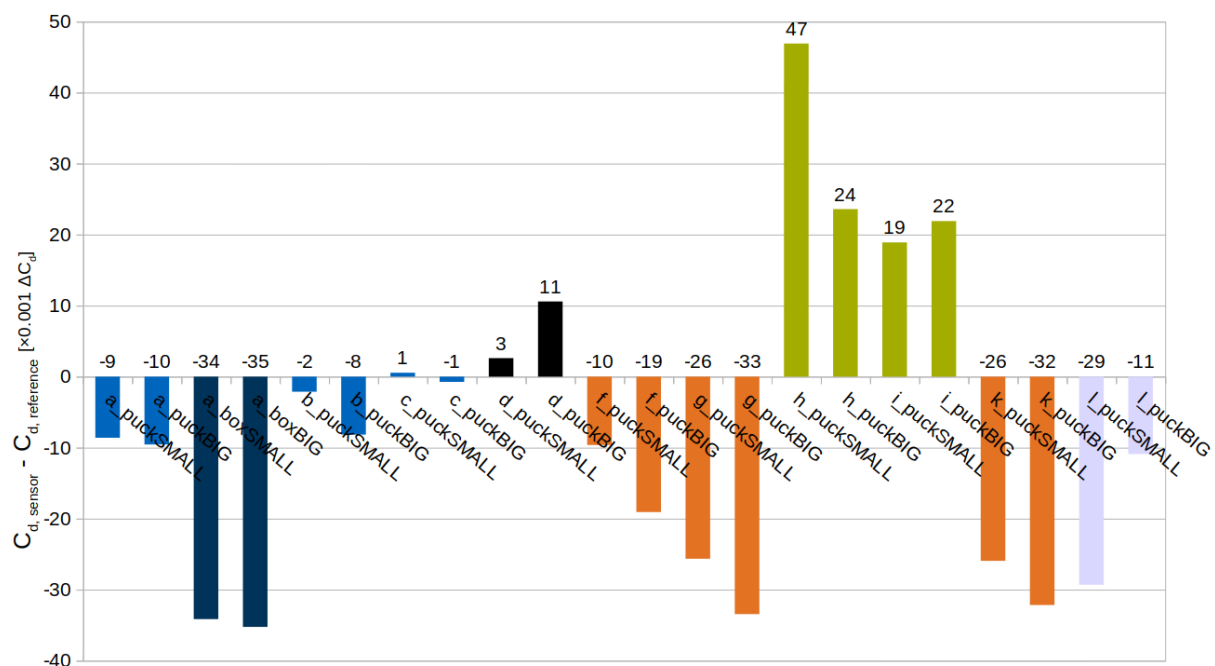


Figure 4.9: Single sensor position ΔC_d clustered by their impact on the flow structures α , β , γ , δ and ζ

Figure 4.10 depicts the sensor position location by cluster. The box sensors are represented as the dark blue perimeter surrounding the a position. Nonetheless, they are treated with the other sensor positions and geometries that affect the top vortex structure (α): a, b and c.

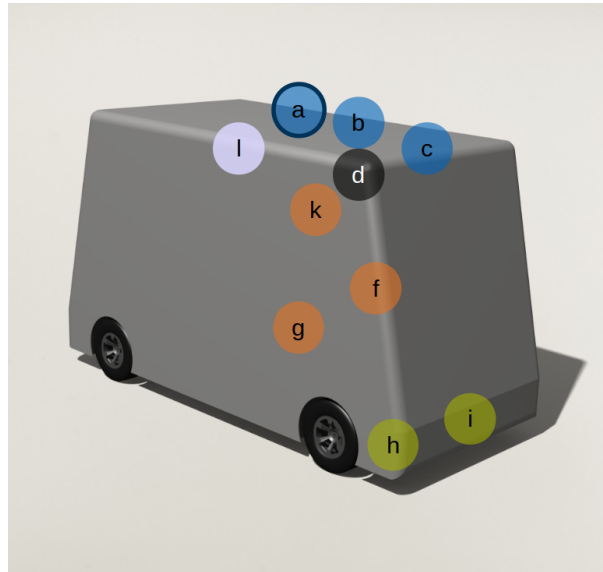


Figure 4.10: Classification of the sensor positions by their impact on the flow structures α , β , γ , δ and ζ

The obtained results (Figure 4.9) are compressed within the range: $\Delta C_d \in [-0.035, 0.047]$, which is substantially smaller than the effect of the rounding edge: $\Delta C_d \in [-0.099, 0.198]$.

In terms of ratio pressure-friction drag, they all behave similarly to the generic shuttle and the design-feature geometries: $97\% \leq C_{d,p} \leq 98\%$.

Surprisingly, several sensor positions reduce the C_d . This behavior (further developed in the upcoming sections) is probably caused by their specific allocation in the vehicle. The selected generic shuttle's edge radius ($r = 98.9$ mm) provokes the detachment of the flow at the top and side vehicle panels. In those areas, the analyzed sensor geometries help the flow reattach, reducing the rear wake, and therefore, the total drag coefficient.

The maximum observed variability of drag delta induced by puck sensors ($\max\{\Delta C_{d,single\ sensor}\} - \min\{\Delta C_{d,single\ sensor}\}$ in %) is 12.1%. This is the closest comparable parameter to drag impact of mirrors and small elements from literature. The reason is that all studies performed on the observation of the effect of these geometries use passenger cars with attached flow on those areas. Hence, under those circumstances, the components almost always increase the drag. This is not the case of this study. Nevertheless, the value 12.1% is still not fully comparable to literature wind tunnel data due to:

- Literature data is generally performed in passenger cars, which have a different surrounding flow state.
- Literature data is generally performed at higher Re , which is observed to affect the C_d of the vehicle [11]. However, the percentage approach could maintain the ratio.
- Literature data evaluate the drag increase in areas of the vehicle with attached flow.

Even though these differences, the simulated impact of the puck sensors is quite not far from the literature values:

- The contribution of a pair of external mirrors is approximately 4% (C_d) [9].
- The impact of the taxi sign is 5.1% (C_d) between 40 km/h and 120 km/h [29] and 11.3% (C_d) between 60 km/h and 120 km/h [30].

This similarity is not maintained in the comparison of the simulated box-like sensors with literature data. There is a clear influence of the flow detachment in the studied area of the simulations, given that Schuetz [9] observed a rooftop add-on maximum drag increase of 40% and Chowdhury [29] and Alam [30] increments of 20.4% and 6.7% by the addition of roof-racks, respectively. They all analyzed the impact on passenger cars. Contrary, the simulated geometries including a rooftop box sensor decrease the C_d by 5.32%.

The studies performed in open-road [28–30] have an additional difference with the simulated cases. The CFD scenario considers air coming exclusively in the longitudinal vehicle direction, which is far from reality. Furthermore, wind tunnels (and simulations) usually use Turbulence Intensity values in the range of 0% to 0.4%. However, [61] observed that this parameter in open-road conditions is not uniform in its three spatial components and that average values are around $\sim 4.2\%$, $\sim 4.1\%$ and $\sim 2.0\%$, in the longitudinal, lateral and vertical directions of the car movement respectively.

Sensor positions a, b and c

These three sensor positions mainly modify/interact with the flow structure α (vortex classification depicted in Figure 4.5). The puck geometries of a and b are fully contained within this turbulence. This is clearly depicted in Figures C.9, C.18, C.45 and C.54. They lay inside this bubble, defined by low fluid velocity magnitude. The decrease in C_d of these geometries is caused by the small reduction of the α wake. The pucks slightly curve the low-velocity bubble by attracting the air from above the turbulent structure. However, the effect is not strong enough to substantially reattach the flow behind them. This is depicted in the representation of the surface shear velocity (Figures C.6, C.15, C.42 and C.51). Under such a working principle, the height and position of the sensor play a big role. The rounding of the front edges defines the exact height of the α flow structure and directly conditions the C_d impact of the sensors. At a, the height of the puck sensor seems not to have a relevant impact on the drag. However, this is not the case at b. The big sensor is substantially better than the small one because the front component (out of the two sensors in the position) almost covers the height of the low-velocity bubble at that location. It is assumed that if the height of the sensor keeps increasing, the ΔC_d would eventually reverse the trend and turn positive.

The aerodynamic working principle of the box-type sensors is similar to the pucks with positions a and b, but having a bigger surface, it is substantially larger. Hence, the C_d decrease is more prominent. In fact, out of all individual studied positions and sensor types, they have the best (lowest) drag coefficient delta. The step-shaped geometry blocks the turbulent region created right behind the top edge and allows the air located above the α flow structure to attach to them: $U_\tau > 0$ m/s (Figures C.25 and C.34). This effect is depicted in Figure 4.11.

In the case of the big box, the flow fully attaches at the top surface of the sensor. In combination with the symmetric placement of the boxes and the rounding of its top edges, this effect provokes a substantial reduction of the rear wake. Surprisingly, the ΔC_d of both sensors is almost the same. Nonetheless, the small box is better if considering the drag force. However, this parameter is not study-relevant.



Figure 4.11: Streamline representation of the aerodynamic working principle of the top-located box shaped sensor. It blocks the turbulence in front of it and allows the attachment of the flow on its top surface

Sensor position *c* impacts differently the turbulent region α compared to the previously studied sensors. The component located at the top front leading edge of the vehicle generates a vortex structure that interacts with α (depicted in Figures C.58 and C.67). The flow detachment region of the top surface enlarges, except for a small area behind the puck, where the air can partially reattach. The rear sensor acts as the front one, generating additional vortices. Nonetheless, neither of the two puck sizes seems to impact the total C_d considerably.

Sensor position *d*

This sensor position mainly interacts with the flow structures β and ζ . At the same time it indirectly influences α (vortex classification depicted in Figure 4.5). The two front sensors create a vortex that moves along the top of the side surface, interacting with β (depicted in Figures C.80 and C.89). This modifies the detachment area of the side panels (depicted in Figures C.78 and C.87), but still is not favorable for the drag. Interestingly, the generation of the vortices in the front corners flattens α (depicted in Figures C.81 and C.90), which slightly reduces the shuttle wake at the rear mid-section. Additionally, the allocation of the rear corner sensors contributes to the expansion of the turbulent structure ζ , which increases the C_d .

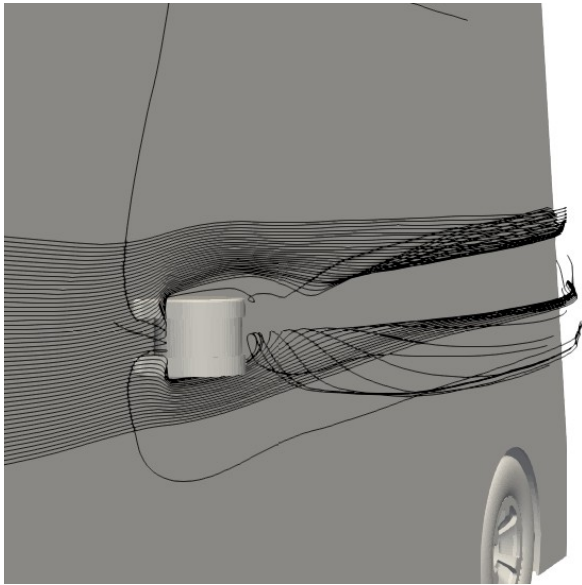
Both sensor sizes increase the drag coefficient $\Delta C_d > 0$. Nonetheless, they are not the positions with a higher positive drag delta.

Sensor positions *f*, *g* and *k*

These sensor positions have direct interaction on the β vortex and indirectly influence α (vortex classification depicted in Figure 4.5). They all generate two small, turbulent structures that swirl around the sensor geometry and pull the air towards the back of the sensor. This effect is depicted in Figure 4.12.

Images 4.12a and 4.12b illustrate streamlines impacting at mid-height of the puck (in the direction away from the side panel), splitting and creating these swirling vortices on each side. These two flow structures are the source of the partial reattachment of β . Images 4.12c and 4.12d illustrate how the fluid that impacts the furthest part of the sensor curves towards the shuttle.

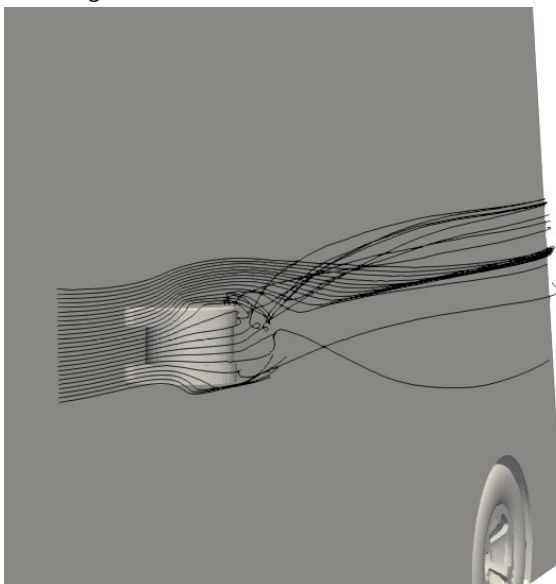
The generation of these small vortex structures creates a visible area without flow detachment behind and around them. This effect is more appreciable with the puck's biggest size (depicted



(a) Isometric view of streamlines impacting at mid-height the big puck sensor of position g



(b) Top view of streamlines impacting at mid-height the big puck sensor of position g



(c) Isometric view of streamlines impacting at the most outer part the big puck sensor of position g



(d) Top view of streamlines impacting at the most outer part the big puck sensor of position g

Figure 4.12: Streamlines impacting the big puck sensor of position g

in Figures C.105, C.123 and C.177). Additionally, the allocation of the sensors in those positions flattens the α vortex. This curious aerodynamic effect strongly reduces the rear wake of the shuttle, subsequently decreasing the C_d . It is observed with the vorticity (Figures C.98, C.107, C.116, C.125, C.170 and C.179) and velocity representations (Figures C.99, C.108, C.117, C.126, C.171, C.180).

Due to the size reduction of the α vortex structure, the six combinations of sensor position and size reduce the vehicle's drag coefficient. Peculiarly, g and k have almost the same impact: $\Delta C_{d,smallpuck} = -0.026$ and $\Delta C_{d,bigpuck} \simeq -0.033$. The drag decrease is shallower in the f configurations. Nonetheless, in all configurations, the big puck performs better than the small.

Sensor positions h and i

These two sensor arrangements, in both sizes, create a re-circulation of the flow at the rear end of the vehicle. This is observed in the C_p surface representation as an over-pressure in the bottom-back of the geometry (Figures C.129, C.138, C.147 and C.156). The Q-criterion isosurfaces and the shear velocity illustrate this behavior as well. The first one depicts how "dirty" the air is right behind the shuttle. This highly turbulent character negatively impacts the pressure drag. Moreover, the front components of position h create turbulence that interacts with the flow structures δ and γ (vortex classification depicted in Figure 4.5), which expand substantially and increase the wake of the car.

Both combinations of sensors and dimensions increase the drag coefficient. Interestingly, the small puck geometries allocated in the h configuration have the highest impact ($\Delta C_d = 0.047$), whereas the other three combinations increase the drag coefficient by half ($\Delta C_d \in [0.019, 0.024]$).

Sensor position l

This sensor position slightly interacts with the vortex ζ , which should increase the C_d . However, it has a similar effect as the positions f, g and k: it induces the flatten of the vortex area α . In this case the influence is upstream since the geometries are allocated at higher x-coordinates. The effect is more noticeable with the small pucks (Figures C.188 and C.189). In this configuration the wake is substantially small, fact that reduces the drag coefficient: $\Delta C_d = -0.029$.

Sensor size sensibility

The complete study of the two puck sizes at all configurations (Figure 4.9) enables the possibility to evaluate the size sensibility of the sensor geometries. Figure 4.13 depicts the drag coefficient difference between the big and the small pucks. Note that the chart depicts the delta defined as $C_{d,big\ sensor} - C_{d,small\ sensor}$.

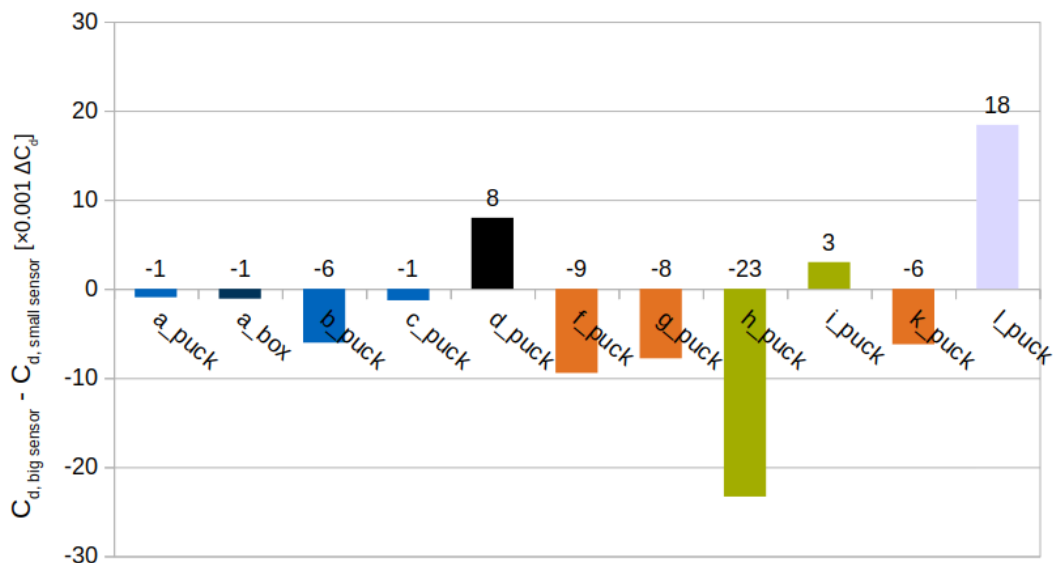


Figure 4.13: Size influence on the drag coefficient: $C_{d,big\ sensor} - C_{d,small\ sensor}$

Since each sensor has specific housing/supporting geometries, the results can not be strictly compared to each other. However, it gives a good idea of how the scale-up of the sensor in each position affects the drag.

From Figure 4.13, the following observations can be stated from the previously classified sensor positions:

- Sensor positions a, b and c: The impact induced by the size increase is not significant, except at b with a sensor-puck geometry. This effect is probably caused by the front component (out of the two sensors of the position), whose z-dimension almost overcomes the height of the turbulence region α . Interestingly, the size of the sensor at c is not influential.
- Sensor position d: The increase in the size of the sensors at these locations increment the drag coefficient. This effect could be considered intuitive.
- Sensor positions f, g and k: The use of the studied puck big sensors on these positions and distributions is beneficial for the C_d , compared to the smaller geometries. Furthermore, the decrease in drag is similar.
- Sensor positions h and i: Even though these two sensor locations have a similar effect (creation of a rear-end over-pressure), their size sensibility is extremely different. At position h, the big sensor geometry lowers the C_d substantially compared to the small one. Instead, at position i, there is not significant change between them.
- Sensor position l: The impact on the drag coefficient by the increase of the sensor dimensions is positive, meaning that $C_{d, big\ sensor} > C_{d, small\ sensor}$.

Figure 4.14 illustrates the ΔC_d induced by studied sensor positions. The left-hand image depicts the impact of the small puck geometries, whereas the right-hand image the one of the big pucks. The box-shaped sensors are not included.

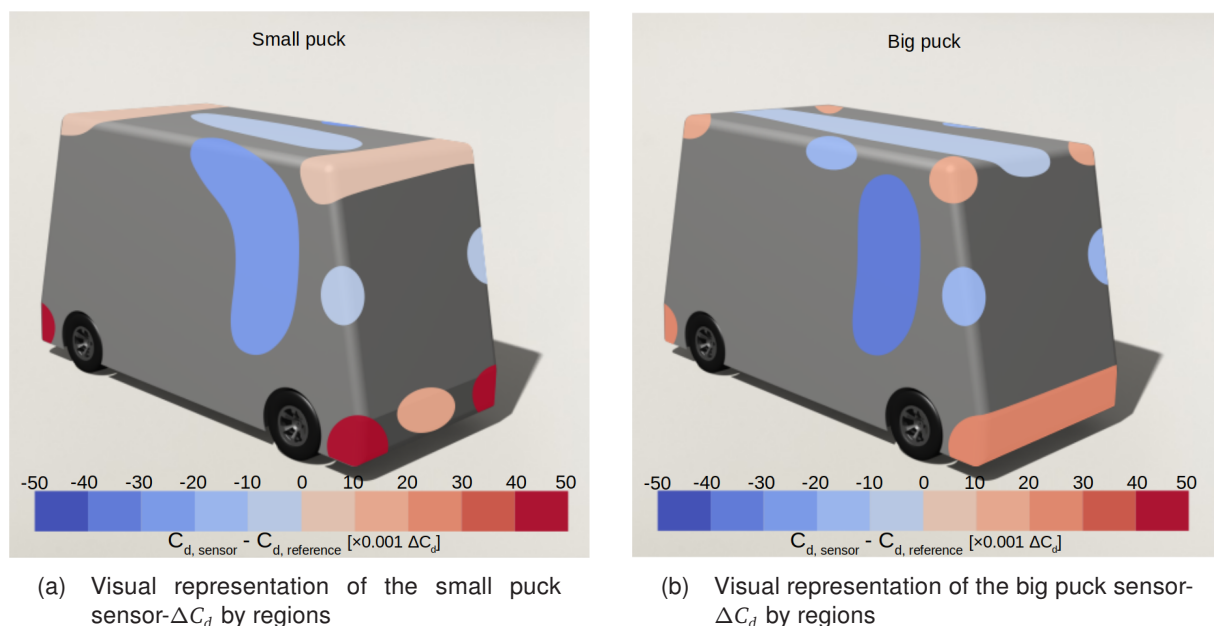


Figure 4.14: Visual representation of the ΔC_d by sensor size (only puck)

In Figure 4.14, the approximated areas of good and bad influence on the C_d are depicted in blue and red tones, respectively. There is a noticeable area of $\Delta C_d < 0$ located on the shuttle's side (where the big $U_\tau = 0$ m/s is developed) for both sensor sizes. Instead, the zones of worse drag coefficient impact are the front and rear lower edges.

Even though the increase in sensor size reduces the C_d in several positions (Figure 4.13) under the studied conditions and geometries, it is expected that the further expansion of the dimensions eventually has the opposite effect. This would be caused by the sensors' height overcoming the "height" of the identified turbulent structures (mainly α and β) at those locations.

These findings evaluate the addition of sensor setups under the defined edge-rounding value, which induces the turbulent structures α , β , γ , δ and ζ . If that was not the case, like in the studied simulations $r0$ and $r198$ (edge radius $r = 0$ mm and $r = 198$ mm), the impact of sensors and their geometrical sensibility would be most certainly highly different. Hence, the front edge's radius not only impacts the total drag of the vehicle but strongly determines the effect of the add-on sensors and their geometrical sensibility.

4.3.1 Sensor impact evaluation: functional approach

Since the protruding sensors of the current (studied) autonomous shuttles are mainly lidars, it makes sense to classify and aerodynamically evaluate the sensor positions by their field of view. This new cluster is depicted in Figure 4.15.

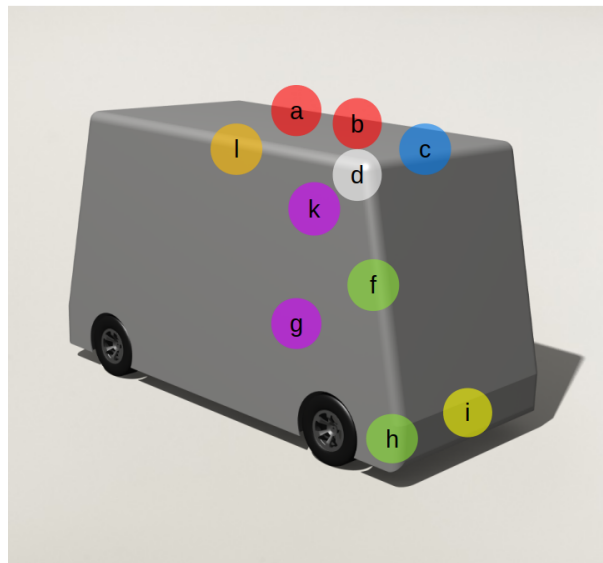
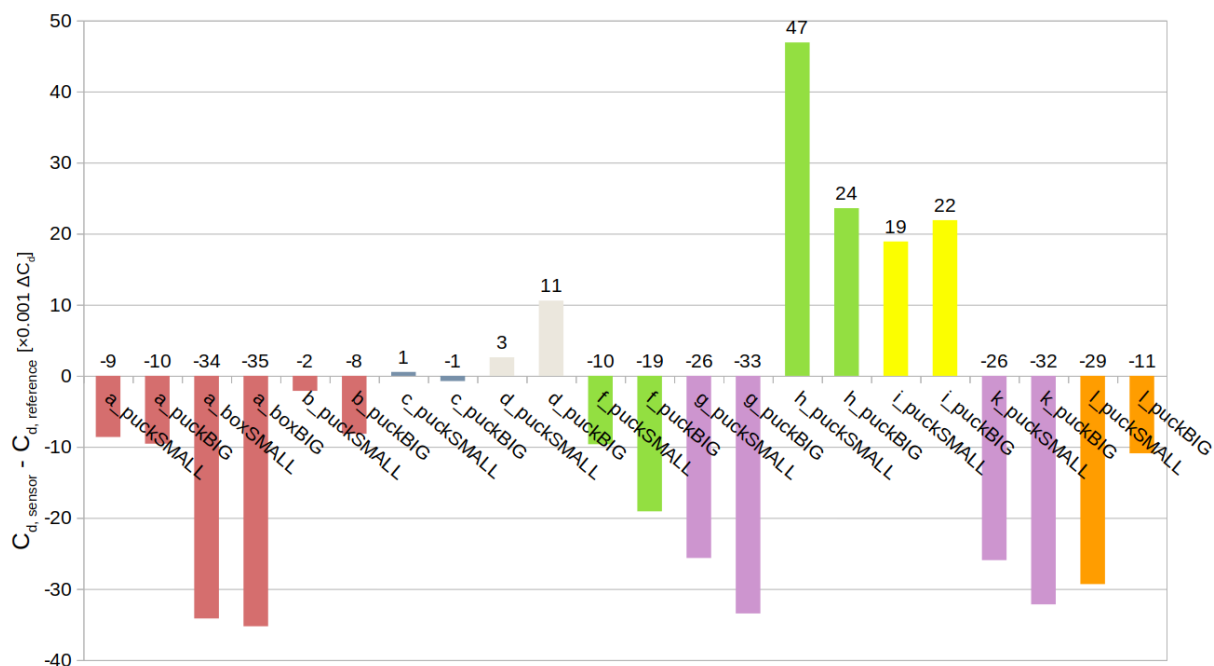


Figure 4.15: Classification of the sensor positions by their common field of view

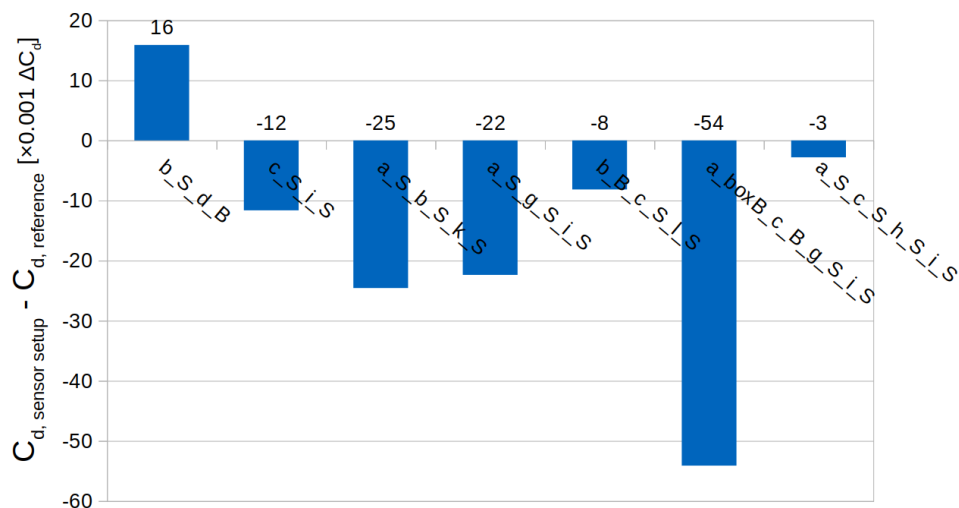
The field of view is considered in a quarter of the vehicle. Under that assumption, positions f and h are grouped together. However, the symmetry of the studied distributions of the sensors is not the same: position f includes two sensors, whereas h 4. Nevertheless, considering the field of view classification, the obtained results are depicted in Figure 4.16.

This sensor-functional clustering enables the selection of the best aerodynamic sensor position with specific field of view requirements.

Figure 4.16: Single sensor position ΔC_d clustered by their common field of view

4.4 Evaluation of sensor setup on the generic shuttle

Figure 4.17 collects the results of the simulated sensor setups (derived in Section 3.7.1).

Figure 4.17: Sensor setup ΔC_d

Surprisingly, the big majority of the layouts produce a decrease in the drag coefficient. The results are compressed within the range: $\Delta C_d \in [-0.054, 0.016]$. Compared to the design influence, the impact is not as prominent. Nevertheless, in comparison with the single sensor position, the results have a similar order of magnitude. Figure 4.18 illustrates the comparison in ranges and values of all performed simulations. The black points represent the single simulation results.

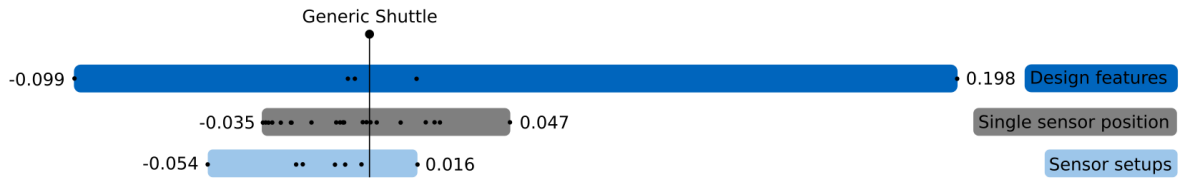


Figure 4.18: Visual representation of the ΔC_d impact of design features, single sensor positions and sensor setups

The contribution of the pressure drag coefficient over the total is between 97% and 98%, in line with all previously studied geometries.

The following sections briefly describe the main observable effects of each evaluated sensor setup.

4.4.1 Sensor setup $b_S_d_B$

This sensor setup is the combination of the single sensor geometries: $b_puckSMALL$ and $d_puckBIG$.

The fluid field representations (Figures D.2 to D.9) look very similar to the ones obtained in the $d_puckBIG$ simulation. The effect of the sensors in this configuration prevails over the effect of the two components allocated at b . These last slightly increase the drag coefficient instead of lowering it, unlike in the simulation $b_puckSMALL$. This is caused by the change on the turbulent structure α , induced by the positioning of the frontal d sensors (effect depicted in Figure D.8). Therefore, the flattening of the α contributes the sensors located in position b to slightly increase the drag coefficient.

4.4.2 Sensor setup $c_S_i_S$

This sensor setup is the combination of the single sensor geometries: $c_puckSMALL$ and $i_puckSMALL$.

The isolated simulations of both sensor positions, increase the C_d by 0.001 and 0.019 (c and i respectively). However, the interaction between both produces the opposite effect. The allocation of the small puck geometries at position c eliminates the over-pressure observable in the rear-end of the vehicle in the simulation $i_puckSMALL$ (Figure D.12). Hence, the air is more clean and intuitively the ΔC_d should be lower than 0.019.

The global fluid regimen (Figure D.17) is similar to the observed in the simulation $c_puckSMALL$ (Figure C.62). However, due to non-observable reasons, the drag coefficient is even lower than the obtained in that scenario.

4.4.3 Sensor setup $a_S_b_S_k_S$

This sensor setup is the combination of the single sensor geometries: $a_puckSMALL$, $b_puckSMALL$ and $k_puckSMALL$.

The first sensor geometry interacting with the air in the freestream direction is at position k . As in the simulation with the isolated sensor, the generated vortices at the sides of the shuttle flatten the α turbulence. This one, interacts with sensors from positions a and b . However, their

effect of flow reattachment is neutralized by the change in α . In a similar way as the sensor setup $b_S_d_B$, the flattening of the flow structure α causes the puck sensors located on top of the shuttle (positions a and b) to slightly increase the drag in comparison with the simulation $k_puckSMALL$. This effect is illustrated in Figure D.27, where the bubble of low velocity located on top of the car is so slim that the sensor geometries overcome its height. Additionally, Figure D.25 depicts how 2 out of 3 sensors of the top panel are located in a region of non detachment. This prevents the air from moving along the surface smoothly, creating turbulence and consequently drag increase. Nonetheless, the strong drag reduction effect of $k_puckSMALL$ prevails over the slight bad impact ($\Delta C_d > 0$) of the other two sensor positions. Therefore, the total drag delta is $\Delta C_d < 0$.

4.4.4 Sensor setup $a_S_g_S_i_S$

This sensor setup is the combination of the single sensor geometries: $a_puckSMALL$, $g_puckSMALL$ and $i_puckSMALL$.

Similarly to the setup $c_S_i_S$, the presence of other sensors cancel out the over-pressure effect (Figure D.30) of the isolated sensor position i (Figure C.147). Moreover, interaction between the sensors located at g and a behave in a similar way as k with a and b. The geometry at g flattens the flow structure α , and this fact modifies the drag influence of a. However, in this case the height of α is not drastically reduce (visible in Figure D.36), contrary to the isolated simulation $g_puckSMALL$ (Figure C.117). This effect could be caused by location of the i geometry underneath the windshield. In any case, the puck located at a probably facilitates the flow reattachment. Hence, the total drag is reduced by the neutralization of the bad effect of i and the prevailing $\Delta C_d < 0$ contribution of the $g_puckSMALL$.

4.4.5 Sensor setup $b_B_c_S_l_S$

This sensor setup is the combination of the single sensor geometries: $b_puckBIG$, $c_puckSMALL$ and $l_puckSMALL$.

The turbulent regimen of the shuttle's surrounding flow (Figure D.44) is similar to the simulation $c_puckSMALL$ (Figure C.62). This similarity is caused by the fact that the first protruding geometry that the flow encounters is the front component of that position. This causes disturbance in the air at the top of the vehicle, which prevents the big pucks located at b to reattach the flow of α (Figure D.45). Moreover, the vortex generated by the front puck at c blocks the flatten action of the turbulent structure α , induced by the allocation of sensors at position l. However, these protruding geometries seem to have a good contribution to drag ($\Delta C_d < 0$) in such a way that the total drag coefficient is reduced.

4.4.6 Sensor setup $a_boxB_c_B_g_S_i_S$

This sensor setup is the combination of the single sensor geometries: a_boxBIG , $c_puckBIG$, $g_puckSMALL$ and $i_puckSMALL$.

The flow behavior around the vehicle is predominantly influenced by the effect of the box sensor. The allocation of the small puck at the frontal c position do not impact the working principle of the box, which blocks the turbulence of α and attaches the flow on its top (Figure 4.11). However, the rear top edge sensor (position c) induces turbulence (Figure D.59). The protruding geometries at g slightly reduce the wake in that area (D.58), like in the simulation $g_puckSMALL$ (Figure

C.112). Finally, the allocation of sensors at i do not seem to impact the drag in any way. They do not generate the over-pressure observable in the simulation $i_puckSMALL$.

Since the effect of $c_puckBIG$ and $i_puckSMALL$ are neutralized and the working principle of a_boxBIG and $g_puckSMALL$ prevails, the total reduction of the drag coefficient is substantial. In fact, it sensor setup with lowest ΔC_d from the simulated.

4.4.7 Sensor setup $a_S_c_S_h_S_i_S$

This sensor setup is the combination of the single sensor geometries: $a_puckSMALL$, $c_puckSMALL$, $h_puckSMALL$ and $i_puckSMALL$.

This case is yet another example of the neutralization of the rear-end over-pressure (Figure D.48) by the allocation of sensors on the top surface of the vehicle. Hence, even though the positions in h induce visible turbulent structures (Figure D.49), the high $\Delta C_d > 0$ impact of $h_puckSMALL$ and $i_puckSMALL$ is not present.

On the vehicle's top panel, the front component at c creates a flow structure that interacts with α (Figure D.53). This modifies the working principle (of flow reattachment) of the small puck at a , observed in the simulation $a_puckSMALL$.

The total aerodynamic impact of this sensor setup is barely relevant ($\Delta C_d = -0.003$).

4.5 Creation of the mathematical model to assess the impact of sensor setups

Figure 4.19 breaks down the sensor setups in individual positions, including their ΔC_d . The coloring of the sensor cells is based on the clustering performed in 4.3, which collects sensors considering the impact on the identified turbulent structures α , β , γ , δ and ζ (Figure 4.5). Those assemblies are named aerodynamic categories.

Using the information displayed in Figure 4.19, two simple models to approximate the sensor setup ΔC_d are generated. They use the non-weighted add up contributions of:

1. The individual simulated value from the sensors that compose the setup.
2. The average value of the aerodynamic category to which the sensors (that compose the setup) belong.

The real simulated data and these two simple linear ΔC_d models are depicted in Figure 4.20.

Figure 4.20 illustrates the massive difference between the real values and the approximations employing the two linear models. It points out the high interaction between the sensor positions. This effect is named interaction drag.

Given the limited number of data points to create a ΔC_d -approximation model, it is pointless to use weighted contributions of single sensor positions. The mathematical approximation would be correct only for the seven studied geometries. Hence, the modeling should take a more aerodynamic-related approach.

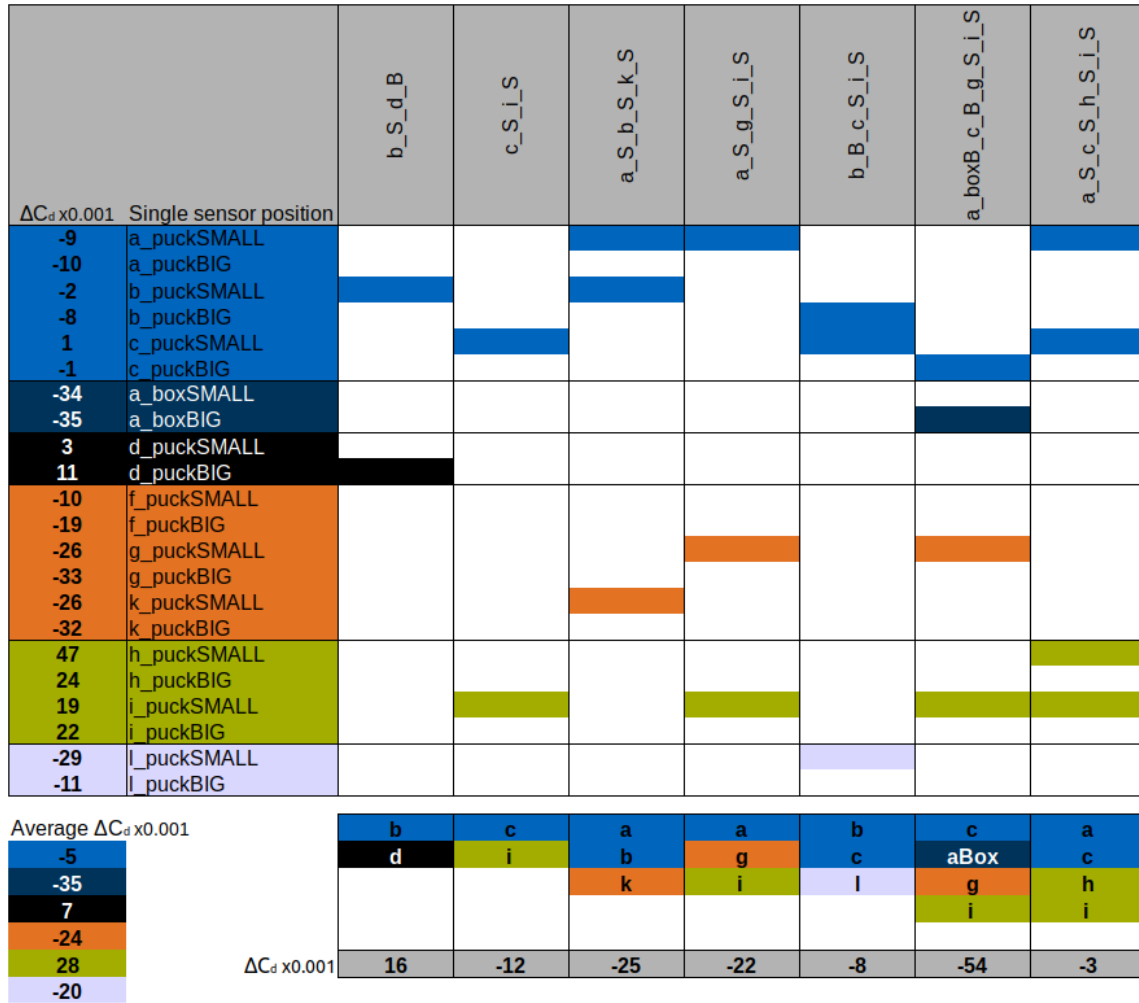


Figure 4.19: Decomposition of the sensor setups by the contribution of each sensor position

4.5.1 Model

A model is developed considering the observed flow interactions in the analysis of the sensor setups (Section 4.4). This approach accounts for the predominant effects from each sensor layout, clustered in the groups 1, 2 or 3 (depicted in Figure 4.22), and assigns the total ΔC_d to the contributions of each of them. This group classification is derived from the analysis of the simulations of multiple-sensors setups and considers the possible interaction between the three.

By the analysis performed in Section 4.4, the single sensor positions (considering box-type as well) are classified in a hierarchy scale (p) and sorted into three groups (G) (Figure 4.22).

Group 1 gathers the sensor positions that are placed in the longitudinal symmetry plane of the vehicle. They exclusively induce changes to the turbulent structure α . This group is divided in two sets. They denote the susceptibility of losing their flow-impact by sensors of other groups. This is the case of set 2. Besides, the last two sensor positions from group 1 (h and i) do not fulfill the placement condition nor the α influence. They are included in this group, as they could be considered in any of the other two. Combined with another sensor from a different position, their negative contribution identified as a rear-end over-pressure ($\Delta C_d > 0$) cancels out. For that reason they are highlighted with an asterisk and denoted with $p = 0$. Therefore, since the model contemplates multiple-sensor setups, h and i account always as $\Delta C_d = 0$.

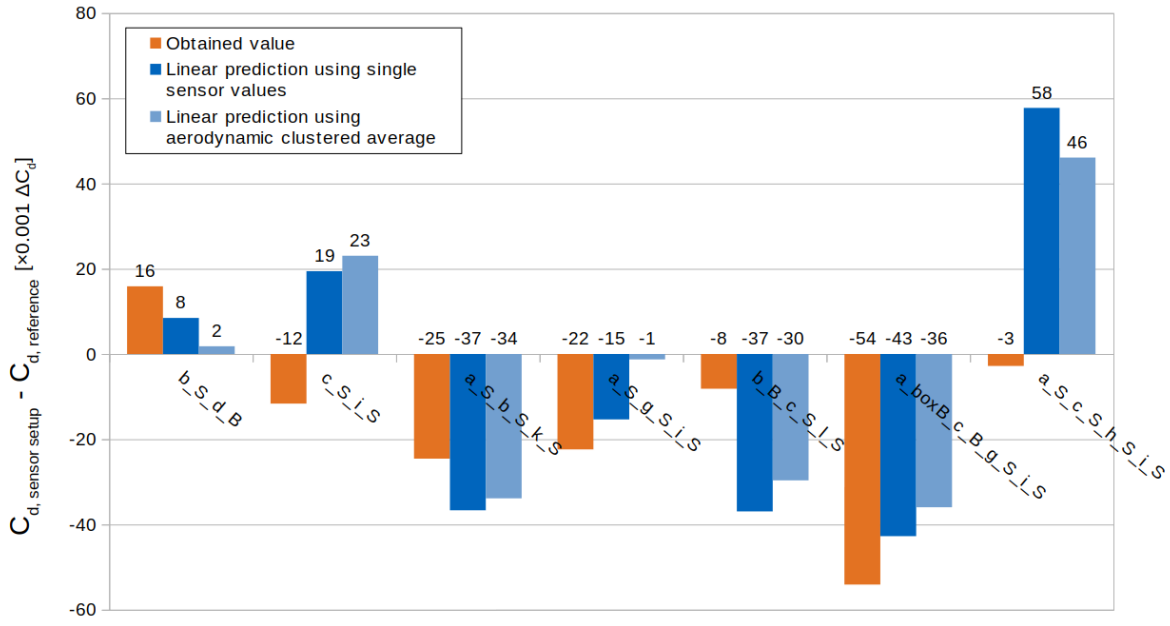


Figure 4.20: Comparison of obtained sensor setup drag values and two models based on linear predictions without considering interference drag

Group 2 collects the sensor positions that are placed in the side panel of the shuttle. They have two sub-effects: reduce the drag by partially reattaching the flow structure β and simultaneously they flatten α . This second effect produces an interaction with the sensors of the group 1 set 2, annulling their drag contribution.

Group 3 includes the sensor positions that are allocated along the top side edges of the vehicle, including the top corners. They have influence on the ζ and α . Like the sensors from group 2, they dissolve the effect of the sensors of the group 1 set 2.

The priority p indicates the domination of the sensor position drag delta over the other. Higher values denote more importance. The sensor with the highest p is the predominant within a group, canceling out other ones from the same group.

The total ΔC_d is calculated as the addition of the effects of group 1, 2 and 3, under the mentioned rule of "contribution elimination" of group 1 set 2. Mathematically, the nomenclature for drag contribution of a sensor position is: $\Delta C_{d,p,G}$, where p is the priority value and G the group. Therefore, the model is written as follows:

$$\Delta C_d = \begin{cases} \sum_{G=1}^3 \Delta C_{d_{\max\{p\},G}} & \text{if } \max\{p\} = 9 \text{ for } G = 1 \\ \Delta C_{d_{\max\{p\},1}} & \text{if } \max\{p\} \neq 9 \text{ for } G = 1 \text{ and } \Delta C_{d_{\max\{p\},2}} = \Delta C_{d_{\max\{p\},3}} = \emptyset \\ \sum_{G=2}^3 \Delta C_{d_{\max\{p\},G}} & \text{else} \end{cases} \quad (4.1)$$

The Equation 4.1 reads (in the order of the three conditions) as:

- If the multiple-sensor setup contains a combination of sensors of the three groups, being the $p = 9$ of $G = 1$, the total ΔC_d is the contribution of the three sensors with highest priority (p) of each group.
- If the multiple-sensor setup contains a combination of sensors of $G = 1$, with $p \neq 9$, the total ΔC_d is the contribution of the sensor of with highest priority.

- If the multiple-sensor setup contains a combination of sensors of $G = 2$ or $G = 3$ and from the $G = 1$ $p \neq 9$, the total ΔC_d is the contribution of the sensor of with highest priority from the groups 2 and 3.

In the mathematical model it is not considered the option that Table 4.1 lists the depicted sensor positions in hierarchy order (Figure 4.22).

Table 4.1: Priority value assignation to the single sensor simulations

| | p=9 | p=8 | p=7 | p=6 | p=5 | p=4 | p=3 | p=2 | p=1 | p=0 | p=0 |
|-----------------|-----|------|------|------|------|------|------|------|------|------|------|
| sensor position | a | k | g | f | d | l | c | b | a | h | i |
| sensor type | box | puck | puck | puck | puck | puck | puck | puck | puck | puck | puck |

Figure 4.21 depicts the real values compared to the approximations using the described method.

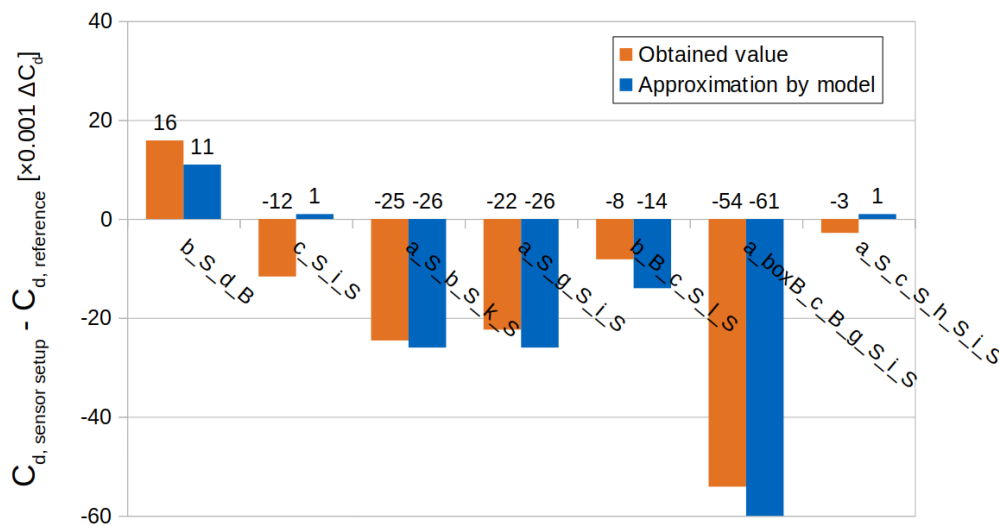


Figure 4.21: Comparison of obtained sensor setup drag values and the flow-structure based model

Excluding the setup $c_s_i_S$, which has a peculiar interaction effect (described in Section 4.4.2), the average of drag coefficient error induced by the model is $\Delta C_d \simeq 0.004$. This result is extremely better than the two previously proposed simple linear predictions (Figure 4.20). Nonetheless, this model is based on the observation of seven simulations. This small range of values is caused by:

- The low number of current autonomous shuttles.
- The high variation on the sensor location of current autonomous shuttles.
- Time and computational limitations.

These factors reduced the number of simulations, which ultimately limited the data points to develop the model. Therefore, its validity can not be confirmed without any further study or experimental testing.

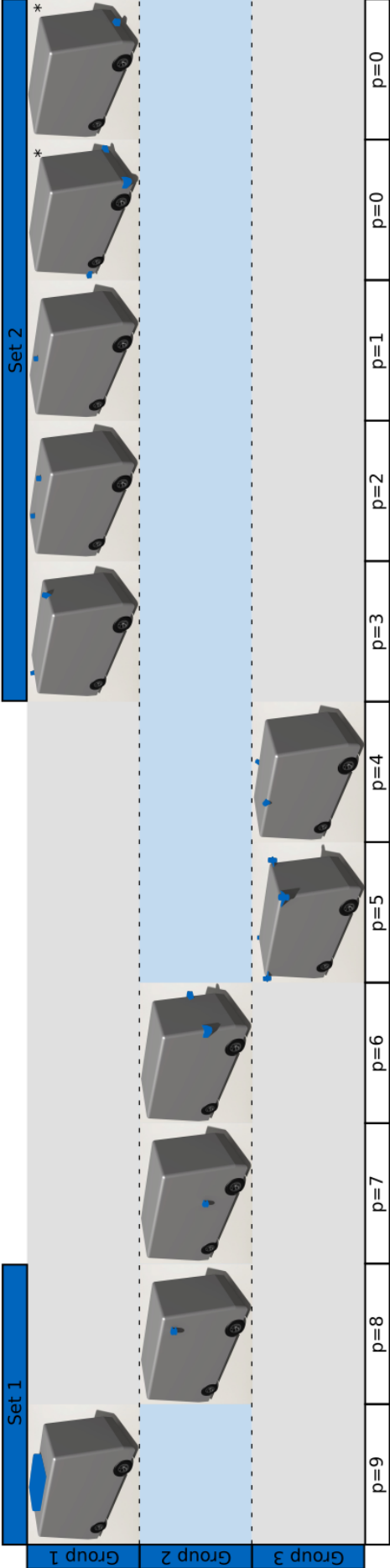


Figure 4.22: Priority and group classification of the single sensor positions to obtain the prevailing flow-effects that determine the ΔC_d

5 Discussion

Autonomous shuttle aerodynamics is still nowadays an unexplored topic. This is partly caused by the profound lack of published technical vehicle data and the novelty of the vehicle concept. These challenging circumstances accentuate the difficulty of defining a framework that represents current autonomous shuttles and disputes the results' validity. Furthermore, the high variability observed in the layout of sensor setups and the time and computational restrictions imposed by the simulations limit the extent of the aerodynamic analysis. Nevertheless, this study includes 63% of the current passenger autonomous shuttles and 80% of all observed protruding sensor positions. The approach taken investigates the effect of single factors over a reference geometry. For that purpose, this study revolves around a designed generic shuttle representative of this vehicle concept. This geometry defines the starting point of the design space exploration and uses as the ground for the analysis of the impact of sensor setups examined as the combination of single sensor contributions.

From the aerodynamic analysis of the design features of the generic shuttle, the impact of the edge rounding variable prevails above all. High radius values reduce the drag by $\Delta C_d = -0.099$, whereas sharp edges increase it by $\Delta C_d = 0.198$. It unequivocally controls the flow detachment around the vehicle and, therefore, its drag coefficient. Consequently, and given that the findings reveal how geometries in flow detachment regions reduce the C_d , this design feature governs the drag impact of the sensors. Compared to bus [23] and van [8] aerodynamics, the influence of the edge radius on the C_d of autonomous shuttles lies in between the two. The windshield slope has a modest drag delta compared to the previous design variable: for an angle of $\alpha = 88.65^\circ$ $\Delta C_d = 0.016$ and for $\alpha = 67.80^\circ$ $\Delta C_d = -0.005$. However, it controls the shape of the flow detachment regions, a fact that is relevant. High windshield angles produce a constant detachment area on the side panels thought the vehicle's height and along the longitudinal direction, whereas low angles reshape that region to be wider on the top of the side panel. Furthermore, this last geometrical condition enables the re-circulation of the air at the rear end. Finally, the influence of closed-style rims is barely noticeable in the generic shuttle geometry compared to the other studied design features ($\Delta C_d = 0.007$).

Intuitively, any add-on geometry incorporated over the vehicle's bodywork should increase the drag coefficient. Nonetheless, the generic shuttle designed in this study considers an edge radius condition $r/b = 0.05$ (radius/vehicle width), which creates flow detachment areas in the side and top panels of the shuttle. This causes that geometries allocated on those regions reduce the drag coefficient, with minimum values of $\Delta C_d = -0.035$ for single sensor positions. This effect is explained by the generation of swirl flow structures that suck the air towards the vehicle, reattaching it if the suction is strong enough. These areas of strong drag decrease are controlled by the edge radius and the windshield angle. Differently, the sensors exposed to the flow (no detachment areas) increase the drag coefficient of the shuttle in a similar magnitude. This behavior is detected on the vehicle's four front and rear corners, increasing the drag up to $\Delta C_d = 0.047$. The total range of drag delta coefficient (positive and negative) is 12.1% over

the total C_d . This value lays between the observed contribution on drag of external mirrors (4% (C_d) [9]) and rooftop add-on elements (up to 40% (C_d) [9]). Nonetheless, these findings are not fully comparable to literature data due to the different Reynolds numbers and the flow "attachment-characterization." Even though the approach followed in this study evaluates the changes in the C_d , the modification of the Re might trigger some unpredictable effects that change the ΔC_d (in %) of the geometry. Furthermore, previous studies assess the impact of mirrors or add-on geometries in areas of vehicles with attached flow. This unquestionably modifies the aerodynamic effect of the add-on geometry.

The sensor size sensibility is highly dependent on its location. In areas with detached flow, the proximity of the geometry to the limit of the detached turbulent structure is relevant. In these studied positions, bigger sensors reduce the drag by $\Delta C_d \in [-0.009, -0.001]$. Due to its height, the big sensors are closer to the limit of the detached flow structure but still contained inside of it. This accentuates the effect of reattaching the flow, which decreases the C_d . However, this trend is expected to be reversed when the geometry overcomes the limit of such flow structure, producing additional flow disturbance, hence, increasing the drag coefficient. On the areas with no visible flow detachment, like in the four front and rear corners, along the top longitudinal edges, and in the middle of the front and rear bottom edges, the expansion of the geometry has no clear pattern on the C_d . Most of these positions increase the drag by $\Delta C_d \in [0.003, 0.018]$, typical for flow-exposed geometries. However, bigger sensors allocated on four bottom corners of the vehicle reduce the drag by $\Delta C_d = -0.023$. This is caused by the pressure effect of these on the rear-end of the generic shuttle.

The analysis of the sensor setups suggests a high interaction effect between sensors. From the observed simulations, the oversight of this drag component induces high error values, up to $\Delta C_{d,error} = 0.061$. A mathematical model that considers the main sensor contributions of each setup is developed to account for that impact. This model contains a hierarchy and grouping of sensors based on their influence on the surrounding flow structures and the predominance in the interaction with other sensors. This approach aims to approximate the total ΔC_d from a less-mathematical perspective. Even though the model is seemly accurate in many cases ($\Delta C_{d,error} \simeq 0.004$), as a matter of fact, it can not be stated that it is valid for other sensor setups. Nonetheless, the groups considered in the model disassociate areas of the vehicle with identifiable impact on different flow structures. This could indicate the possible extrapolation to other sensor setups, as well as other edge rounding and windshield angle values. However, this simple model does not consider counter-intuitive interaction effects, which are frequently observed in the field of automotive external aerodynamics.

In the frame of the vast number of possible variables considered in this study, the final analysis-space reduction comes at the price of induced error. This is originated in each stage of a chain of assumptions under data and time limitations, a fact that is reflected in the validity of the derived model. These are: the limited current autonomous shuttle's published specifications, the choice of design variables that define the generic shuttle, the self-designed rim styles and wheels, the studied simulation conditions, the numerical accuracy of the simulations, the *Pacefish*[®] treatment of geometry rotation, the selected study-relevant sensor positions, the self-designed sensor and housing geometries and the limited number of sensor setup simulations to derive the model. However, each study stage has been rigorously assessed to minimize (or at least acknowledge) the induced error and cover the maximum representation of currently used shuttles under the study limitations. At the same time, this brings the necessity to validate the findings of this work and further analyze geometrical and Reynolds' variations to sketch the basics of autonomous shuttle aerodynamics. Especially, it is of general interest to perform a similar sensor setup

impact analysis in the shuttle profiles with almost no side and top flow detachment. Eventually, the extension of the C_d analysis of this vehicle concept should expand to include the impact on the range, the center of pressure, the cross-wind sensibility and vehicle dynamics in general. In the rapidly changing urban transportation mobility, the aerodynamic optimization of autonomous shuttles is an inevitable step to a cleaner and more efficient future.

6 Summary

This study aims to simulate and model the aerodynamic impact of sensor setups on autonomous road vehicles. To achieve that, it focuses on the analysis of the ΔC_d contribution of sensor setups in comparison to a reference self-designed generic shuttle geometry, employing the CFD simulation software *Pacefish*[®].

In Chapter 2 the fundamentals of aerodynamics are explained, with a focus on external vehicle aerodynamics. They collect the fluid field concepts required to interpret the simulation post-processings. Additionally, this chapter gathers literature on aerodynamic data of similar vehicle shapes and add-on elements. However, due to the topic's novelty, no previous studies on autonomous shuttle aerodynamics are stated. Finally, this chapter is concluded with the technical data collection of current autonomous shuttles.

Chapter 3 describes the adopted methodology. It includes the validation of the simulation software, followed by the derivation and design of a generic shuttle, which defines the aerodynamic reference. Based on that geometry, this study assesses the impact of the modification of design features and the incorporation of single sensor positions and multi-sensor setups. The drag influence of such geometrical alterations is measured in ΔC_d , which aligns with the validation methodology of *Pacefish*[®].

Major results in Chapter 4 indicate the huge impact of the edge rounding ($\Delta C_d \in [-0.099, 0.198]$) design variable compared to the single sensor ($\Delta C_d \in [-0.035, 0.047]$) and multi-sensor setup ($\Delta C_d \in [-0.054, 0.016]$) influence. Differently from literature data, add-on geometries located in specific positions reduce the drag of the generic shuttle due to the appearance of flow detachment in such areas. However, the magnitude of the sensor impact is similar to the one observed in specific previous studies. Furthermore, this chapter includes the mathematical model to estimate the ΔC_d of sensor setups based on the simulation results.

Finally, Chapter 5 discusses the thesis' results and suggests possible future studies that could help to corroborate the validity of the proposed mathematical model and expand the understanding of autonomous shuttle aerodynamics.

This study aims to shed some light on the barely studied topic of autonomous shuttle aerodynamics and the impact of sensor setups, which inevitably will gain relevance in the future of road transportation.

List of Figures

| | | |
|--------------|--|----|
| Figure 2.1: | Current spectrum of autonomous driving road vehicles (in production or under development) in terms of external design | 3 |
| Figure 2.2: | Drag coefficient C_d function of Reynolds number of a sphere (Dillmann, 2016, p. 127, Fig 2.43) [2] | 7 |
| Figure 2.3: | Influence of the surface roughness on the drag (chart (a)) and influence of the turbulence intensity (Tu) on the critical Re number (chart (b)) (Dillmann, 2016, p. 128, Fig 2.44) [2] | 8 |
| Figure 2.4: | Defined volume with single inflow and outflow surfaces | 9 |
| Figure 2.5: | Kolmogorov energy transfer theory | 11 |
| Figure 2.6: | Reynolds decomposition applied to property φ | 13 |
| Figure 2.7: | Overview of the mainstream turbulence models | 14 |
| Figure 2.8: | Overview of the turbulent viscosity concept applied to LBM..... | 14 |
| Figure 2.9: | Blending y^+ positions of the SST-DDES and SST-IDDES in the turbulent boundary layer | 15 |
| Figure 2.10: | Boundary layer evolution over a flat plate (Cengel, 2006, p. 579, Fig. 11-25) [6]..... | 18 |
| Figure 2.11: | C_d evolution during the years across vehicle categories (Woll, 2017, p. 153, Fig 3.3) [1] | 20 |
| Figure 2.12: | Driving resistance (Woll, 2017, p. 10, Fig 3.9) [1] | 21 |
| Figure 2.13: | Energy flows in the NEDC: To the left, for a vehicle with a combustion engine; to the right, for a vehicle with a battery-electric drive (Woll, 2017, p. 178, Fig 3.20) [1]..... | 23 |
| Figure 2.14: | DrivAer body with different tops (Heft, 2012, p. 3, Fig 4) [11]..... | 23 |
| Figure 2.15: | Effect of the side corner radius (left-hand side) and top corner radius (right-hand side) on the C_d (McDonald, 1980, p. 4473, Fig 6 and 7) [21]... | 25 |
| Figure 2.16: | Influence of the Reynolds number on the drag of rounded front edges vehicle (Gilhaus, 1981, p. 80, Fig 3) [22]..... | 26 |
| Figure 2.17: | Effect of the leading-edge radius on drag of a bus (Gotz, 1987, p. 773, Fig 10.82) [23]..... | 26 |
| Figure 2.18: | Effect of the side-edge radius on drag of a van (Hucho, 1987, p. 45, Fig 1.48) [8]..... | 27 |

| | | |
|--------------|--|----|
| Figure 2.19: | Boundary layer detachment in the front edge of a van (Hucho, 1987, p. 44, Fig 1.47) [8] | 27 |
| Figure 2.20: | Drag impact of different sky carriers (Schuetz, 2016, p. 365, Fig 4.170) [9] | 28 |
| Figure 2.21: | Cluster of current autonomous driving road vehicles | 30 |
| Figure 3.1: | Study process by steps | 34 |
| Figure 3.2: | Data workflow | 34 |
| Figure 3.3: | Approach considered for the validation of the CFD software <i>Pacefish</i> [®] | 35 |
| Figure 3.4: | Derivation of simulation setup from the software validation step | 35 |
| Figure 3.5: | Approach considered for the analysis of design and sensor aerodynamic influence | 36 |
| Figure 3.6: | Width/length and height/length of current autonomous shuttles..... | 38 |
| Figure 3.7: | Clustered height of the shuttles (excluding the object transportation vehicles)..... | 38 |
| Figure 3.8: | Clustered windshield angle..... | 39 |
| Figure 3.9: | Selected DrivAer state geometries. Bottom-left image depicts the Estate (or Squareback) car. Right-hand side highlighted images depict the detailed (top) and smooth (bottom) underbodies (Yazdani R., 2015, p. 4, Fig 3.1) [20] | 41 |
| Figure 3.10: | Setup report of the DrivAer simulations..... | 42 |
| Figure 3.11: | Simulation domain and refinement levels representation of the DrivAer simulations | 43 |
| Figure 3.12: | Comparison of the distribution of the pressure coefficient in the $y = 0$ mm plane at the top of the vehicle configuration E_D_wM_wW with GS with literature data..... | 45 |
| Figure 3.13: | Comparison of the distribution of the pressure coefficient in the $y = 0$ mm plane at the bottom of the vehicle configuration E_D_wM_wW with GS with literature data..... | 45 |
| Figure 3.14: | Tire and rim dimensions of a wheel 215/60 R17 (https://tiresize.com/calculator/) | 47 |
| Figure 3.15: | Impact of streamlined front-mounted structures on cuboids on the c_D value at ground level (Gotz, 1987, p. 774, Fig 10.83) [23] | 48 |
| Figure 3.16: | Generic shuttle design | 48 |
| Figure 3.17: | Setup report of the generic shuttle simulation | 49 |
| Figure 3.18: | Visualization of the rotation ground and tires in the generic shuttle simulation | 50 |
| Figure 3.19: | Design-influence simulation geometries..... | 52 |
| Figure 3.20: | Identification of all sensor placements in current autonomous shuttles | 53 |
| Figure 3.21: | Symmetric and asymmetric sensor position c | 54 |
| Figure 3.22: | Symmetric and asymmetric sensor position h | 55 |

| | | |
|--------------|---|----|
| Figure 3.23: | Histogram of sensor positions by number of single sensors | 55 |
| Figure 3.24: | Histogram of number of cars with sensor position..... | 55 |
| Figure 3.25: | Histogram of symmetric and asymmetric distributions per sensor position | 56 |
| Figure 3.26: | Position locations for the simulations of the single sensor case..... | 57 |
| Figure 3.27: | Puck sensor dimensions | 58 |
| Figure 3.28: | Puck sensor over top surface without supporting structure (positions a and b) | 59 |
| Figure 3.29: | Puck sensors on top edge with underneath supporting structure | 59 |
| Figure 3.30: | Big puck sensor in position d with supporting structure..... | 59 |
| Figure 3.31: | Puck sensor on lateral surfaces with supporting structure | 60 |
| Figure 3.32: | Puck sensor on lateral edges with supporting structure | 60 |
| Figure 3.33: | Puck sensor on front and rear surfaces with supporting structure..... | 60 |
| Figure 3.34: | Sensor setups | 63 |
| Figure 4.1: | Pressure-Friction drag ratio over the total C_d for the generic shuttle | 65 |
| Figure 4.2: | C_p surface distribution of the reference geometry | 66 |
| Figure 4.3: | U_τ surface distribution of the reference geometry | 67 |
| Figure 4.4: | Q-criteria (value $q = 2000 \text{ s}^{-2}$) isosurface representation around the reference geometry | 67 |
| Figure 4.5: | Side view of the vorticity (value $ \omega = 10 \text{ s}^{-1}$) of the reference geometry with identified flow structures $\alpha, \beta, \gamma, \delta$ and ζ | 68 |
| Figure 4.6: | Side view symmetry plane of the velocity magnitude of the reference geometry | 69 |
| Figure 4.7: | Design features ΔC_d | 69 |
| Figure 4.8: | Observed radius effect of the leading-edge compared to literature results [8] [23] | 70 |
| Figure 4.9: | Single sensor position ΔC_d clustered by their impact on the flow structures $\alpha, \beta, \gamma, \delta$ and ζ | 71 |
| Figure 4.10: | Classification of the sensor positions by their impact on the flow structures $\alpha, \beta, \gamma, \delta$ and ζ | 72 |
| Figure 4.11: | Streamline representation of the aerodynamic working principle of the top-located box shaped sensor. It blocks the turbulence in front of it and allows the attachment of the flow on its top surface | 74 |
| Figure 4.12: | Streamlines impacting the big puck sensor of position g..... | 75 |
| Figure 4.13: | Size influence on the drag coefficient: $C_{d,big \text{ sensor}} - C_{d,small \text{ sensor}}$ | 76 |
| Figure 4.14: | Visual representation of the ΔC_d by sensor size (only puck)..... | 77 |
| Figure 4.15: | Classification of the sensor positions by their common field of view | 78 |
| Figure 4.16: | Single sensor position ΔC_d clustered by their common field of view..... | 79 |

| | | |
|--------------|--|--------|
| Figure 4.17: | Sensor setup ΔC_d | 79 |
| Figure 4.18: | Visual representation of the ΔC_d impact of design features, single sensor positions and sensor setups | 80 |
| Figure 4.19: | Decomposition of the sensor setups by the contribution of each sensor position | 83 |
| Figure 4.20: | Comparison of obtained sensor setup drag values and two models based on linear predictions without considering interference drag | 84 |
| Figure 4.21: | Comparison of obtained sensor setup drag values and the flow-structure based model | 85 |
| Figure 4.22: | Priority and group classification of the single sensor positions to obtain the prevailing flow-effects that determine the ΔC_d | 86 |
| Figure A.1: | C_d impact of the sensor position | xxv |
| Figure A.2: | Render of the generic shuttle | xxvi |
| Figure A.3: | Front isometric view of the C_p of the generic shuttle | xxvi |
| Figure A.4: | Rear isometric view of the C_p of the generic shuttle | xxvi |
| Figure A.5: | Front isometric view of the Q-criteria (value $q = 2000 \text{ s}^{-2}$) of the generic shuttle | xxvi |
| Figure A.6: | Rear isometric view of the Q-criteria (value $q = 2000 \text{ s}^{-2}$) of the generic shuttle | xxvi |
| Figure A.7: | Front isometric view of the u_τ of the generic shuttle | xxvii |
| Figure A.8: | Rear isometric view of the u_τ of the generic shuttle | xxvii |
| Figure A.9: | Side view of the vorticity (value $ \omega = 10 \text{ s}^{-1}$) of the generic shuttle | xxvii |
| Figure A.10: | Side view symmetry plane of the velocity magnitude of the generic shuttle | xxvii |
| Figure B.1: | C_d impact of the sensor position | xxix |
| Figure B.2: | Render of design modification: windshield at 67.8° | xxxi |
| Figure B.3: | Front isometric view of the C_p of design modification: windshield at 67.8° | xxxi |
| Figure B.4: | Rear isometric view of the C_p of design modification: windshield at 67.8° | xxxi |
| Figure B.5: | Front isometric view of the Q-criteria (value $q = 2000 \text{ s}^{-2}$) of design modification: windshield at 67.8° | xxxi |
| Figure B.6: | Rear isometric view of the Q-criteria (value $q = 2000 \text{ s}^{-2}$) of design modification: windshield at 67.8° | xxxi |
| Figure B.7: | Front isometric view of the u_τ of design modification: windshield at 67.8° | xxxii |
| Figure B.8: | Rear isometric view of the u_τ of design modification: windshield at 67.8° | xxxii |
| Figure B.9: | Side view of the vorticity (value $ \omega = 10 \text{ s}^{-1}$) of design modification: windshield at 67.8° | xxxii |
| Figure B.10: | Side view symmetry plane of the velocity magnitude of design modification: windshield at 67.8° | xxxii |
| Figure B.11: | Render of design modification: windshield at 88.65° | xxxiii |

| | | |
|--------------|--|---------|
| Figure B.12: | Front isometric view of the C_p of design modification: windshield at 88.65° | xxxiii |
| Figure B.13: | Rear isometric view of the C_p of design modification: windshield at 88.65° | xxxiii |
| Figure B.14: | Front isometric view of the Q-criteria (value $q = 2000 \text{ s}^{-2}$) of design modification: windshield at 88.65° | xxxiii |
| Figure B.15: | Rear isometric view of the Q-criteria (value $q = 2000 \text{ s}^{-2}$) of design modification: windshield at 88.65° | xxxiii |
| Figure B.16: | Front isometric view of the u_τ of design modification: windshield at 88.65° | xxxiv |
| Figure B.17: | Rear isometric view of the u_τ of design modification: windshield at 88.65° | xxxiv |
| Figure B.18: | Side view of the vorticity (value $ \omega = 10 \text{ s}^{-1}$) of design modification: windshield at 88.65° | xxxiv |
| Figure B.19: | Side view symmetry plane of the velocity magnitude of design modification: windshield at 88.65° | xxxiv |
| Figure B.20: | Render of design modification: rounding of 0mm | xxxv |
| Figure B.21: | Front isometric view of the C_p of design modification: rounding of 0mm | xxxv |
| Figure B.22: | Rear isometric view of the C_p of design modification: rounding of 0mm | xxxv |
| Figure B.23: | Front isometric view of the Q-criteria (value $q = 2000 \text{ s}^{-2}$) of design modification: rounding of 0mm | xxxv |
| Figure B.24: | Rear isometric view of the Q-criteria (value $q = 2000 \text{ s}^{-2}$) of design modification: rounding of 0mm | xxxv |
| Figure B.25: | Front isometric view of the u_τ of design modification: rounding of 0mm | xxxvi |
| Figure B.26: | Rear isometric view of the u_τ of design modification: rounding of 0mm | xxxvi |
| Figure B.27: | Side view of the vorticity (value $ \omega = 10 \text{ s}^{-1}$) of design modification: rounding of 0mm | xxxvi |
| Figure B.28: | Side view symmetry plane of the velocity magnitude of design modification: rounding of 0mm | xxxvi |
| Figure B.29: | Render of design modification: rounding of 197.8 mm | xxxvii |
| Figure B.30: | Front isometric view of the C_p of design modification: rounding of 197.8 mm | xxxvii |
| Figure B.31: | Rear isometric view of the C_p of design modification: rounding of 197.8 mm | xxxvii |
| Figure B.32: | Front isometric view of the Q-criteria (value $q = 2000 \text{ s}^{-2}$) of design modification: rounding of 197.8 mm | xxxvii |
| Figure B.33: | Rear isometric view of the Q-criteria (value $q = 2000 \text{ s}^{-2}$) of design modification: rounding of 197.8 mm | xxxvii |
| Figure B.34: | Front isometric view of the u_τ of design modification: rounding of 197.8 mm | xxxviii |
| Figure B.35: | Rear isometric view of the u_τ of design modification: rounding of 197.8 mm | xxxviii |
| Figure B.36: | Side view of the vorticity (value $ \omega = 10 \text{ s}^{-1}$) of design modification: rounding of 197.8 mm | xxxviii |

| | | |
|--------------|--|---------|
| Figure B.37: | Side view symmetry plane of the velocity magnitude of design modification: rounding of 197.8 mm..... | xxxviii |
| Figure B.38: | Render of design modification: closed wheels | xxxix |
| Figure B.39: | Front isometric view of the C_p of design modification: closed wheels | xxxix |
| Figure B.40: | Rear isometric view of the C_p of design modification: closed wheels | xxxix |
| Figure B.41: | Front isometric view of the Q-criteria (value $q = 2000 \text{ s}^{-2}$) of design modification: closed wheels | xxxix |
| Figure B.42: | Rear isometric view of the Q-criteria (value $q = 2000 \text{ s}^{-2}$) of design modification: closed wheels | xxxix |
| Figure B.43: | Front isometric view of the u_τ of design modification: closed wheels..... | xl |
| Figure B.44: | Rear isometric view of the u_τ of design modification: closed wheels | xl |
| Figure B.45: | Side view of the vorticity (value $ \omega = 10 \text{ s}^{-1}$) of design modification: closed wheels | xl |
| Figure B.46: | Side view symmetry plane of the velocity magnitude of design modification: closed wheels | xl |
| Figure C.1: | Render of sensor position a and type small puck..... | xlii |
| Figure C.2: | Front isometric view of the C_p of sensor position a and type small puck.... | xlii |
| Figure C.3: | Rear isometric view of the C_p of sensor position a and type small puck | xlii |
| Figure C.4: | Front isometric view of the Q-criteria (value $q = 2000 \text{ s}^{-2}$) of sensor position a and type small puck | xlii |
| Figure C.5: | Rear isometric view of the Q-criteria (value $q = 2000 \text{ s}^{-2}$) of sensor position a and type small puck | xlii |
| Figure C.6: | Front isometric view of the u_τ of sensor position a and type small puck.... | xliii |
| Figure C.7: | Rear isometric view of the u_τ of sensor position a and type small puck | xliii |
| Figure C.8: | Side view of the vorticity (value $ \omega = 10 \text{ s}^{-1}$) of sensor position a and type small puck | xliii |
| Figure C.9: | Side view symmetry plane of the velocity magnitude of sensor position a and type small puck | xliii |
| Figure C.10: | Render of sensor position a and type big puck..... | xliv |
| Figure C.11: | Front isometric view of the C_p of sensor position a and type big puck..... | xliv |
| Figure C.12: | Rear isometric view of the C_p of sensor position a and type big puck | xliv |
| Figure C.13: | Front isometric view of the Q-criteria (value $q = 2000 \text{ s}^{-2}$) of sensor position a and type big puck | xliv |
| Figure C.14: | Rear isometric view of the Q-criteria (value $q = 2000 \text{ s}^{-2}$) of sensor position a and type big puck | xliv |
| Figure C.15: | Front isometric view of the u_τ of sensor position a and type big puck..... | xlv |
| Figure C.16: | Rear isometric view of the u_τ of sensor position a and type big puck | xlv |

| | | |
|--------------|---|--------|
| Figure C.17: | Side view of the vorticity (value $ \omega = 10 \text{ s}^{-1}$) of sensor position <i>a</i> and type big puck..... | xliv |
| Figure C.18: | Side view symmetry plane of the velocity magnitude of sensor position <i>a</i> and type big puck | xliv |
| Figure C.19: | Render of sensor position <i>a</i> and type small box | xlvi |
| Figure C.20: | Front isometric view of the C_p of sensor position <i>a</i> and type small box | xlvi |
| Figure C.21: | Rear isometric view of the C_p of sensor position <i>a</i> and type small box..... | xlvi |
| Figure C.22: | Front isometric view of the Q-criteria (value $q = 2000 \text{ s}^{-2}$) of sensor position <i>a</i> and type small box | xlvi |
| Figure C.23: | Rear isometric view of the Q-criteria (value $q = 2000 \text{ s}^{-2}$) of sensor position <i>a</i> and type small box | xlvi |
| Figure C.24: | Front isometric view of the u_τ of sensor position <i>a</i> and type small box | xlvii |
| Figure C.25: | Rear isometric view of the u_τ of sensor position <i>a</i> and type small box..... | xlvii |
| Figure C.26: | Side view of the vorticity (value $ \omega = 10 \text{ s}^{-1}$) of sensor position <i>a</i> and type small box | xlvii |
| Figure C.27: | Side view symmetry plane of the velocity magnitude of sensor position <i>a</i> and type small box | xlvii |
| Figure C.28: | Render of sensor position <i>a</i> and type big box | xlviii |
| Figure C.29: | Front isometric view of the C_p of sensor position <i>a</i> and type big box | xlviii |
| Figure C.30: | Rear isometric view of the C_p of sensor position <i>a</i> and type big box | xlviii |
| Figure C.31: | Front isometric view of the Q-criteria (value $q = 2000 \text{ s}^{-2}$) of sensor position <i>a</i> and type big box | xlviii |
| Figure C.32: | Rear isometric view of the Q-criteria (value $q = 2000 \text{ s}^{-2}$) of sensor position <i>a</i> and type big box | xlviii |
| Figure C.33: | Front isometric view of the u_τ of sensor position <i>a</i> and type big box | xliv |
| Figure C.34: | Rear isometric view of the u_τ of sensor position <i>a</i> and type big box | xliv |
| Figure C.35: | Side view of the vorticity (value $ \omega = 10 \text{ s}^{-1}$) of sensor position <i>a</i> and type big box | xliv |
| Figure C.36: | Side view symmetry plane of the velocity magnitude of sensor position <i>a</i> and type big box | xliv |
| Figure C.37: | Render of sensor position <i>b</i> and type small puck..... | l |
| Figure C.38: | Front isometric view of the C_p of sensor position <i>b</i> and type small puck.... | l |
| Figure C.39: | Rear isometric view of the C_p of sensor position <i>b</i> and type small puck | l |
| Figure C.40: | Front isometric view of the Q-criteria (value $q = 2000 \text{ s}^{-2}$) of sensor position <i>b</i> and type small puck | l |
| Figure C.41: | Rear isometric view of the Q-criteria (value $q = 2000 \text{ s}^{-2}$) of sensor position <i>b</i> and type small puck | l |
| Figure C.42: | Front isometric view of the u_τ of sensor position <i>b</i> and type small puck.... | li |

| | | |
|--------------|--|------|
| Figure C.43: | Rear isometric view of the u_τ of sensor position b and type small puck | li |
| Figure C.44: | Side view of the vorticity (value $ \omega = 10 \text{ s}^{-1}$) of sensor position b and type small puck | li |
| Figure C.45: | Side view symmetry plane of the velocity magnitude of sensor position b and type small puck | li |
| Figure C.46: | Render of sensor position b and type big puck..... | lii |
| Figure C.47: | Front isometric view of the C_p of sensor position b and type big puck..... | lii |
| Figure C.48: | Rear isometric view of the C_p of sensor position b and type big puck | lii |
| Figure C.49: | Front isometric view of the Q-criteria (value $q = 2000 \text{ s}^{-2}$) of sensor position b and type big puck | lii |
| Figure C.50: | Rear isometric view of the Q-criteria (value $q = 2000 \text{ s}^{-2}$) of sensor position b and type big puck | lii |
| Figure C.51: | Front isometric view of the u_τ of sensor position b and type big puck..... | liii |
| Figure C.52: | Rear isometric view of the u_τ of sensor position b and type big puck | liii |
| Figure C.53: | Side view of the vorticity (value $ \omega = 10 \text{ s}^{-1}$) of sensor position b and type big puck..... | liii |
| Figure C.54: | Side view symmetry plane of the velocity magnitude of sensor position b and type big puck | liii |
| Figure C.55: | Render of sensor position c and type small puck..... | liv |
| Figure C.56: | Front isometric view of the C_p of sensor position c and type small puck.... | liv |
| Figure C.57: | Rear isometric view of the C_p of sensor position c and type small puck | liv |
| Figure C.58: | Front isometric view of the Q-criteria (value $q = 2000 \text{ s}^{-2}$) of sensor position c and type small puck | liv |
| Figure C.59: | Rear isometric view of the Q-criteria (value $q = 2000 \text{ s}^{-2}$) of sensor position c and type small puck | liv |
| Figure C.60: | Front isometric view of the u_τ of sensor position c and type small puck.... | lv |
| Figure C.61: | Rear isometric view of the u_τ of sensor position c and type small puck | lv |
| Figure C.62: | Side view of the vorticity (value $ \omega = 10 \text{ s}^{-1}$) of sensor position c and type small puck | lv |
| Figure C.63: | Side view symmetry plane of the velocity magnitude of sensor position c and type small puck | lv |
| Figure C.64: | Render of sensor position c and type big puck..... | lvi |
| Figure C.65: | Front isometric view of the C_p of sensor position c and type big puck..... | lvi |
| Figure C.66: | Rear isometric view of the C_p of sensor position c and type big puck | lvi |
| Figure C.67: | Front isometric view of the Q-criteria (value $q = 2000 \text{ s}^{-2}$) of sensor position c and type big puck | lvi |
| Figure C.68: | Rear isometric view of the Q-criteria (value $q = 2000 \text{ s}^{-2}$) of sensor position c and type big puck | lvi |

| | | |
|--------------|--|-------|
| Figure C.69: | Front isometric view of the u_τ of sensor position c and type big puck..... | lvii |
| Figure C.70: | Rear isometric view of the u_τ of sensor position c and type big puck | lvii |
| Figure C.71: | Side view of the vorticity (value $ \omega = 10 \text{ s}^{-1}$) of sensor position c and type big puck..... | lvii |
| Figure C.72: | Side view symmetry plane of the velocity magnitude of sensor position c and type big puck | lvii |
| Figure C.73: | Render of sensor position d and type small puck | lviii |
| Figure C.74: | Front isometric view of the C_p of sensor position d and type small puck ... | lviii |
| Figure C.75: | Rear isometric view of the C_p of sensor position d and type small puck | lviii |
| Figure C.76: | Front isometric view of the Q-criteria (value $q = 2000 \text{ s}^{-2}$) of sensor position d and type small puck | lviii |
| Figure C.77: | Rear isometric view of the Q-criteria (value $q = 2000 \text{ s}^{-2}$) of sensor position d and type small puck | lviii |
| Figure C.78: | Front isometric view of the u_τ of sensor position d and type small puck ... | lix |
| Figure C.79: | Rear isometric view of the u_τ of sensor position d and type small puck | lix |
| Figure C.80: | Side view of the vorticity (value $ \omega = 10 \text{ s}^{-1}$) of sensor position d and type small puck | lix |
| Figure C.81: | Side view symmetry plane of the velocity magnitude of sensor position d and type small puck | lix |
| Figure C.82: | Render of sensor position d and type big puck..... | lx |
| Figure C.83: | Front isometric view of the C_p of sensor position d and type big puck | lx |
| Figure C.84: | Rear isometric view of the C_p of sensor position d and type big puck..... | lx |
| Figure C.85: | Front isometric view of the Q-criteria (value $q = 2000 \text{ s}^{-2}$) of sensor position d and type big puck | lx |
| Figure C.86: | Rear isometric view of the Q-criteria (value $q = 2000 \text{ s}^{-2}$) of sensor position d and type big puck | lx |
| Figure C.87: | Front isometric view of the u_τ of sensor position d and type big puck..... | lxi |
| Figure C.88: | Rear isometric view of the u_τ of sensor position d and type big puck | lxi |
| Figure C.89: | Side view of the vorticity (value $ \omega = 10 \text{ s}^{-1}$) of sensor position d and type big puck..... | lxi |
| Figure C.90: | Side view symmetry plane of the velocity magnitude of sensor position d and type big puck | lxi |
| Figure C.91: | Render of sensor position f and type small puck | lxii |
| Figure C.92: | Front isometric view of the C_p of sensor position f and type small puck | lxii |
| Figure C.93: | Rear isometric view of the C_p of sensor position f and type small puck..... | lxii |
| Figure C.94: | Front isometric view of the Q-criteria (value $q = 2000 \text{ s}^{-2}$) of sensor position f and type small puck..... | lxii |

| | | |
|---------------|--|--------|
| Figure C.95: | Rear isometric view of the Q-criteria (value $q = 2000 \text{ s}^{-2}$) of sensor position f and type small puck..... | lxii |
| Figure C.96: | Front isometric view of the u_τ of sensor position f and type small puck | lxiii |
| Figure C.97: | Rear isometric view of the u_τ of sensor position f and type small puck..... | lxiii |
| Figure C.98: | Side view of the vorticity (value $ \omega = 10 \text{ s}^{-1}$) of sensor position f and type small puck | lxiii |
| Figure C.99: | Side view symmetry plane of the velocity magnitude of sensor position f and type small puck | lxiii |
| Figure C.100: | Render of sensor position f and type big puck | lxiv |
| Figure C.101: | Front isometric view of the C_p of sensor position f and type big puck | lxiv |
| Figure C.102: | Rear isometric view of the C_p of sensor position f and type big puck..... | lxiv |
| Figure C.103: | Front isometric view of the Q-criteria (value $q = 2000 \text{ s}^{-2}$) of sensor position f and type big puck..... | lxiv |
| Figure C.104: | Rear isometric view of the Q-criteria (value $q = 2000 \text{ s}^{-2}$) of sensor position f and type big puck..... | lxiv |
| Figure C.105: | Front isometric view of the u_τ of sensor position f and type big puck | lxv |
| Figure C.106: | Rear isometric view of the u_τ of sensor position f and type big puck..... | lxv |
| Figure C.107: | Side view of the vorticity (value $ \omega = 10 \text{ s}^{-1}$) of sensor position f and type big puck..... | lxv |
| Figure C.108: | Side view symmetry plane of the velocity magnitude of sensor position f and type big puck | lxv |
| Figure C.109: | Render of sensor position g and type small puck..... | lxvi |
| Figure C.110: | Front isometric view of the C_p of sensor position g and type small puck.... | lxvi |
| Figure C.111: | Rear isometric view of the C_p of sensor position g and type small puck | lxvi |
| Figure C.112: | Front isometric view of the Q-criteria (value $q = 2000 \text{ s}^{-2}$) of sensor position g and type small puck | lxvi |
| Figure C.113: | Rear isometric view of the Q-criteria (value $q = 2000 \text{ s}^{-2}$) of sensor position g and type small puck | lxvi |
| Figure C.114: | Front isometric view of the u_τ of sensor position g and type small puck.... | lxvii |
| Figure C.115: | Rear isometric view of the u_τ of sensor position g and type small puck | lxvii |
| Figure C.116: | Side view of the vorticity (value $ \omega = 10 \text{ s}^{-1}$) of sensor position g and type small puck | lxvii |
| Figure C.117: | Side view symmetry plane of the velocity magnitude of sensor position g and type small puck | lxvii |
| Figure C.118: | Render of sensor position g and type big puck..... | lxviii |
| Figure C.119: | Front isometric view of the C_p of sensor position g and type big puck..... | lxviii |
| Figure C.120: | Rear isometric view of the C_p of sensor position g and type big puck | lxviii |

| | | |
|---------------|--|--------|
| Figure C.121: | Front isometric view of the Q-criteria (value $q = 2000 \text{ s}^{-2}$) of sensor position g and type big puck | lxviii |
| Figure C.122: | Rear isometric view of the Q-criteria (value $q = 2000 \text{ s}^{-2}$) of sensor position g and type big puck | lxviii |
| Figure C.123: | Front isometric view of the u_τ of sensor position g and type big puck..... | lxix |
| Figure C.124: | Rear isometric view of the u_τ of sensor position g and type big puck | lxix |
| Figure C.125: | Side view of the vorticity (value $ \omega = 10 \text{ s}^{-1}$) of sensor position g and type big puck..... | lxix |
| Figure C.126: | Side view symmetry plane of the velocity magnitude of sensor position g and type big puck | lxix |
| Figure C.127: | Render of sensor position h and type small puck..... | lxx |
| Figure C.128: | Front isometric view of the C_p of sensor position h and type small puck.... | lxx |
| Figure C.129: | Rear isometric view of the C_p of sensor position h and type small puck | lxx |
| Figure C.130: | Front isometric view of the Q-criteria (value $q = 2000 \text{ s}^{-2}$) of sensor position h and type small puck | lxx |
| Figure C.131: | Rear isometric view of the Q-criteria (value $q = 2000 \text{ s}^{-2}$) of sensor position h and type small puck | lxx |
| Figure C.132: | Front isometric view of the u_τ of sensor position h and type small puck.... | lxxi |
| Figure C.133: | Rear isometric view of the u_τ of sensor position h and type small puck | lxxi |
| Figure C.134: | Side view of the vorticity (value $ \omega = 10 \text{ s}^{-1}$) of sensor position h and type small puck | lxxi |
| Figure C.135: | Side view symmetry plane of the velocity magnitude of sensor position h and type small puck | lxxi |
| Figure C.136: | Render of sensor position h and type big puck..... | lxxii |
| Figure C.137: | Front isometric view of the C_p of sensor position h and type big puck..... | lxxii |
| Figure C.138: | Rear isometric view of the C_p of sensor position h and type big puck | lxxii |
| Figure C.139: | Front isometric view of the Q-criteria (value $q = 2000 \text{ s}^{-2}$) of sensor position h and type big puck | lxxii |
| Figure C.140: | Rear isometric view of the Q-criteria (value $q = 2000 \text{ s}^{-2}$) of sensor position h and type big puck | lxxii |
| Figure C.141: | Front isometric view of the u_τ of sensor position h and type big puck..... | lxxiii |
| Figure C.142: | Rear isometric view of the u_τ of sensor position h and type big puck | lxxiii |
| Figure C.143: | Side view of the vorticity (value $ \omega = 10 \text{ s}^{-1}$) of sensor position h and type big puck..... | lxxiii |
| Figure C.144: | Side view symmetry plane of the velocity magnitude of sensor position h and type big puck | lxxiii |
| Figure C.145: | Render of sensor position i and type small puck | lxxiv |
| Figure C.146: | Front isometric view of the C_p of sensor position i and type small puck ... | lxxiv |

Figure C.147: Rear isometric view of the C_p of sensor position i and type small pucklxxiv

Figure C.148: Front isometric view of the Q-criteria (value $q = 2000 \text{ s}^{-2}$) of sensor position i and type small pucklxxiv

Figure C.149: Rear isometric view of the Q-criteria (value $q = 2000 \text{ s}^{-2}$) of sensor position i and type small pucklxxiv

Figure C.150: Front isometric view of the u_τ of sensor position i and type small puck....lxxv

Figure C.151: Rear isometric view of the u_τ of sensor position i and type small pucklxxv

Figure C.152: Side view of the vorticity (value $|\omega| = 10 \text{ s}^{-1}$) of sensor position i and type small pucklxxv

Figure C.153: Side view symmetry plane of the velocity magnitude of sensor position i and type small pucklxxv

Figure C.154: Render of sensor position i and type big puck.....lxxvi

Figure C.155: Front isometric view of the C_p of sensor position i and type big puck.....lxxvi

Figure C.156: Rear isometric view of the C_p of sensor position i and type big pucklxxvi

Figure C.157: Front isometric view of the Q-criteria (value $q = 2000 \text{ s}^{-2}$) of sensor position i and type big pucklxxvi

Figure C.158: Rear isometric view of the Q-criteria (value $q = 2000 \text{ s}^{-2}$) of sensor position i and type big pucklxxvi

Figure C.159: Front isometric view of the u_τ of sensor position i and type big puck.....lxxvii

Figure C.160: Rear isometric view of the u_τ of sensor position i and type big pucklxxvii

Figure C.161: Side view of the vorticity (value $|\omega| = 10 \text{ s}^{-1}$) of sensor position i and type big puck.....lxxvii

Figure C.162: Side view symmetry plane of the velocity magnitude of sensor position i and type big pucklxxvii

Figure C.163: Render of sensor position k and type small puck.....lxxviii

Figure C.164: Front isometric view of the C_p of sensor position k and type small puck.lxxviii

Figure C.165: Rear isometric view of the C_p of sensor position k and type small puck .lxxviii

Figure C.166: Front isometric view of the Q-criteria (value $q = 2000 \text{ s}^{-2}$) of sensor position k and type small pucklxxviii

Figure C.167: Rear isometric view of the Q-criteria (value $q = 2000 \text{ s}^{-2}$) of sensor position k and type small pucklxxviii

Figure C.168: Front isometric view of the u_τ of sensor position k and type small puck...lxxix

Figure C.169: Rear isometric view of the u_τ of sensor position k and type small puck ...lxxix

Figure C.170: Side view of the vorticity (value $|\omega| = 10 \text{ s}^{-1}$) of sensor position k and type small pucklxxix

Figure C.171: Side view symmetry plane of the velocity magnitude of sensor position k and type small pucklxxix

Figure C.172: Render of sensor position k and type big puck.....lxxx

| | | |
|---------------|--|------|
| Figure C.173: | Front isometric view of the C_p of sensor position k and type big puck..... | lxxx |
| Figure C.174: | Rear isometric view of the C_p of sensor position k and type big puck | lxxx |
| Figure C.175: | Front isometric view of the Q-criteria (value $q = 2000 \text{ s}^{-2}$) of sensor position k and type big puck | lxxx |
| Figure C.176: | Rear isometric view of the Q-criteria (value $q = 2000 \text{ s}^{-2}$) of sensor position k and type big puck | lxxx |
| Figure C.177: | Front isometric view of the u_τ of sensor position k and type big puck..... | lxxx |
| Figure C.178: | Rear isometric view of the u_τ of sensor position k and type big puck | lxxx |
| Figure C.179: | Side view of the vorticity (value $ \omega = 10 \text{ s}^{-1}$) of sensor position k and type big puck..... | lxxx |
| Figure C.180: | Side view symmetry plane of the velocity magnitude of sensor position k and type big puck | lxxx |
| Figure C.181: | Render of sensor position l and type small puck | lxxx |
| Figure C.182: | Front isometric view of the C_p of sensor position l and type small puck .. | lxxx |
| Figure C.183: | Rear isometric view of the C_p of sensor position l and type small puck ... | lxxx |
| Figure C.184: | Front isometric view of the Q-criteria (value $q = 2000 \text{ s}^{-2}$) of sensor position l and type small puck | lxxx |
| Figure C.185: | Rear isometric view of the Q-criteria (value $q = 2000 \text{ s}^{-2}$) of sensor position l and type small puck | lxxx |
| Figure C.186: | Front isometric view of the u_τ of sensor position l and type small puck.. | lxxx |
| Figure C.187: | Rear isometric view of the u_τ of sensor position l and type small puck .. | lxxx |
| Figure C.188: | Side view of the vorticity (value $ \omega = 10 \text{ s}^{-1}$) of sensor position l and type small puck | lxxx |
| Figure C.189: | Side view symmetry plane of the velocity magnitude of sensor position l and type small puck | lxxx |
| Figure C.190: | Render of sensor position l and type big puck..... | lxxx |
| Figure C.191: | Front isometric view of the C_p of sensor position l and type big puck..... | lxxx |
| Figure C.192: | Rear isometric view of the C_p of sensor position l and type big puck | lxxx |
| Figure C.193: | Front isometric view of the Q-criteria (value $q = 2000 \text{ s}^{-2}$) of sensor position l and type big puck | lxxx |
| Figure C.194: | Rear isometric view of the Q-criteria (value $q = 2000 \text{ s}^{-2}$) of sensor position l and type big puck | lxxx |
| Figure C.195: | Front isometric view of the u_τ of sensor position l and type big puck..... | lxxx |
| Figure C.196: | Rear isometric view of the u_τ of sensor position l and type big puck | lxxx |
| Figure C.197: | Side view of the vorticity (value $ \omega = 10 \text{ s}^{-1}$) of sensor position l and type big puck..... | lxxx |
| Figure C.198: | Side view symmetry plane of the velocity magnitude of sensor position l and type big puck | lxxx |

| | | |
|--------------|--|----------|
| Figure D.1: | Render of sensor layout coded: b_S_d_B | lxxxviii |
| Figure D.2: | Front isometric view of the C_p of sensor layout coded: b_S_d_B | lxxxviii |
| Figure D.3: | Rear isometric view of the C_p of sensor layout coded: b_S_d_B..... | lxxxviii |
| Figure D.4: | Front isometric view of the Q-criteria (value $q = 2000 s^{-2}$) of sensor layout coded: b_S_d_B..... | lxxxviii |
| Figure D.5: | Rear isometric view of the Q-criteria (value $q = 2000 s^{-2}$) of sensor layout coded: b_S_d_B..... | lxxxviii |
| Figure D.6: | Front isometric view of the u_τ of sensor layout coded: b_S_d_B | lxxxix |
| Figure D.7: | Rear isometric view of the u_τ of sensor layout coded: b_S_d_B..... | lxxxix |
| Figure D.8: | Side view of the vorticity (value $ \omega = 10 s^{-1}$) of sensor layout coded: b_S_d_B | lxxxix |
| Figure D.9: | Side view symmetry plane of the velocity magnitude of sensor layout coded: b_S_d_B..... | lxxxix |
| Figure D.10: | Render of sensor layout coded: c_S_i_S | xc |
| Figure D.11: | Front isometric view of the C_p of sensor layout coded: c_S_i_S | xc |
| Figure D.12: | Rear isometric view of the C_p of sensor layout coded: c_S_i_S..... | xc |
| Figure D.13: | Front isometric view of the Q-criteria (value $q = 2000 s^{-2}$) of sensor layout coded: c_S_i_S..... | xc |
| Figure D.14: | Rear isometric view of the Q-criteria (value $q = 2000 s^{-2}$) of sensor layout coded: c_S_i_S..... | xc |
| Figure D.15: | Front isometric view of the u_τ of sensor layout coded: c_S_i_S | xc |
| Figure D.16: | Rear isometric view of the u_τ of sensor layout coded: c_S_i_S..... | xc |
| Figure D.17: | Side view of the vorticity (value $ \omega = 10 s^{-1}$) of sensor layout coded: c_S_i_S | xc |
| Figure D.18: | Side view symmetry plane of the velocity magnitude of sensor layout coded: c_S_i_S..... | xc |
| Figure D.19: | Render of sensor layout coded: a_S_b_S_k_S | xcii |
| Figure D.20: | Front isometric view of the C_p of sensor layout coded: a_S_b_S_k_S | xcii |
| Figure D.21: | Rear isometric view of the C_p of sensor layout coded: a_S_b_S_k_S | xcii |
| Figure D.22: | Front isometric view of the Q-criteria (value $q = 2000 s^{-2}$) of sensor layout coded: a_S_b_S_k_S..... | xcii |
| Figure D.23: | Rear isometric view of the Q-criteria (value $q = 2000 s^{-2}$) of sensor layout coded: a_S_b_S_k_S..... | xcii |
| Figure D.24: | Front isometric view of the u_τ of sensor layout coded: a_S_b_S_k_S | xciii |
| Figure D.25: | Rear isometric view of the u_τ of sensor layout coded: a_S_b_S_k_S..... | xciii |
| Figure D.26: | Side view of the vorticity (value $ \omega = 10 s^{-1}$) of sensor layout coded: a_S_b_S_k_S | xciii |

| | |
|--------------|--|
| Figure D.27: | Side view symmetry plane of the velocity magnitude of sensor layout coded: a_S_b_S_k_S.....xciii |
| Figure D.28: | Render of sensor layout coded: a_S_g_S_i_S.....xciv |
| Figure D.29: | Front isometric view of the C_p of sensor layout coded: a_S_g_S_i_S.....xciv |
| Figure D.30: | Rear isometric view of the C_p of sensor layout coded: a_S_g_S_i_S.....xciv |
| Figure D.31: | Front isometric view of the Q-criteria (value $q = 2000 s^{-2}$) of sensor layout coded: a_S_g_S_i_S.....xciv |
| Figure D.32: | Rear isometric view of the Q-criteria (value $q = 2000 s^{-2}$) of sensor layout coded: a_S_g_S_i_S.....xciv |
| Figure D.33: | Front isometric view of the u_τ of sensor layout coded: a_S_g_S_i_S.....xcv |
| Figure D.34: | Rear isometric view of the u_τ of sensor layout coded: a_S_g_S_i_S.....xcv |
| Figure D.35: | Side view of the vorticity (value $ \omega = 10 s^{-1}$) of sensor layout coded: a_S_g_S_i_S.....xcv |
| Figure D.36: | Side view symmetry plane of the velocity magnitude of sensor layout coded: a_S_g_S_i_S.....xcv |
| Figure D.37: | Render of sensor layout coded: b_B_c_S_l_S.....xcvi |
| Figure D.38: | Front isometric view of the C_p of sensor layout coded: b_B_c_S_l_S.....xcvi |
| Figure D.39: | Rear isometric view of the C_p of sensor layout coded: b_B_c_S_l_S.....xcvi |
| Figure D.40: | Front isometric view of the Q-criteria (value $q = 2000 s^{-2}$) of sensor layout coded: b_B_c_S_l_S.....xcvi |
| Figure D.41: | Rear isometric view of the Q-criteria (value $q = 2000 s^{-2}$) of sensor layout coded: b_B_c_S_l_S.....xcvi |
| Figure D.42: | Front isometric view of the u_τ of sensor layout coded: b_B_c_S_l_S.....xcvii |
| Figure D.43: | Rear isometric view of the u_τ of sensor layout coded: b_B_c_S_l_S.....xcvii |
| Figure D.44: | Side view of the vorticity (value $ \omega = 10 s^{-1}$) of sensor layout coded: b_B_c_S_l_S.....xcvii |
| Figure D.45: | Side view symmetry plane of the velocity magnitude of sensor layout coded: b_B_c_S_l_S.....xcvii |
| Figure D.46: | Render of sensor layout coded: a_S_c_S_h_S_i_S.....xcviii |
| Figure D.47: | Front isometric view of the C_p of sensor layout coded: a_S_c_S_h_S_i_S.....xcviii |
| Figure D.48: | Rear isometric view of the C_p of sensor layout coded: a_S_c_S_h_S_i_S.....xcviii |
| Figure D.49: | Front isometric view of the Q-criteria (value $q = 2000 s^{-2}$) of sensor layout coded: a_S_c_S_h_S_i_S.....xcviii |
| Figure D.50: | Rear isometric view of the Q-criteria (value $q = 2000 s^{-2}$) of sensor layout coded: a_S_c_S_h_S_i_S.....xcviii |
| Figure D.51: | Front isometric view of the u_τ of sensor layout coded: a_S_c_S_h_S_i_S.....xcix |
| Figure D.52: | Rear isometric view of the u_τ of sensor layout coded: a_S_c_S_h_S_i_S.....xcix |

Figure D.53: Side view of the vorticity (value $|\omega| = 10 \text{ s}^{-1}$) of sensor layout coded: a_S_c_S_h_S_i_S.....xcix

Figure D.54: Side view symmetry plane of the velocity magnitude of sensor layout coded: a_S_c_S_h_S_i_Sxcix

Figure D.55: Render of sensor layout coded: a_boxB_c_B_g_S_i_S..... c

Figure D.56: Front isometric view of the C_p of sensor layout coded: a_boxB_c_B_g_S_i_S c

Figure D.57: Rear isometric view of the C_p of sensor layout coded: a_boxB_c_B_g_S_i_S c

Figure D.58: Front isometric view of the Q-criteria (value $q = 2000 \text{ s}^{-2}$) of sensor layout coded: a_boxB_c_B_g_S_i_S c

Figure D.59: Rear isometric view of the Q-criteria (value $q = 2000 \text{ s}^{-2}$) of sensor layout coded: a_boxB_c_B_g_S_i_S c

Figure D.60: Front isometric view of the u_τ of sensor layout coded: a_boxB_c_B_g_S_i_S ci

Figure D.61: Rear isometric view of the u_τ of sensor layout coded: a_boxB_c_B_g_S_i_S ci

Figure D.62: Side view of the vorticity (value $|\omega| = 10 \text{ s}^{-1}$) of sensor layout coded: a_boxB_c_B_g_S_i_S..... ci

Figure D.63: Side view symmetry plane of the velocity magnitude of sensor layout coded: a_boxB_c_B_g_S_i_S ci

List of Tables

| | | |
|-------------|--|--------|
| Table 2.1: | Summary of the collected data of the current autonomous shuttles | 31 |
| Table 3.1: | Summary of the collected data of the current autonomous shuttles with derived parameters | 37 |
| Table 3.2: | Collected literature C_d E_S_wW_wM with GS and E_D_wW_wM with GS data..... | 41 |
| Table 3.3: | Description of the system used for the simulations | 44 |
| Table 3.4: | Rating of the Difference Between Numerical and Experimental Data (Karniadakis, 2019, p. 1081, Table 14.2) [58]..... | 46 |
| Table 3.5: | Break down of the features selection of the design-influence simulations | 51 |
| Table 3.6: | Sensor classification of current autonomous vehicles | 53 |
| Table 3.7: | Classification of current autonomous shuttles by number of sensor positions and highlighting of geometries simulated (in blue) and to simulate (in gray) . | 61 |
| Table 4.1: | Priority value assignation to the single sensor simulations | 85 |
| Table B.1: | Data table of design modification: windshield at 67.8°..... | xxxi |
| Table B.2: | Data table of design modification: windshield at 88.65°..... | xxxiii |
| Table B.3: | Data table of design modification: rounding of 0mm | xxxv |
| Table B.4: | Data table of design modification: rounding of 197.8 mm..... | xxxvii |
| Table B.5: | Data table of design modification: closed wheels | xxxix |
| Table C.1: | Data table of sensor position a and type small puck | xlii |
| Table C.2: | Data table of sensor position a and type big puck | xliv |
| Table C.3: | Data table of sensor position a and type small box | xlvi |
| Table C.4: | Data table of sensor position a and type big box | xlviii |
| Table C.5: | Data table of sensor position b and type small puck | l |
| Table C.6: | Data table of sensor position b and type big puck | lii |
| Table C.7: | Data table of sensor position c and type small puck | liv |
| Table C.8: | Data table of sensor position c and type big puck..... | lvi |
| Table C.9: | Data table of sensor position d and type small puck | lviii |
| Table C.10: | Data table of sensor position d and type big puck | lx |
| Table C.11: | Data table of sensor position f and type small puck..... | lxii |

| | | |
|-------------|--|----------|
| Table C.12: | Data table of sensor position f and type big puck | lxiv |
| Table C.13: | Data table of sensor position g and type small puck | lxvi |
| Table C.14: | Data table of sensor position g and type big puck | lxviii |
| Table C.15: | Data table of sensor position h and type small puck | lxx |
| Table C.16: | Data table of sensor position h and type big puck | lxxii |
| Table C.17: | Data table of sensor position i and type small puck | lxxiv |
| Table C.18: | Data table of sensor position i and type big puck | lxxvi |
| Table C.19: | Data table of sensor position k and type small puck | lxxviii |
| Table C.20: | Data table of sensor position k and type big puck | lxxx |
| Table C.21: | Data table of sensor position l and type small puck | lxxxii |
| Table C.22: | Data table of sensor position l and type big puck | lxxxiv |
| Table D.1: | Data table of sensor layout coded: $b_S_d_B$ | lxxxviii |
| Table D.2: | Data table of sensor layout coded: $c_S_i_S$ | xc |
| Table D.3: | Data table of sensor layout coded: $a_S_b_S_k_S$ | xcii |
| Table D.4: | Data table of sensor layout coded: $a_S_g_S_i_S$ | xciv |
| Table D.5: | Data table of sensor layout coded: $b_B_c_S_l_S$ | xcvi |
| Table D.6: | Data table of sensor layout coded: $a_S_c_S_h_S_i_S$ | xcviii |
| Table D.7: | Data table of sensor layout coded: $a_boxB_c_B_g_S_i_S$ | c |

Bibliography

- [1] T. Woll, „Consumption and Performance Improvement,“ *SAE Technical Papers*, pp. 151–196, 2017, ISBN: 9780768082531. DOI: 10.4271/R-430.
- [2] A. Dillmann, „The Physical Principles of Astronautics,“ *Physics Today*, vol. 15, no. 8, pp. 56–58, 1962, DOI: 10.1063/1.3058329.
- [3] S. Chen and G. D. Doolen, „Lattice boltzmann method for fluid flows,“ *Annual Review of Fluid Mechanics*, vol. 30, no. Kadanoff 1986, pp. 329–364, 1998, DOI: 10.1146/annurev.fluid.30.1.329.
- [4] D. Yu et al., „Viscous flow computations with the method of lattice Boltzmann equation,“ *Progress in Aerospace Sciences*, vol. 39, no. 5, pp. 329–367, 2003, DOI: 10.1016/S0376-0421(03)00003-4.
- [5] Y. H. Qian, D. D’Humières and P. Lallemand, „Lattice bgk models for navier-stokes equation,“ *Epl*, vol. 17, no. 6, pp. 479–484, 1992, DOI: 10.1209/0295-5075/17/6/001.
- [6] Y. A. Çengel and J. M. Cimbala, „McGraw-Hill Series in Mechanical Engineering,“ *Fluid Mechanics, Fundamentals and Applications*, p. 968, 2006, ISBN: 007124493X. arXiv: 1003.3921v1.
- [7] A. Brandstädt and R. Mosca, „On variations of P4-sparse graphs,“ *Discrete Applied Mathematics*, vol. 129, no. 2-3, pp. 521–532, 2003, DOI: 10.1016/s0166-218x(03)00180-x.
- [8] W. H. Hucho, „Introduction to automobile aerodynamics.“ 1987, ISBN: 0408014229. DOI: 10.1016/b978-0-7506-1267-8.50005-1.
- [9] T. Schuetz and L. Krüger, „Aerodynamic Forces and Their Influence on Passenger Vehicles,“ *SAE Technical Papers*, ISBN: 9780768082531. DOI: 10.4271/R-430.
- [10] United Nations, „AE/ECE/TRANS/505/Rev.2/Add.100/Rev.3 Uniform provisions concerning the approval of passenger cars powered by an internal combustion engine only, or powered by a hybrid electric power train with regard to the measurement of the emission of carbon dioxide a,“ *Usa Gov*, no. April, p. 100, 2013. Available: <http://www.unece.org/fileadmin/DAM/trans/main/wp29/wp29regs/updates/R101r3e.pdf>.
- [11] A. I. Heft, T. Indinger and N. A. Adams, „Introduction of a new realistic generic car model for aerodynamic investigations,“ *SAE Technical Papers*, 2012, DOI: 10.4271/2012-01-0168.
- [12] A. I. Heft, T. Indinger and N. A. Adams, „Experimental and numerical investigation of the driver model,“ *American Society of Mechanical Engineers, Fluids Engineering Division (Publication) FEDSM*, vol. 1, no. PARTS A AND B, pp. 41–51, 2012, ISBN: 9780791844755. DOI: 10.1115/FEDSM2012-72272.
- [13] L. Miao, S. Mack and T. Indinger, „EXPERIMENTAL AND NUMERICAL INVESTIGATION OF AUTOMOTIVE AERODYNAMICS USING DRIVER MODEL,“ pp. 1–8, 2016.

- [14] C. Collin et al., „A Numerical and Experimental Evaluation of Open Jet Wind Tunnel Interferences using the DrivAer Reference Model,“ *SAE International Journal of Passenger Cars - Mechanical Systems*, vol. 9, no. 2, pp. 657–679, 2016, DOI: 10.4271/2016-01-1597.
- [15] T. Avadiar et al., „Characterisation of the wake of the DrivAer estate vehicle,“ *Journal of Wind Engineering and Industrial Aerodynamics*, vol. 177, no. March, pp. 242–259, 2018, DOI: 10.1016/j.jweia.2018.04.013. Available: <https://doi.org/10.1016/j.jweia.2018.04.013>.
- [16] T. Avadiar et al., „The influence of reduced Reynolds number on the wake of the DrivAer estate vehicle,“ *Journal of Wind Engineering and Industrial Aerodynamics*, vol. 188, no. 2, pp. 207–216, 2019, DOI: 10.1016/j.jweia.2019.02.024. Available: <https://doi.org/10.1016/j.jweia.2019.02.024>.
- [17] M. Maier and K. Muller, „Experimental and Numerical Study of the DrivAer Model Aerodynamics,“ *SAE paper No.950757*, pp. 1–15, 1996, DOI: 10.4271/2018-01-0741.Abstract.
- [18] N. Ashton and A. Revell, „Comparison of RANS and des methods for the DrivAer automotive body,“ *SAE Technical Papers*, vol. 2015-April, no. April, 2015, DOI: 10.4271/2015-01-1538.
- [19] S. Wang et al., „Effect of moving ground on the aerodynamics of a generic automotive model: The DrivAer-Estate,“ *Journal of Wind Engineering and Industrial Aerodynamics*, vol. 195, no. September, p. 104000, 2019, DOI: 10.1016/j.jweia.2019.104000. Available: <https://doi.org/10.1016/j.jweia.2019.104000>.
- [20] R. Yazdani, „Steady and Unsteady Numerical Analysis of the DrivAer Model,“ p. 43, 2015.
- [21] A. T. McDonald and G. M. Palmer, „Aerodynamic drag reduction of intercity buses,“ *SAE Technical Papers*, 1980, DOI: 10.4271/801404.
- [22] A. Gilhaus, „The influence of cab shape on air drag of trucks,“ *Journal of Wind Engineering and Industrial Aerodynamics*, vol. 9, no. 1-2, pp. 77–87, 1981, DOI: 10.1016/0167-6105(81)90079-9.
- [23] H. Gotz, „Commercial vehicles.“ Pp. 711–794, 1987, ISBN: 0408014229. DOI: 10.1201/9781482281132-11.
- [24] A. F. A. Rodrigues et al., „Aerodynamic Analysis of a Vehicle Minibus,“ *SAE Technical Papers*, p. 12, 2014, DOI: 10.4271/2014-36-0327.
- [25] M. H. Kim, J. Y. Kuk and I. B. Chyun, „A numerical simulation on the drag reduction of large-sized bus using rear-spoiler,“ *SAE Technical Papers*, no. 724, 2002, DOI: 10.4271/2002-01-3070.
- [26] L. Jiang, Z. C. He and T. Chen, „Optimization of local body shape about a minibus based on CFD and wind tunnel test,“ *Applied Mechanics and Materials*, vol. 318, pp. 257–262, 2013, ISBN: 9783037857021. DOI: 10.4028/www.scientific.net/AMM.318.257.
- [27] K. Hirose et al., „Application of Prediction Formulas to Aerodynamic Drag Reduction of Door Mirrors,“ *SAE Technical Papers*, vol. 2015-April, no. April, 2015, ISBN: 2015011528. DOI: 10.4271/2015-01-1528.
- [28] M. Lenner, „Influence of roof-rack, trailer etc on automobile fuel consumption and exhaust emissions, measured on-the-road,“ *SAE Technical Papers*, no. 724, 1998, DOI: 10.4271/980682.
- [29] H. Chowdhury et al., „Impact of vehicle add-ons on energy consumption and greenhouse gas emissions,“ *Procedia Engineering*, vol. 49, no. 1, pp. 294–302, 2012, DOI: 10.1016/j.proeng.2012.10.140.

- [30] F. Alam, H. Chowdhury and S. Watkins, „Aerodynamics of Vehicle Add-Ons,“ vol. 2009, no. December, pp. 26–28, 2009.
- [31] M. Taiebat et al., „A review on energy, environmental, and sustainability implications of connected and automated vehicles,“ *Environmental Science and Technology*, vol. 52, no. 20, pp. 11449–11465, 2018, DOI: 10.1021/acs.est.8b00127.
- [32] J. H. Gawron et al., „Life Cycle Assessment of Connected and Automated Vehicles: Sensing and Computing Subsystem and Vehicle Level Effects,“ *Environmental Science and Technology*, vol. 52, no. 5, pp. 3249–3256, 2018, DOI: 10.1021/acs.est.7b04576.
- [33] Y. Chen and A. Meier, „Fuel consumption impacts of auto roof racks,“ *Energy Policy*, vol. 92, pp. 325–333, 2016, DOI: 10.1016/j.enpol.2016.02.031. Available: <http://dx.doi.org/10.1016/j.enpol.2016.02.031>.
- [34] F. Antonialli, „International benchmark on experimentations with Autonomous Shuttles for Collective Transport To cite this version : HAL Id : hal-02489797 International benchmark on experimentations with Autonomous Shuttles for Collective Transport,“ 2021.
- [35] L. Labriga and S. M. Bonnardel, „Autonomous Vehicles to Evolve to a New Urban Experience,“ no. 769033, pp. 1–72, 2020.
- [36] S. Francis. „Top 25 autonomous shuttle manufacturers,“ [Online]. Available: <https://roboticsandautomationnews.com/2020/10/15/top-25-autonomous-shuttle-manufacturers/37291/>.
- [37] LeddarTech. „The MILLA Group Selects the Leddar Pixell From LeddarTech for the MILLA POD Autonomous Shuttle,“ [Online]. Available: <https://www.globenewswire.com/news-release/2020/11/25/2133309/0/en/The-MILLA-Group-Selects-the-Leddar-Pixell-From-LeddarTech-for-the-MILLA-POD-Autonomous-Shuttle.html>.
- [38] C. Hampel. „NEVS presents electric robotaxi for sharing services,“ [Online]. Available: <https://www.electrive.com/2020/07/01/nevs-presents-electric-robotaxi-for-sharing-services/>.
- [39] Zoox. „Zoox vehicle brochure,“ [Online]. Available: <https://www.zoox.com/wp-content/uploads/zoox-vehicle-brochure-1.pdf>.
- [40] NAVYA. „Autonom Shuttle Evo,“ [Online]. Available: <https://navya.tech/wp-content/uploads/documents/Brochure-Autonom-Shuttle-Evo-EN.pdf>.
- [41] R. A. University. „UNICARagil news,“ [Online]. Available: https://www.unicaragil.de/images/medien/news/NewsletterHZE_07-2020_DE.pdf.
- [42] Rostec. „KAMAZ Demonstrates 'Shuttle' Unmanned Minibuses,“ [Online]. Available: <https://rostec.ru/en/news/4518846/>.
- [43] 2getthere. „GRT Vehicle: Automated Minibus,“ [Online]. Available: <https://www.2getthere.eu/technology/vehicle-types/grt-vehicle-automated-minibus/>.
- [44] Toyota. „Specially-Designed Toyota 'Tokyo 2020 Version' e-Palette to Provide Automated Mobility to Athletes,“ [Online]. Available: <https://global.toyota/en/newsroom/corporate/29933371.html>.
- [45] Apollo. „Apollo Minibus,“ [Online]. Available: <https://apollo.auto/minibus/index.html>.
- [46] P. Russo, „Olli,“ *Food Logistics*, no. 131, pp. 18–22, 2011. Available: <http://search.ebscohost.com/login.aspx?direct=true{\&}db=bth{\&}AN=65365095{\&}site=ehost-live>.

- [47] M. Matousek. „I rode in a self-driving shuttle in Times Square — and it showed what the early years of fully-autonomous vehicles might look like,“ [Online]. Available: <https://www.businessinsider.com/what-its-like-to-ride-in-a-self-driving-shuttle-2018-7>.
- [48] R. D. Roy. „Helping Create an Entire Autonomous Vehicles Eco-System – New Zealand’s Ohmio Automotion,“ [Online]. Available: <https://www.autofutures.tv/2021/03/16/helping-create-an-entire-autonomous-vehicles-eco-system-new-zealands-ohmio-automotion/>.
- [49] Easymile. „Shared Electric Driverless Shuttle,“ [Online]. Available: <https://transportation.ncsu.edu/wp-content/uploads/2019/12/New-Brochure-Gen-3-light.pdf>.
- [50] LOHRGroup. „The new autonomous,electric and accessible shuttle,“ [Online]. Available: <https://lohr.fr/lohruploads/2018/09/2018-07-plaquette-i-cristal-gb.pdf>.
- [51] Sensible4. „GACHA AUTONOMOUS SHUTTLE BUS,“ [Online]. Available: <https://sensible4.fi/gacha/>.
- [52] Westfield. „Our Products - the pod,“ [Online]. Available: <https://westfieldavs.com/westfield-pod/>.
- [53] H. Electric and A. Transportation, „HEAT – Hamburg Electric Autonomous Transportation Presse-Information – Ergänzung HEAT – Hamburg Electric Autonomous Transportation,“ pp. 1–8, 2019.
- [54] P. Dannecker, „Delivering safety.“ *Occupational health & safety (Waco, Tex.)* vol. 77, no. 9, 2008.
- [55] A. Wong. „KFC deploys autonomous 5G ‘food trucks’ in China,“ [Online]. Available: <https://soyacincau.com/2020/11/18/kfc-autonomous-5g-restaurant-on-wheels-china/>.
- [56] A. J. Hawkins. „Intel’s Mobileye will launch a fully driverless delivery service in 2023,“ [Online]. Available: <https://www.theverge.com/2021/4/12/22375759/intel-mobileye-udelv-autonomous-vehicle-delivery-2023>.
- [57] M. E. Gleason, „Detailed analysis of the bluff body blockage phenomenon in closed wall wind tunnels utilizing CFD,“ *SAE Technical Papers*, vol. 2007, no. 724, pp. 776–790, 2007, DOI: 10.4271/2007-01-1046.
- [58] G. E. Karniadakis and J. A. T. Machado, „Numerical methods,“ *Numerical Methods*, pp. 1–349, 2019, ISBN: 9783110571684. DOI: 10.1515/9783110571684.
- [59] Velodyne, „Datasheet Velodyne Ultra Puck,“ *Soviet Powder Metallurgy and Metal Ceramics*, vol. 6, no. 12, pp. 964–968, 1967.
- [60] Velodyne, „Velodyne Alpha Prime,“ pp. 5–6, 2019, ISBN: 1202440002.
- [61] S. Wordley and J. Saunders, „On-road Turbulence,“ *SAE Technical Papers*, no. 2007, 2008, DOI: 10.4271/2008-01-0475.

Appendix

- A Appendix 1: Aerodynamic report of reference geometryxxv
- B Appendix 2: Aerodynamic report of design iterationsxxix
- C Appendix 3: Aerodynamic report of single sensor positions xli
- D Appendix 4: Aerodynamic report of sensor layoutslxxxvii
- E Appendix 5: Content of the attached SD card ciii

A Appendix 1: Aerodynamic report of reference geometry

The structure of the aerodynamic report is depicted in Figure A.1.

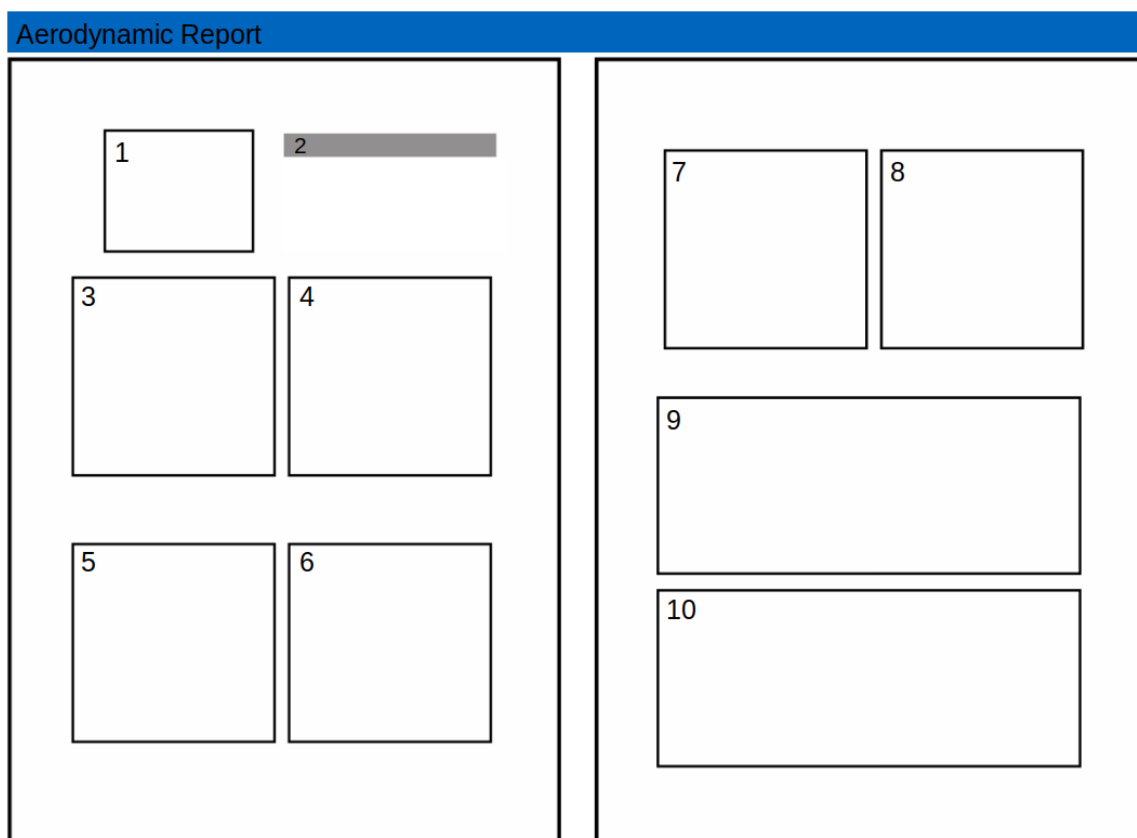
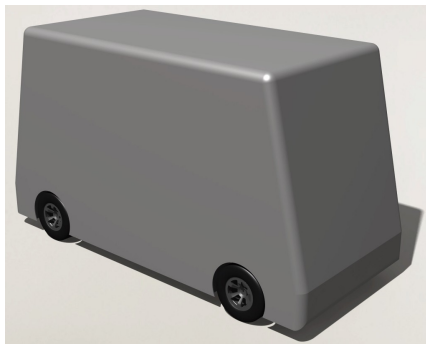


Figure A.1: C_d impact of the sensor position

The description of the items found in the report follows:

- 1: Render of the geometry.
- 2: Description of the simulation: Generic shuttle.
- 3 & 4: Front and rear isometric view of the pressure coefficient (C_p).
- 5 & 6: Front and rear isometric view of the isosurface $q = 2000 \text{ s}^{-2}$.
- 7 & 8: Front and rear isometric view of the shear velocity magnitude (u_τ).
- 9: Side isometric view of the isosurface vorticity magnitude $|\omega| = 10 \text{ s}^{-1}$.
- 10: Side view symmetry plane of the velocity magnitude.



Generic shuttle

Figure A.2: Render of the generic shuttle

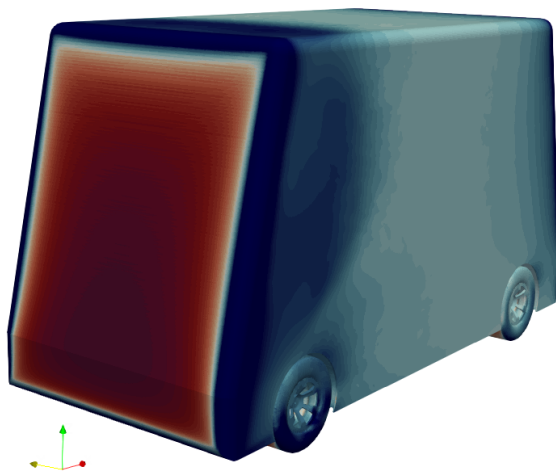
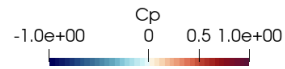
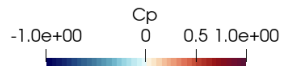


Figure A.3: Front isometric view of the C_p of the generic shuttle

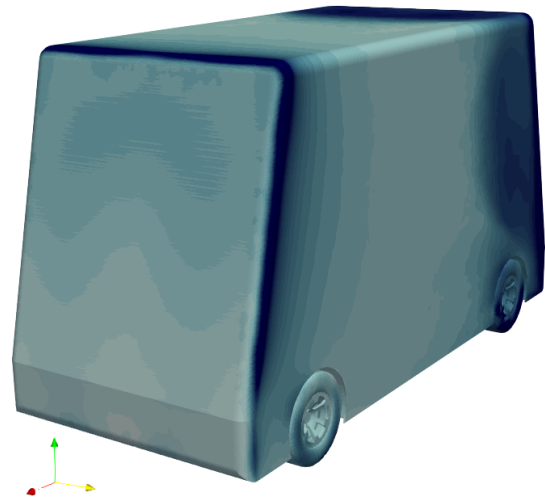


Figure A.4: Rear isometric view of the C_p of the generic shuttle

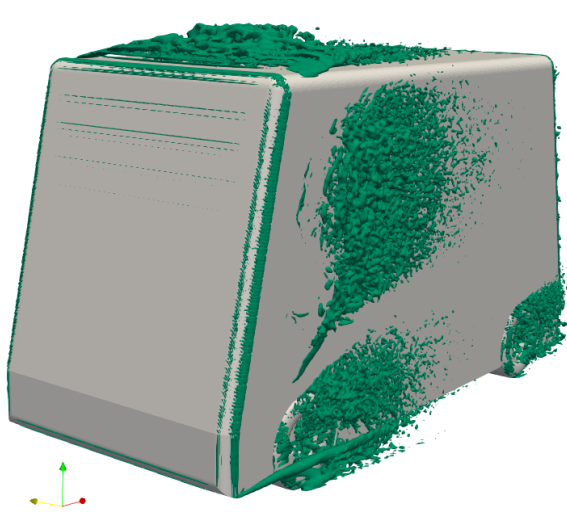


Figure A.5: Front isometric view of the Q-criteria (value $q = 2000 \text{ s}^{-2}$) of the generic shuttle

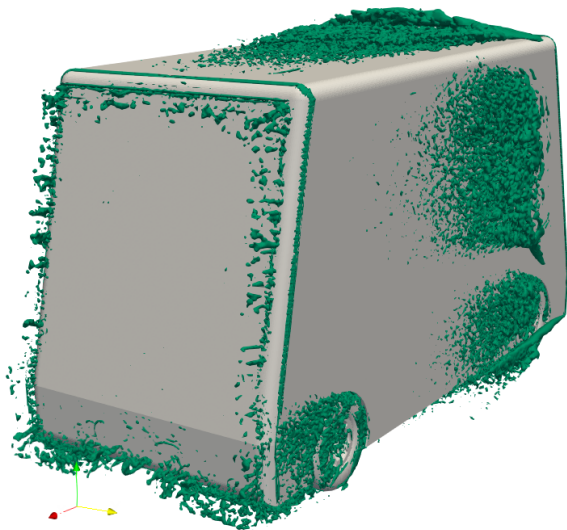


Figure A.6: Rear isometric view of the Q-criteria (value $q = 2000 \text{ s}^{-2}$) of the generic shuttle

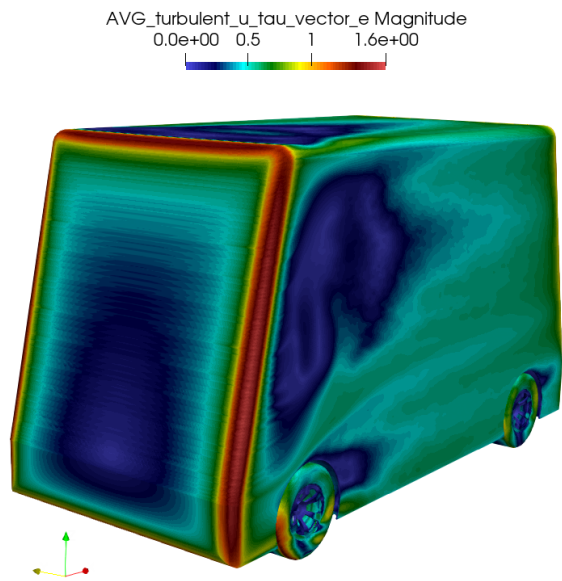


Figure A.7: Front isometric view of the u_τ of the generic shuttle

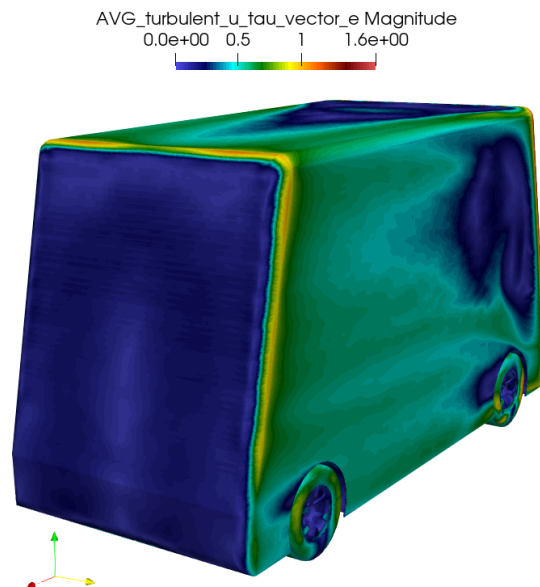


Figure A.8: Rear isometric view of the u_τ of the generic shuttle

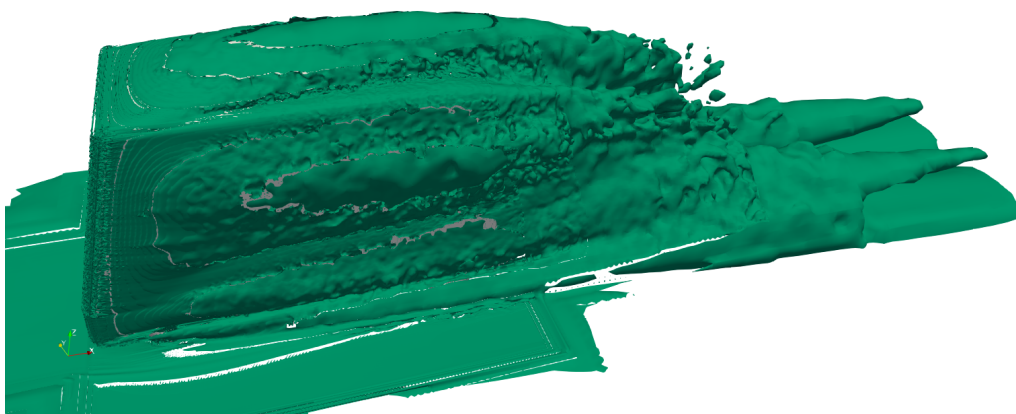


Figure A.9: Side view of the vorticity (value $|\omega| = 10 \text{ s}^{-1}$) of the generic shuttle

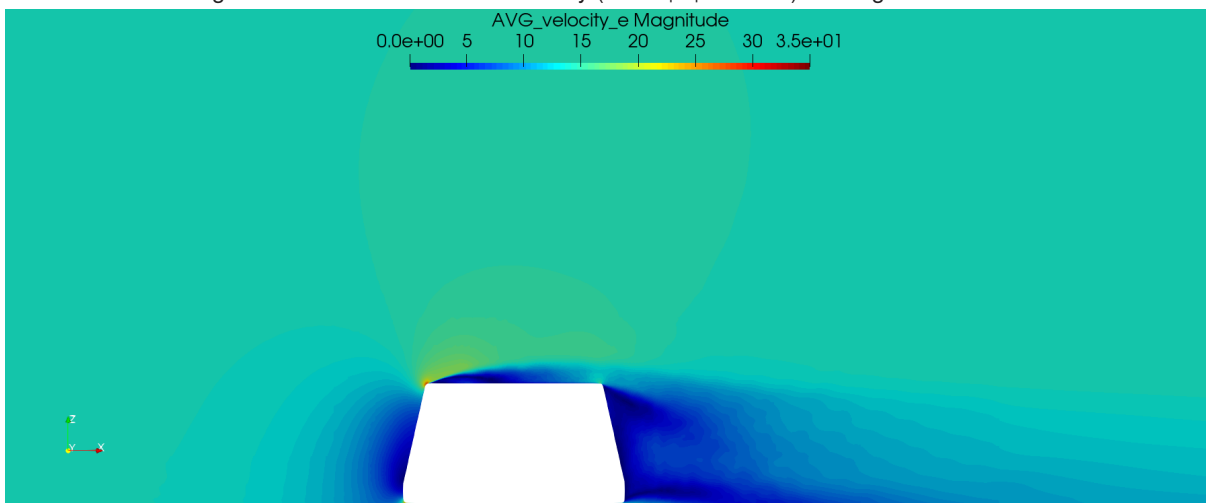


Figure A.10: Side view symmetry plane of the velocity magnitude of the generic shuttle

B Appendix 2: Aerodynamic report of design iterations

Differently to the generic shuttle, the structure of the aerodynamic report of design iterations includes a table to track the geometry changes and the drag coefficient delta. This is depicted in Figure B.1.

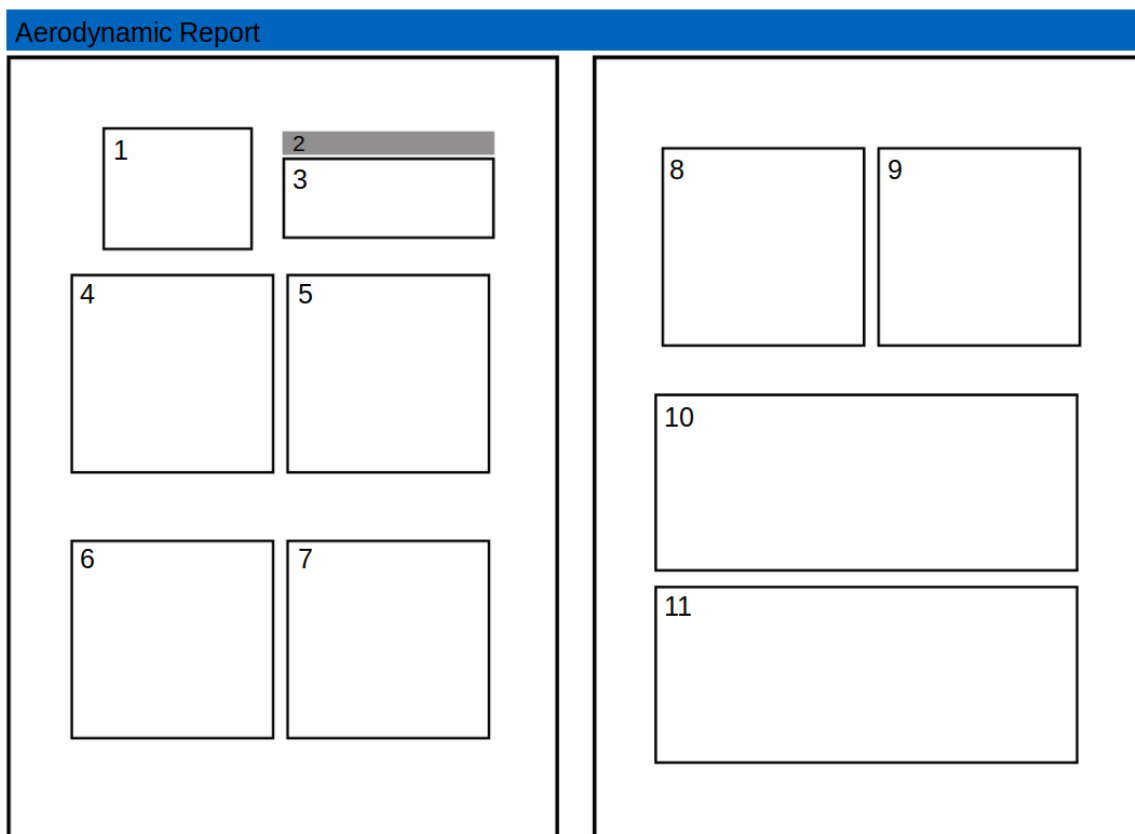


Figure B.1: C_d impact of the sensor position

The description of the reorganized items of the aerodynamic report follows:

- 1: Render of the geometry.
- 2: Description of the simulation modification.
- 3: Table with geometry description and ΔC_d
- 4 & 5: Front and rear isometric view of the pressure coefficient (C_p).
- 6 & 7: Front and rear isometric view of the isosurface $q = 2000 \text{ s}^{-2}$.
- 8 & 9: Front and rear isometric view of the shear velocity magnitude (u_τ).

10: Side isometric view of the isosurface vorticity magnitude $|\omega| = 10 \text{ s}^{-1}$.

11: Side view symmetry plane of the velocity magnitude.

The included simulations are:

- Windshield at 67.8° .
- Windshield at 88.65° .
- Edge rounding of 0 mm.
- Edge rounding of 197.8 mm.
- Closed wheel profile.

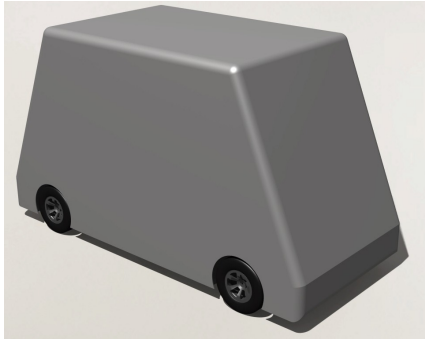


Figure B.2: Render of design modification: windshield at 67.8°

Design modification: **windshield at 67.8°**

Table B.1: Data table of design modification: windshield at 67.8°

| Design modification | Windshield at 67.8° |
|---------------------|---------------------|
| ΔC_d | -5 |

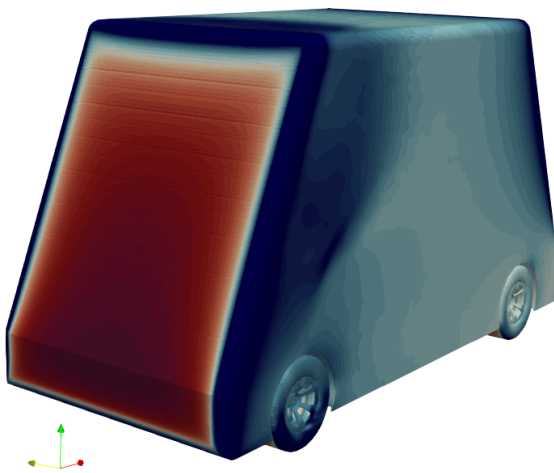
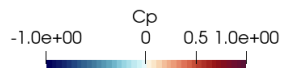


Figure B.3: Front isometric view of the C_p of design modification: windshield at 67.8°

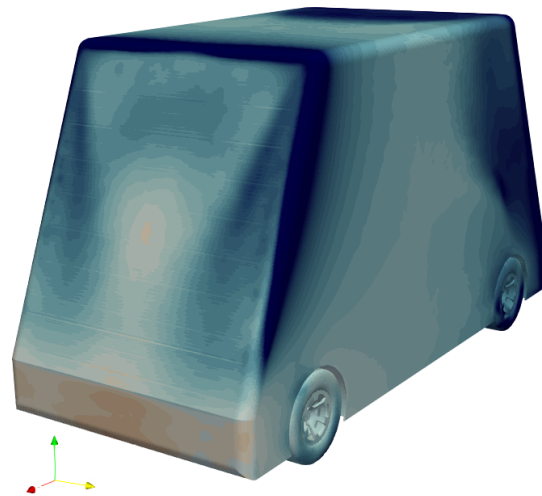
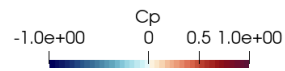


Figure B.4: Rear isometric view of the C_p of design modification: windshield at 67.8°

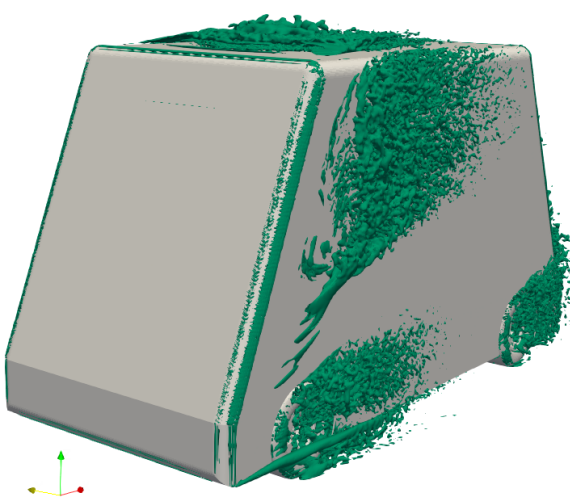


Figure B.5: Front isometric view of the Q-criteria (value $q = 2000 \text{ s}^{-2}$) of design modification: windshield at 67.8°

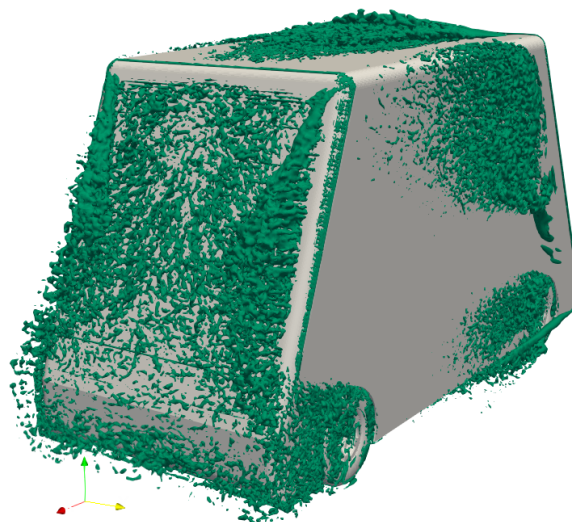


Figure B.6: Rear isometric view of the Q-criteria (value $q = 2000 \text{ s}^{-2}$) of design modification: windshield at 67.8°

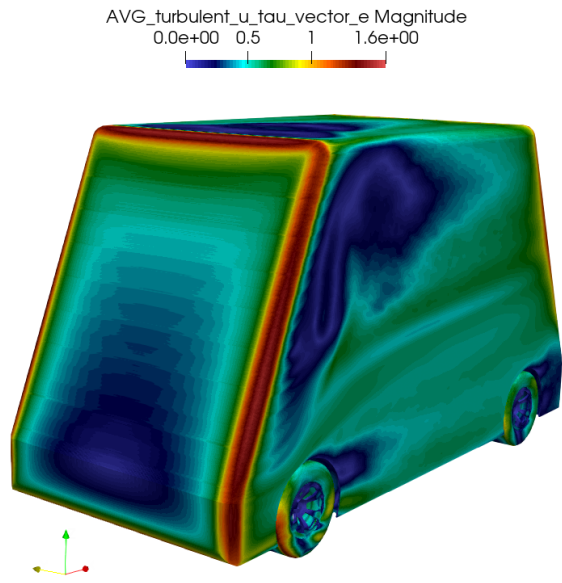


Figure B.7: Front isometric view of the u_τ of design modification: windshield at 67.8°

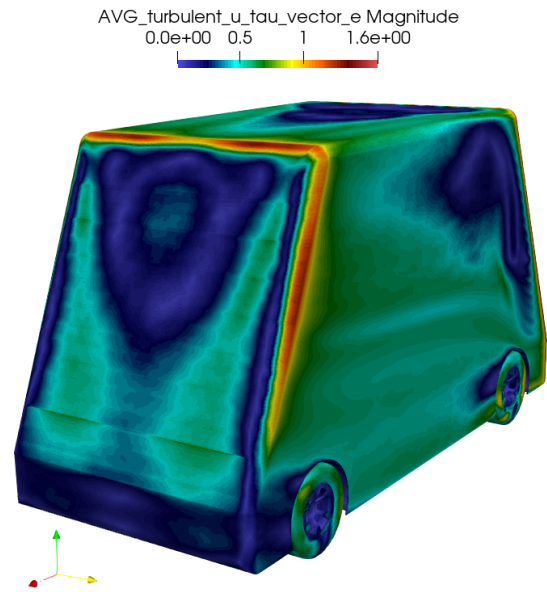


Figure B.8: Rear isometric view of the u_τ of design modification: windshield at 67.8°

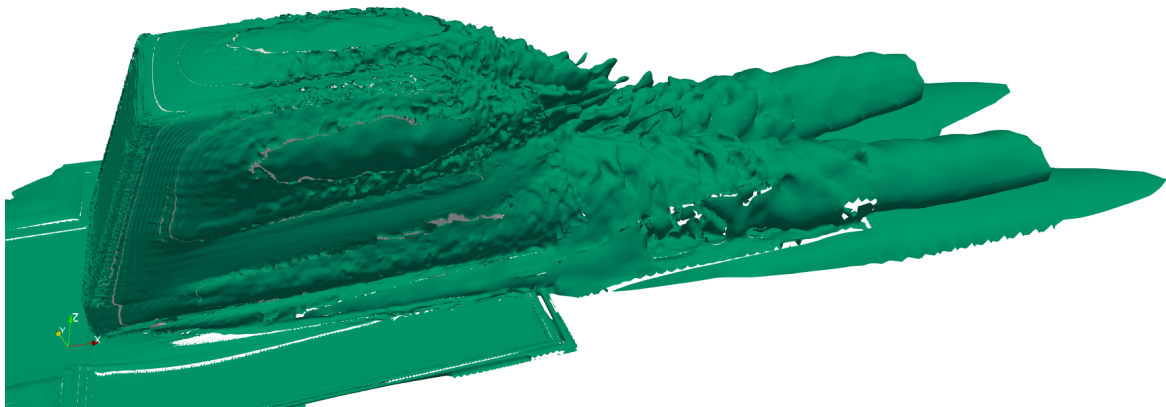


Figure B.9: Side view of the vorticity (value $|\omega| = 10 \text{ s}^{-1}$) of design modification: windshield at 67.8°

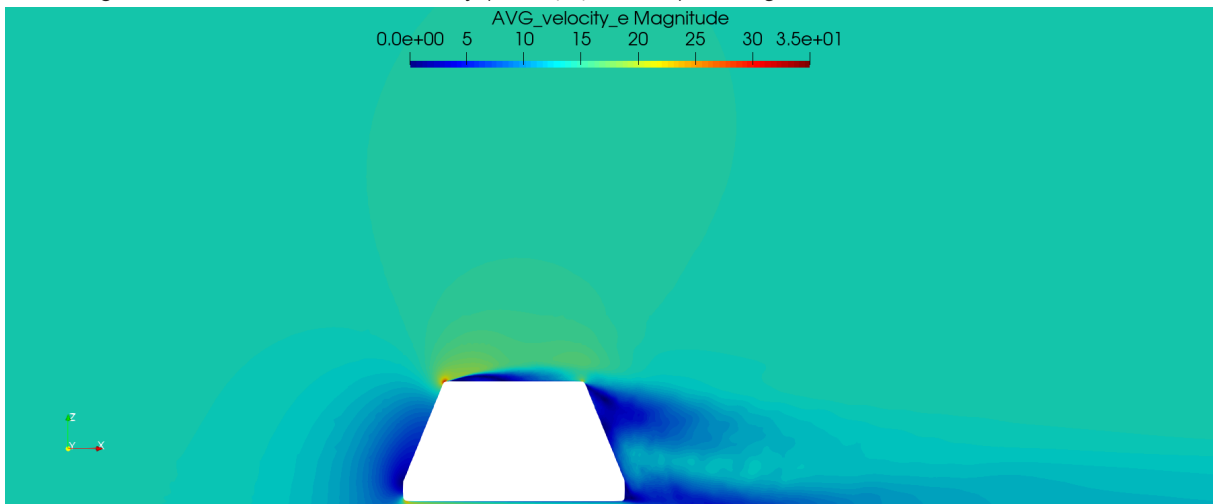


Figure B.10: Side view symmetry plane of the velocity magnitude of design modification: windshield at 67.8°

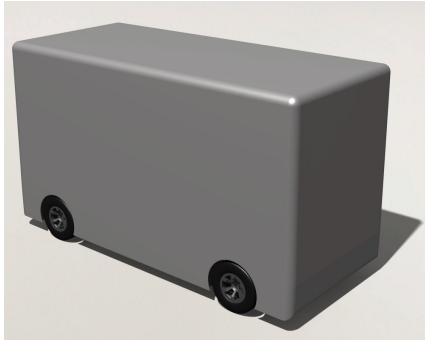


Figure B.11: Render of design modification: windshield at 88.65°

Design modification: **windshield at 88.65°**

Table B.2: Data table of design modification: windshield at 88.65°

| Design modification | Windshield at 88.65° |
|---------------------|----------------------|
| ΔC_d | 16 |

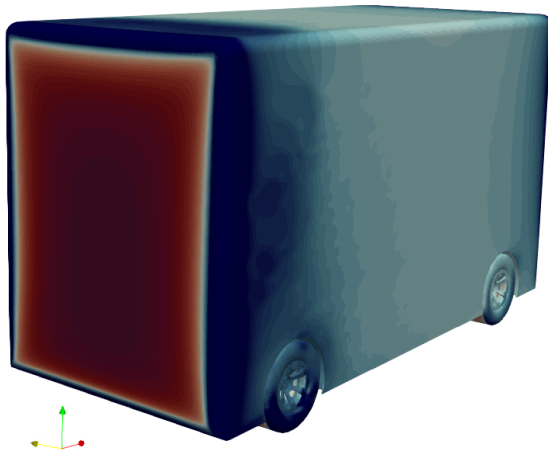
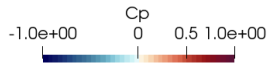


Figure B.12: Front isometric view of the C_p of design modification: windshield at 88.65°

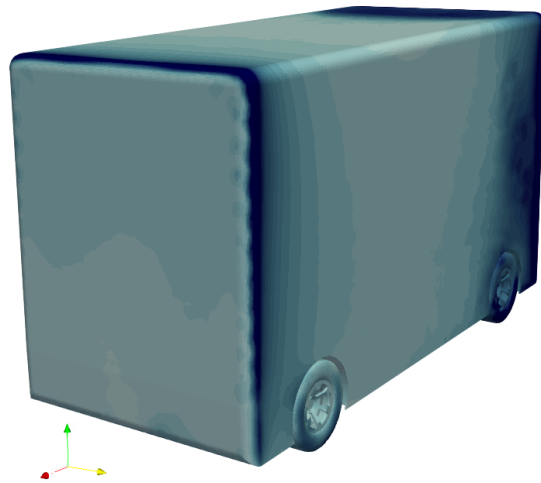
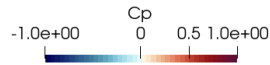


Figure B.13: Rear isometric view of the C_p of design modification: windshield at 88.65°

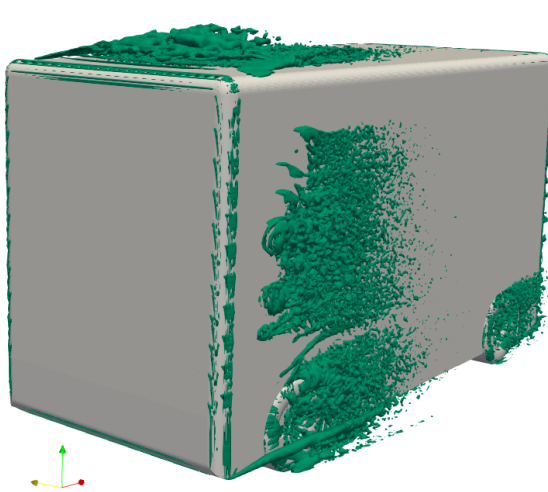


Figure B.14: Front isometric view of the Q-criteria (value $q = 2000 \text{ s}^{-2}$) of design modification: windshield at 88.65°

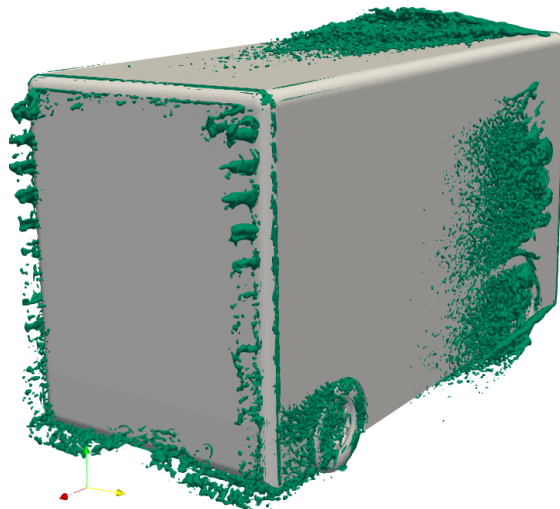


Figure B.15: Rear isometric view of the Q-criteria (value $q = 2000 \text{ s}^{-2}$) of design modification: windshield at 88.65°

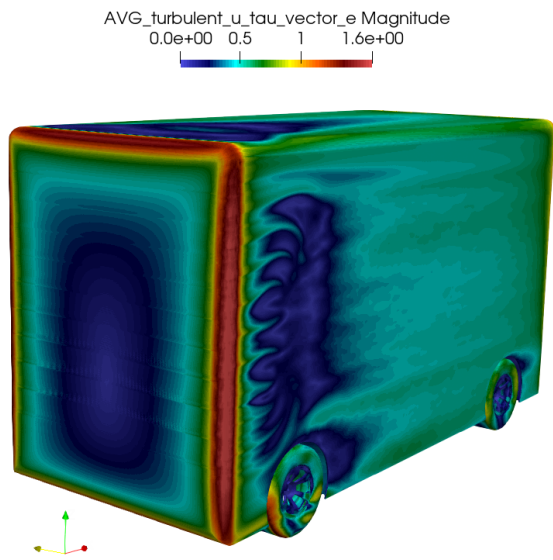


Figure B.16: Front isometric view of the u_τ of design modification: windshield at 88.65°

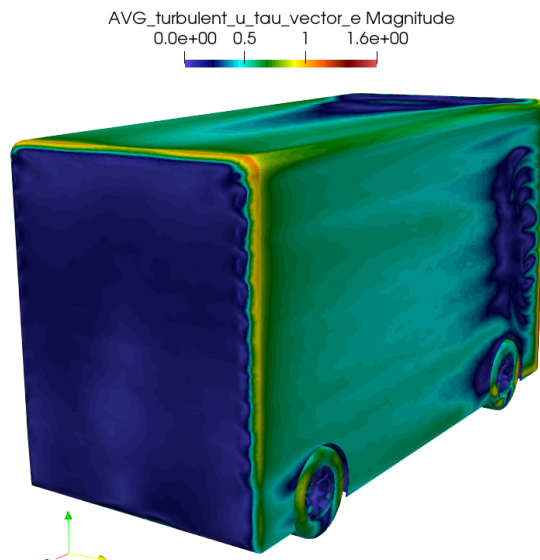


Figure B.17: Rear isometric view of the u_τ of design modification: windshield at 88.65°

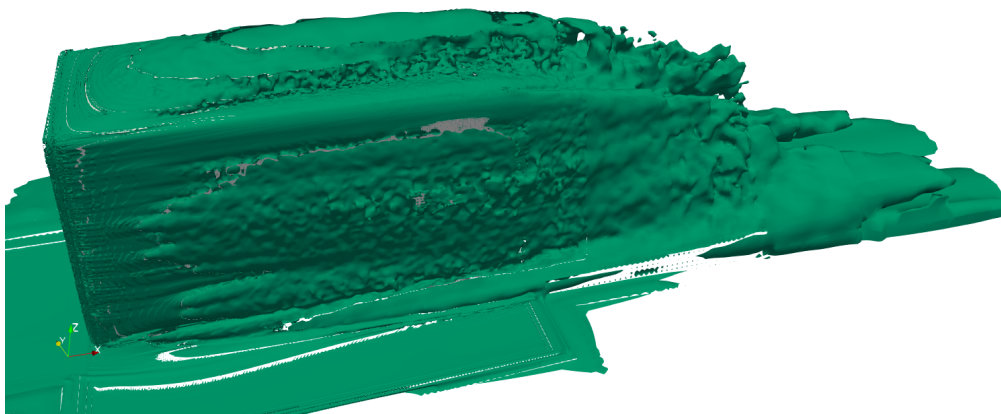


Figure B.18: Side view of the vorticity (value $|\omega| = 10 \text{ s}^{-1}$) of design modification: windshield at 88.65°

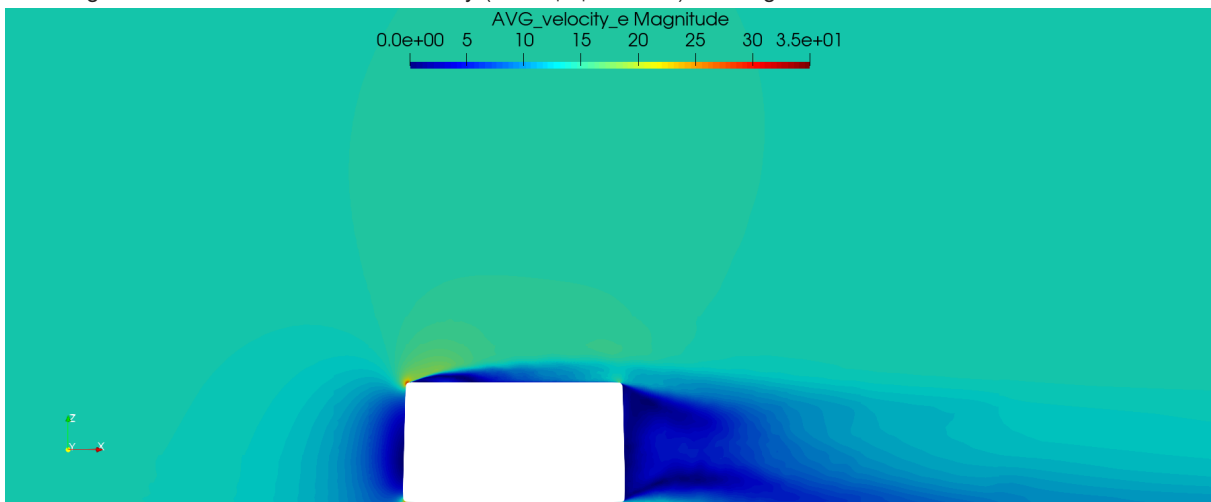


Figure B.19: Side view symmetry plane of the velocity magnitude of design modification: windshield at 88.65°

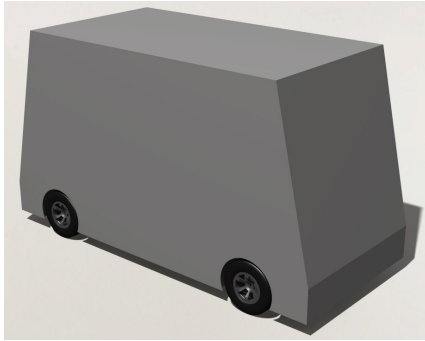


Figure B.20: Render of design modification: rounding of 0mm

Design modification: **rounding of 0mm**

Table B.3: Data table of design modification: rounding of 0mm

| Design modification | Rounding of 0mm |
|---------------------|-----------------|
| ΔC_d | 198 |

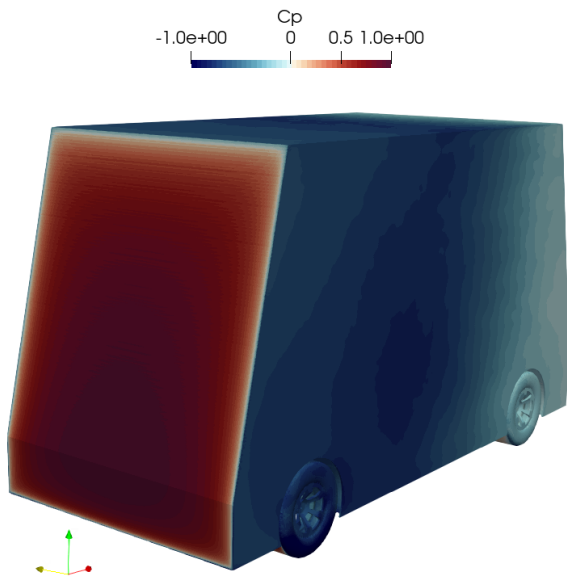


Figure B.21: Front isometric view of the C_p of design modification: rounding of 0mm

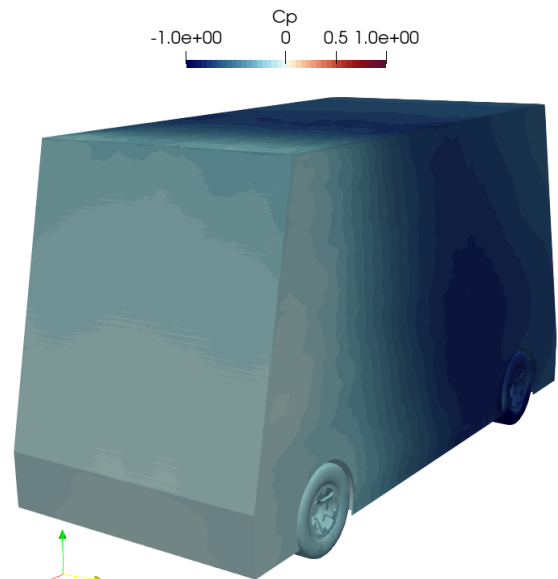


Figure B.22: Rear isometric view of the C_p of design modification: rounding of 0mm

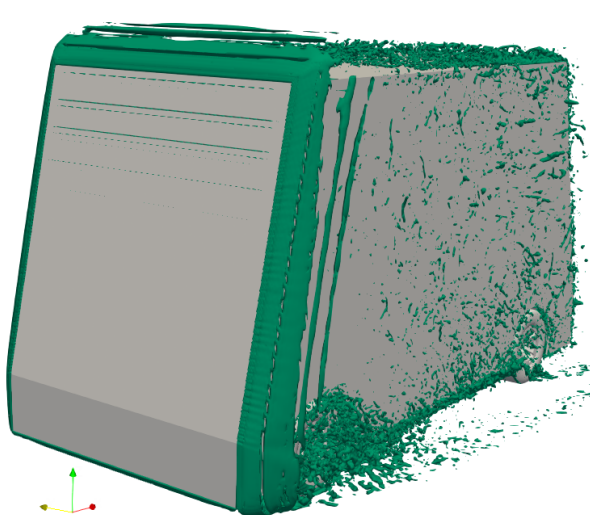


Figure B.23: Front isometric view of the Q-criteria (value $q = 2000 \text{ s}^{-2}$) of design modification: rounding of 0mm

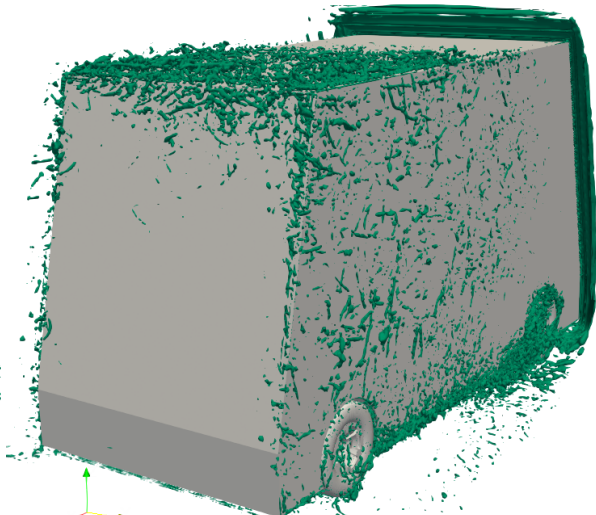


Figure B.24: Rear isometric view of the Q-criteria (value $q = 2000 \text{ s}^{-2}$) of design modification: rounding of 0mm

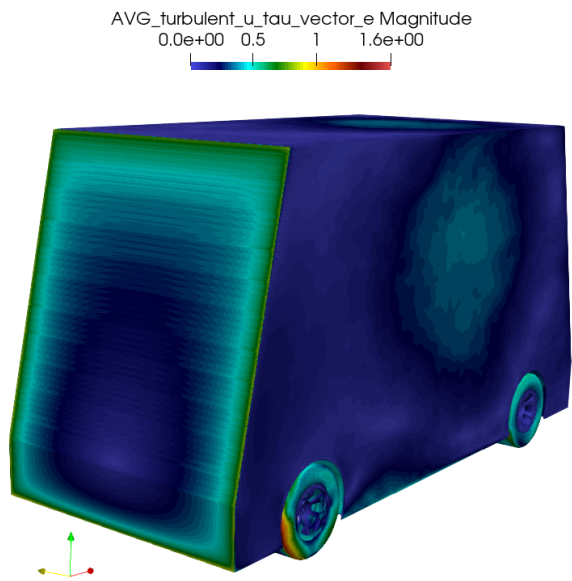


Figure B.25: Front isometric view of the u_τ of design modification: rounding of 0mm

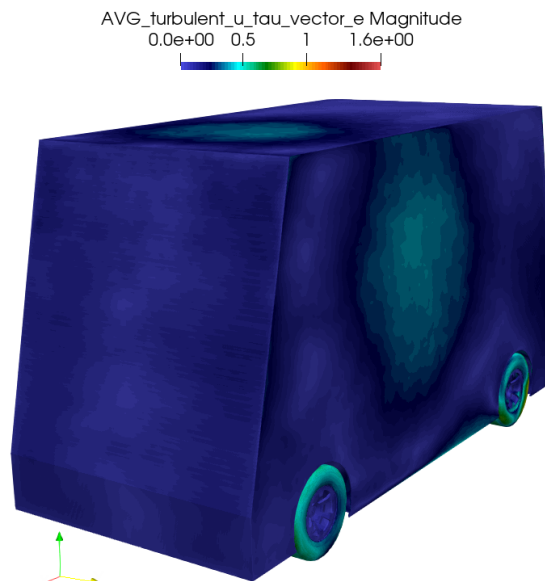


Figure B.26: Rear isometric view of the u_τ of design modification: rounding of 0mm

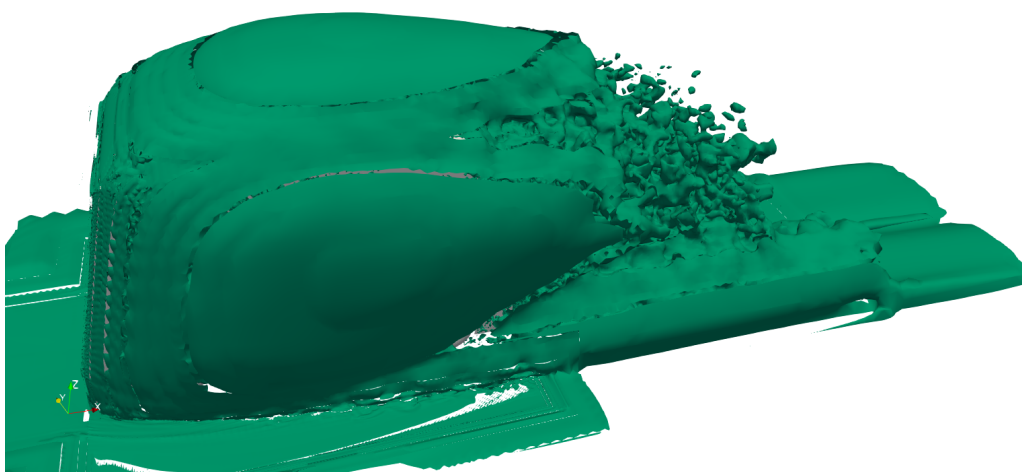


Figure B.27: Side view of the vorticity (value $|\omega| = 10 \text{ s}^{-1}$) of design modification: rounding of 0mm

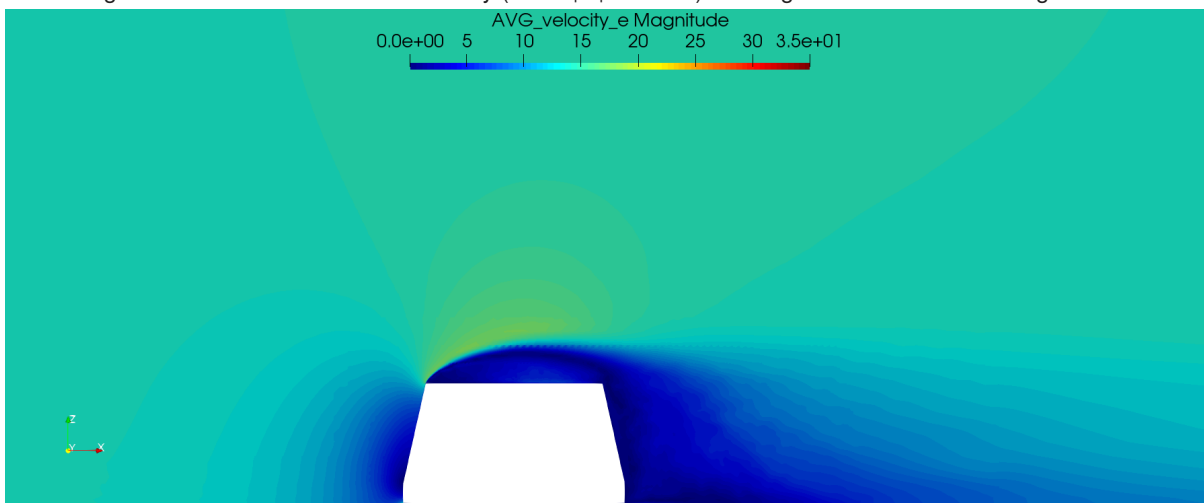


Figure B.28: Side view symmetry plane of the velocity magnitude of design modification: rounding of 0mm

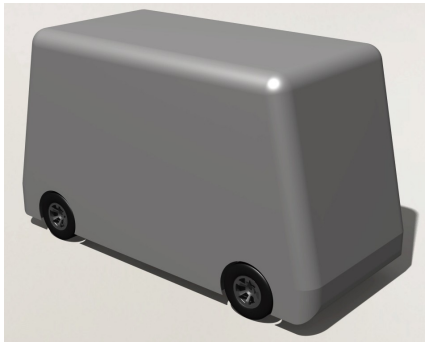


Figure B.29: Render of design modification: rounding of 197.8 mm

Design modification: rounding of 197.8 mm

Table B.4: Data table of design modification: rounding of 197.8 mm

| Design modification | Rounding of 197.8 mm |
|---------------------|----------------------|
| ΔC_d | -99 |

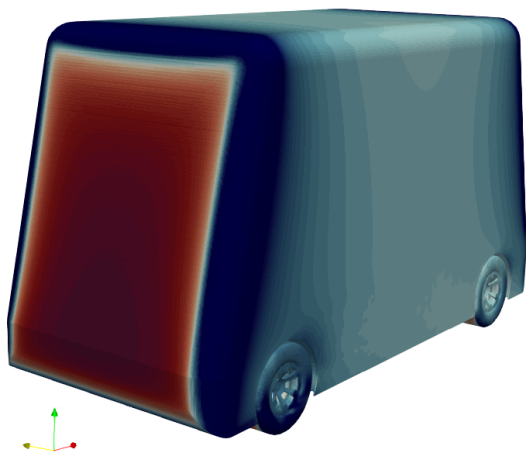
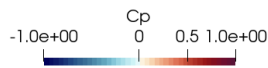


Figure B.30: Front isometric view of the C_p of design modification: rounding of 197.8 mm

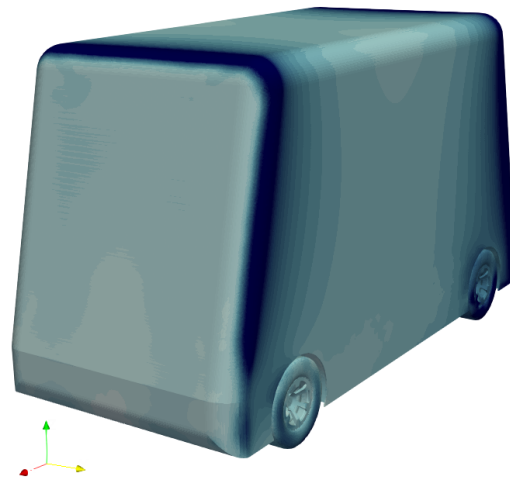
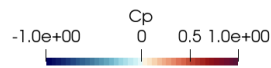


Figure B.31: Rear isometric view of the C_p of design modification: rounding of 197.8 mm

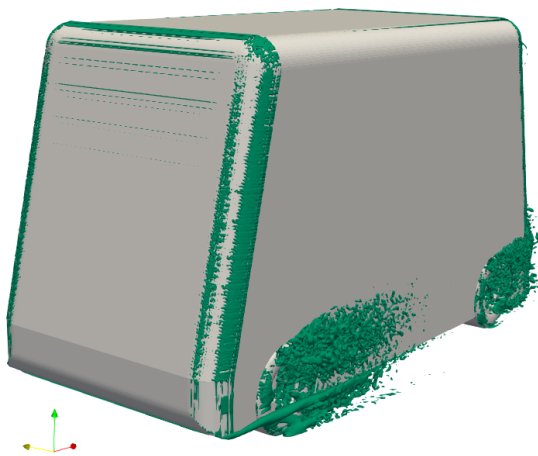


Figure B.32: Front isometric view of the Q-criteria (value $q = 2000 \text{ s}^{-2}$) of design modification: rounding of 197.8 mm

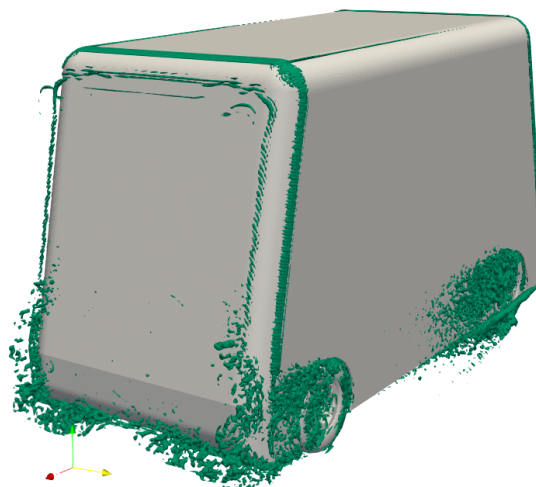


Figure B.33: Rear isometric view of the Q-criteria (value $q = 2000 \text{ s}^{-2}$) of design modification: rounding of 197.8 mm

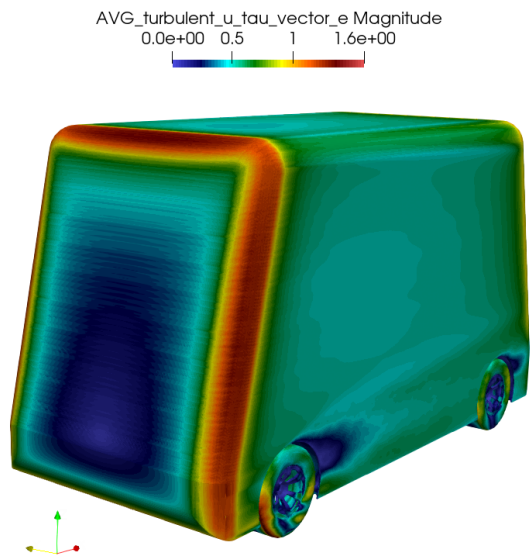


Figure B.34: Front isometric view of the u_τ of design modification: rounding of 197.8 mm

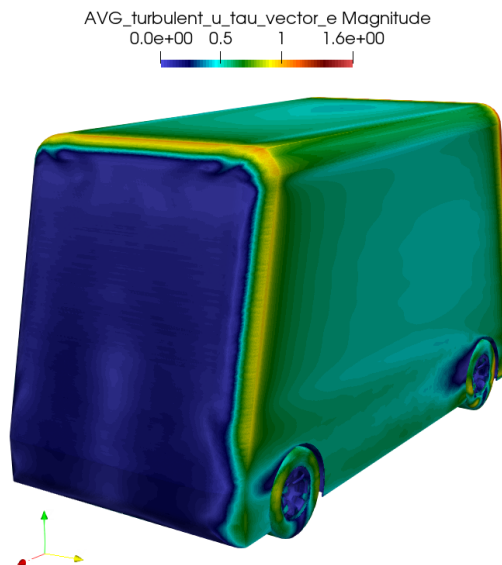


Figure B.35: Rear isometric view of the u_τ of design modification: rounding of 197.8 mm



Figure B.36: Side view of the vorticity (value $|\omega| = 10 \text{ s}^{-1}$) of design modification: rounding of 197.8 mm

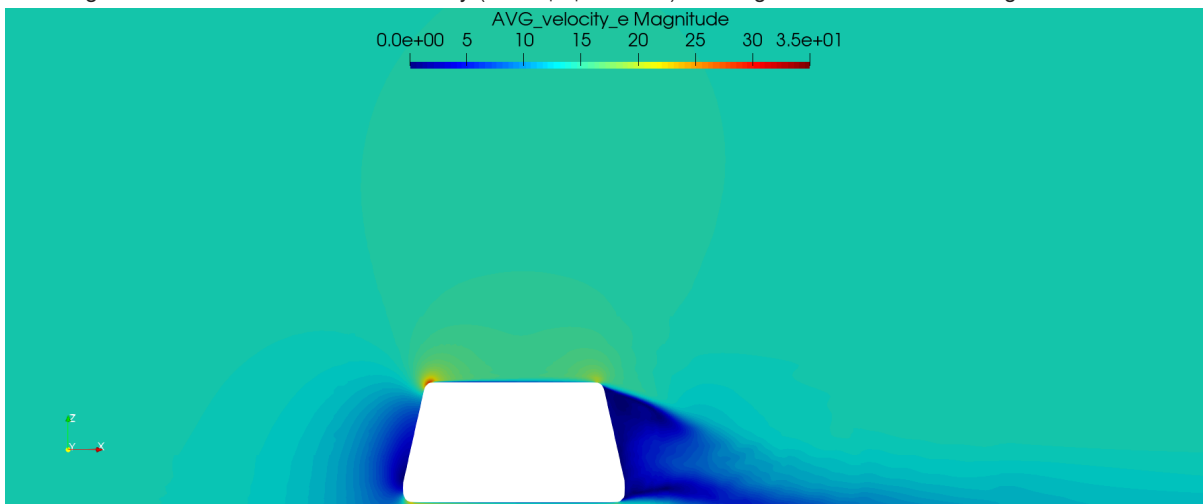


Figure B.37: Side view symmetry plane of the velocity magnitude of design modification: rounding of 197.8 mm

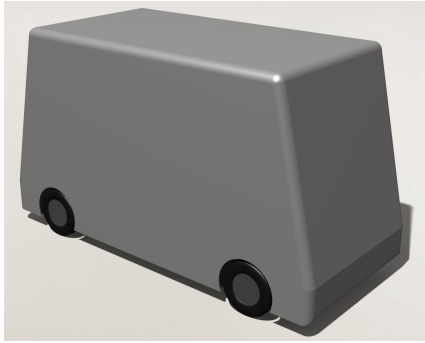


Figure B.38: Render of design modification: closed wheels

Design modification: **closed wheels**

Table B.5: Data table of design modification: closed wheels

| Design modification | Closed wheels |
|---------------------|---------------|
| ΔC_d | -7 |

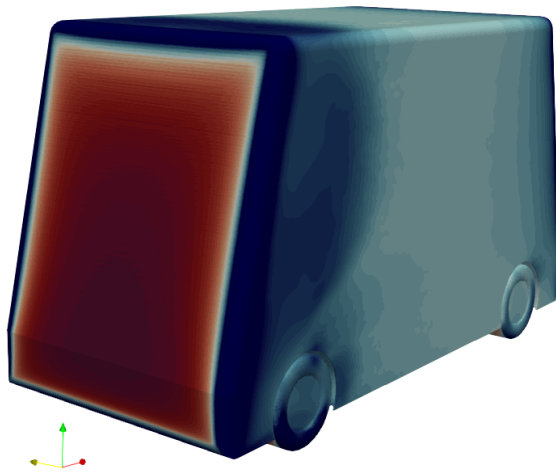
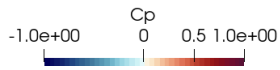


Figure B.39: Front isometric view of the C_p of design modification: closed wheels

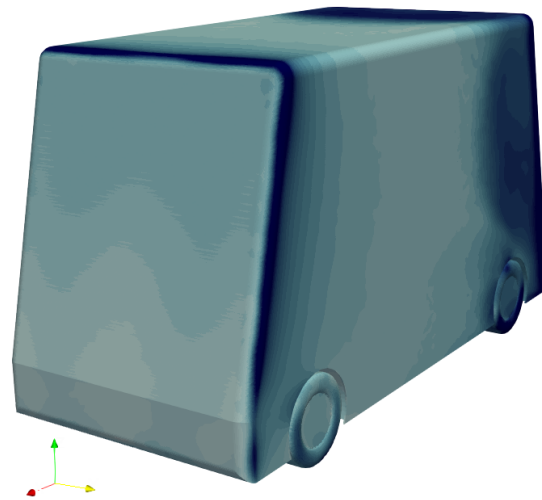
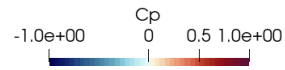


Figure B.40: Rear isometric view of the C_p of design modification: closed wheels

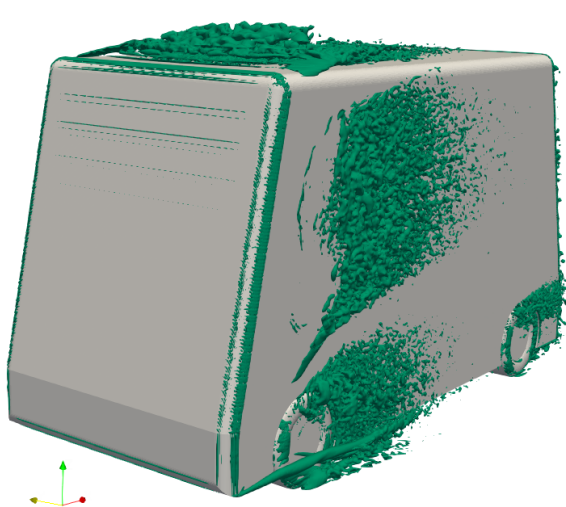


Figure B.41: Front isometric view of the Q-criteria (value $q = 2000 \text{ s}^{-2}$) of design modification: closed wheels

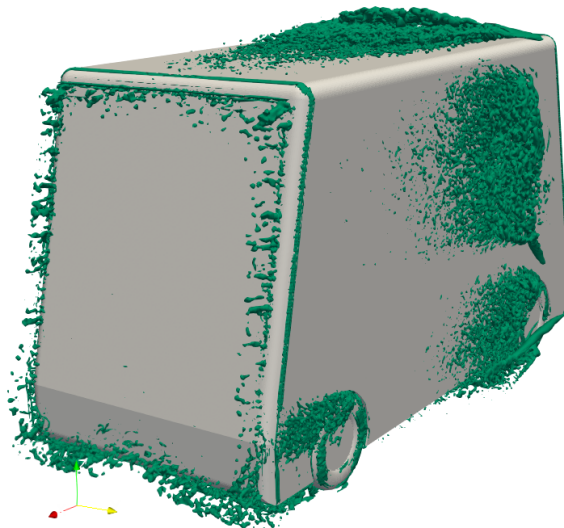


Figure B.42: Rear isometric view of the Q-criteria (value $q = 2000 \text{ s}^{-2}$) of design modification: closed wheels

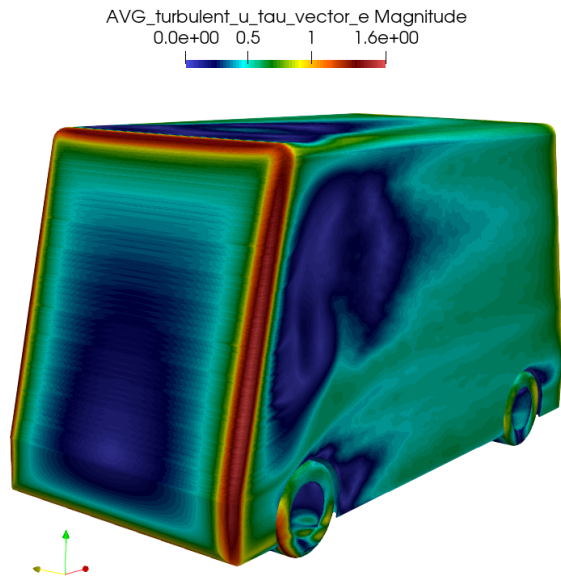


Figure B.43: Front isometric view of the u_{τ} of design modification: closed wheels

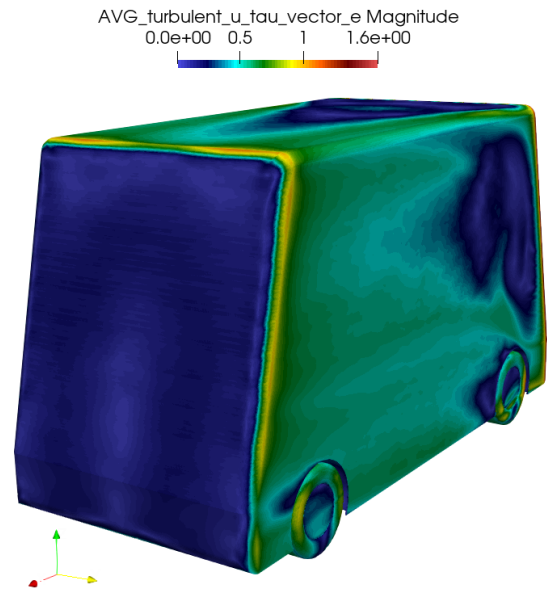


Figure B.44: Rear isometric view of the u_{τ} of design modification: closed wheels

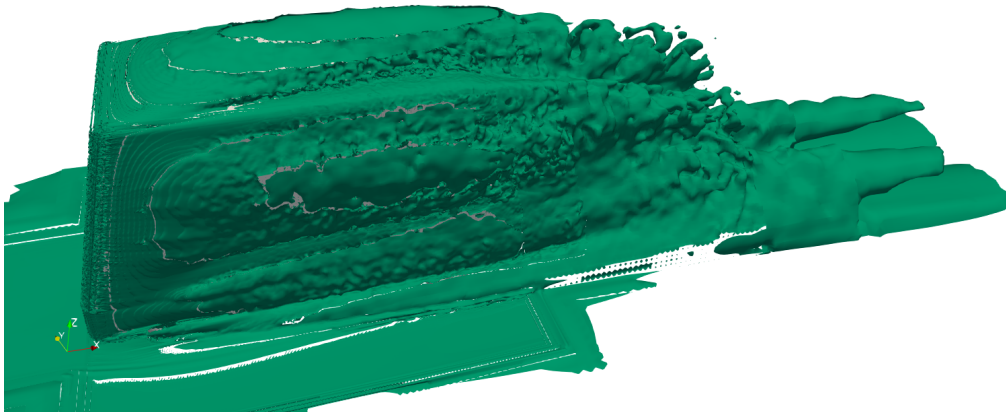


Figure B.45: Side view of the vorticity (value $|\omega| = 10 \text{ s}^{-1}$) of design modification: closed wheels

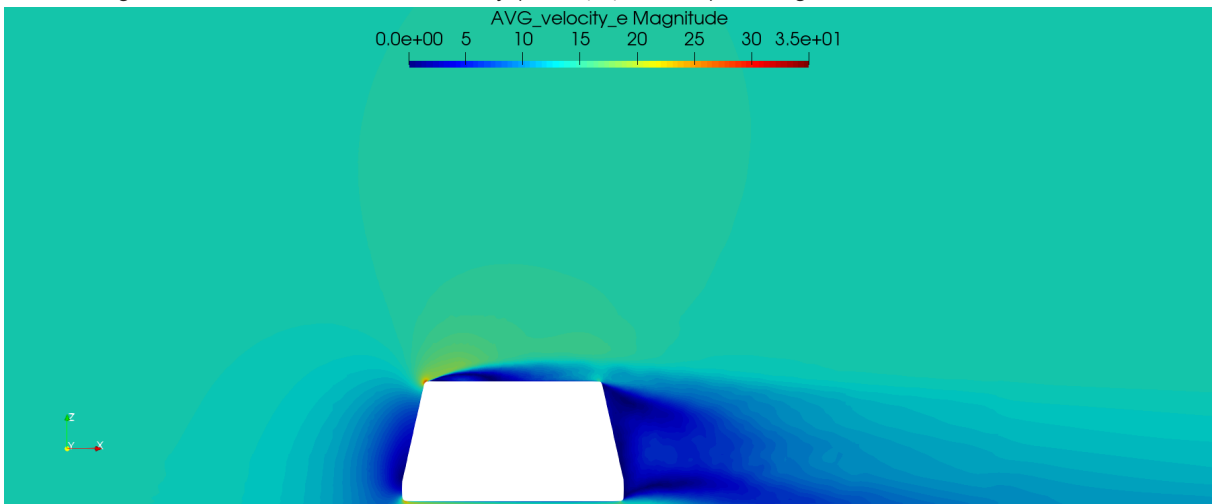


Figure B.46: Side view symmetry plane of the velocity magnitude of design modification: closed wheels

C Appendix 3: Aerodynamic report of single sensor positions

The structure of the aerodynamic report is the same as in the design iterations (Figure B.1). The included simulations are:

- Sensor position a and type small puck. Code: a_puckSMALL.
- Sensor position a and type big puck. Code: a_puckBIG.
- Sensor position a and type small box. Code: a_boxSMALL.
- Sensor position a and type big box. Code: a_boxBIG.
- Sensor position b and type small puck. Code: b_puckSMALL.
- Sensor position b and type big puck. Code: b_puckBIG.
- Sensor position c and type small puck. Code: c_puckSMALL.
- Sensor position c and type big puck. Code: c_puckBIG.
- Sensor position d and type small puck. Code: d_puckSMALL.
- Sensor position d and type big puck. Code: d_puckBIG.
- Sensor position f and type small puck. Code: f_puckSMALL.
- Sensor position f and type big puck. Code: f_puckBIG.
- Sensor position g and type small puck. Code: g_puckSMALL.
- Sensor position g and type big puck. Code: g_puckBIG.
- Sensor position h and type small puck. Code: h_puckSMALL.
- Sensor position h and type big puck. Code: h_puckBIG.
- Sensor position i and type small puck. Code: i_puckSMALL.
- Sensor position i and type big puck. Code: i_puckBIG.
- Sensor position k and type small puck. Code: k_puckSMALL.
- Sensor position k and type big puck. Code: k_puckBIG.
- Sensor position l and type small puck. Code: l_puckSMALL.
- Sensor position l and type big puck. Code: l_puckBIG.

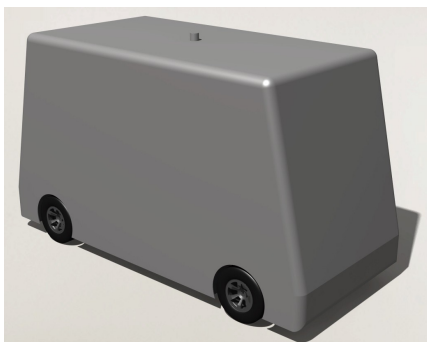


Figure C.1: Render of sensor position *a* and type small puck

Sensor position *a* and type small puck

Table C.1: Data table of sensor position *a* and type small puck

| | |
|-----------------|------------|
| Sensor position | <i>a</i> |
| Sensor type | small puck |
| ΔC_d | -9 |

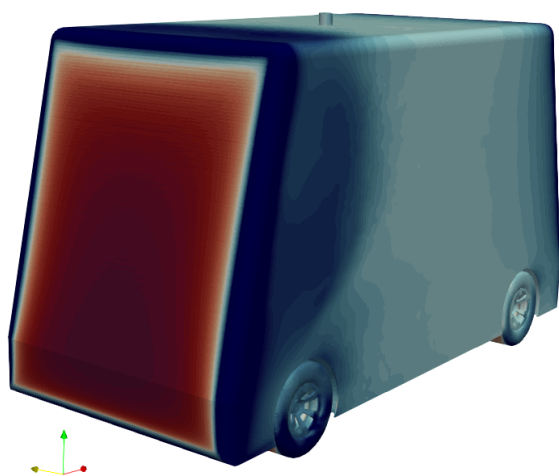


Figure C.2: Front isometric view of the C_p of sensor position *a* and type small puck

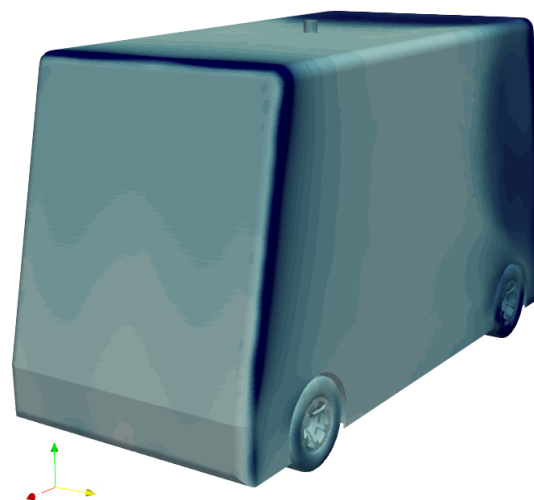


Figure C.3: Rear isometric view of the C_p of sensor position *a* and type small puck

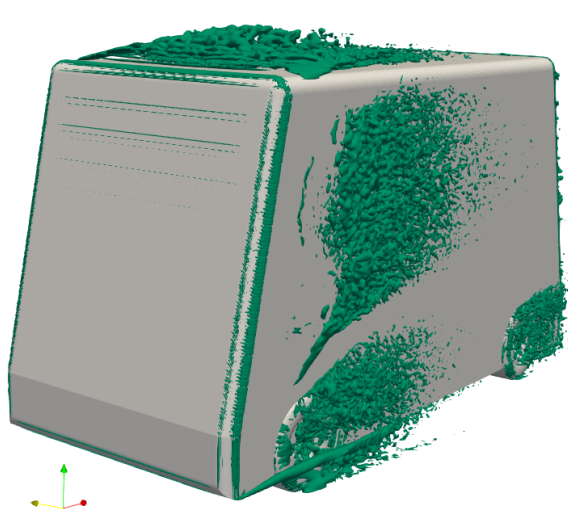


Figure C.4: Front isometric view of the Q-criteria (value $q = 2000 \text{ s}^{-2}$) of sensor position *a* and type small puck



Figure C.5: Rear isometric view of the Q-criteria (value $q = 2000 \text{ s}^{-2}$) of sensor position *a* and type small puck

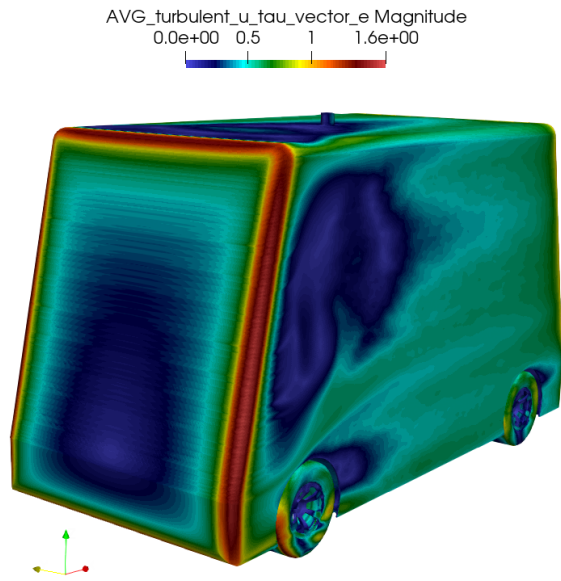


Figure C.6: Front isometric view of the u_τ of sensor position a and type small puck

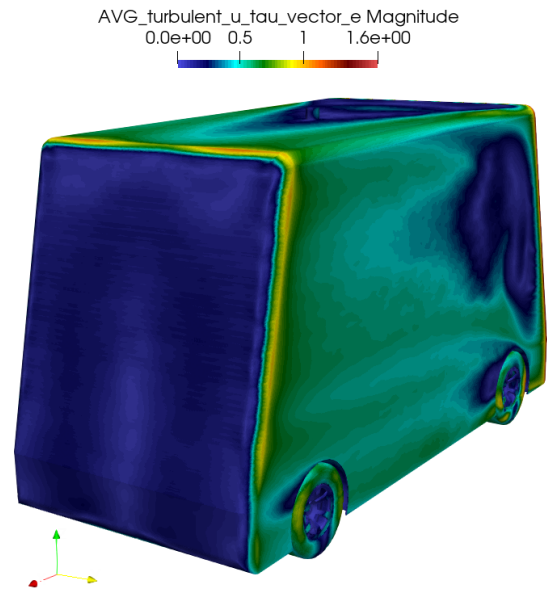


Figure C.7: Rear isometric view of the u_τ of sensor position a and type small puck

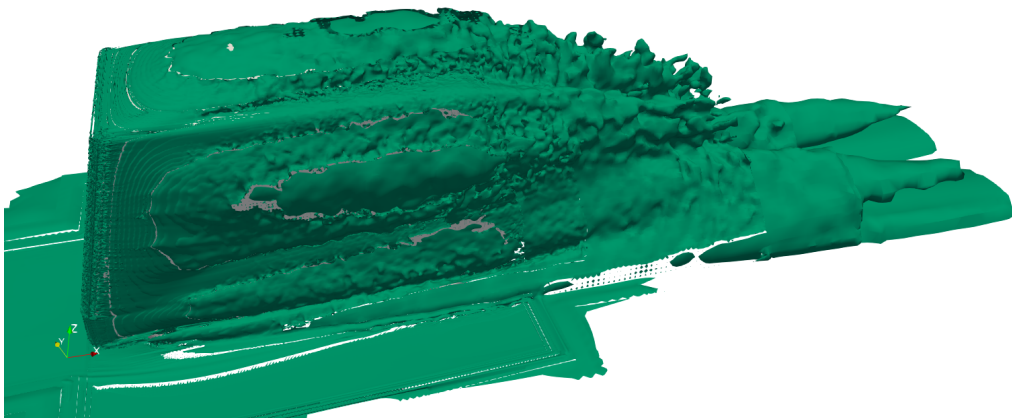


Figure C.8: Side view of the vorticity (value $|\omega| = 10 \text{ s}^{-1}$) of sensor position a and type small puck

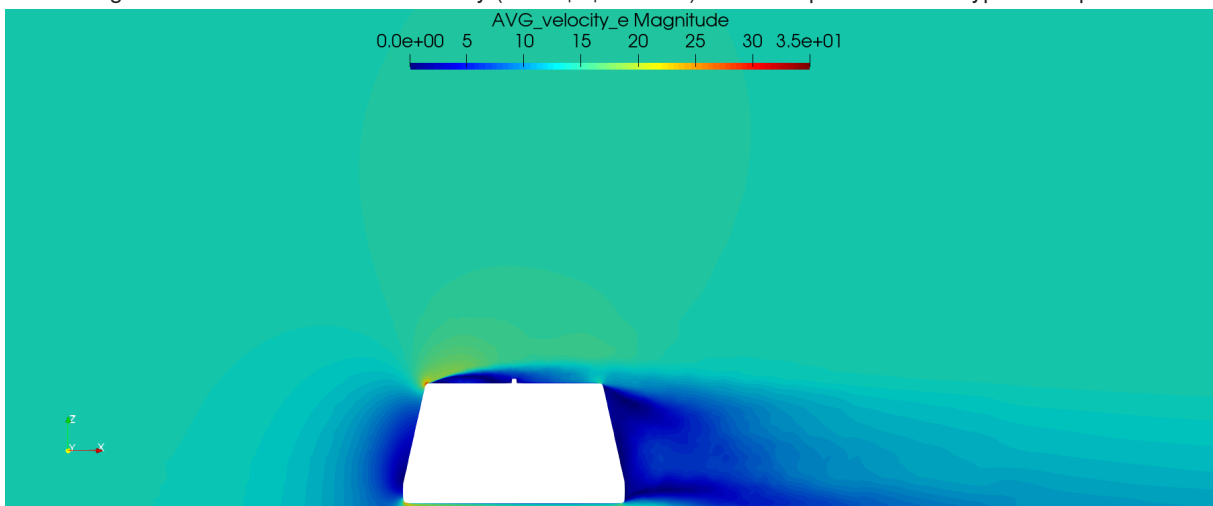


Figure C.9: Side view symmetry plane of the velocity magnitude of sensor position a and type small puck

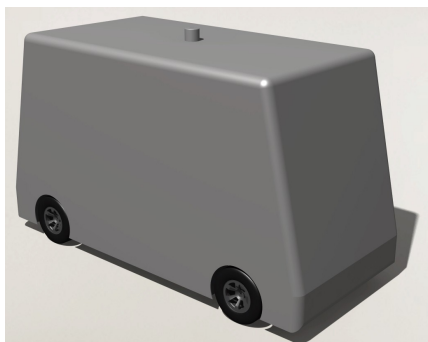


Figure C.10: Render of sensor position *a* and type big puck

Sensor position *a* and type big puck

Table C.2: Data table of sensor position *a* and type big puck

| | |
|-----------------|----------|
| Sensor position | <i>a</i> |
| Sensor type | big puck |
| ΔC_d | -10 |

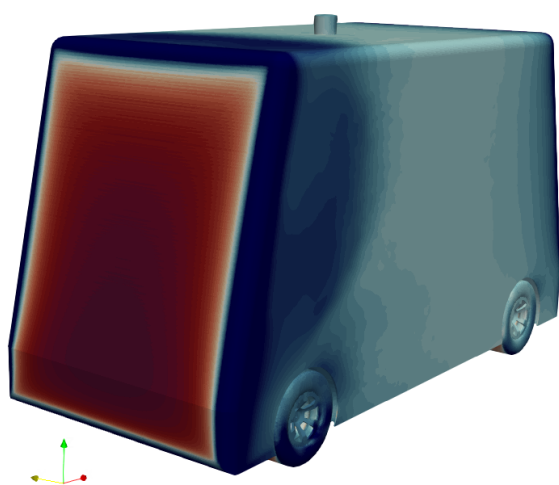


Figure C.11: Front isometric view of the C_p of sensor position *a* and type big puck

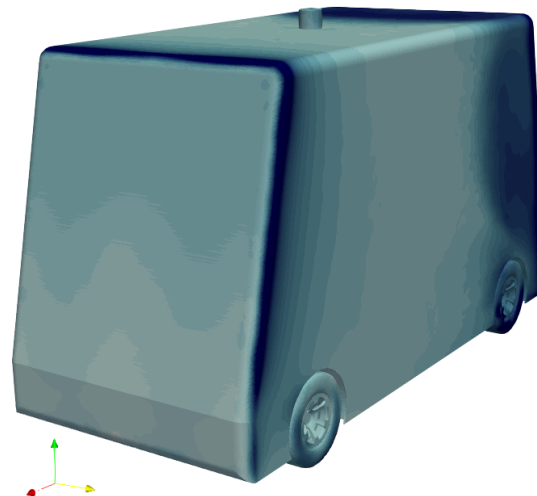
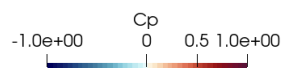


Figure C.12: Rear isometric view of the C_p of sensor position *a* and type big puck

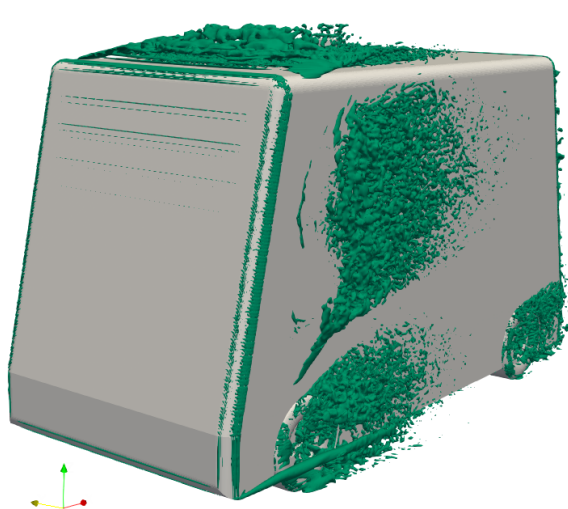


Figure C.13: Front isometric view of the Q-criteria (value $q = 2000 \text{ s}^{-2}$) of sensor position *a* and type big puck



Figure C.14: Rear isometric view of the Q-criteria (value $q = 2000 \text{ s}^{-2}$) of sensor position *a* and type big puck

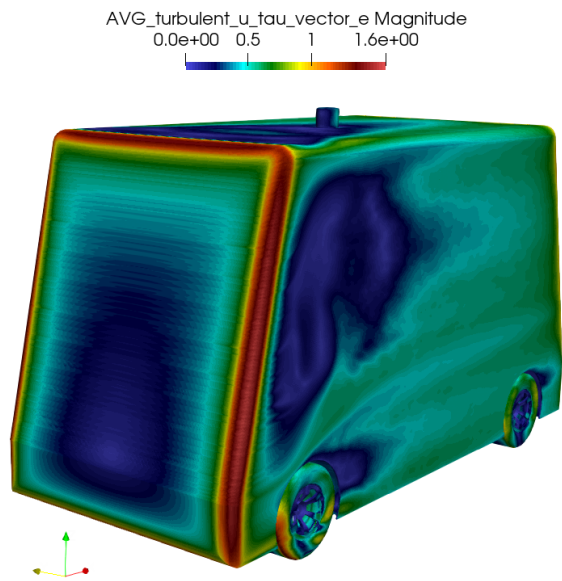


Figure C.15: Front isometric view of the u_τ of sensor position a and type big puck

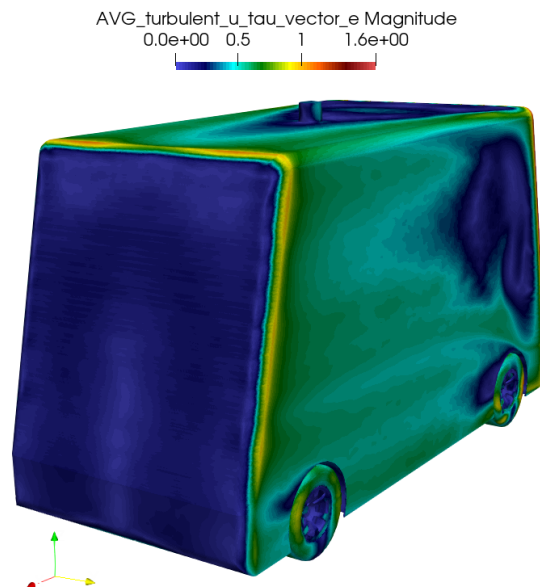


Figure C.16: Rear isometric view of the u_τ of sensor position a and type big puck

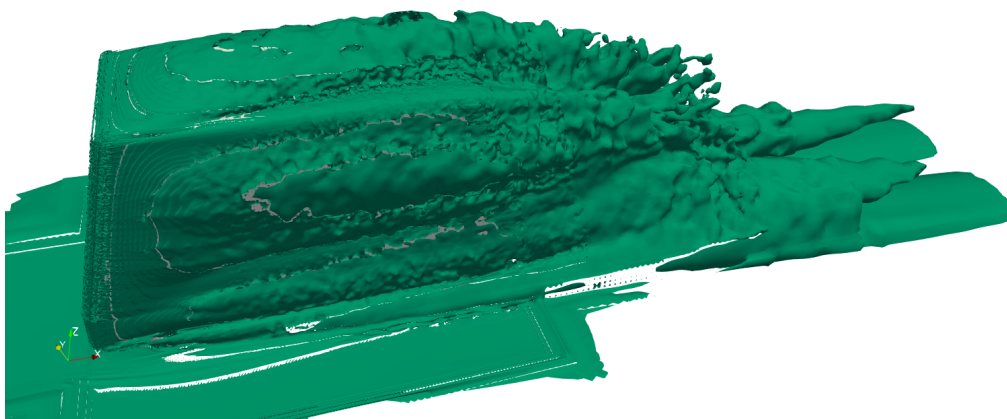


Figure C.17: Side view of the vorticity (value $|\omega| = 10 \text{ s}^{-1}$) of sensor position a and type big puck

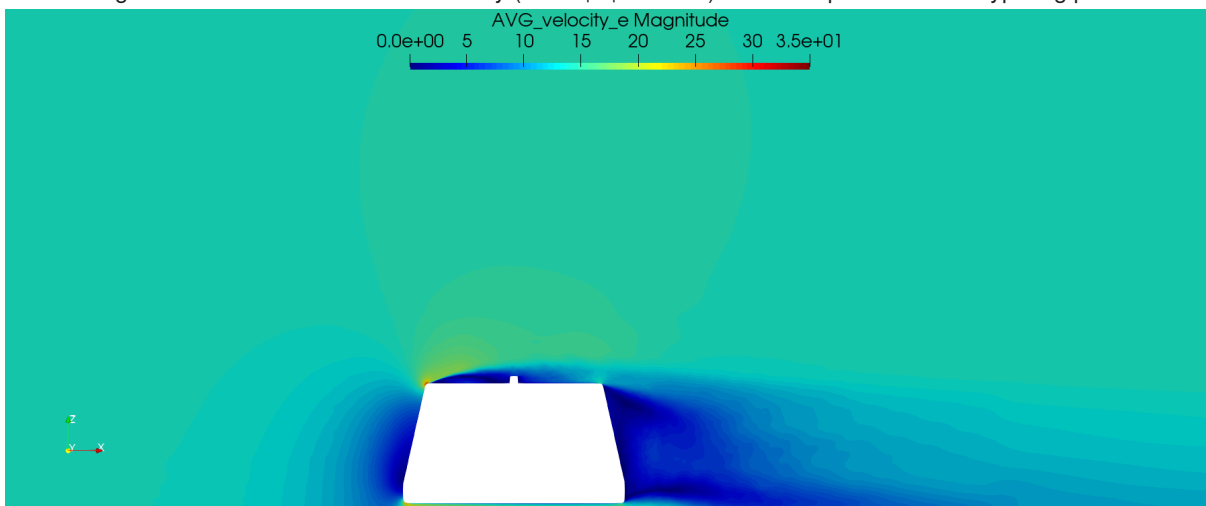


Figure C.18: Side view symmetry plane of the velocity magnitude of sensor position a and type big puck

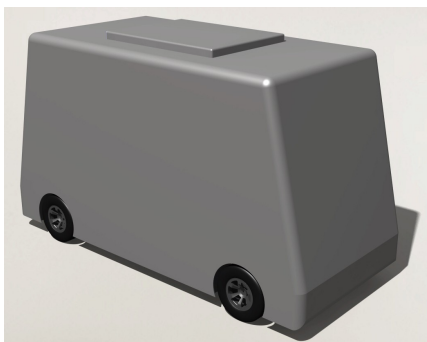


Figure C.19: Render of sensor position *a* and type small box

Sensor position *a* and type **small box**

Table C.3: Data table of sensor position *a* and type small box

| | |
|-----------------|-----------|
| Sensor position | <i>a</i> |
| Sensor type | small box |
| ΔC_d | -34 |

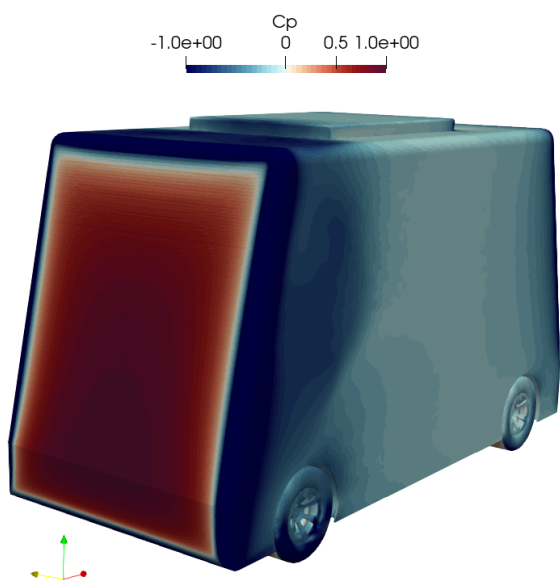


Figure C.20: Front isometric view of the C_p of sensor position *a* and type small box

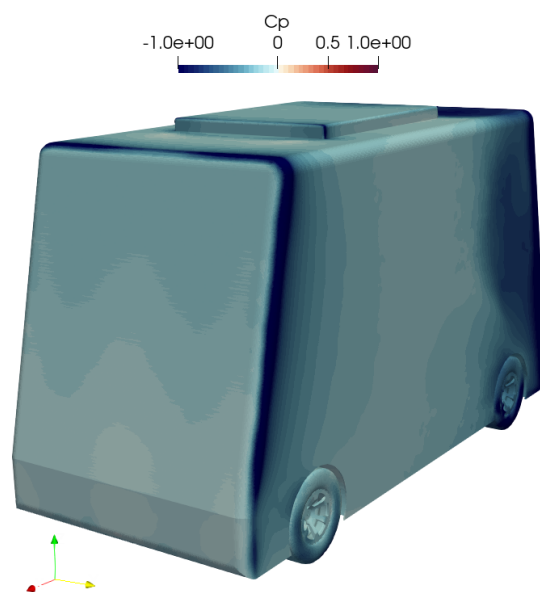


Figure C.21: Rear isometric view of the C_p of sensor position *a* and type small box

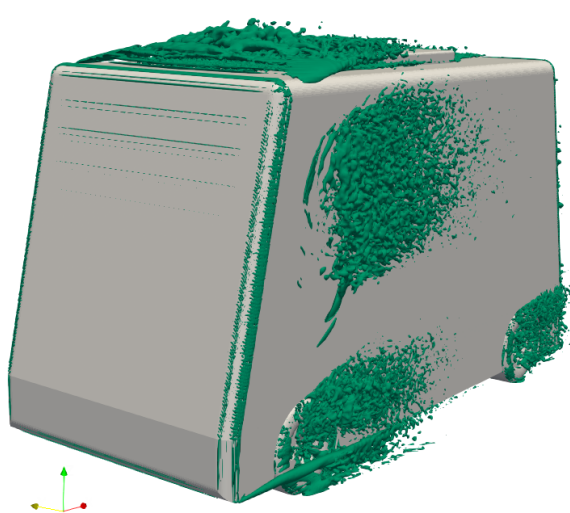


Figure C.22: Front isometric view of the Q-criteria (value $q = 2000 \text{ s}^{-2}$) of sensor position *a* and type small box

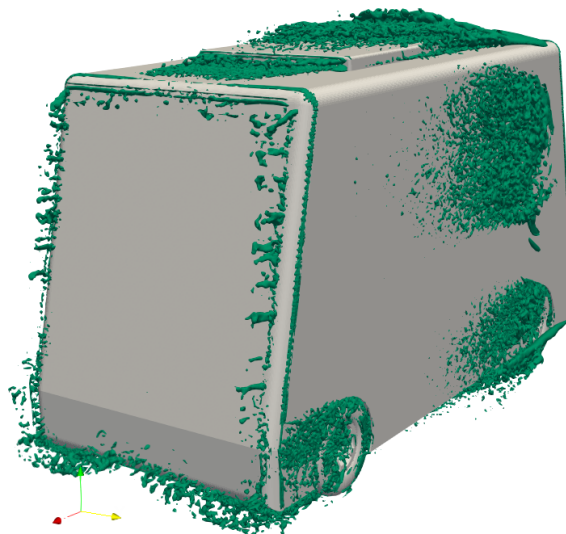


Figure C.23: Rear isometric view of the Q-criteria (value $q = 2000 \text{ s}^{-2}$) of sensor position *a* and type small box

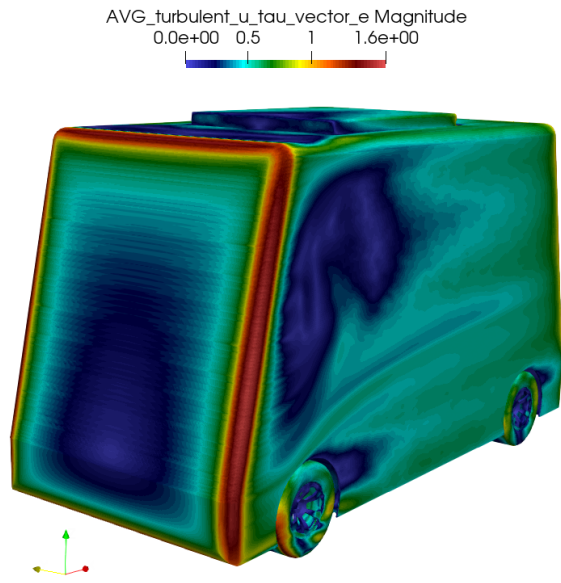


Figure C.24: Front isometric view of the u_τ of sensor position *a* and type small box

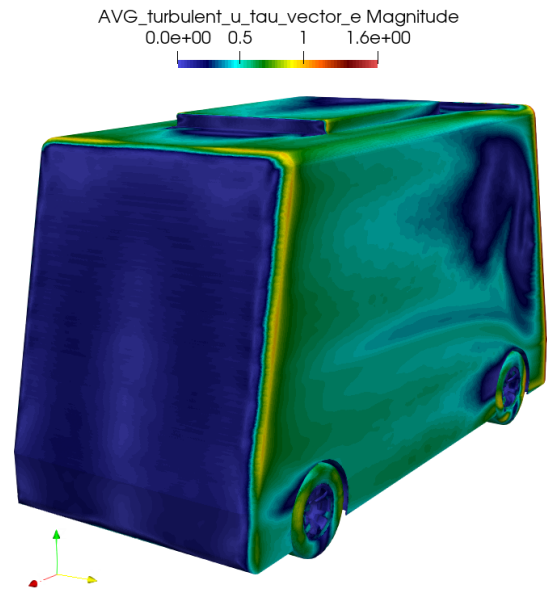


Figure C.25: Rear isometric view of the u_τ of sensor position *a* and type small box

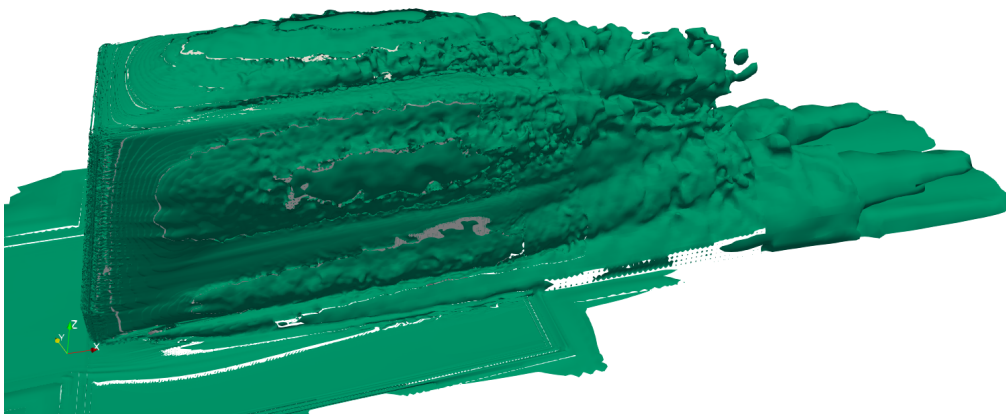


Figure C.26: Side view of the vorticity (value $|\omega| = 10 \text{ s}^{-1}$) of sensor position *a* and type small box

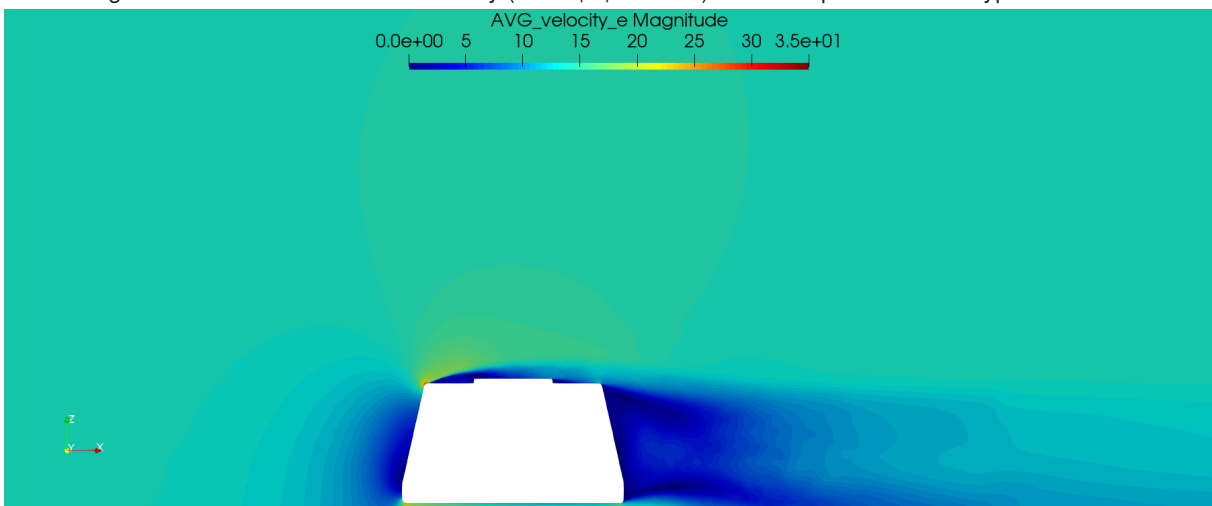


Figure C.27: Side view symmetry plane of the velocity magnitude of sensor position *a* and type small box

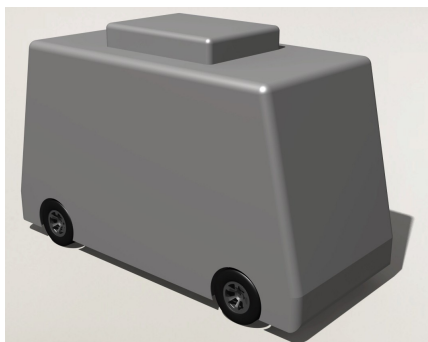


Figure C.28: Render of sensor position *a* and type big box

Sensor position *a* and type **big box**

Table C.4: Data table of sensor position *a* and type big box

| | |
|-----------------|----------|
| Sensor position | <i>a</i> |
| Sensor type | big box |
| ΔC_d | -35 |

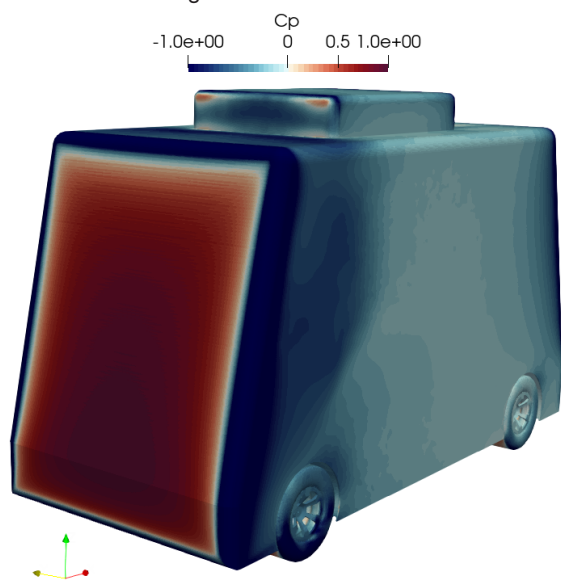


Figure C.29: Front isometric view of the C_p of sensor position *a* and type big box

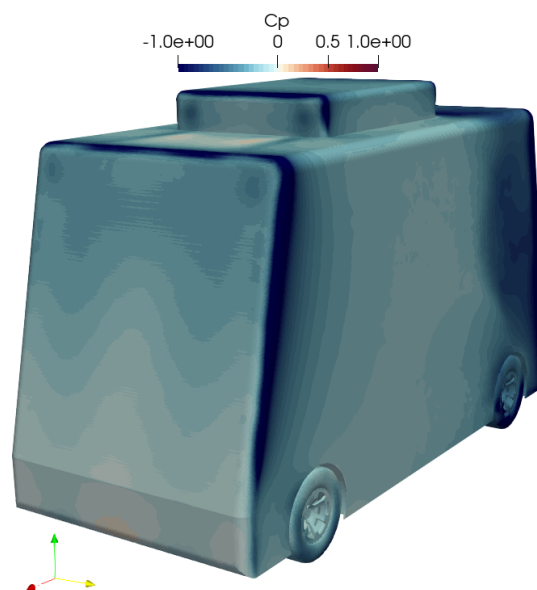


Figure C.30: Rear isometric view of the C_p of sensor position *a* and type big box

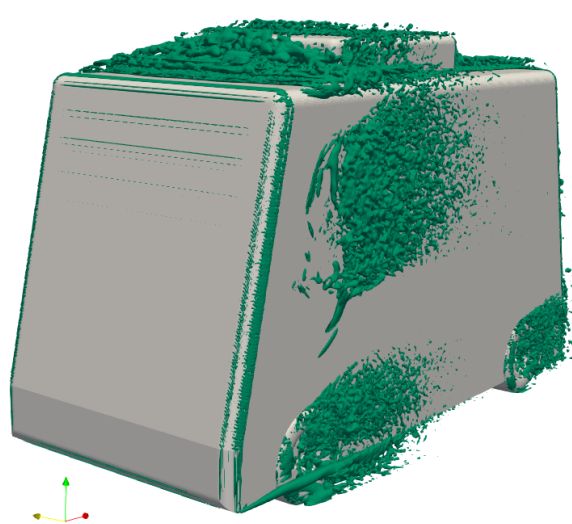


Figure C.31: Front isometric view of the Q-criteria (value $q = 2000 \text{ s}^{-2}$) of sensor position *a* and type big box

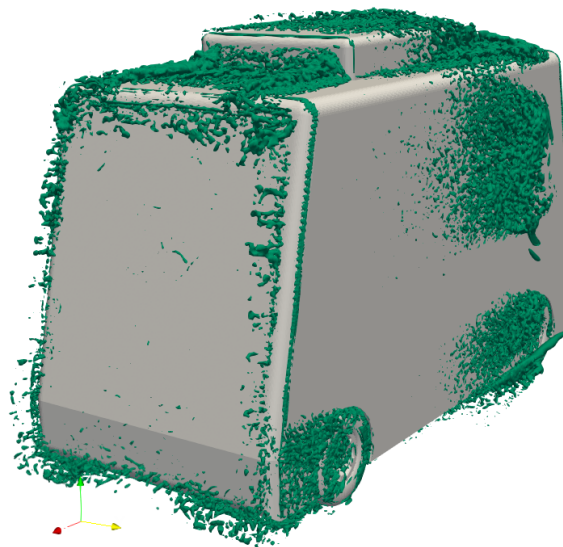


Figure C.32: Rear isometric view of the Q-criteria (value $q = 2000 \text{ s}^{-2}$) of sensor position *a* and type big box

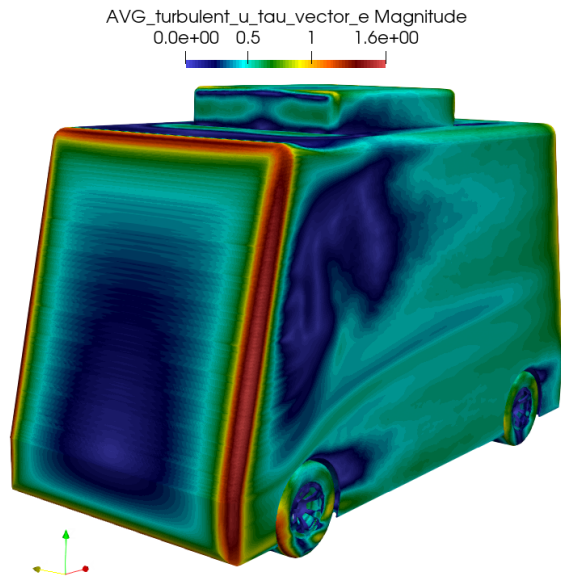


Figure C.33: Front isometric view of the u_τ of sensor position a and type big box

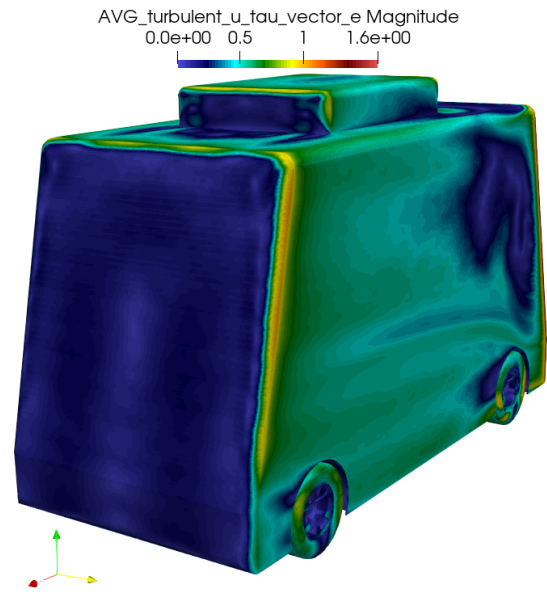


Figure C.34: Rear isometric view of the u_τ of sensor position a and type big box

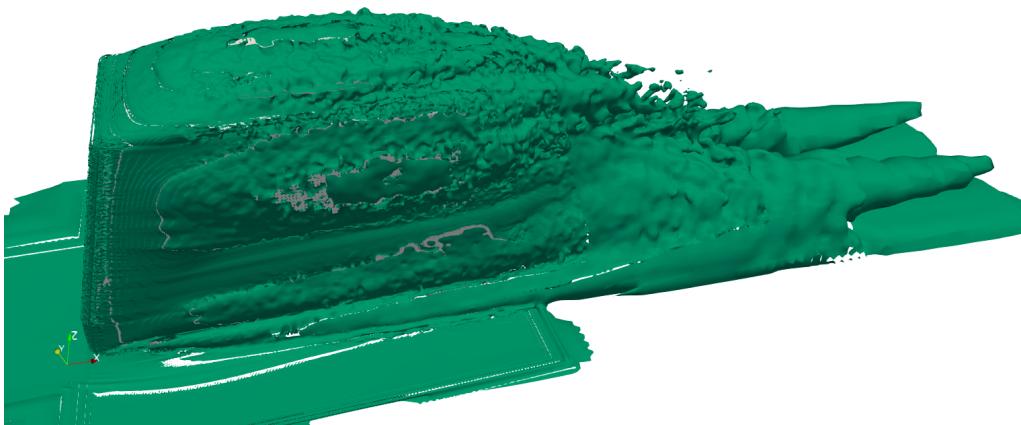


Figure C.35: Side view of the vorticity (value $|\omega| = 10 \text{ s}^{-1}$) of sensor position a and type big box

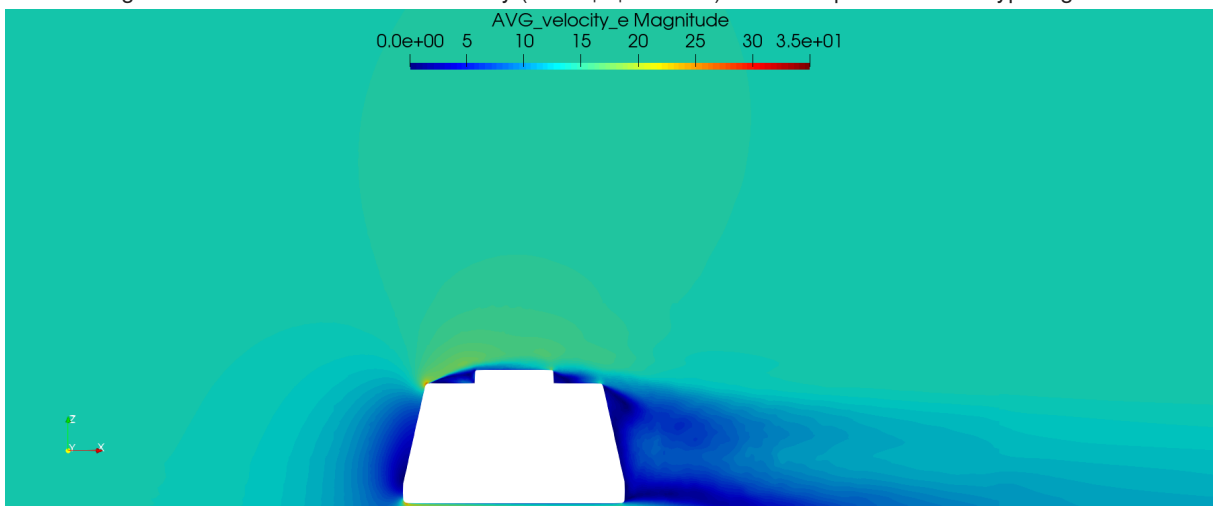


Figure C.36: Side view symmetry plane of the velocity magnitude of sensor position a and type big box

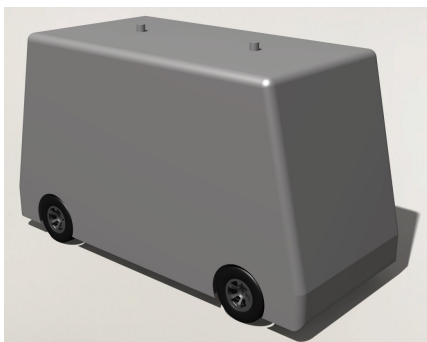


Figure C.37: Render of sensor position b and type small puck

Sensor position b and type small puck

Table C.5: Data table of sensor position b and type small puck

| Sensor position | b |
|-----------------|------------|
| Sensor type | small puck |
| ΔC_d | -2 |

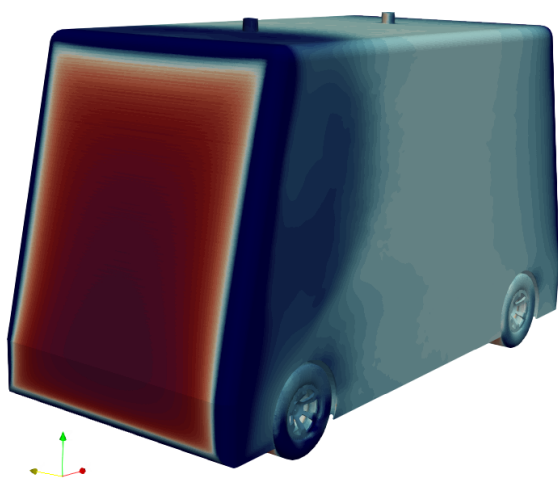


Figure C.38: Front isometric view of the C_p of sensor position b and type small puck

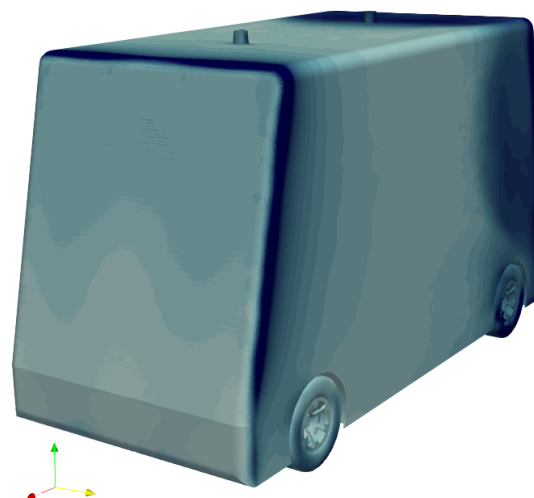


Figure C.39: Rear isometric view of the C_p of sensor position b and type small puck

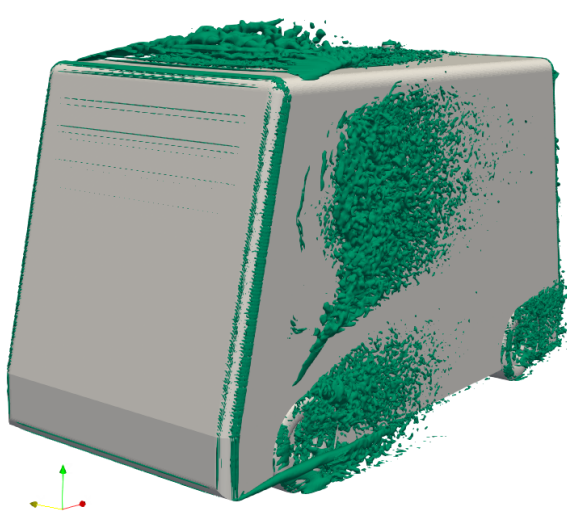


Figure C.40: Front isometric view of the Q-criteria (value $q = 2000 \text{ s}^{-2}$) of sensor position b and type small puck



Figure C.41: Rear isometric view of the Q-criteria (value $q = 2000 \text{ s}^{-2}$) of sensor position b and type small puck

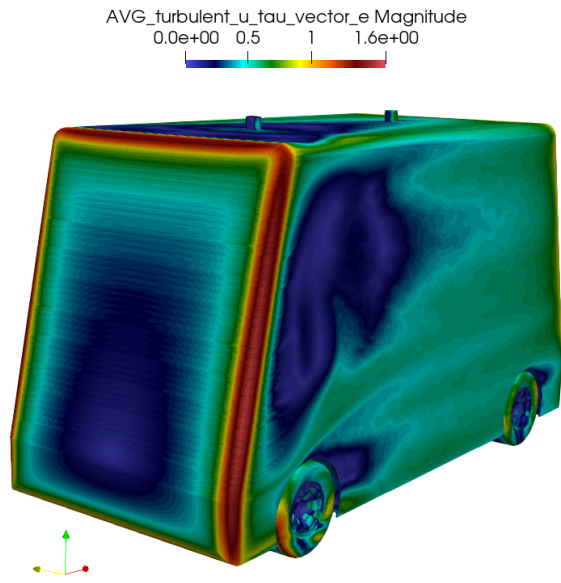


Figure C.42: Front isometric view of the u_τ of sensor position b and type small puck

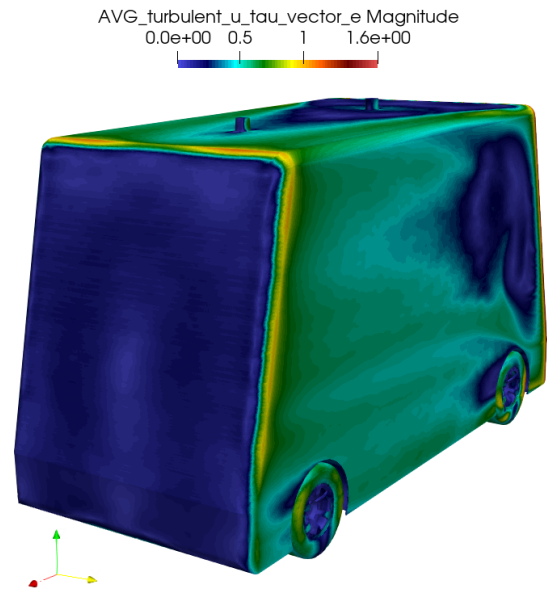


Figure C.43: Rear isometric view of the u_τ of sensor position b and type small puck

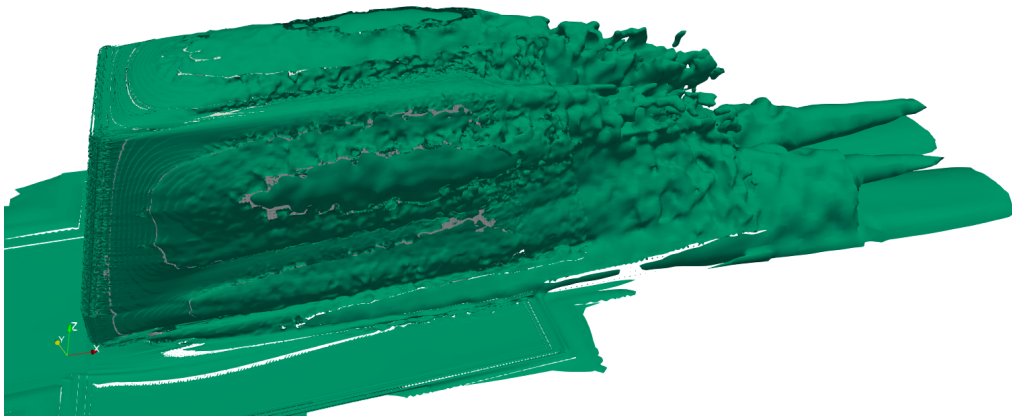


Figure C.44: Side view of the vorticity (value $|\omega| = 10 \text{ s}^{-1}$) of sensor position b and type small puck

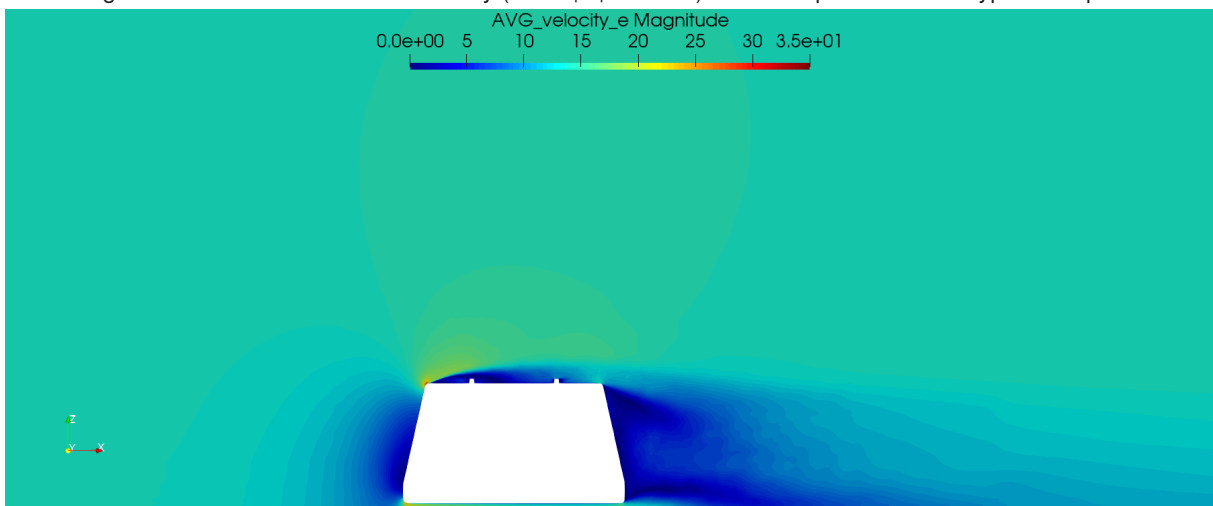


Figure C.45: Side view symmetry plane of the velocity magnitude of sensor position b and type small puck

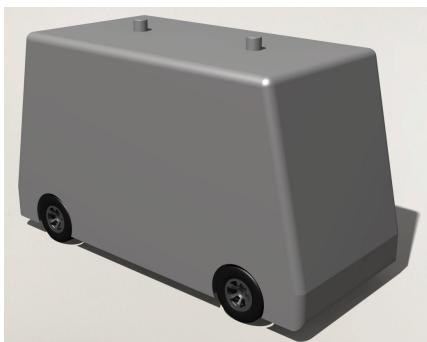


Figure C.46: Render of sensor position b and type big puck

Sensor position b and type big puck

Table C.6: Data table of sensor position b and type big puck

| Sensor position | b |
|-----------------|----------|
| Sensor type | big puck |
| ΔC_d | -8 |

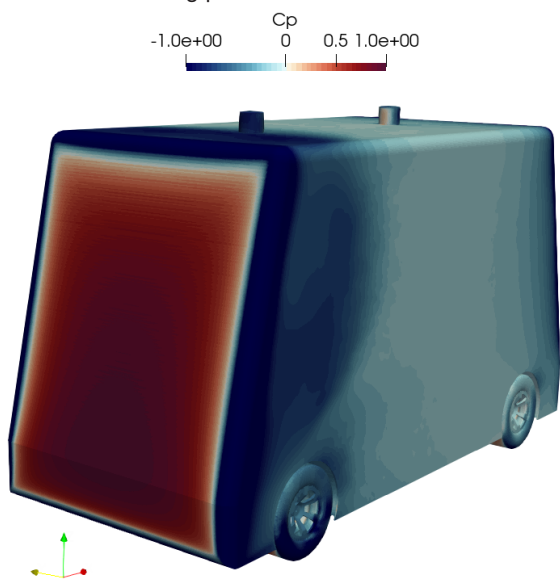


Figure C.47: Front isometric view of the C_p of sensor position b and type big puck

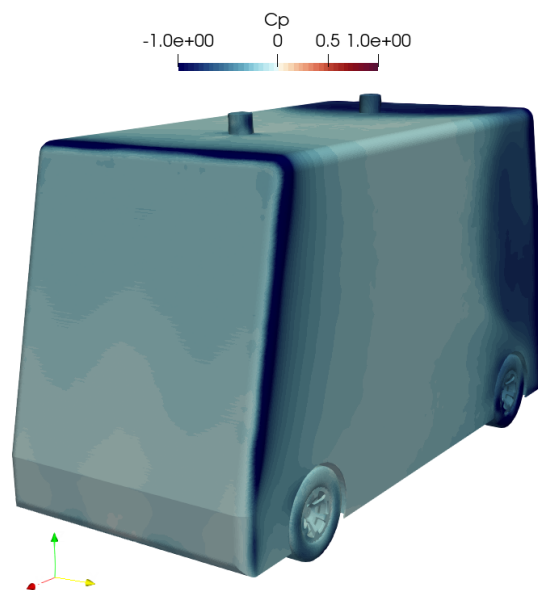


Figure C.48: Rear isometric view of the C_p of sensor position b and type big puck

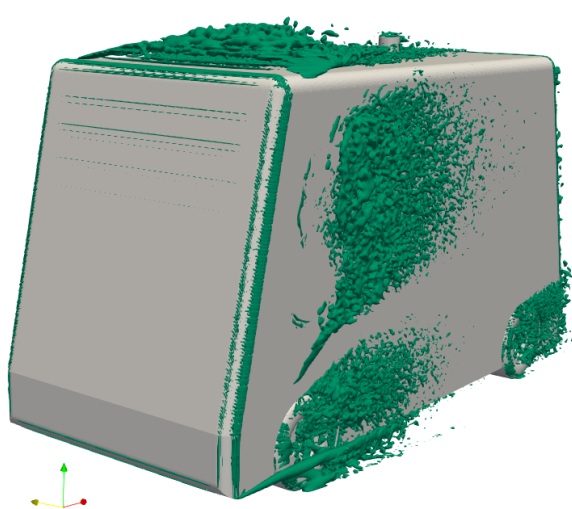


Figure C.49: Front isometric view of the Q-criteria (value $q = 2000 \text{ s}^{-2}$) of sensor position b and type big puck



Figure C.50: Rear isometric view of the Q-criteria (value $q = 2000 \text{ s}^{-2}$) of sensor position b and type big puck

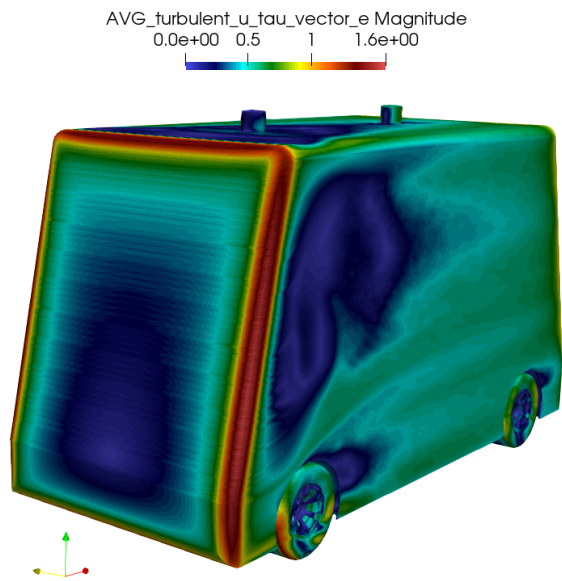


Figure C.51: Front isometric view of the u_τ of sensor position b and type big puck

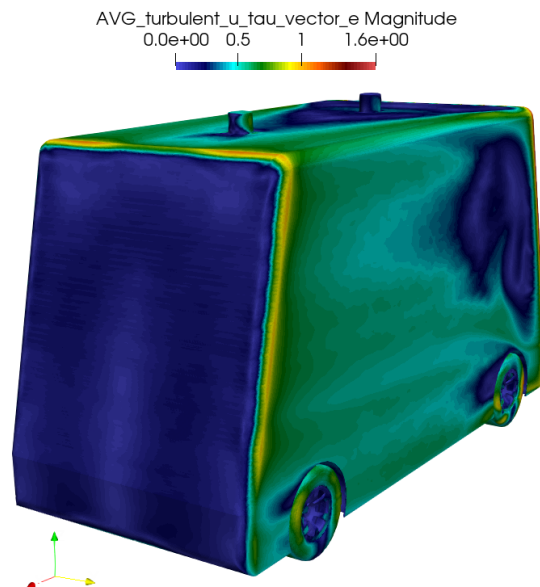


Figure C.52: Rear isometric view of the u_τ of sensor position b and type big puck

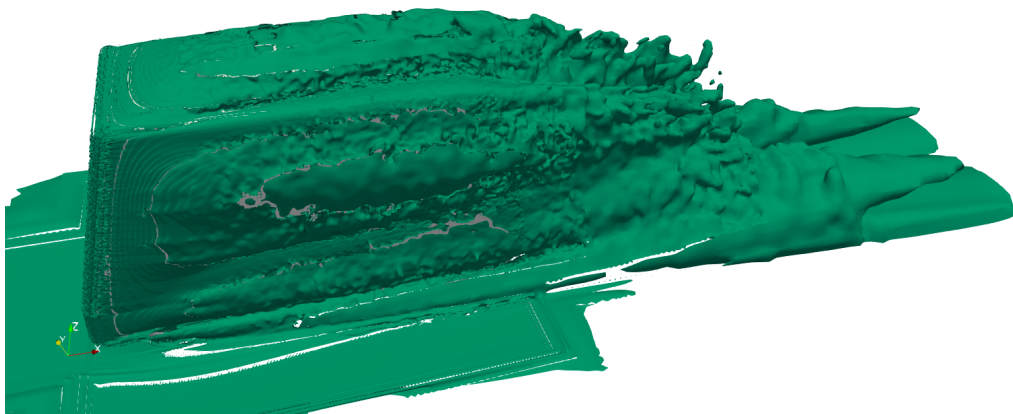


Figure C.53: Side view of the vorticity (value $|\omega| = 10 \text{ s}^{-1}$) of sensor position b and type big puck

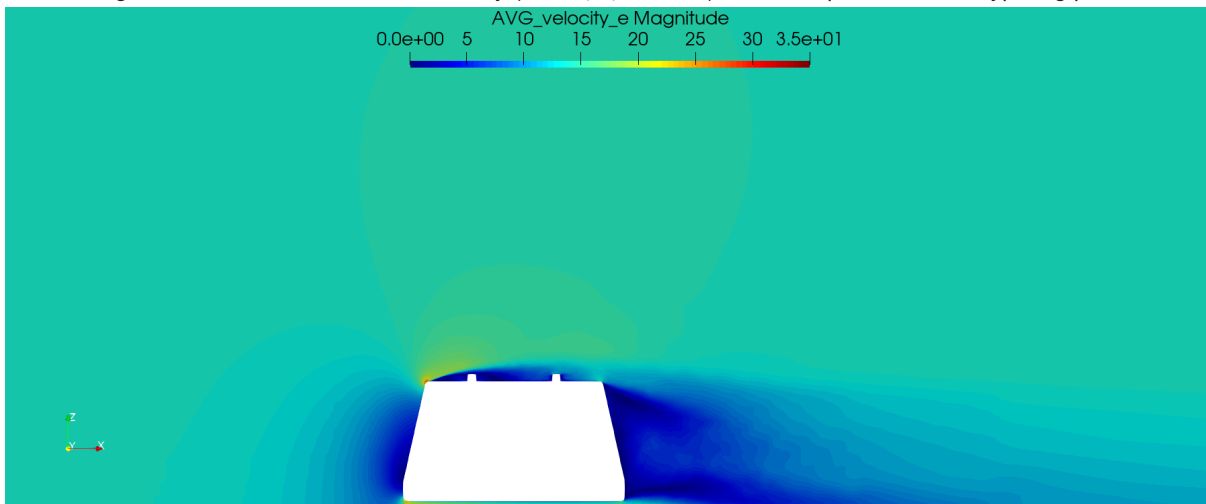


Figure C.54: Side view symmetry plane of the velocity magnitude of sensor position b and type big puck



Figure C.55: Render of sensor position c and type small puck

Sensor position c and type **small puck**

Table C.7: Data table of sensor position c and type small puck

| | |
|-----------------|------------|
| Sensor position | c |
| Sensor type | small puck |
| ΔC_d | 1 |

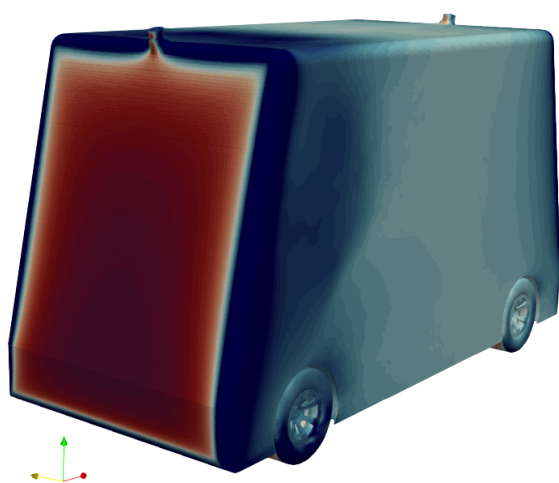


Figure C.56: Front isometric view of the C_p of sensor position c and type small puck

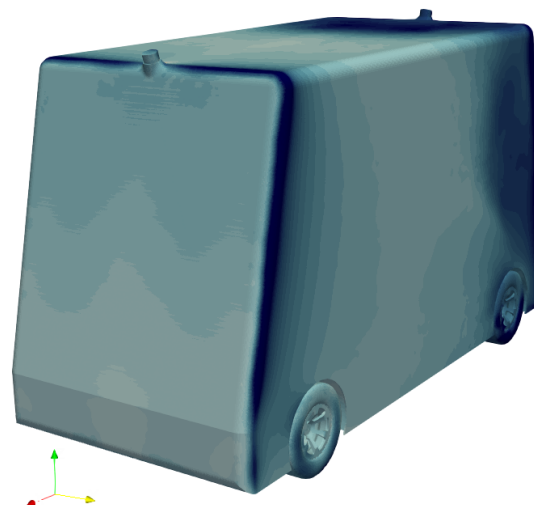


Figure C.57: Rear isometric view of the C_p of sensor position c and type small puck

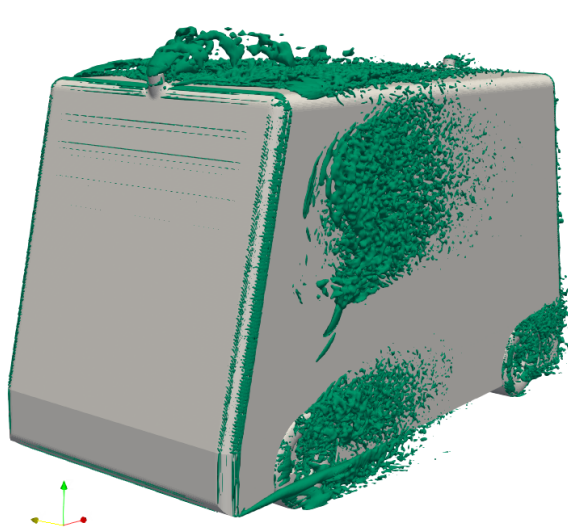


Figure C.58: Front isometric view of the Q-criteria (value $q = 2000 \text{ s}^{-2}$) of sensor position c and type small puck



Figure C.59: Rear isometric view of the Q-criteria (value $q = 2000 \text{ s}^{-2}$) of sensor position c and type small puck

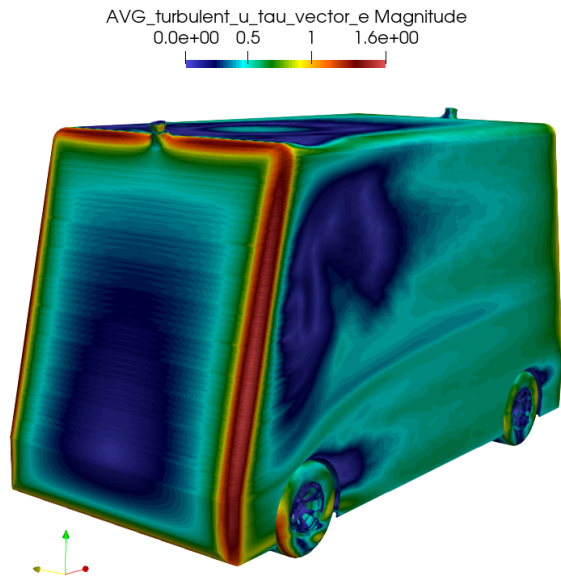


Figure C.60: Front isometric view of the u_τ of sensor position c and type small puck

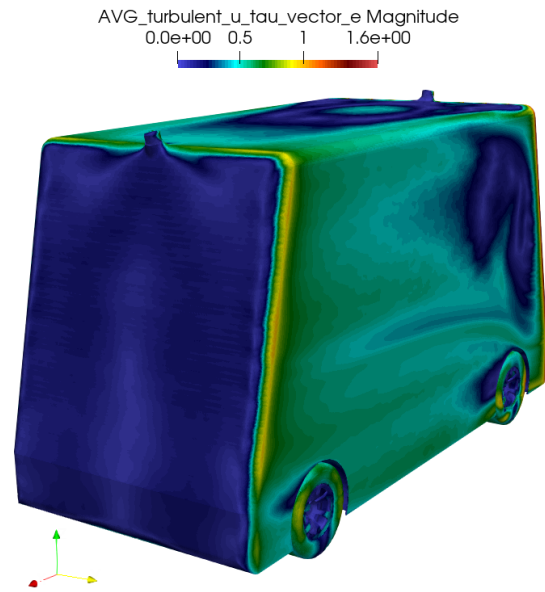


Figure C.61: Rear isometric view of the u_τ of sensor position c and type small puck

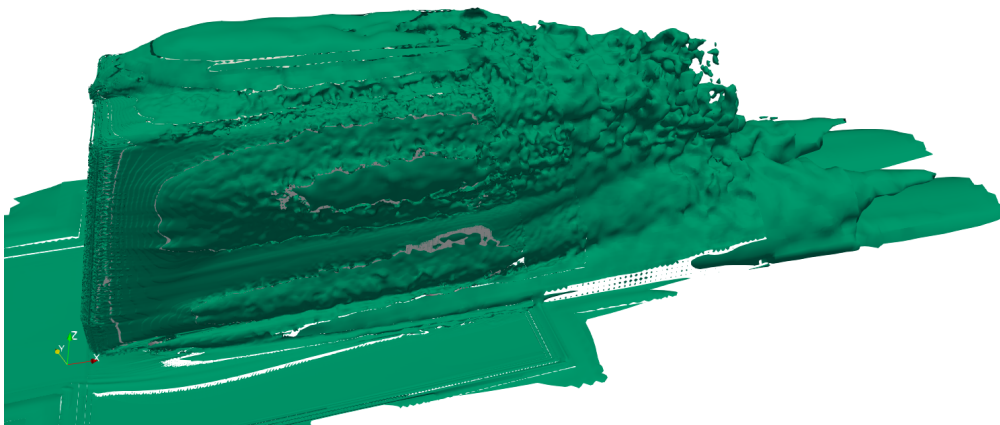


Figure C.62: Side view of the vorticity (value $|\omega| = 10 \text{ s}^{-1}$) of sensor position c and type small puck

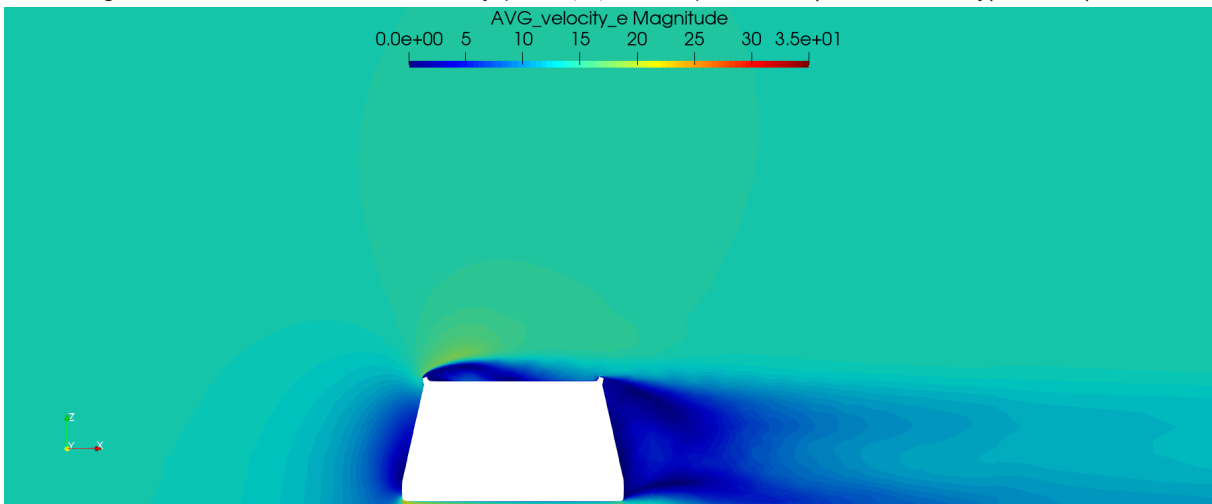


Figure C.63: Side view symmetry plane of the velocity magnitude of sensor position c and type small puck



Figure C.64: Render of sensor position c and type big puck

Sensor position c and type big puck

Table C.8: Data table of sensor position c and type big puck

| Sensor position | c |
|-----------------|----------|
| Sensor type | big puck |
| ΔC_d | -1 |

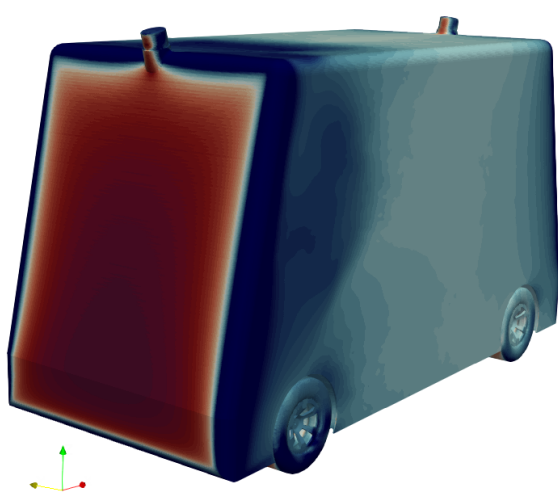


Figure C.65: Front isometric view of the C_p of sensor position c and type big puck

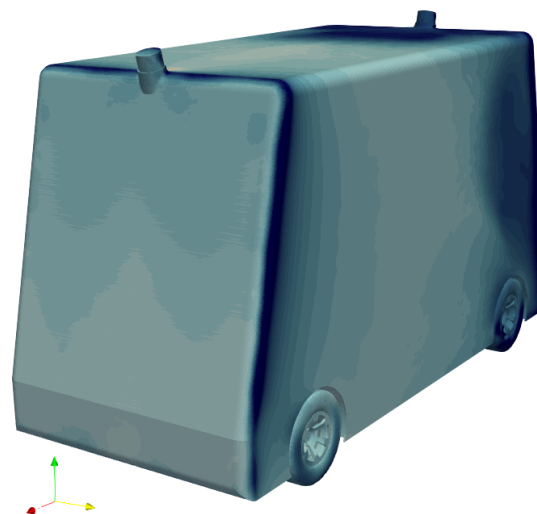


Figure C.66: Rear isometric view of the C_p of sensor position c and type big puck

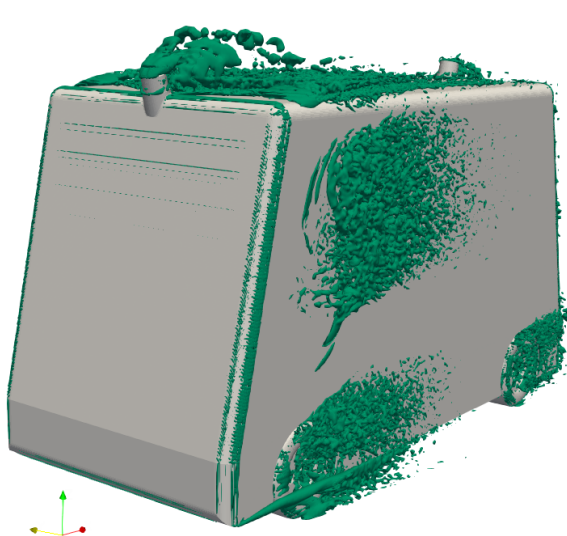


Figure C.67: Front isometric view of the Q-criteria (value $q = 2000 \text{ s}^{-2}$) of sensor position c and type big puck



Figure C.68: Rear isometric view of the Q-criteria (value $q = 2000 \text{ s}^{-2}$) of sensor position c and type big puck

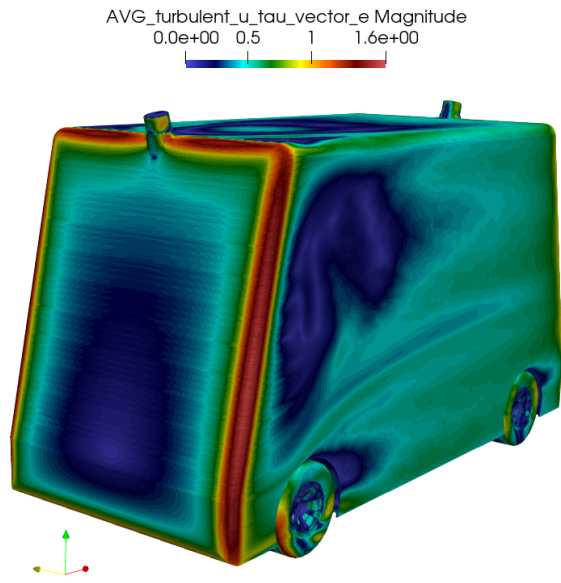


Figure C.69: Front isometric view of the u_τ of sensor position c and type big puck

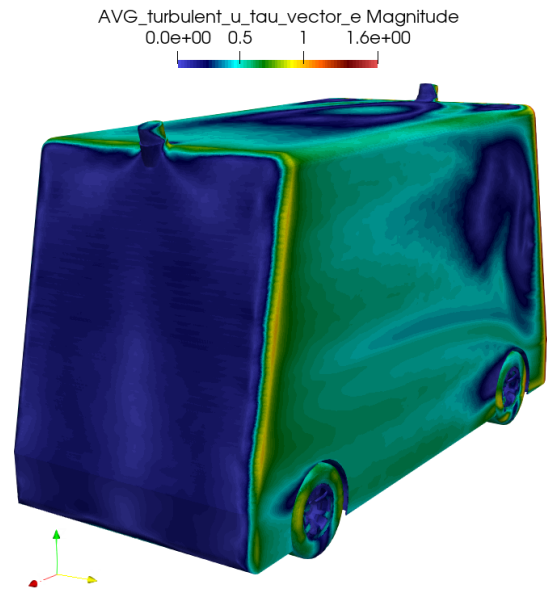


Figure C.70: Rear isometric view of the u_τ of sensor position c and type big puck

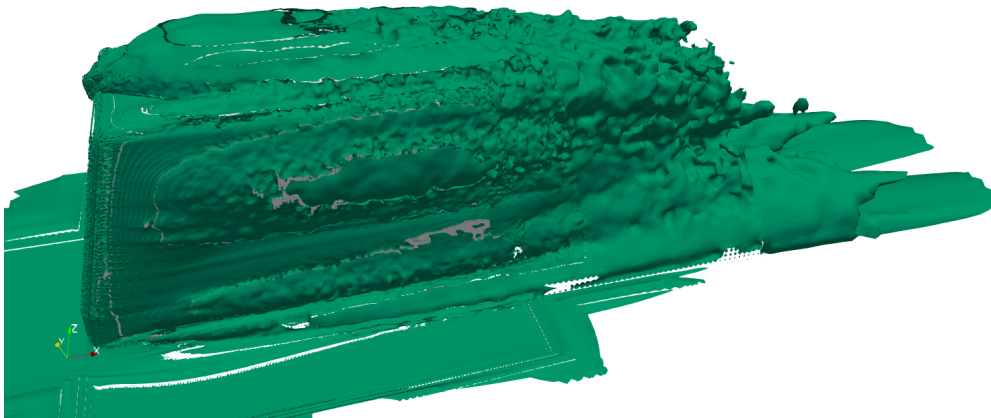


Figure C.71: Side view of the vorticity (value $|\omega| = 10 \text{ s}^{-1}$) of sensor position c and type big puck

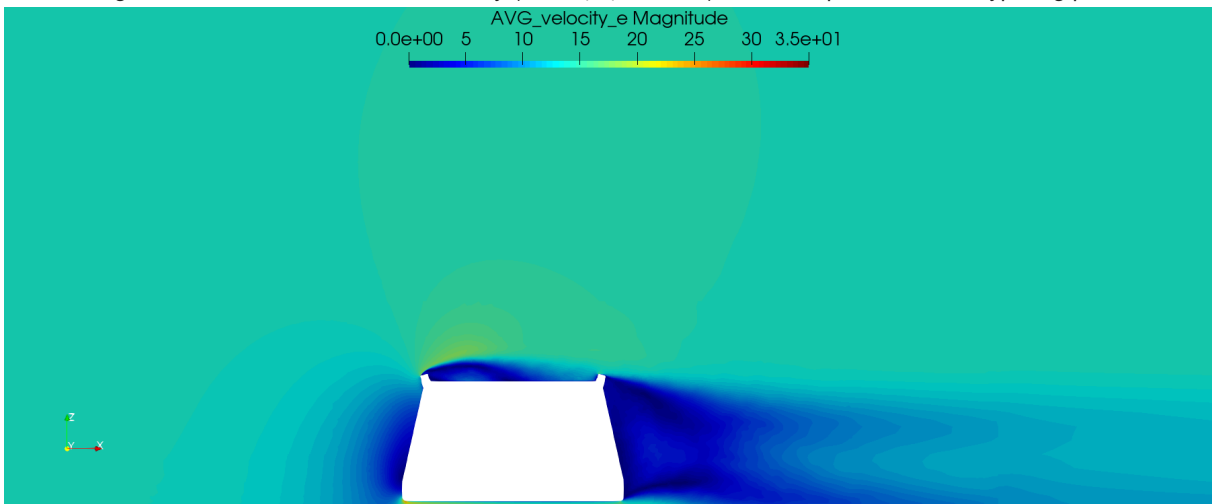


Figure C.72: Side view symmetry plane of the velocity magnitude of sensor position c and type big puck



Figure C.73: Render of sensor position d and type small puck

Sensor position d and type **small puck**

Table C.9: Data table of sensor position d and type small puck

| Sensor position | d |
|-----------------|------------|
| Sensor type | small puck |
| ΔC_d | 3 |

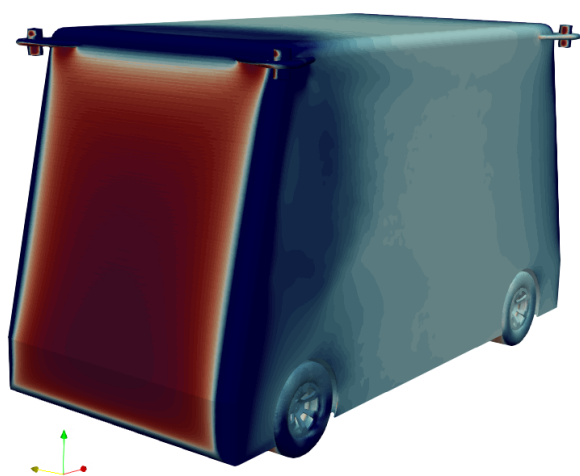


Figure C.74: Front isometric view of the C_p of sensor position d and type small puck

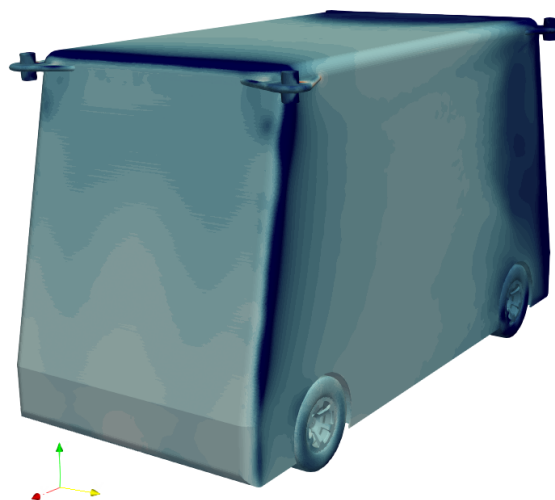


Figure C.75: Rear isometric view of the C_p of sensor position d and type small puck

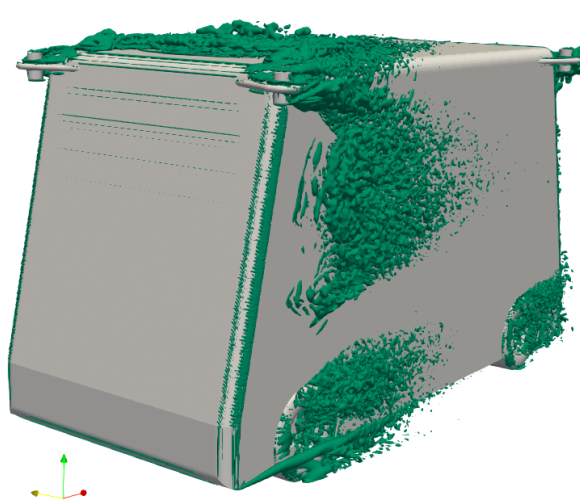


Figure C.76: Front isometric view of the Q-criteria (value $q = 2000 \text{ s}^{-2}$) of sensor position d and type small puck

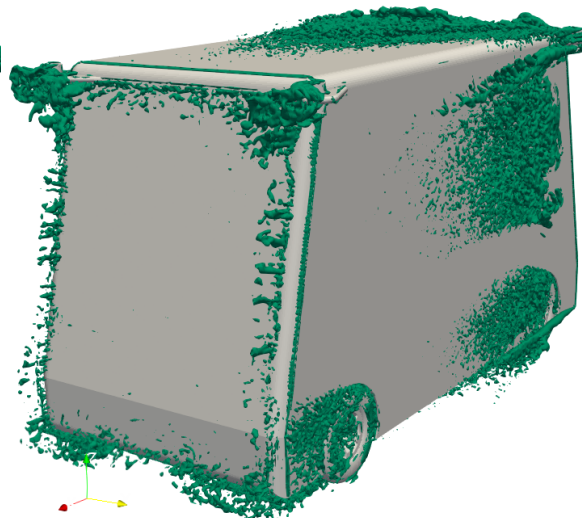


Figure C.77: Rear isometric view of the Q-criteria (value $q = 2000 \text{ s}^{-2}$) of sensor position d and type small puck

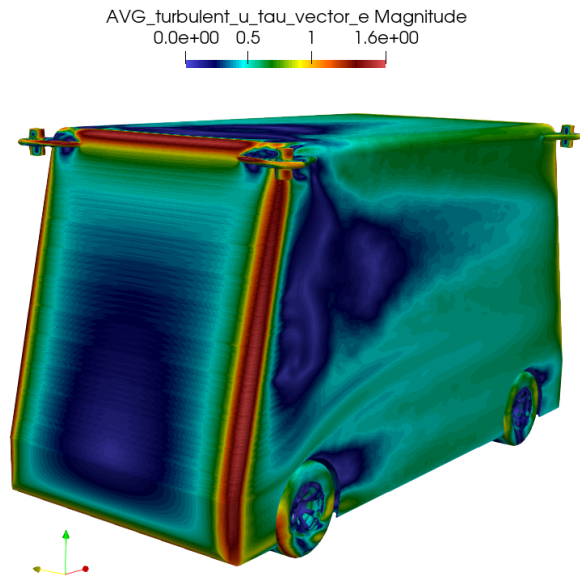


Figure C.78: Front isometric view of the u_τ of sensor position d and type small puck

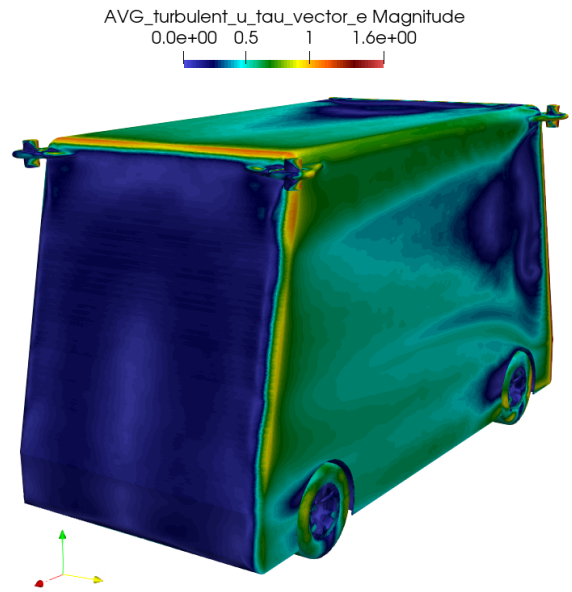


Figure C.79: Rear isometric view of the u_τ of sensor position d and type small puck

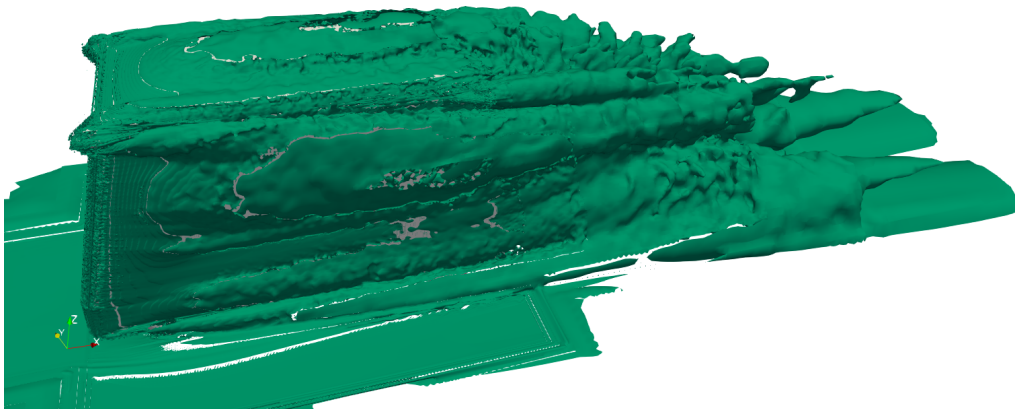


Figure C.80: Side view of the vorticity (value $|\omega| = 10 \text{ s}^{-1}$) of sensor position d and type small puck

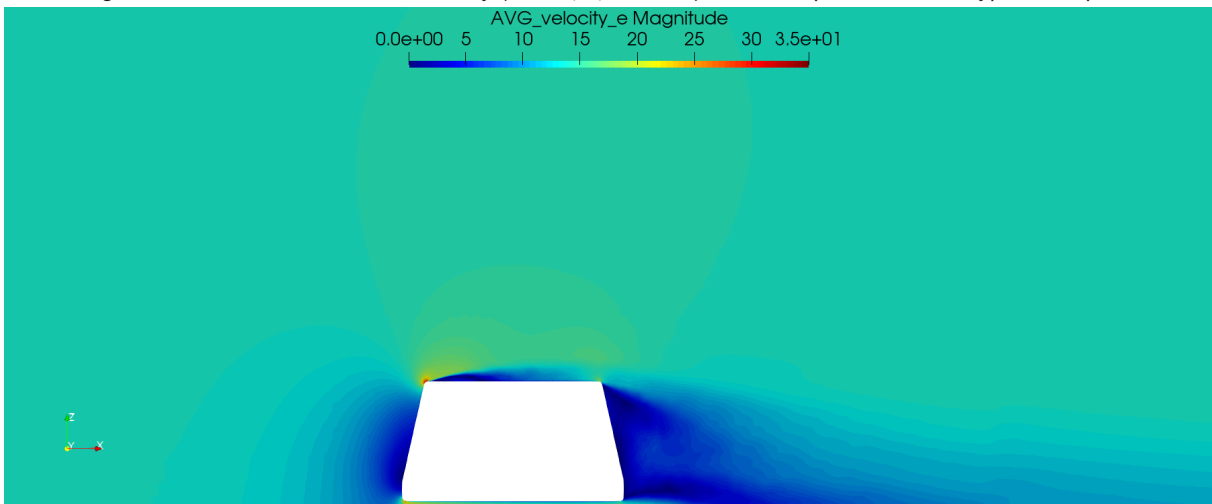


Figure C.81: Side view symmetry plane of the velocity magnitude of sensor position d and type small puck

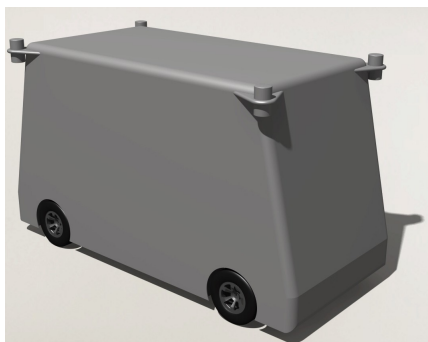


Figure C.82: Render of sensor position d and type big puck

Sensor position d and type big puck

Table C.10: Data table of sensor position d and type big puck

| Sensor position | d |
|-----------------|----------|
| Sensor type | big puck |
| ΔC_d | 11 |

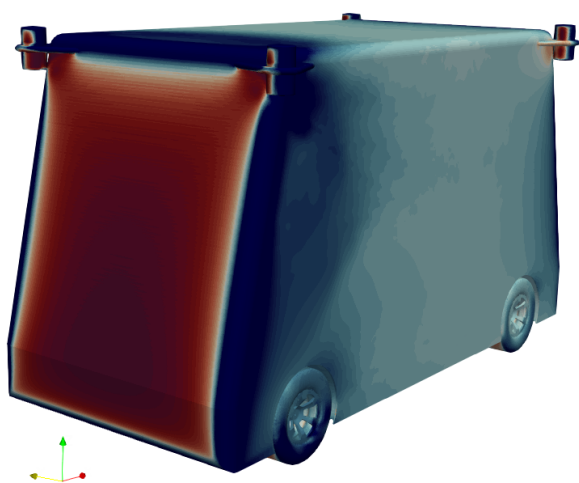


Figure C.83: Front isometric view of the C_p of sensor position d and type big puck

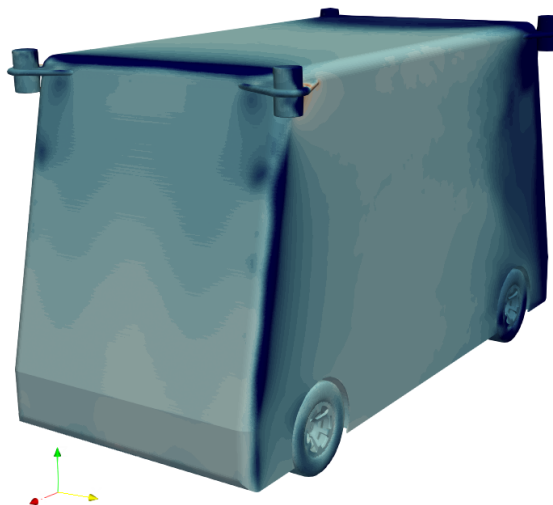


Figure C.84: Rear isometric view of the C_p of sensor position d and type big puck

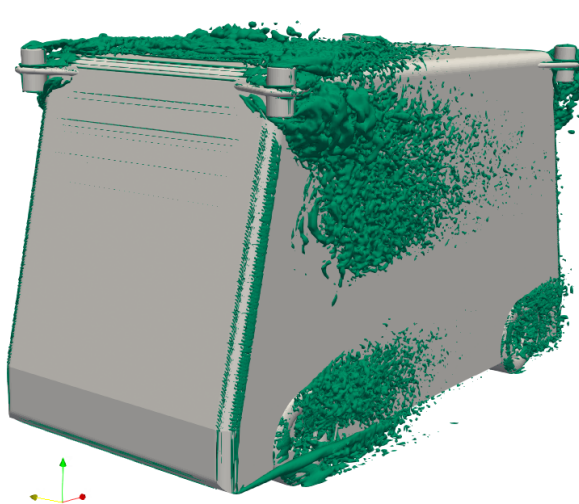


Figure C.85: Front isometric view of the Q-criteria (value $q = 2000 \text{ s}^{-2}$) of sensor position d and type big puck

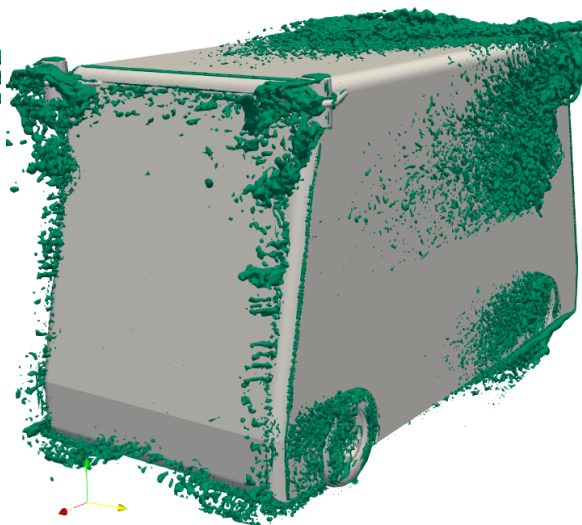


Figure C.86: Rear isometric view of the Q-criteria (value $q = 2000 \text{ s}^{-2}$) of sensor position d and type big puck

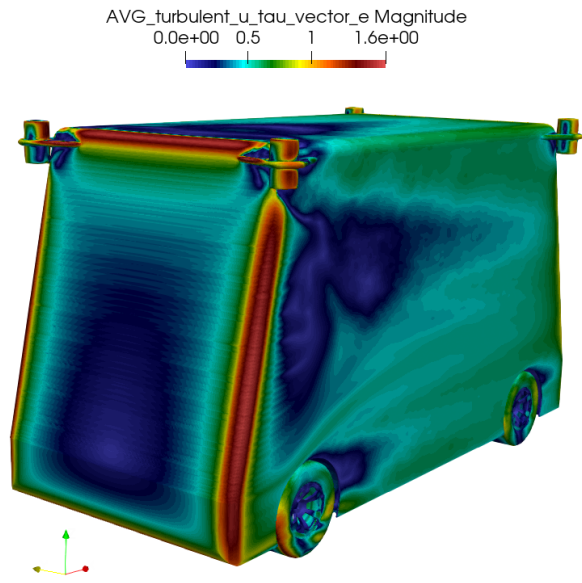


Figure C.87: Front isometric view of the u_τ of sensor position d and type big puck

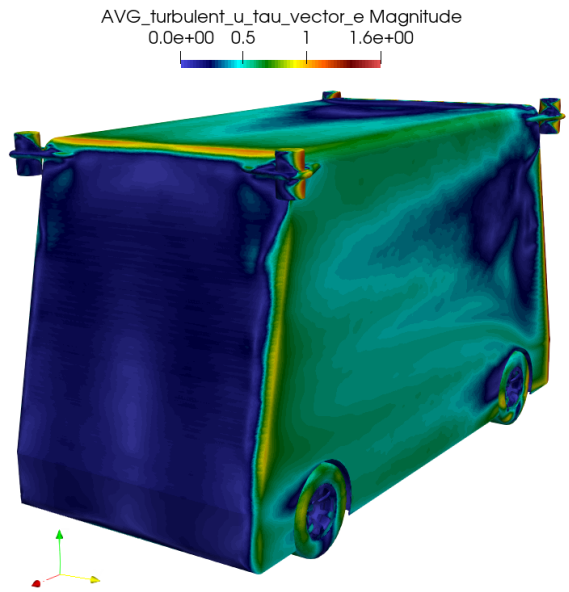


Figure C.88: Rear isometric view of the u_τ of sensor position d and type big puck

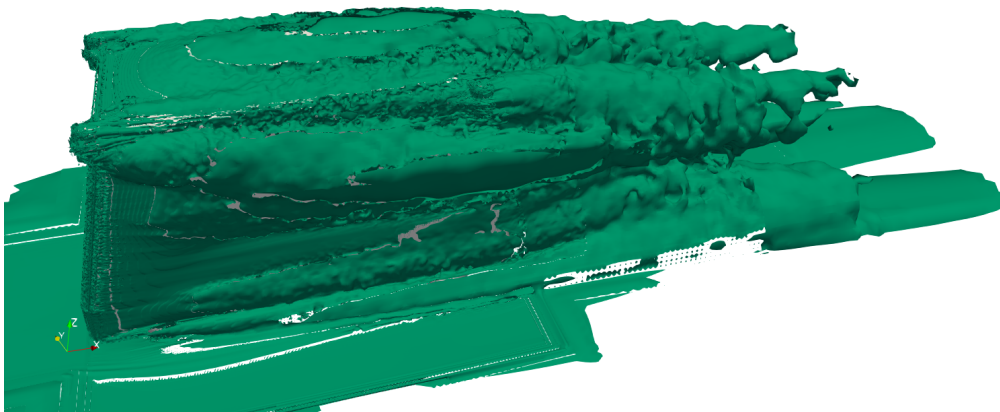


Figure C.89: Side view of the vorticity (value $|\omega| = 10 \text{ s}^{-1}$) of sensor position d and type big puck

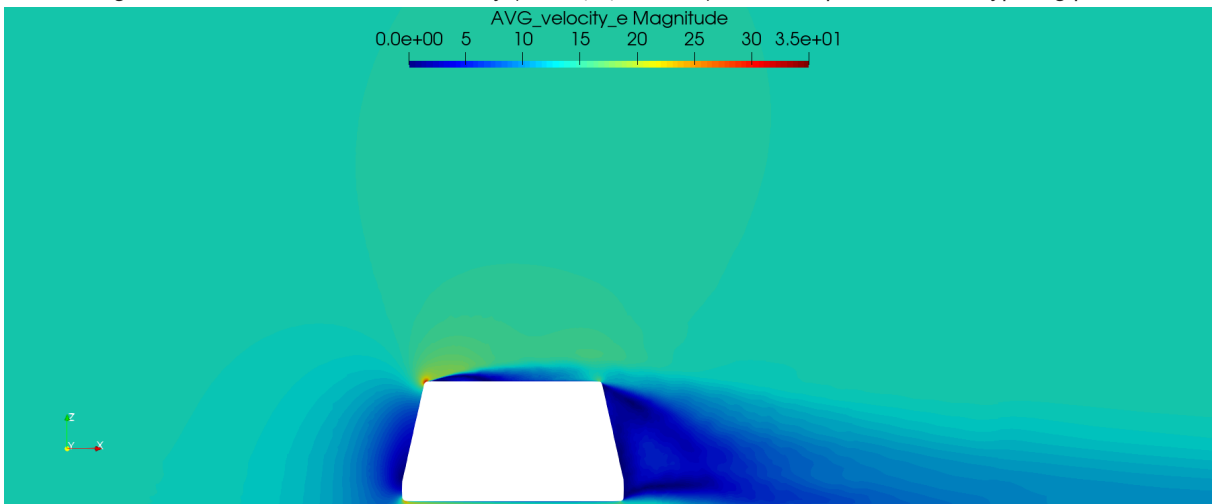


Figure C.90: Side view symmetry plane of the velocity magnitude of sensor position d and type big puck

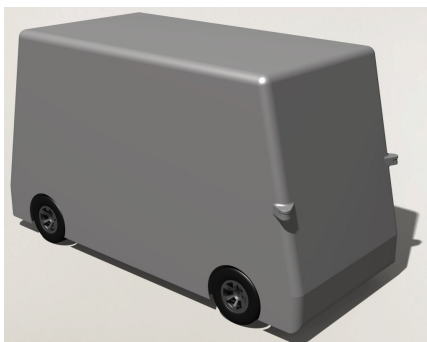


Figure C.91: Render of sensor position f and type small puck

Sensor position f and type **small puck**

Table C.11: Data table of sensor position f and type small puck

| Sensor position | f |
|-----------------|------------|
| Sensor type | small puck |
| ΔC_d | -10 |

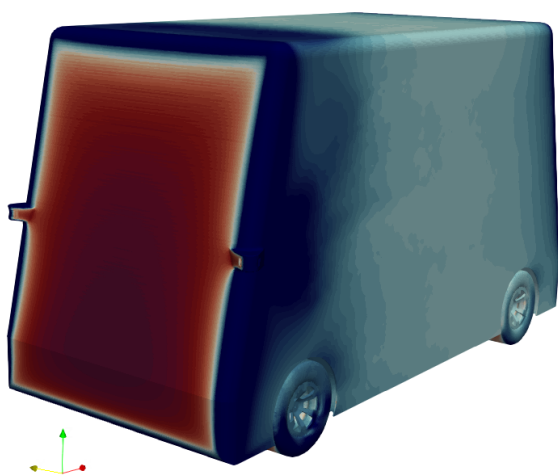


Figure C.92: Front isometric view of the C_p of sensor position f and type small puck

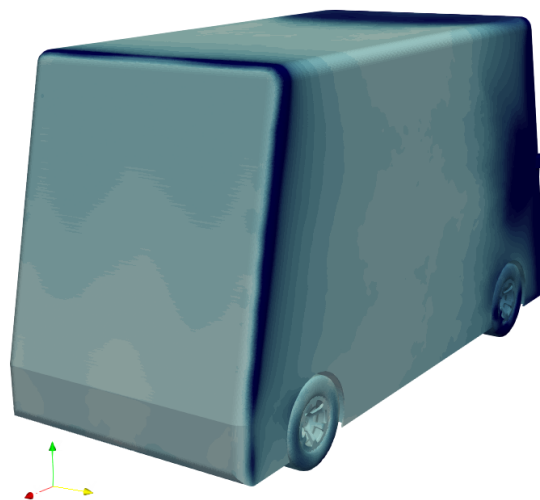
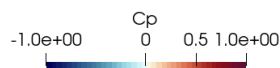


Figure C.93: Rear isometric view of the C_p of sensor position f and type small puck

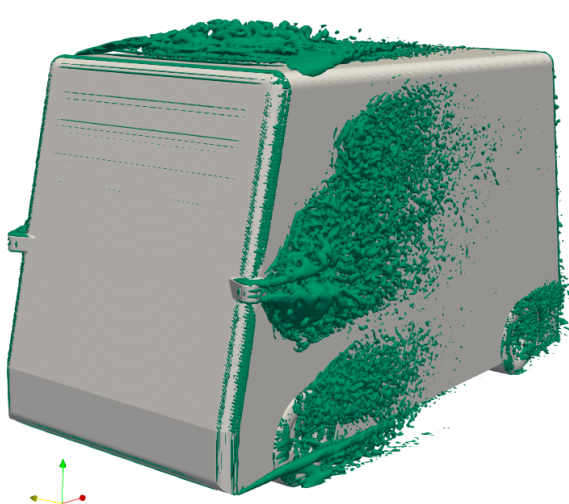


Figure C.94: Front isometric view of the Q-criteria (value $q = 2000 \text{ s}^{-2}$) of sensor position f and type small puck



Figure C.95: Rear isometric view of the Q-criteria (value $q = 2000 \text{ s}^{-2}$) of sensor position f and type small puck

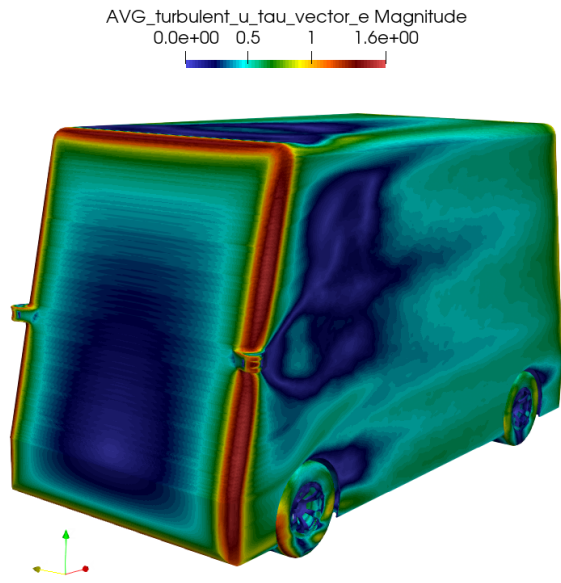


Figure C.96: Front isometric view of the u_τ of sensor position f and type small puck

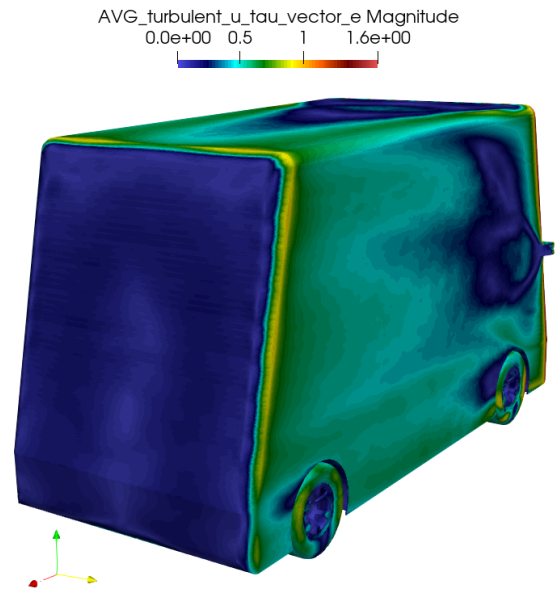


Figure C.97: Rear isometric view of the u_τ of sensor position f and type small puck

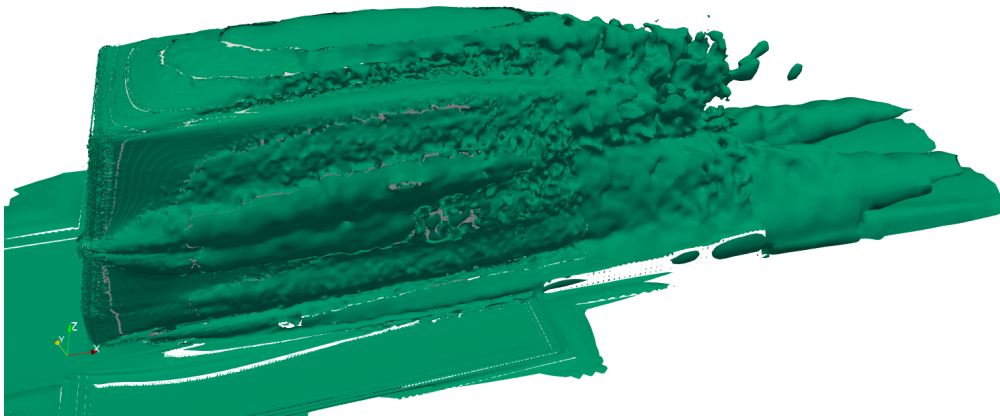


Figure C.98: Side view of the vorticity (value $|\omega| = 10 \text{ s}^{-1}$) of sensor position f and type small puck

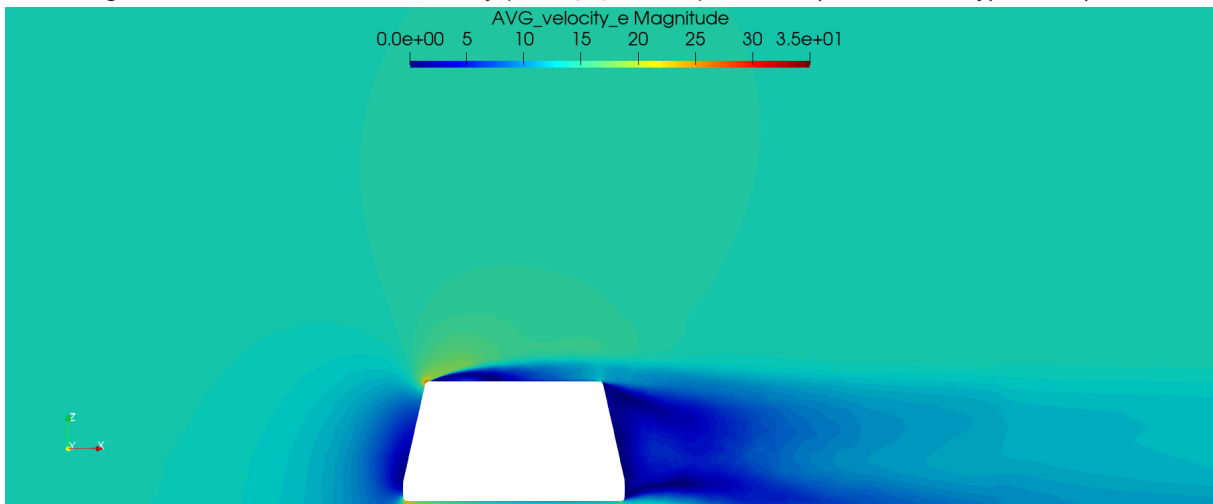


Figure C.99: Side view symmetry plane of the velocity magnitude of sensor position f and type small puck

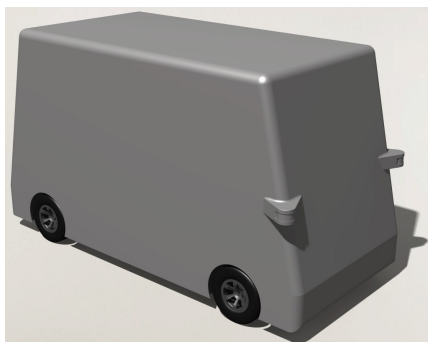


Figure C.100: Render of sensor position f and type big puck

Sensor position f and type **big puck**

Table C.12: Data table of sensor position f and type big puck

| Sensor position | f |
|-----------------|----------|
| Sensor type | big puck |
| ΔC_d | -19 |

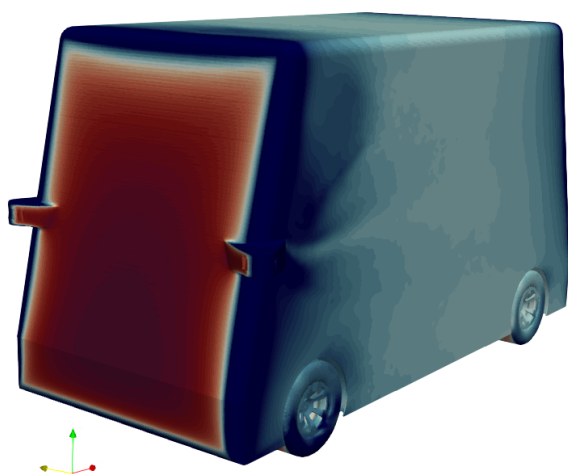
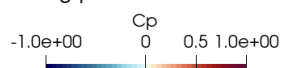


Figure C.101: Front isometric view of the C_p of sensor position f and type big puck

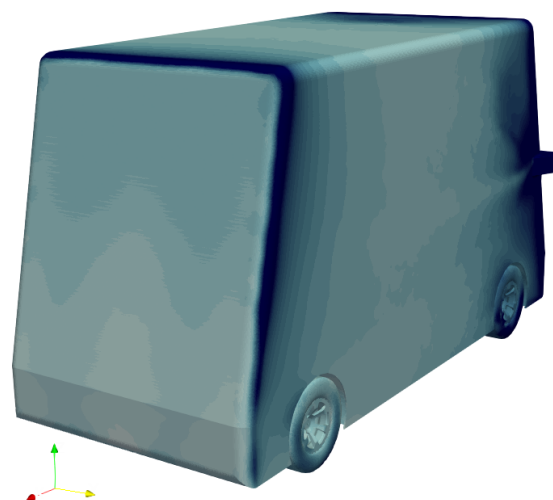


Figure C.102: Rear isometric view of the C_p of sensor position f and type big puck

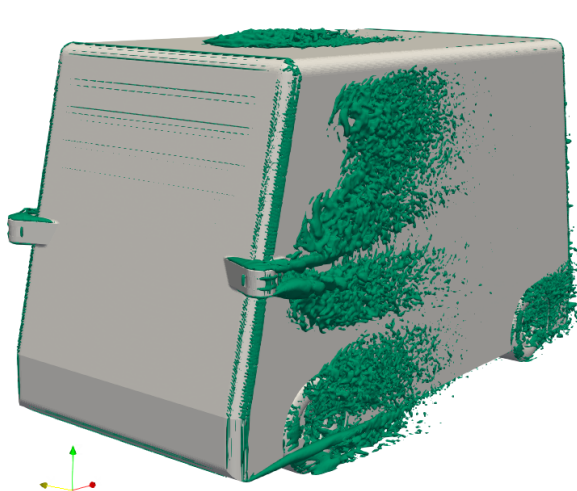


Figure C.103: Front isometric view of the Q-criteria (value $q = 2000 \text{ s}^{-2}$) of sensor position f and type big puck

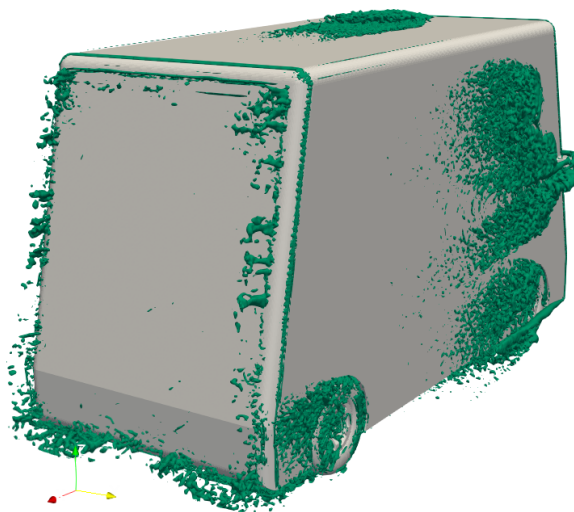


Figure C.104: Rear isometric view of the Q-criteria (value $q = 2000 \text{ s}^{-2}$) of sensor position f and type big puck

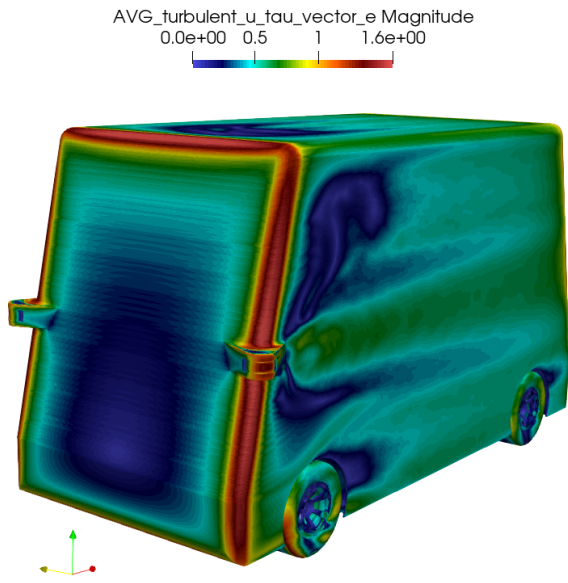


Figure C.105: Front isometric view of the u_τ of sensor position f and type big puck

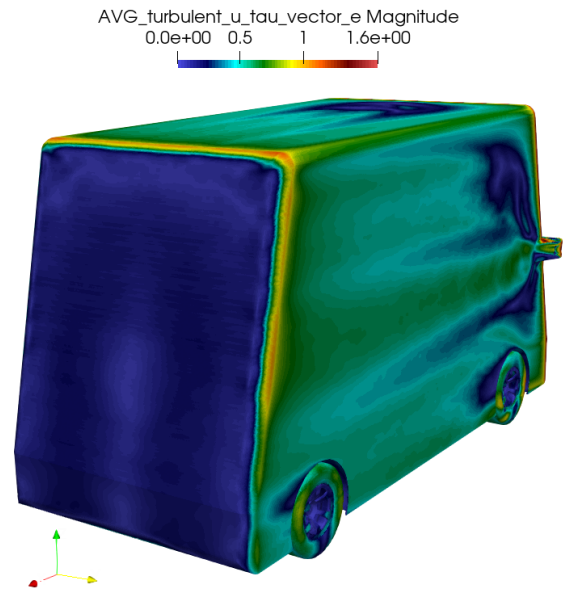


Figure C.106: Rear isometric view of the u_τ of sensor position f and type big puck

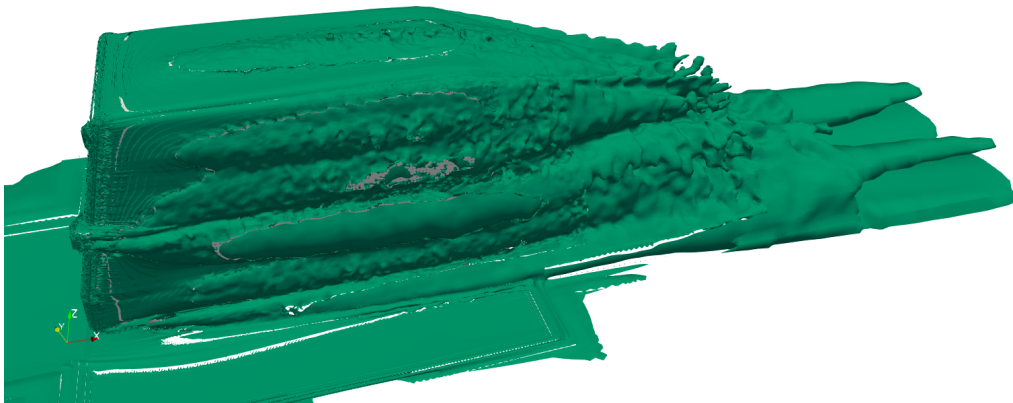


Figure C.107: Side view of the vorticity (value $|\omega| = 10 \text{ s}^{-1}$) of sensor position f and type big puck

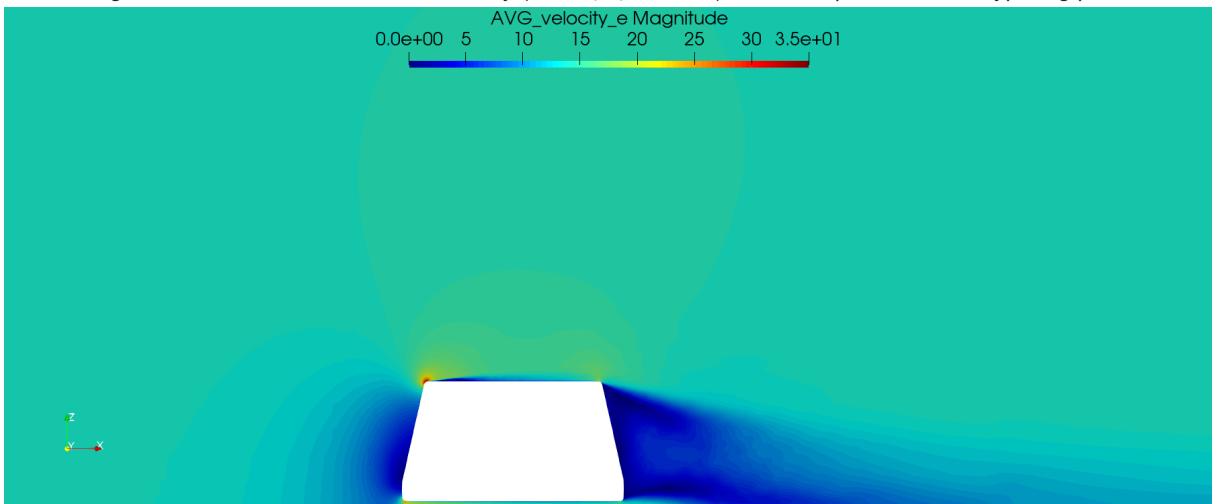


Figure C.108: Side view symmetry plane of the velocity magnitude of sensor position f and type big puck



Figure C.109: Render of sensor position g and type small puck

Sensor position g and type small puck

Table C.13: Data table of sensor position g and type small puck

| | |
|-----------------|------------|
| Sensor position | g |
| Sensor type | small puck |
| ΔC_d | -26 |

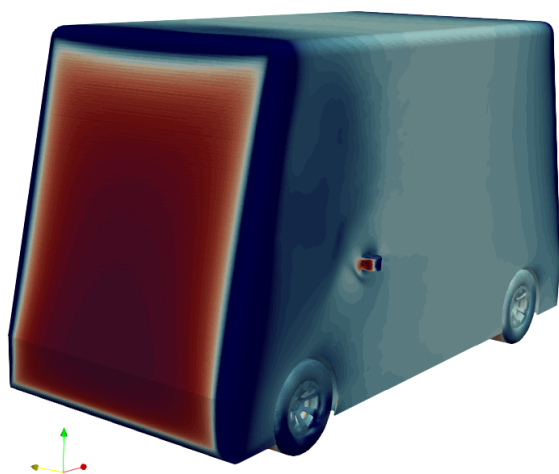


Figure C.110: Front isometric view of the C_p of sensor position g and type small puck

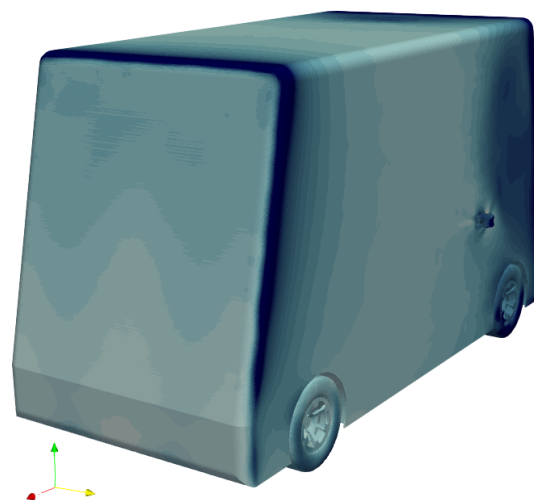


Figure C.111: Rear isometric view of the C_p of sensor position g and type small puck

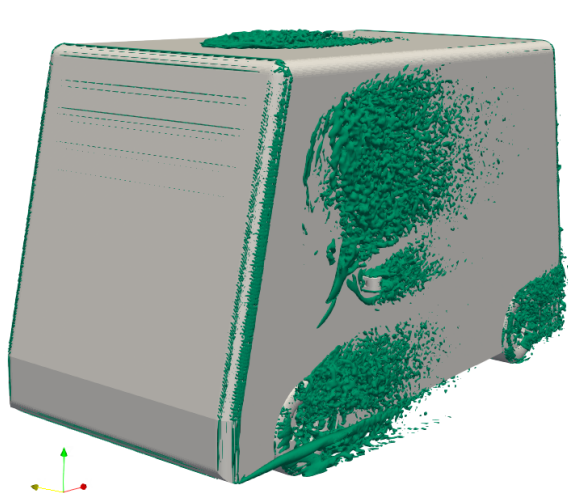


Figure C.112: Front isometric view of the Q-criteria (value $q = 2000 \text{ s}^{-2}$) of sensor position g and type small puck

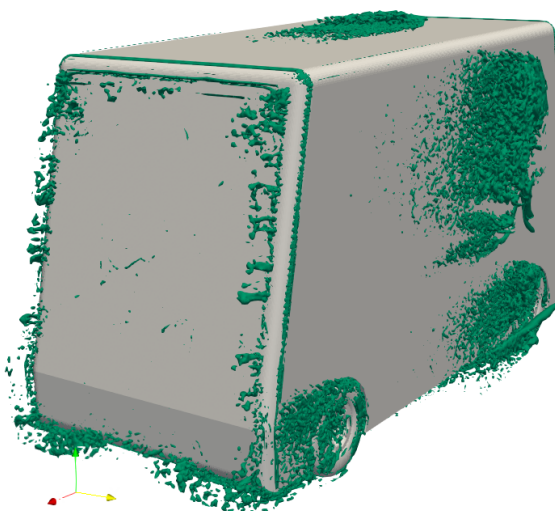


Figure C.113: Rear isometric view of the Q-criteria (value $q = 2000 \text{ s}^{-2}$) of sensor position g and type small puck

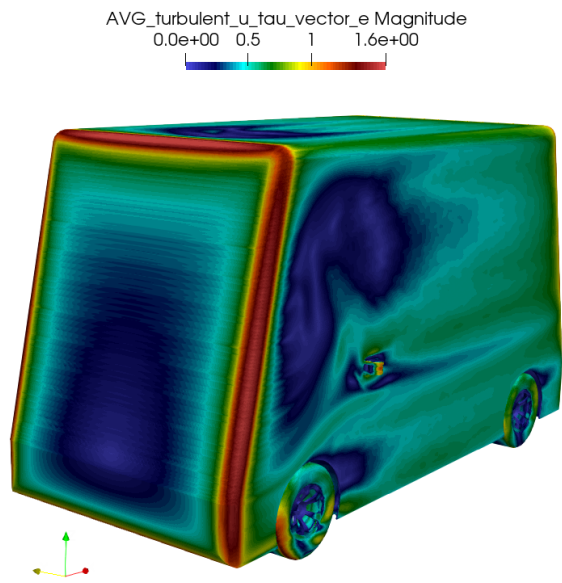


Figure C.114: Front isometric view of the u_τ of sensor position g and type small puck

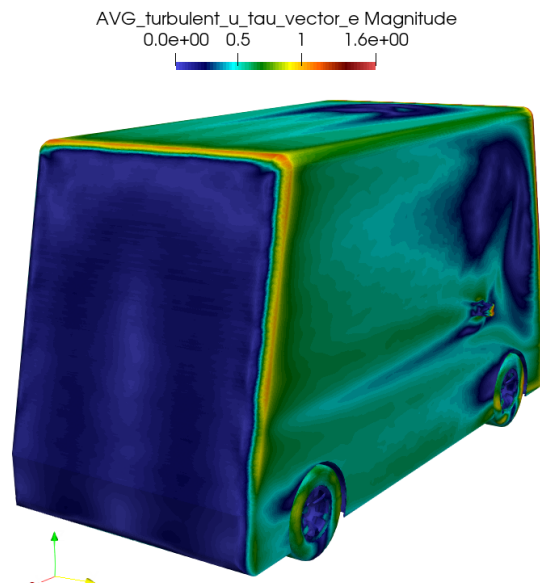


Figure C.115: Rear isometric view of the u_τ of sensor position g and type small puck

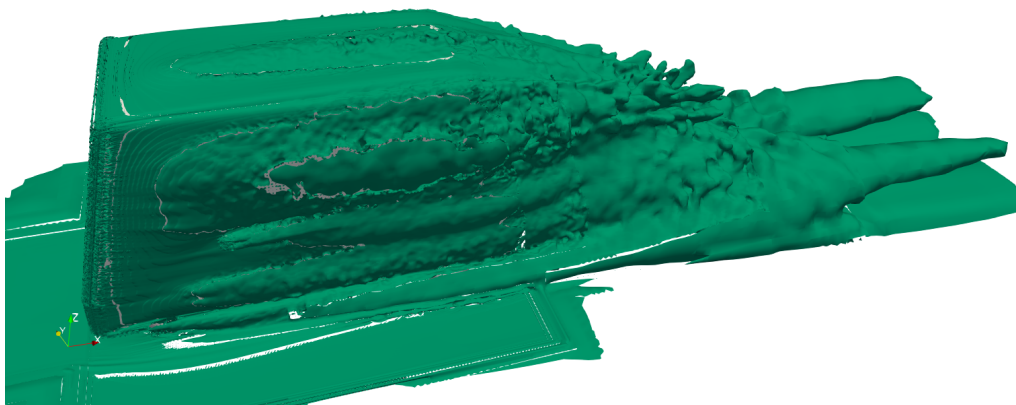


Figure C.116: Side view of the vorticity (value $|\omega| = 10 \text{ s}^{-1}$) of sensor position g and type small puck

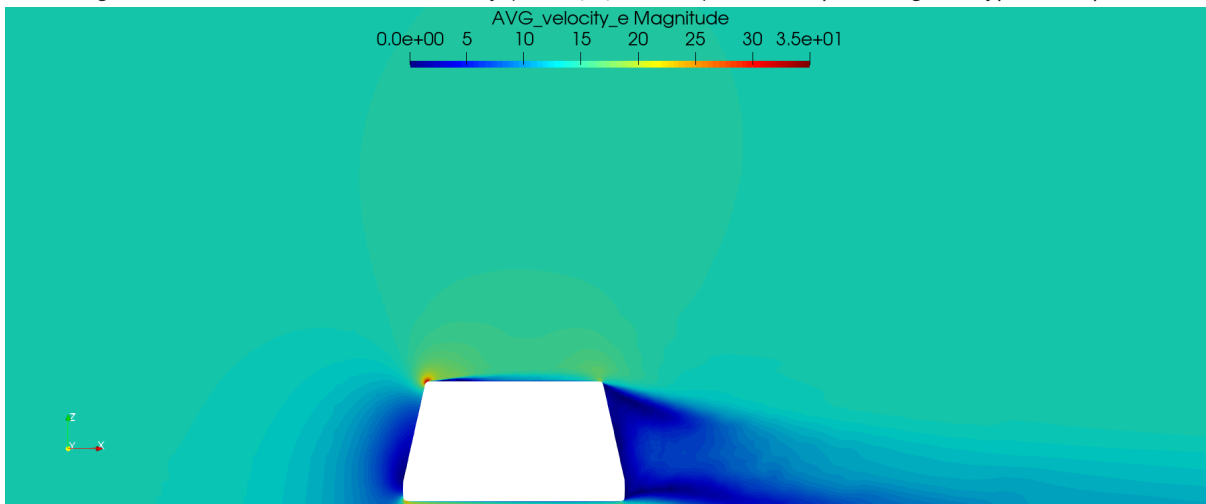


Figure C.117: Side view symmetry plane of the velocity magnitude of sensor position g and type small puck



Figure C.118: Render of sensor position g and type big puck

Sensor position g and type big puck

Table C.14: Data table of sensor position g and type big puck

| | |
|-----------------|----------|
| Sensor position | g |
| Sensor type | big puck |
| ΔC_d | -33 |

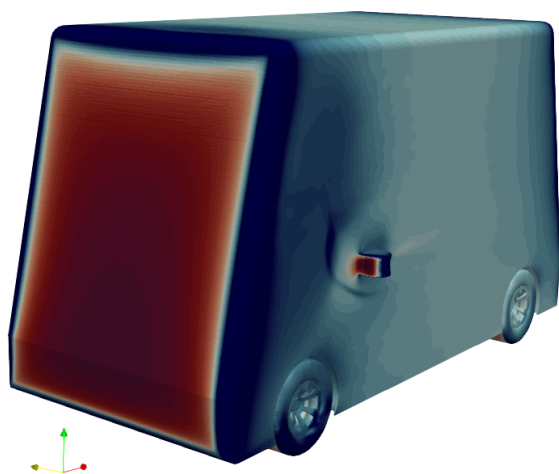


Figure C.119: Front isometric view of the C_p of sensor position g and type big puck

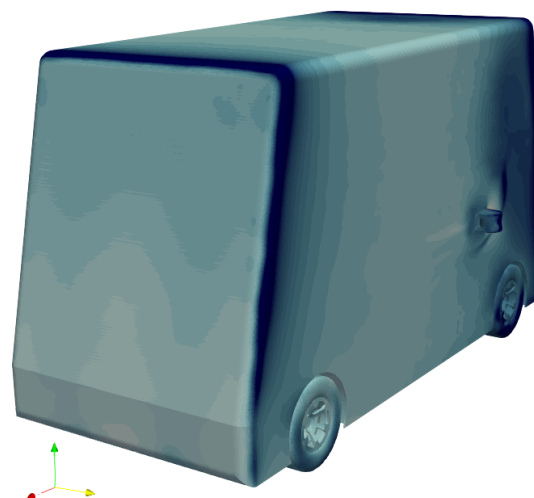
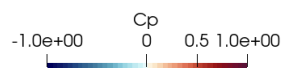


Figure C.120: Rear isometric view of the C_p of sensor position g and type big puck

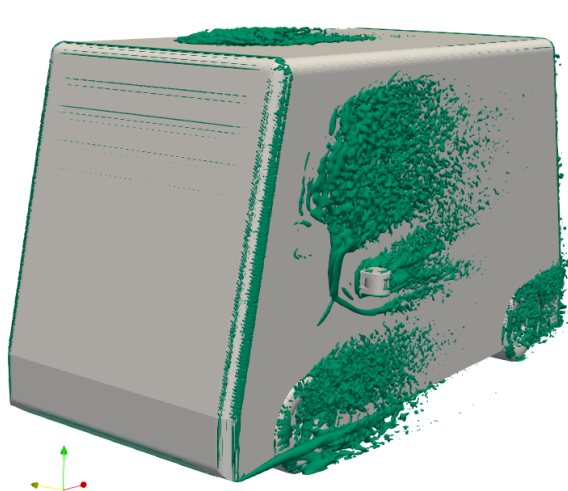


Figure C.121: Front isometric view of the Q-criteria (value $q = 2000 \text{ s}^{-2}$) of sensor position g and type big puck

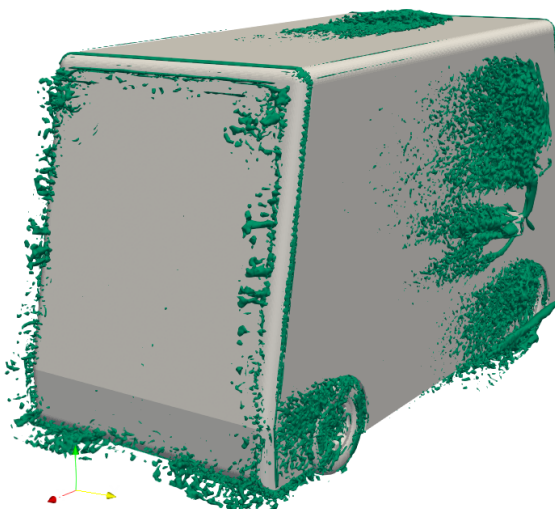


Figure C.122: Rear isometric view of the Q-criteria (value $q = 2000 \text{ s}^{-2}$) of sensor position g and type big puck

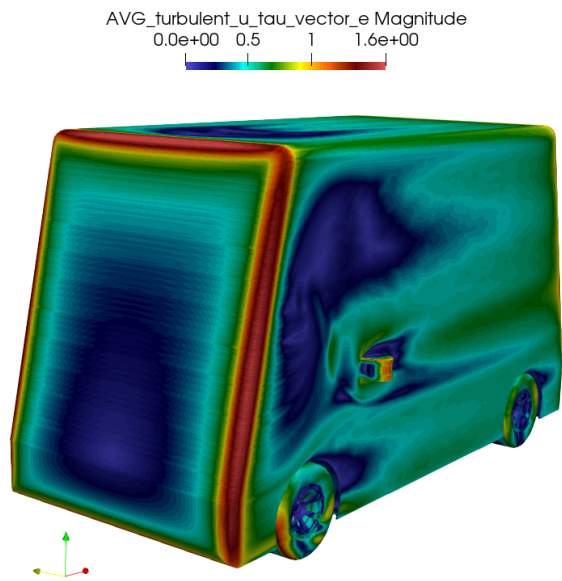


Figure C.123: Front isometric view of the u_τ of sensor position g and type big puck

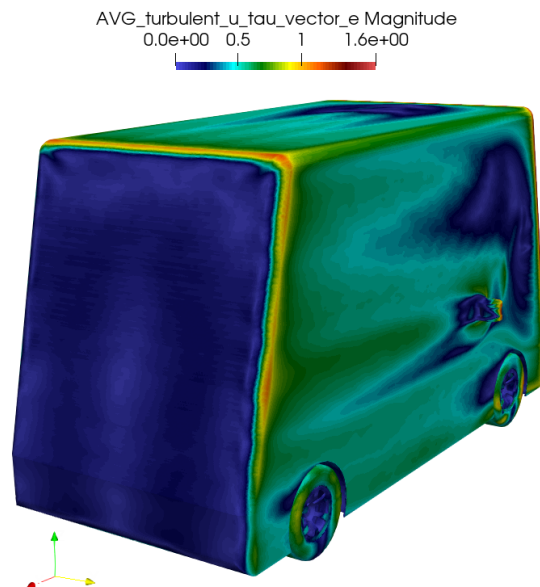


Figure C.124: Rear isometric view of the u_τ of sensor position g and type big puck

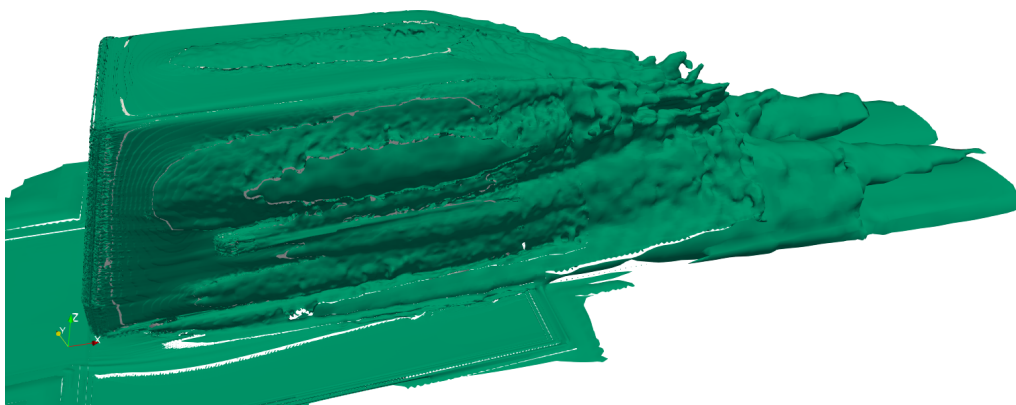


Figure C.125: Side view of the vorticity (value $|\omega| = 10 \text{ s}^{-1}$) of sensor position g and type big puck

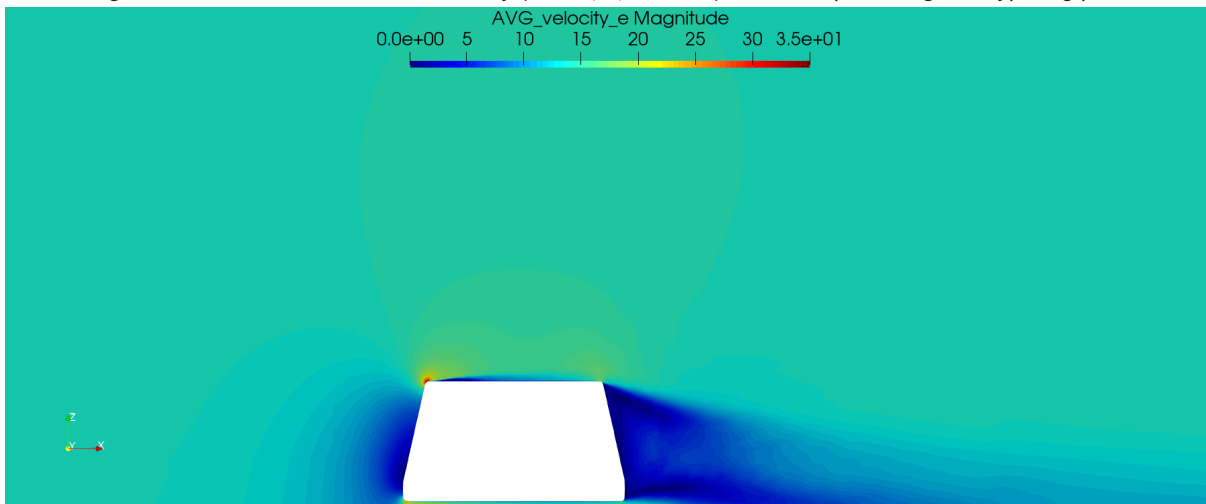


Figure C.126: Side view symmetry plane of the velocity magnitude of sensor position g and type big puck

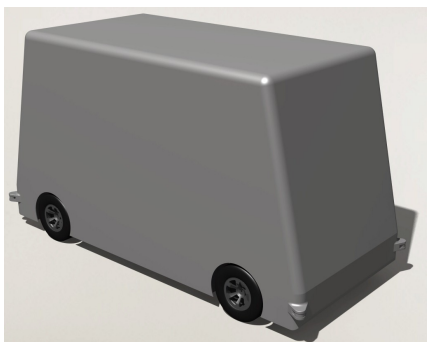


Figure C.127: Render of sensor position h and type small puck

Sensor position h and type **small puck**

Table C.15: Data table of sensor position h and type small puck

| Sensor position | h |
|-----------------|------------|
| Sensor type | small puck |
| ΔC_d | 47 |

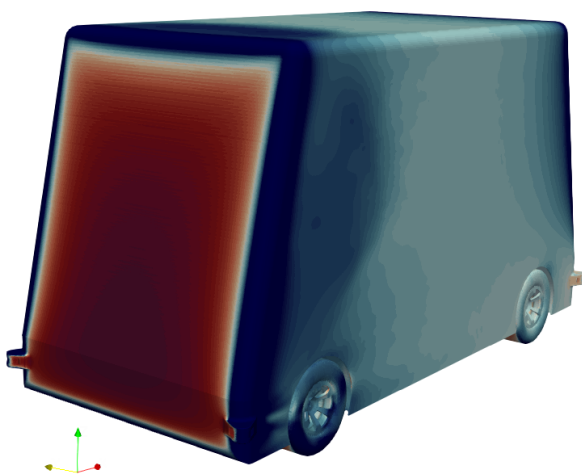


Figure C.128: Front isometric view of the C_p of sensor position h and type small puck

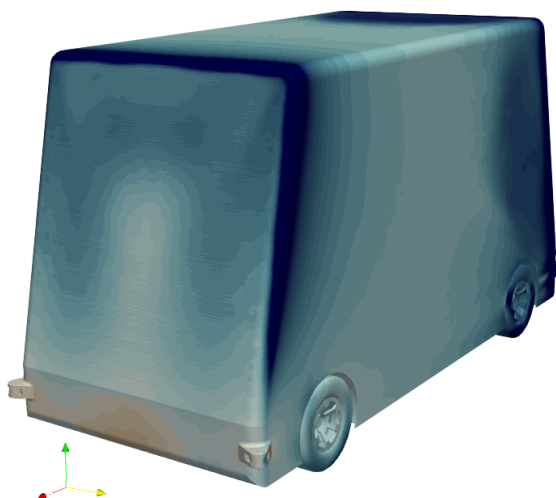


Figure C.129: Rear isometric view of the C_p of sensor position h and type small puck

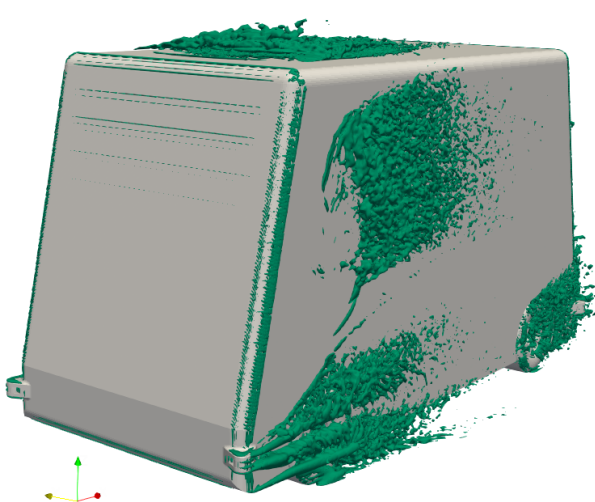


Figure C.130: Front isometric view of the Q-criteria (value $q = 2000 \text{ s}^{-2}$) of sensor position h and type small puck

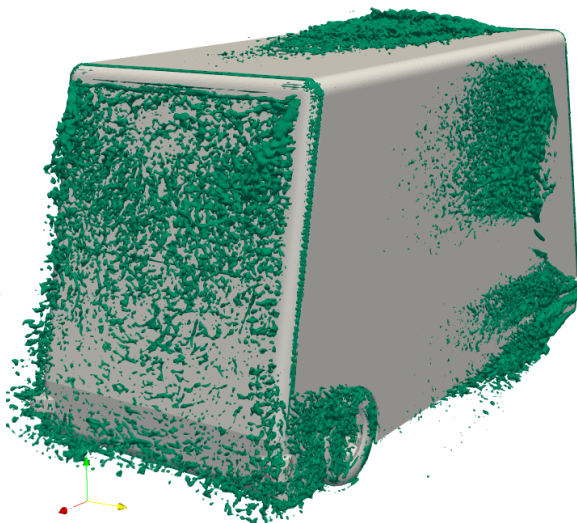


Figure C.131: Rear isometric view of the Q-criteria (value $q = 2000 \text{ s}^{-2}$) of sensor position h and type small puck

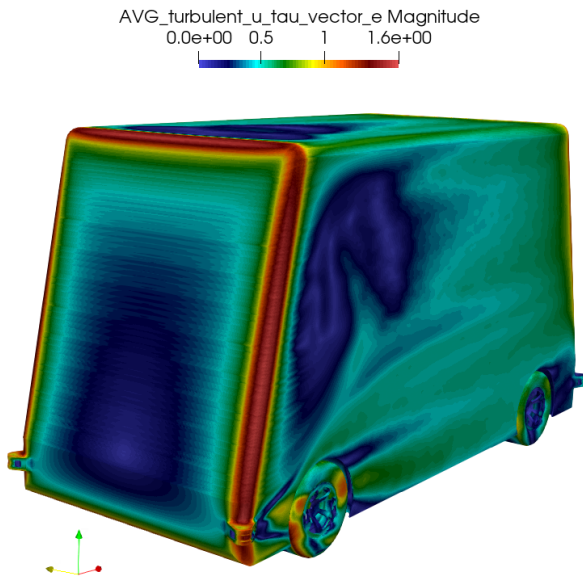


Figure C.132: Front isometric view of the u_τ of sensor position h and type small puck

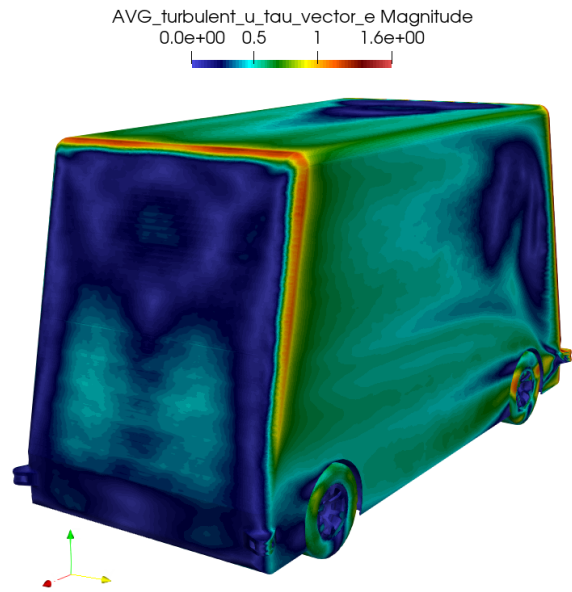


Figure C.133: Rear isometric view of the u_τ of sensor position h and type small puck

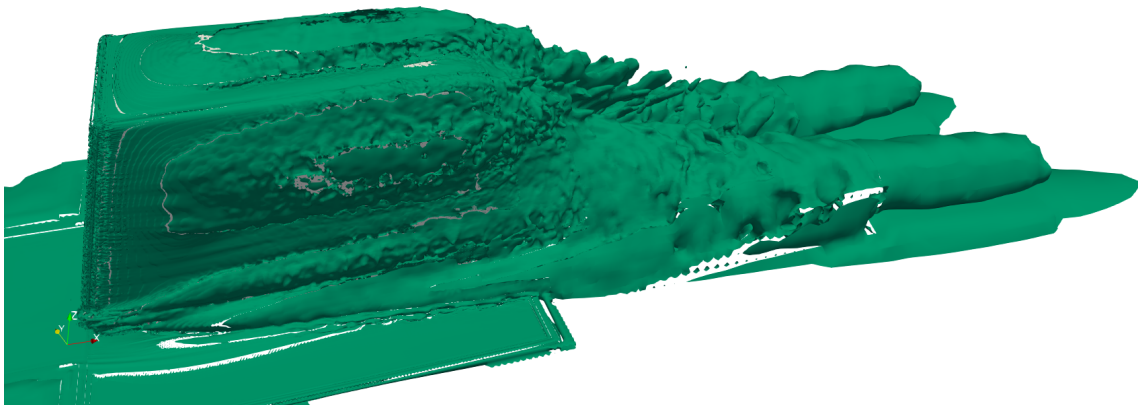


Figure C.134: Side view of the vorticity (value $|\omega| = 10 \text{ s}^{-1}$) of sensor position h and type small puck

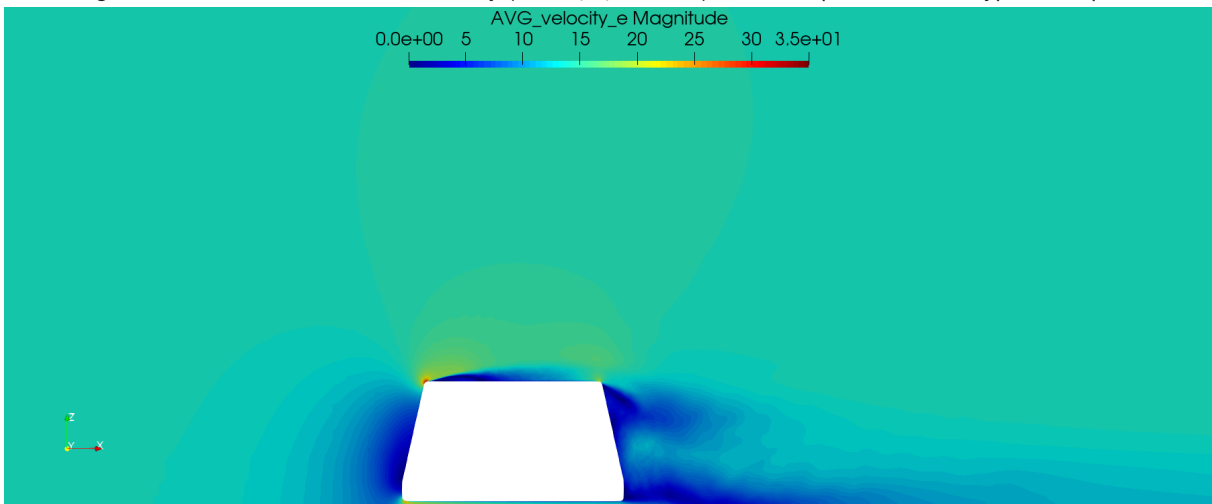


Figure C.135: Side view symmetry plane of the velocity magnitude of sensor position h and type small puck

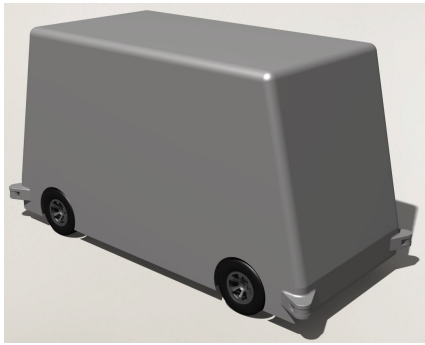


Figure C.136: Render of sensor position h and type big puck

Sensor position h and type **big puck**

Table C.16: Data table of sensor position h and type big puck

| Sensor position | h |
|-----------------|----------|
| Sensor type | big puck |
| ΔC_d | 24 |

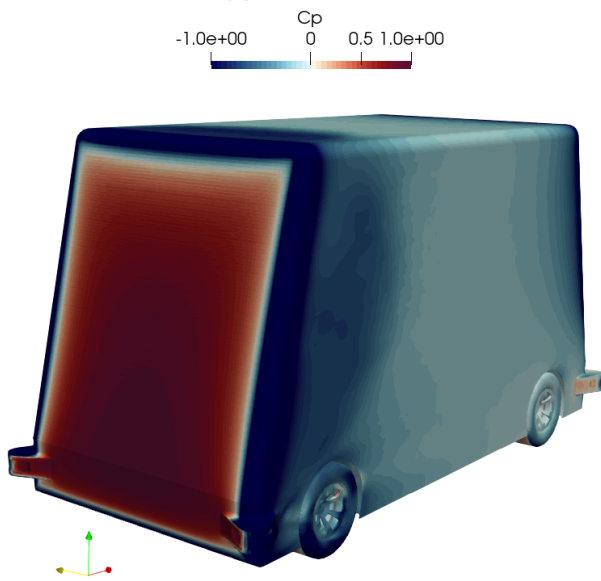


Figure C.137: Front isometric view of the C_p of sensor position h and type big puck

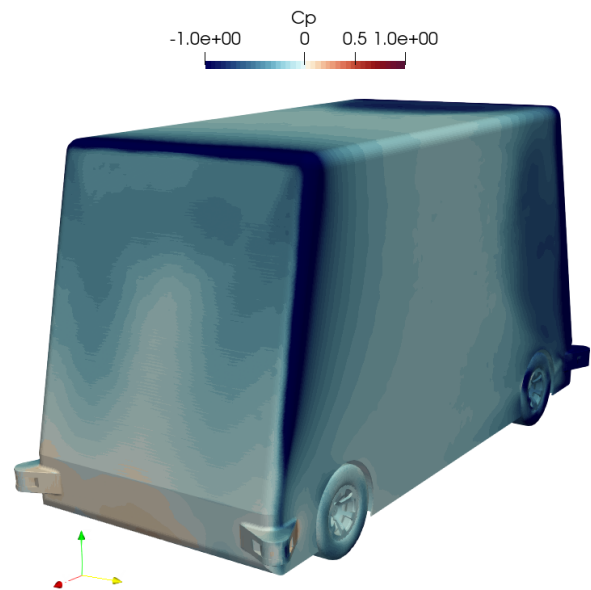


Figure C.138: Rear isometric view of the C_p of sensor position h and type big puck

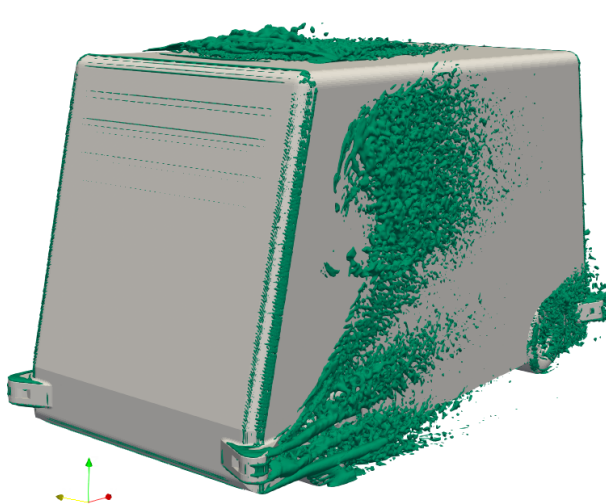


Figure C.139: Front isometric view of the Q-criteria (value $q = 2000 \text{ s}^{-2}$) of sensor position h and type big puck

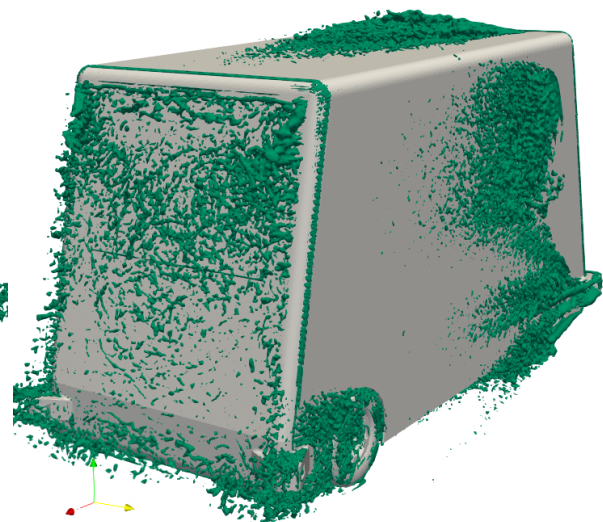


Figure C.140: Rear isometric view of the Q-criteria (value $q = 2000 \text{ s}^{-2}$) of sensor position h and type big puck

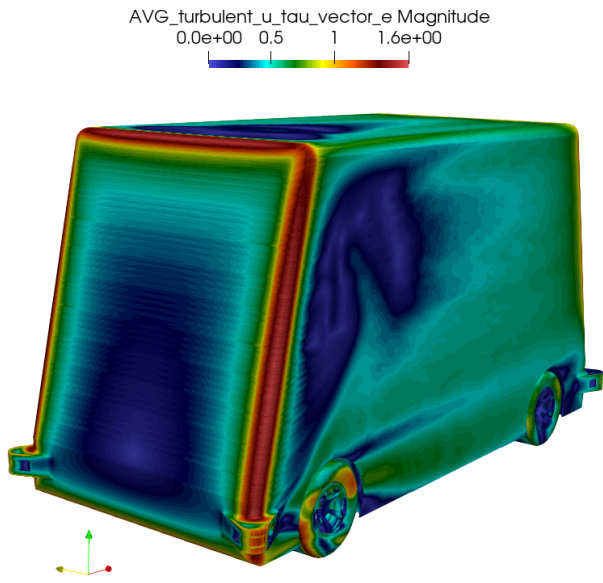


Figure C.141: Front isometric view of the u_τ of sensor position h and type big puck

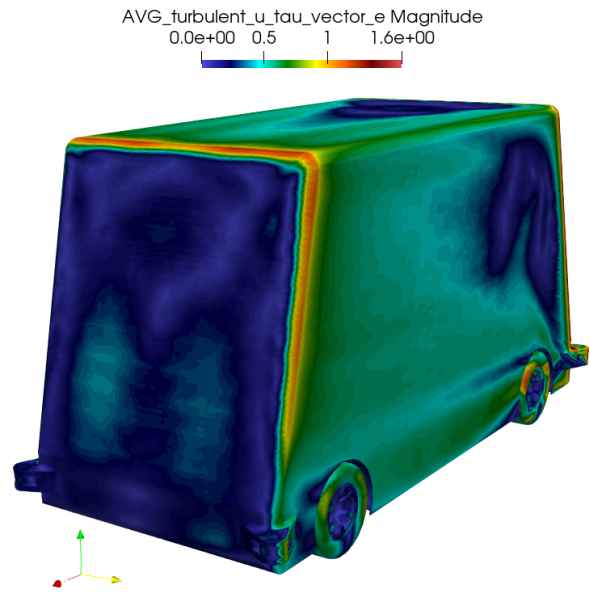


Figure C.142: Rear isometric view of the u_τ of sensor position h and type big puck

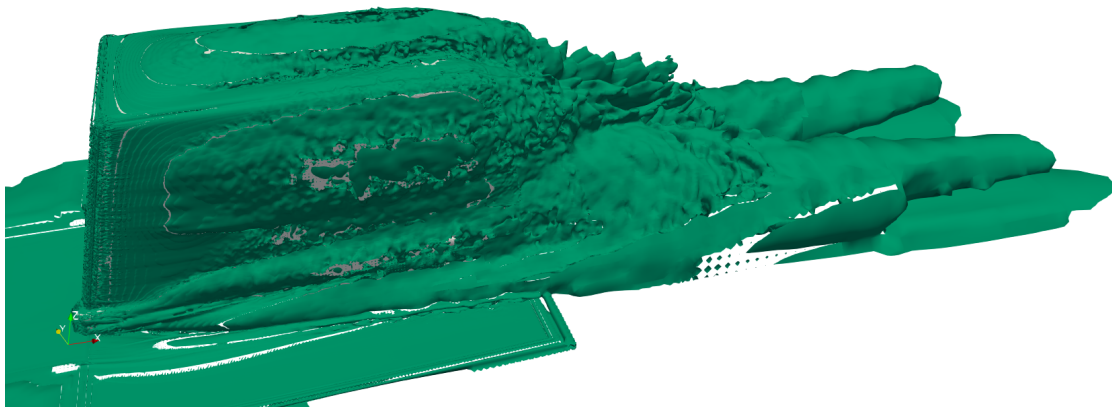


Figure C.143: Side view of the vorticity (value $|\omega| = 10 \text{ s}^{-1}$) of sensor position h and type big puck

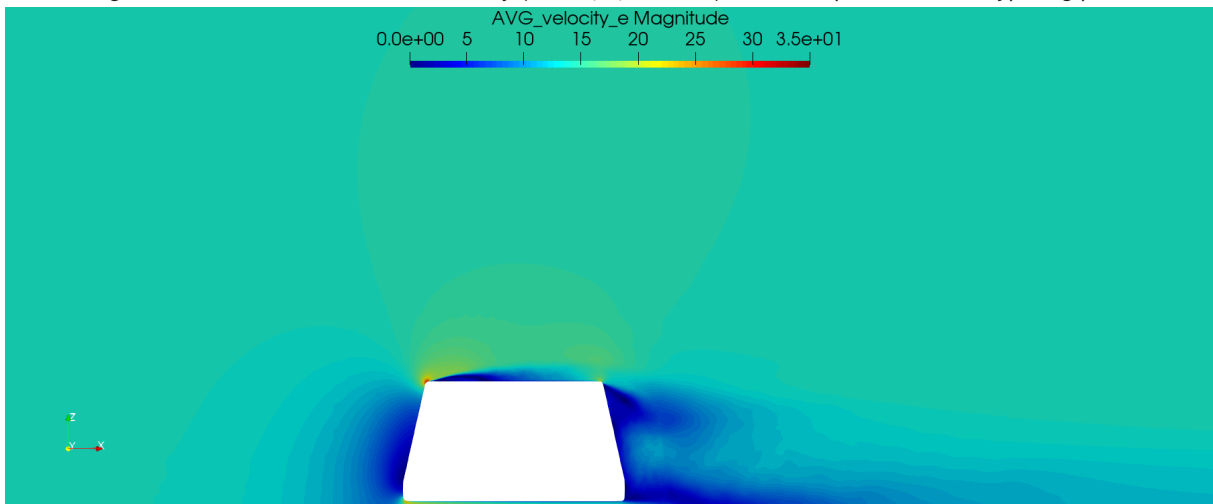


Figure C.144: Side view symmetry plane of the velocity magnitude of sensor position h and type big puck

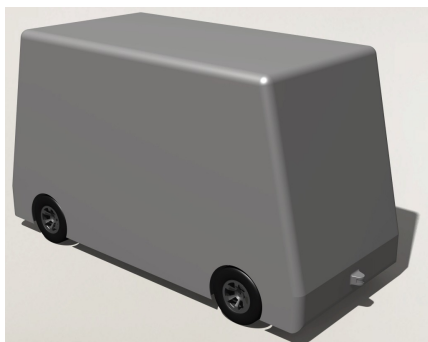


Figure C.145: Render of sensor position i and type small puck

Sensor position i and type **small puck**

Table C.17: Data table of sensor position i and type small puck

| Sensor position | i |
|-----------------|------------|
| Sensor type | small puck |
| ΔC_d | 19 |

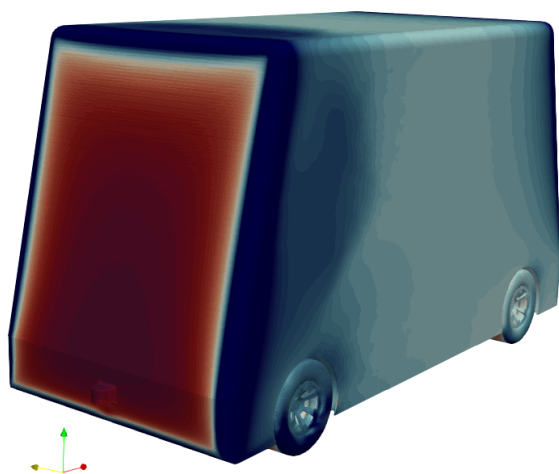


Figure C.146: Front isometric view of the C_p of sensor position i and type small puck

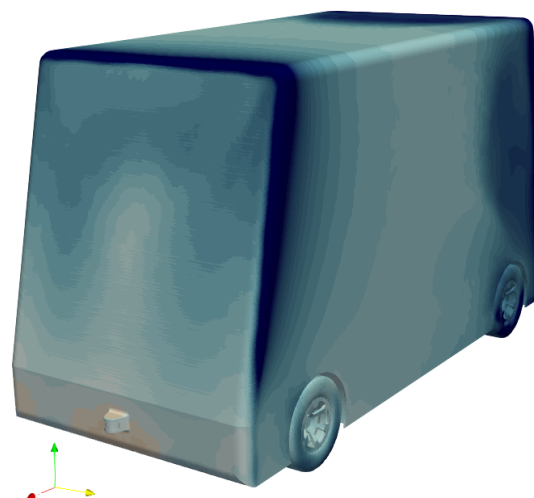


Figure C.147: Rear isometric view of the C_p of sensor position i and type small puck

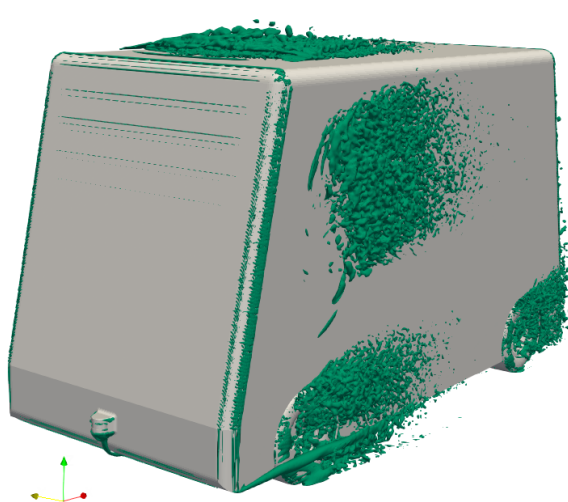


Figure C.148: Front isometric view of the Q-criteria (value $q = 2000 \text{ s}^{-2}$) of sensor position i and type small puck

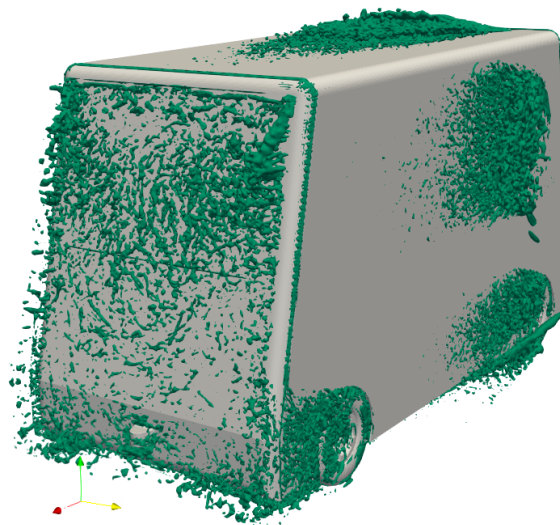


Figure C.149: Rear isometric view of the Q-criteria (value $q = 2000 \text{ s}^{-2}$) of sensor position i and type small puck

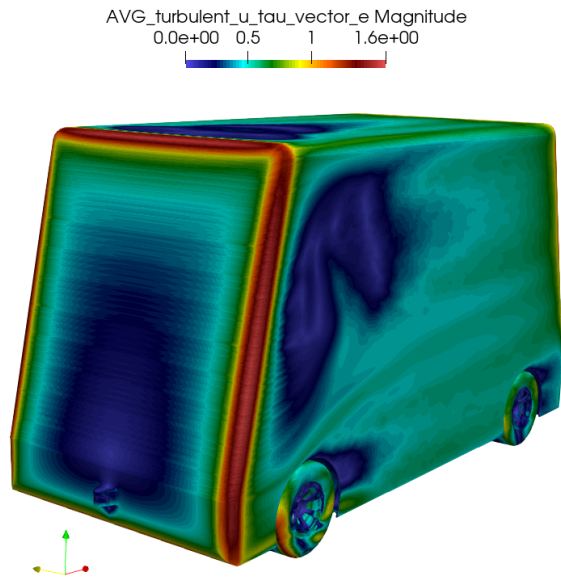


Figure C.150: Front isometric view of the u_τ of sensor position i and type small puck

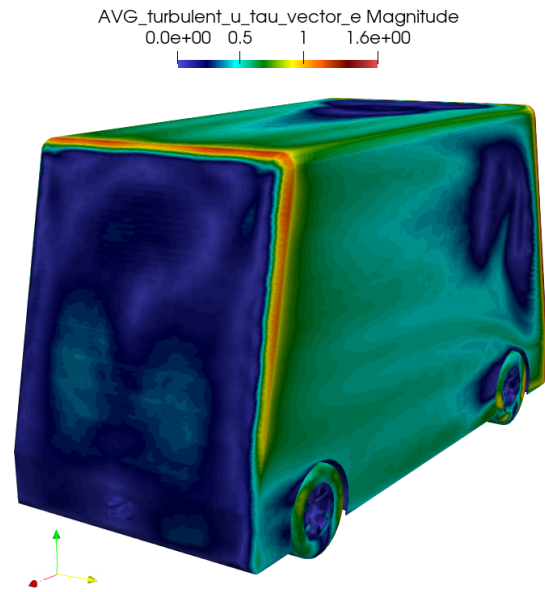


Figure C.151: Rear isometric view of the u_τ of sensor position i and type small puck

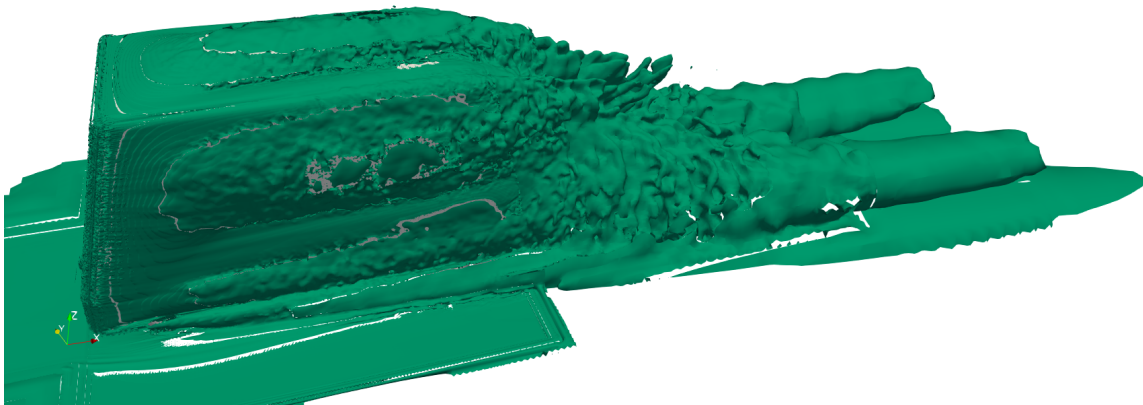


Figure C.152: Side view of the vorticity (value $|\omega| = 10 \text{ s}^{-1}$) of sensor position i and type small puck

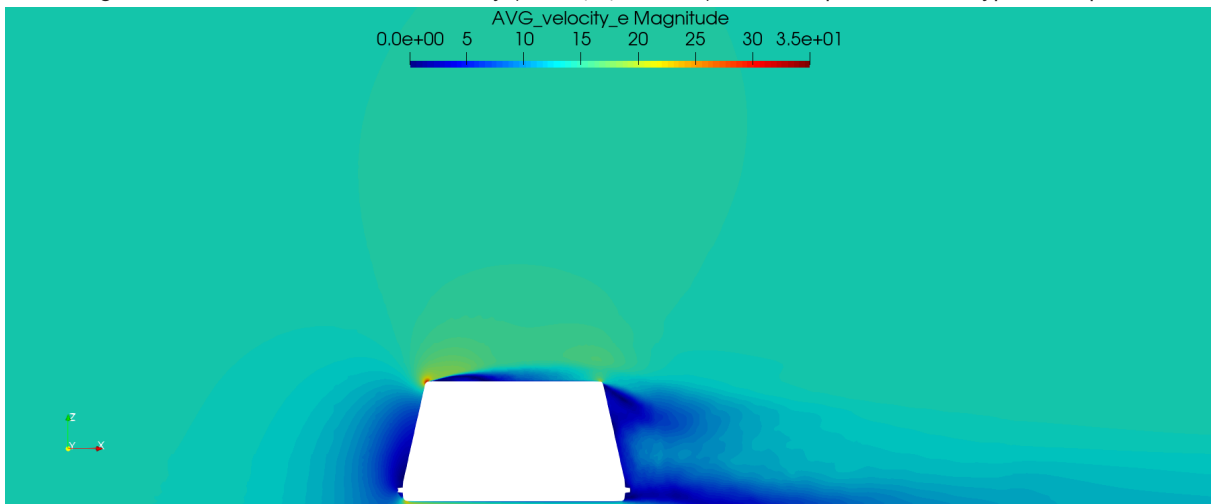


Figure C.153: Side view symmetry plane of the velocity magnitude of sensor position i and type small puck

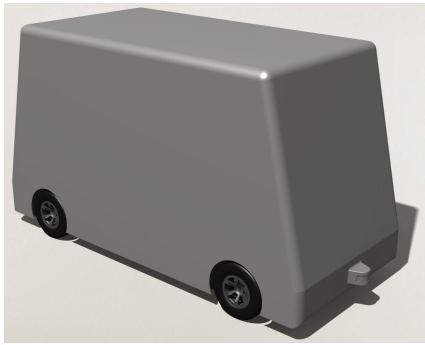


Figure C.154: Render of sensor position i and type big puck

Sensor position i and type **big puck**

Table C.18: Data table of sensor position i and type big puck

| Sensor position | i |
|-----------------|----------|
| Sensor type | big puck |
| ΔC_d | 22 |

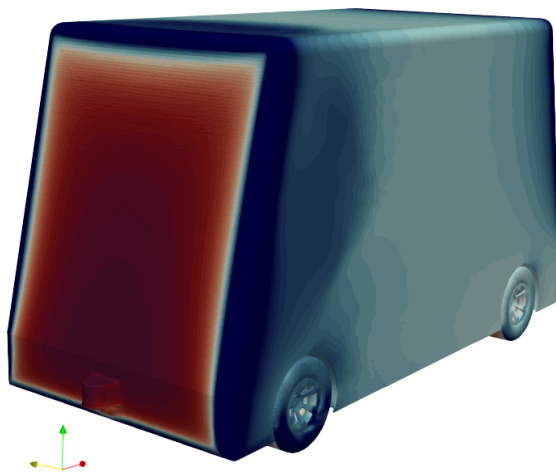
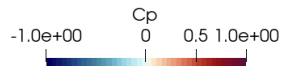


Figure C.155: Front isometric view of the C_p of sensor position i and type big puck

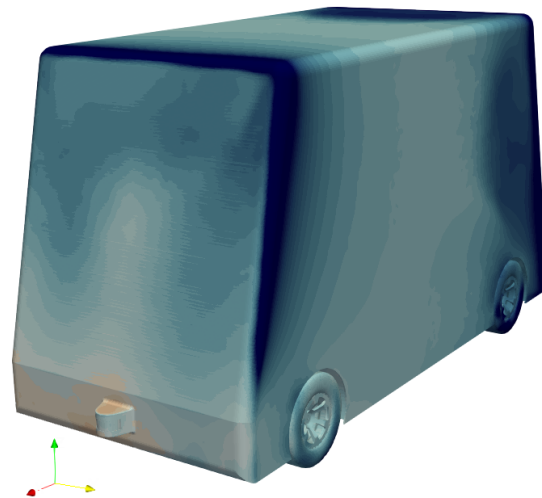
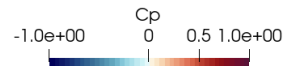


Figure C.156: Rear isometric view of the C_p of sensor position i and type big puck

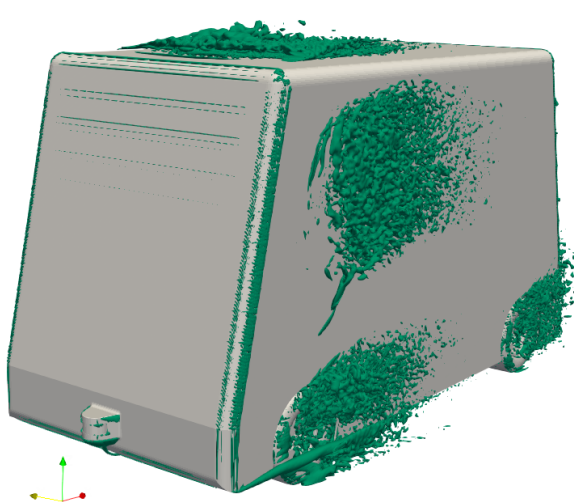


Figure C.157: Front isometric view of the Q-criteria (value $q = 2000 \text{ s}^{-2}$) of sensor position i and type big puck

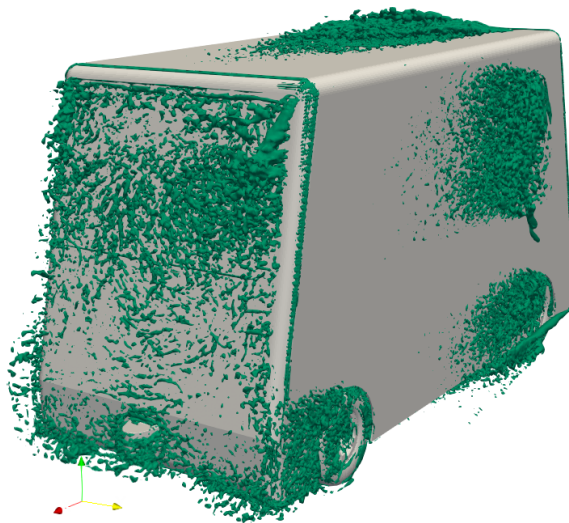


Figure C.158: Rear isometric view of the Q-criteria (value $q = 2000 \text{ s}^{-2}$) of sensor position i and type big puck

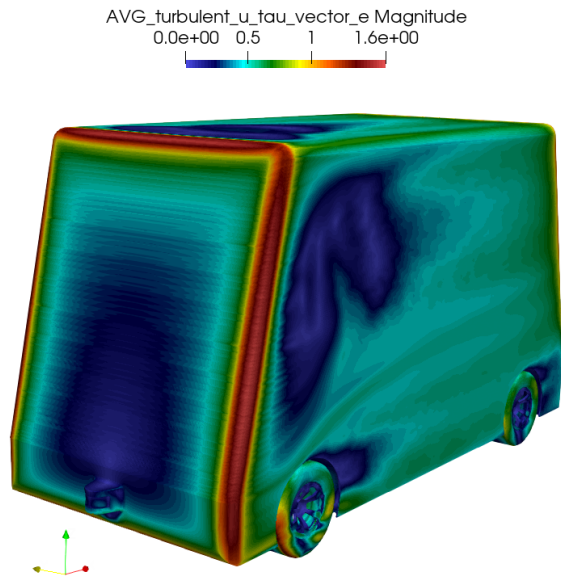


Figure C.159: Front isometric view of the u_τ of sensor position i and type big puck

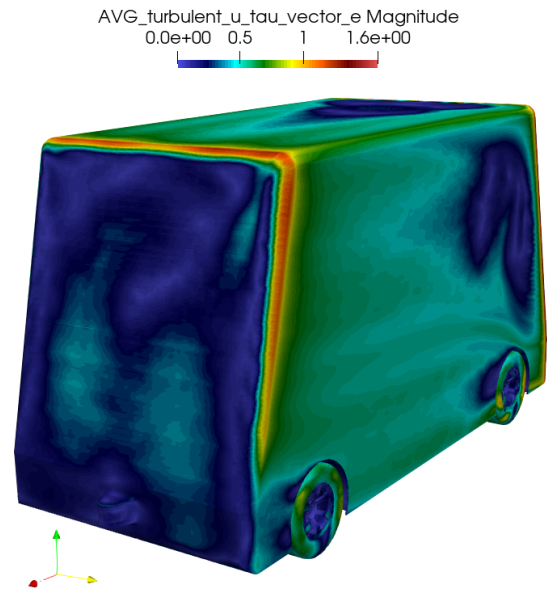


Figure C.160: Rear isometric view of the u_τ of sensor position i and type big puck

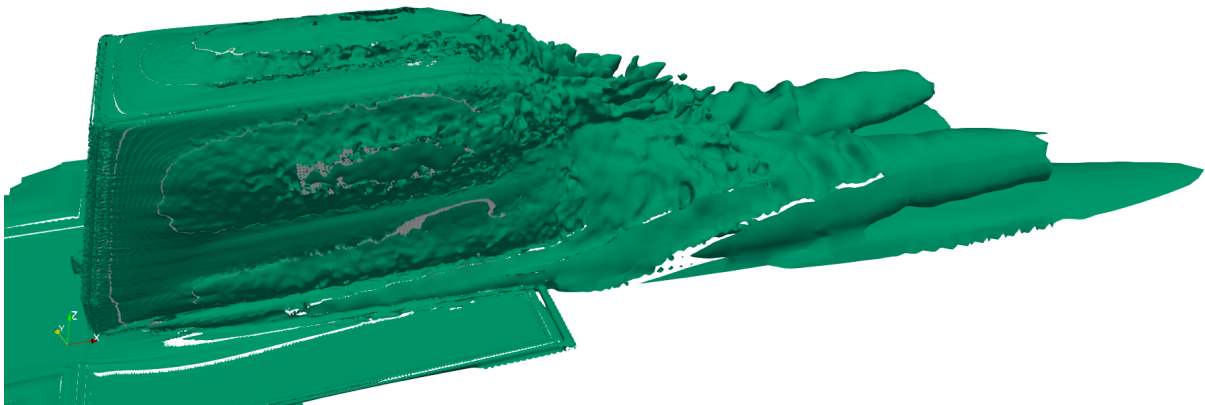


Figure C.161: Side view of the vorticity (value $|\omega| = 10 \text{ s}^{-1}$) of sensor position i and type big puck

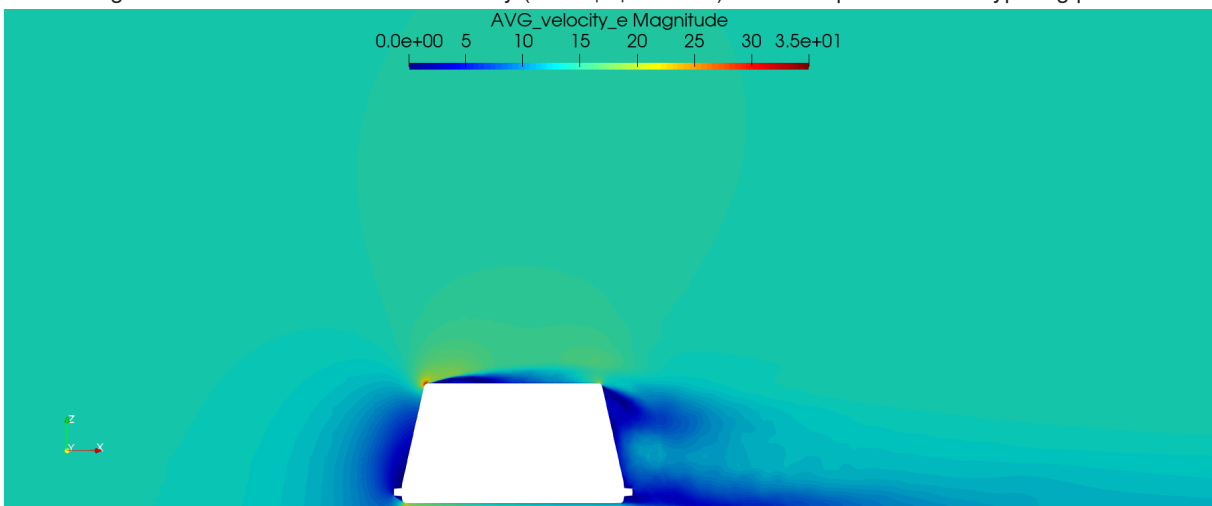


Figure C.162: Side view symmetry plane of the velocity magnitude of sensor position i and type big puck



Figure C.163: Render of sensor position k and type small puck

Sensor position k and type **small puck**

Table C.19: Data table of sensor position k and type small puck

| | |
|-----------------|------------|
| Sensor position | k |
| Sensor type | small puck |
| ΔC_d | -26 |

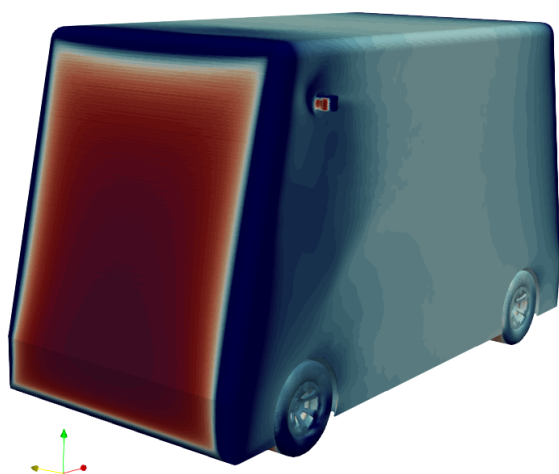


Figure C.164: Front isometric view of the C_p of sensor position k and type small puck

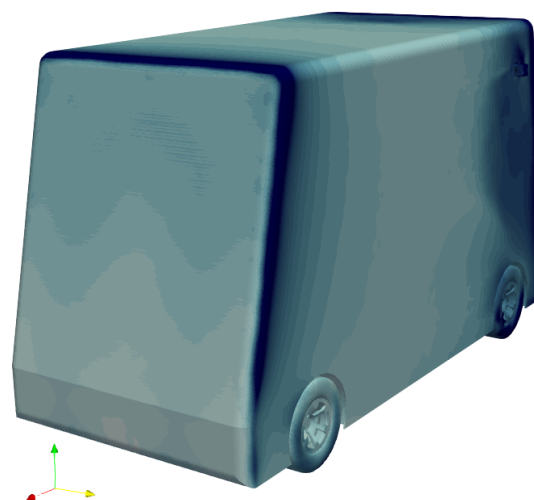


Figure C.165: Rear isometric view of the C_p of sensor position k and type small puck

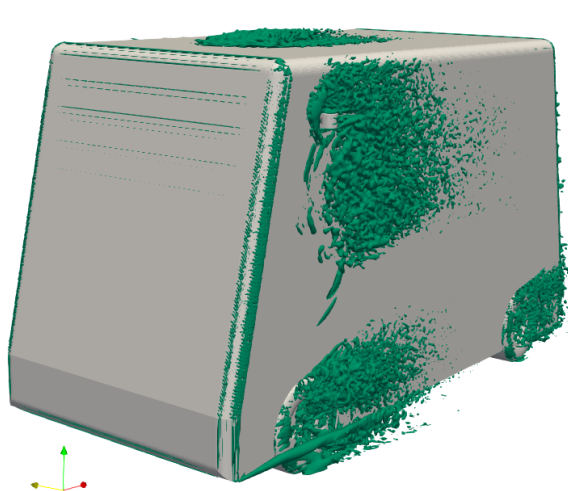


Figure C.166: Front isometric view of the Q-criteria (value $q = 2000 \text{ s}^{-2}$) of sensor position k and type small puck

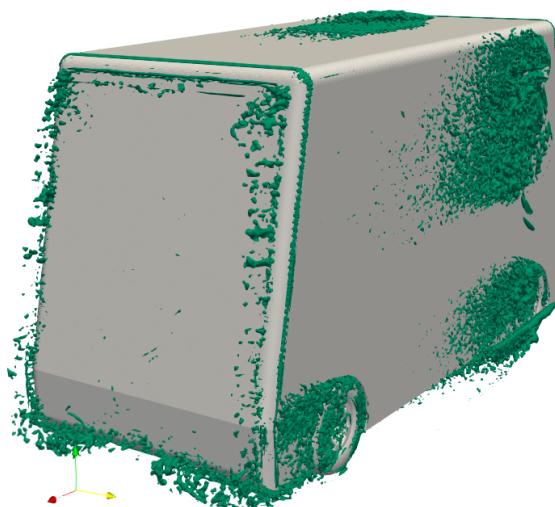


Figure C.167: Rear isometric view of the Q-criteria (value $q = 2000 \text{ s}^{-2}$) of sensor position k and type small puck

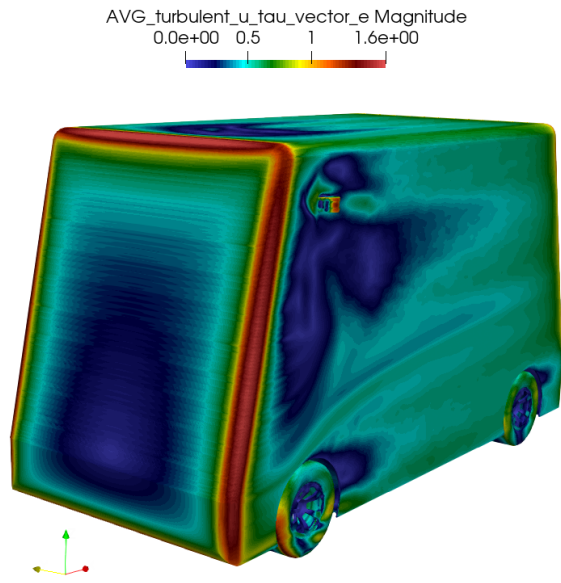


Figure C.168: Front isometric view of the u_τ of sensor position k and type small puck

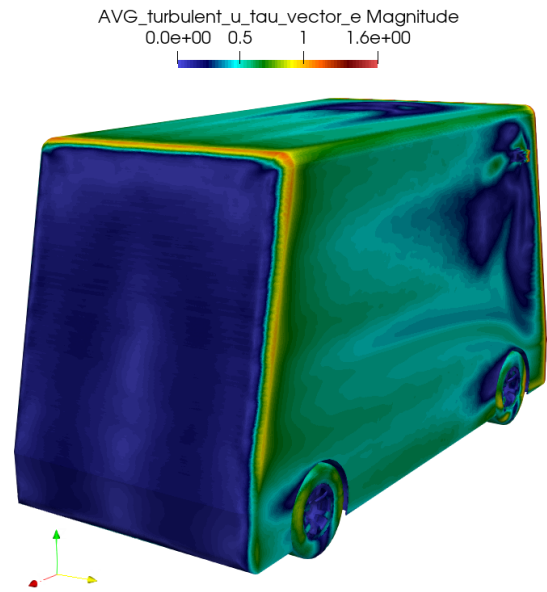


Figure C.169: Rear isometric view of the u_τ of sensor position k and type small puck

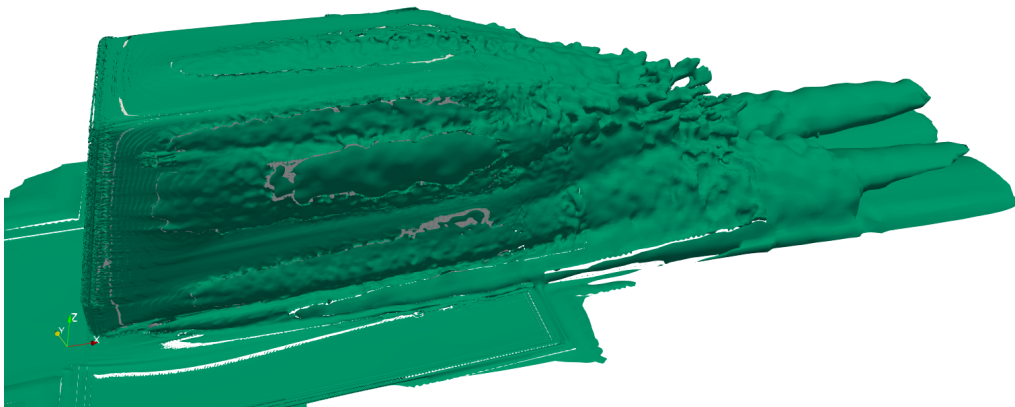


Figure C.170: Side view of the vorticity (value $|\omega| = 10 \text{ s}^{-1}$) of sensor position k and type small puck

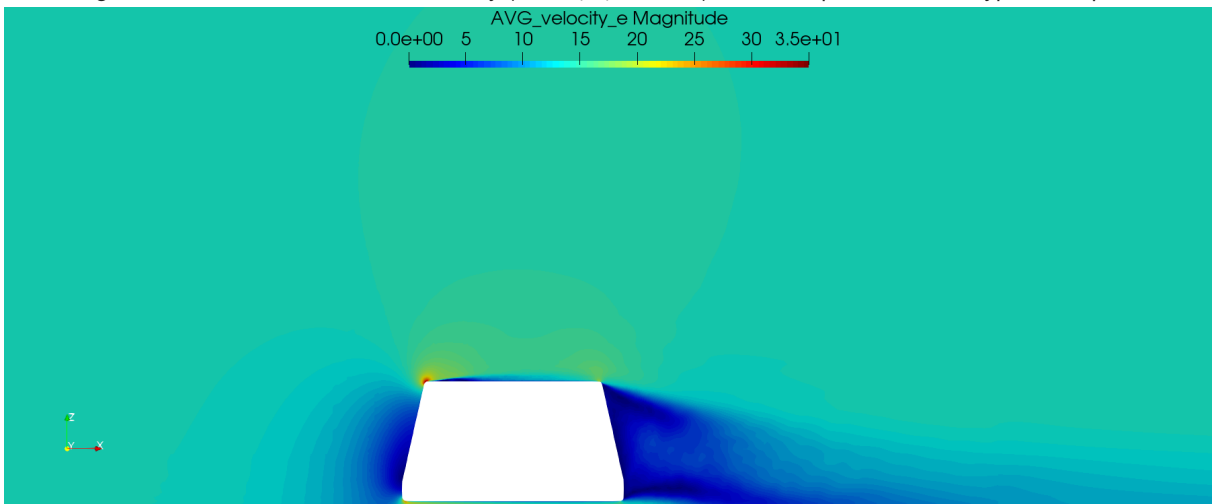


Figure C.171: Side view symmetry plane of the velocity magnitude of sensor position k and type small puck



Figure C.172: Render of sensor position k and type big puck

Sensor position k and type big puck

Table C.20: Data table of sensor position k and type big puck

| Sensor position | k |
|-----------------|----------|
| Sensor type | big puck |
| ΔC_d | -32 |

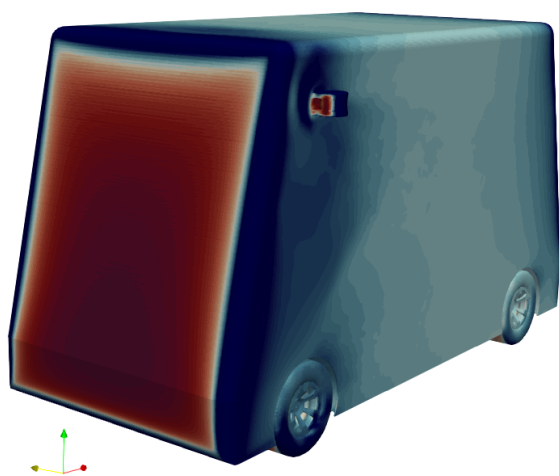
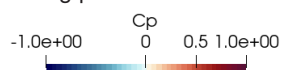


Figure C.173: Front isometric view of the C_p of sensor position k and type big puck

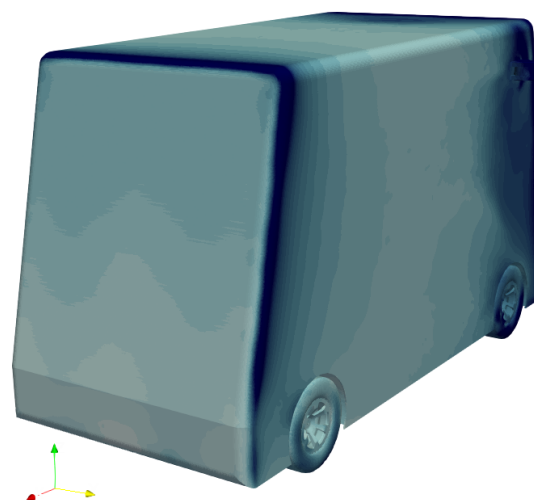


Figure C.174: Rear isometric view of the C_p of sensor position k and type big puck

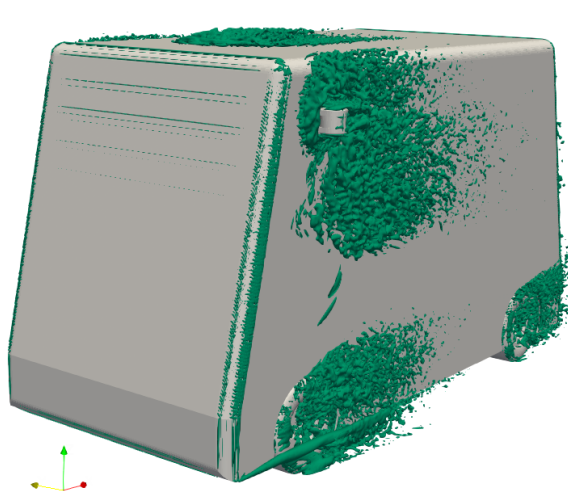


Figure C.175: Front isometric view of the Q-criteria (value $q = 2000 \text{ s}^{-2}$) of sensor position k and type big puck

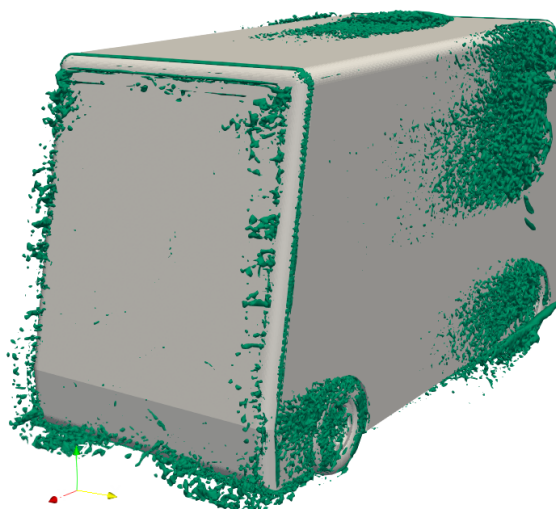


Figure C.176: Rear isometric view of the Q-criteria (value $q = 2000 \text{ s}^{-2}$) of sensor position k and type big puck

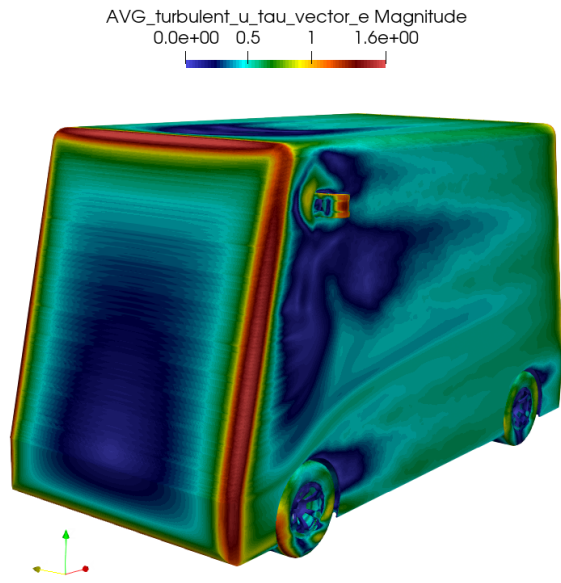


Figure C.177: Front isometric view of the u_τ of sensor position k and type big puck

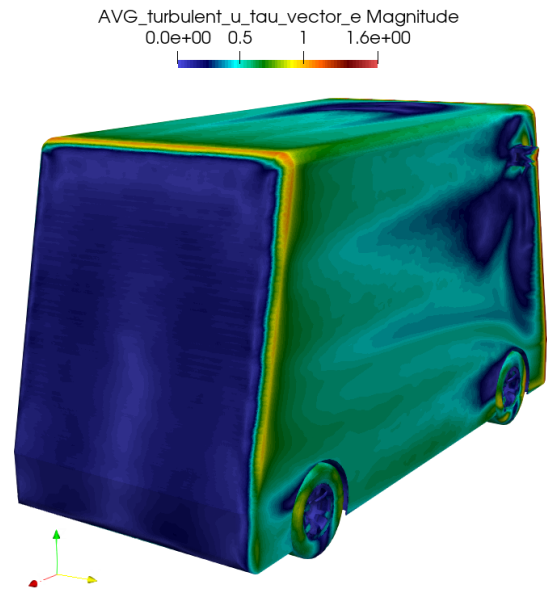


Figure C.178: Rear isometric view of the u_τ of sensor position k and type big puck

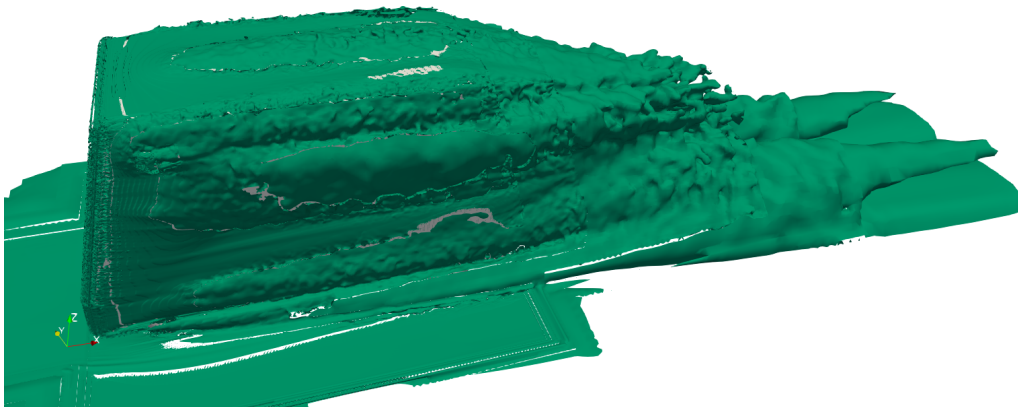


Figure C.179: Side view of the vorticity (value $|\omega| = 10 \text{ s}^{-1}$) of sensor position k and type big puck

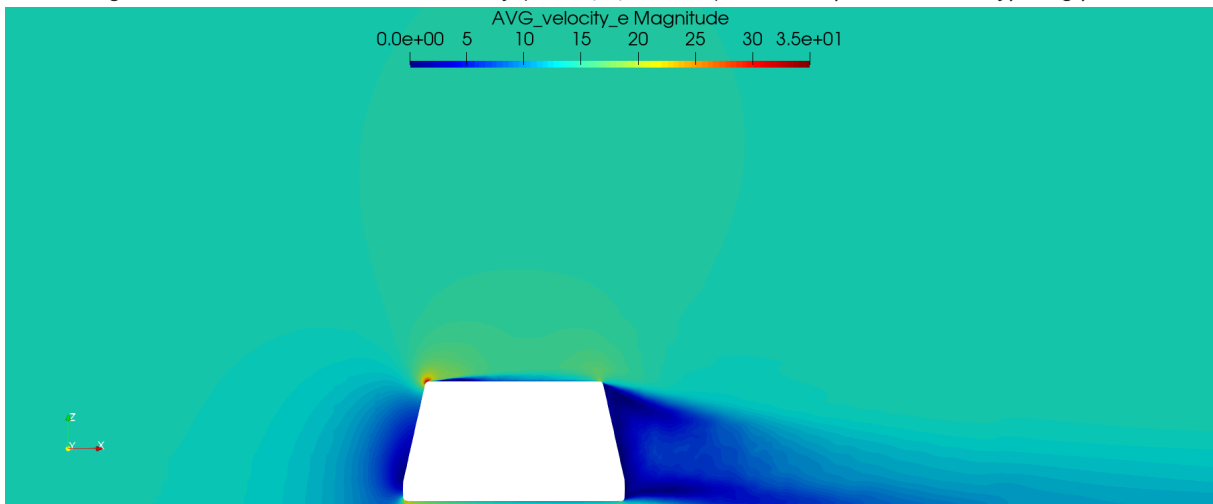


Figure C.180: Side view symmetry plane of the velocity magnitude of sensor position k and type big puck

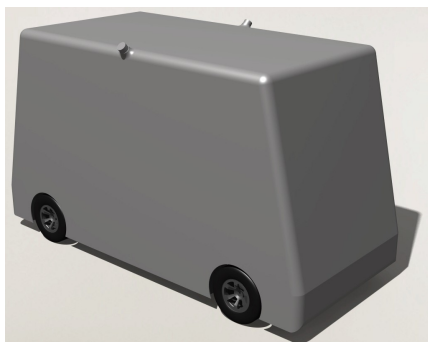


Figure C.181: Render of sensor position I and type small puck

Sensor position I and type **small puck**

Table C.21: Data table of sensor position I and type small puck

| Sensor position | I |
|-----------------|------------|
| Sensor type | small puck |
| ΔC_d | -29 |

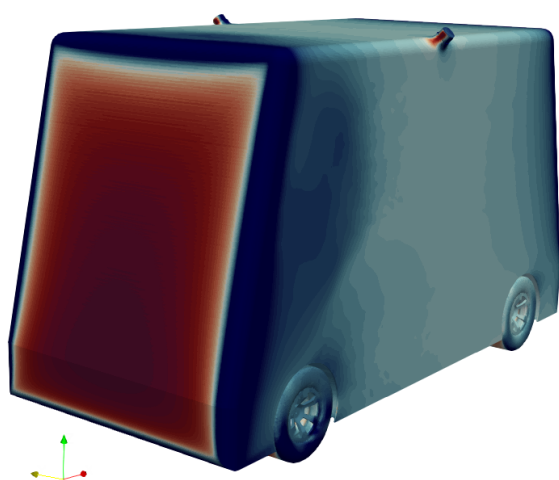


Figure C.182: Front isometric view of the C_p of sensor position I and type small puck

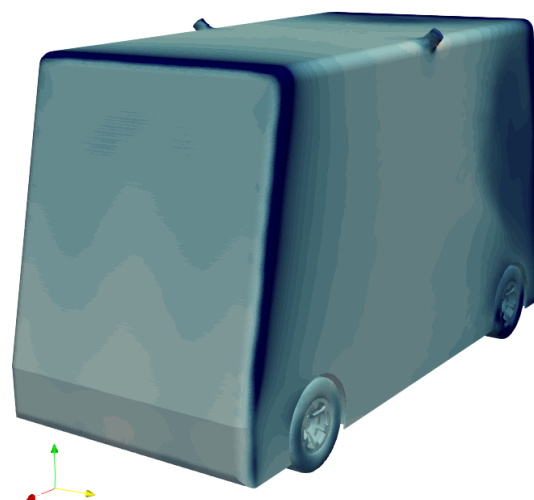


Figure C.183: Rear isometric view of the C_p of sensor position I and type small puck

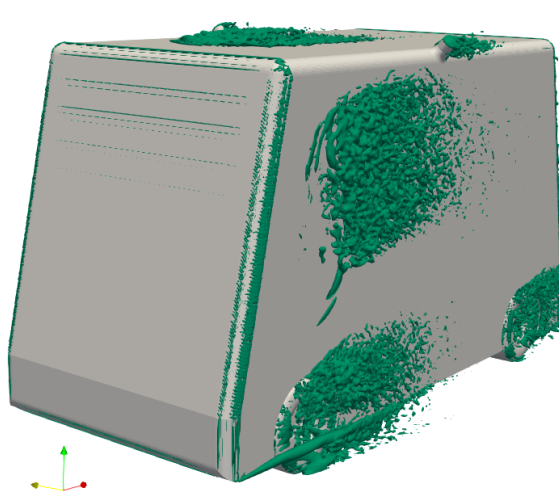


Figure C.184: Front isometric view of the Q-criteria (value $q = 2000 \text{ s}^{-2}$) of sensor position I and type small puck

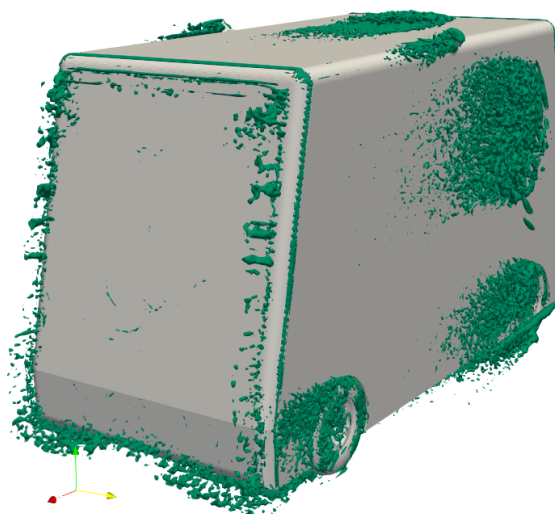


Figure C.185: Rear isometric view of the Q-criteria (value $q = 2000 \text{ s}^{-2}$) of sensor position I and type small puck

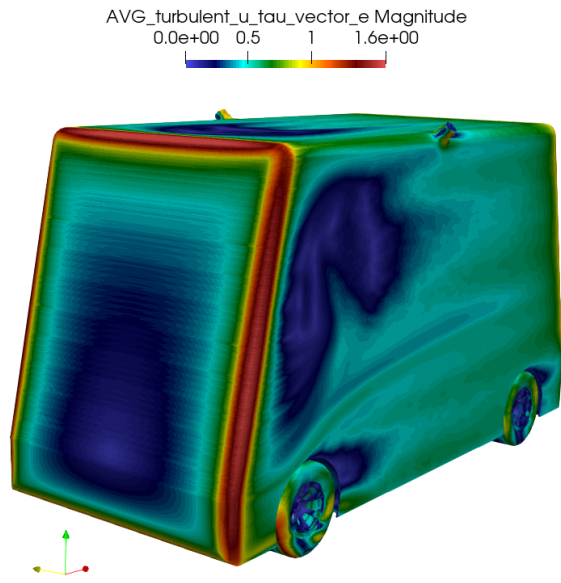


Figure C.186: Front isometric view of the u_τ of sensor position I and type small puck

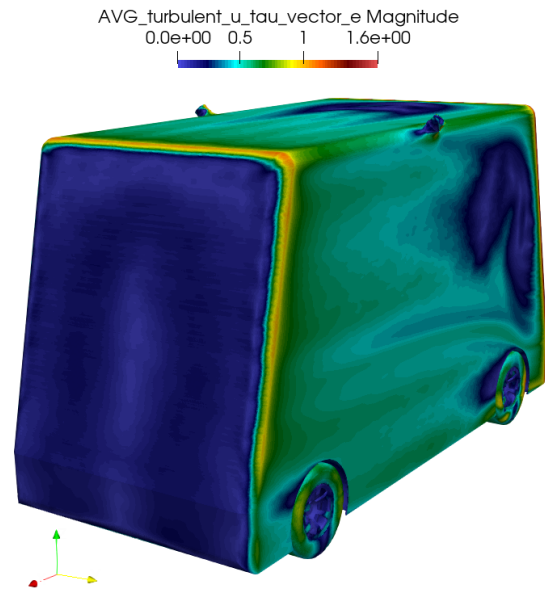


Figure C.187: Rear isometric view of the u_τ of sensor position I and type small puck

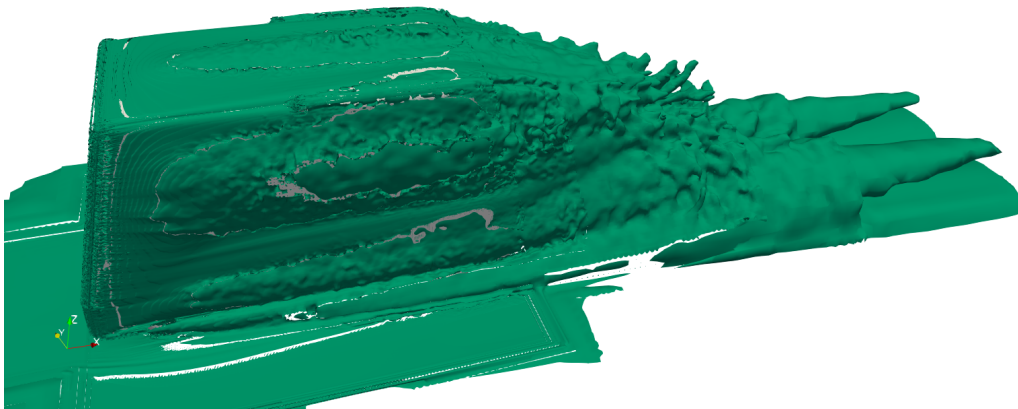


Figure C.188: Side view of the vorticity (value $|\omega| = 10 \text{ s}^{-1}$) of sensor position I and type small puck

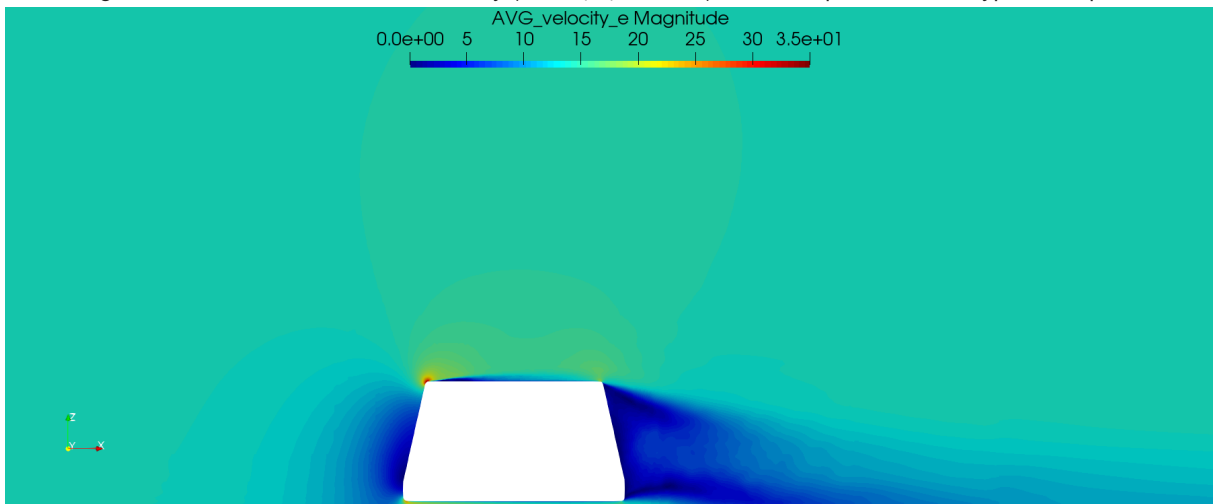


Figure C.189: Side view symmetry plane of the velocity magnitude of sensor position I and type small puck

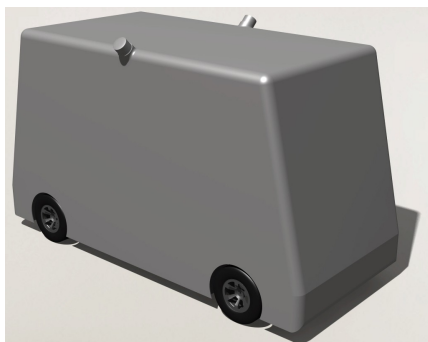


Figure C.190: Render of sensor position / and type big puck

Sensor position / and type **big puck**

Table C.22: Data table of sensor position / and type big puck

| Sensor position | / |
|-----------------|----------|
| Sensor type | big puck |
| ΔC_d | -11 |

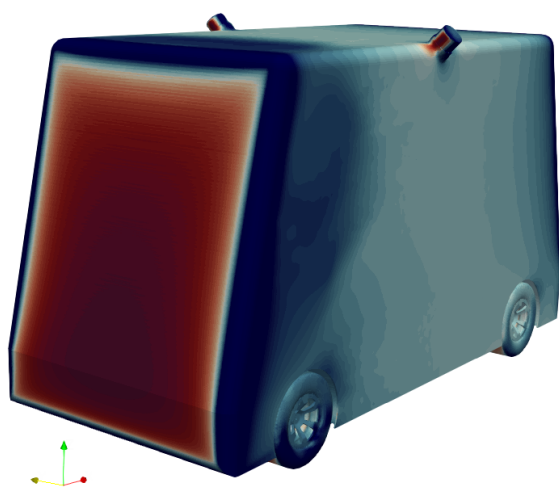


Figure C.191: Front isometric view of the C_p of sensor position / and type big puck

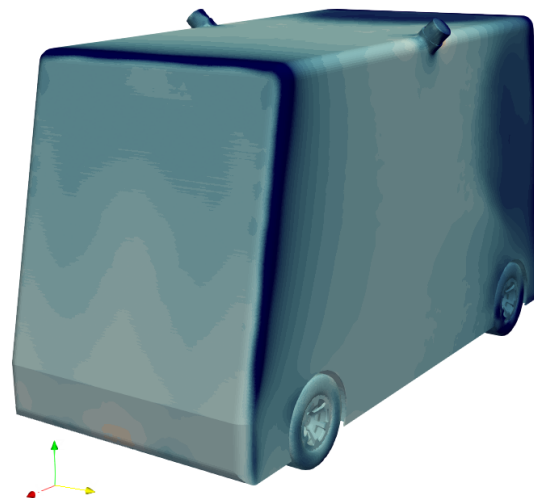
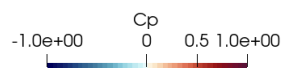


Figure C.192: Rear isometric view of the C_p of sensor position / and type big puck

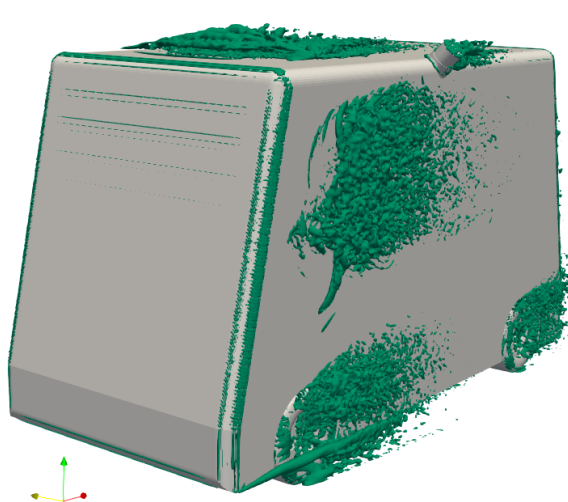


Figure C.193: Front isometric view of the Q-criteria (value $q = 2000 \text{ s}^{-2}$) of sensor position / and type big puck

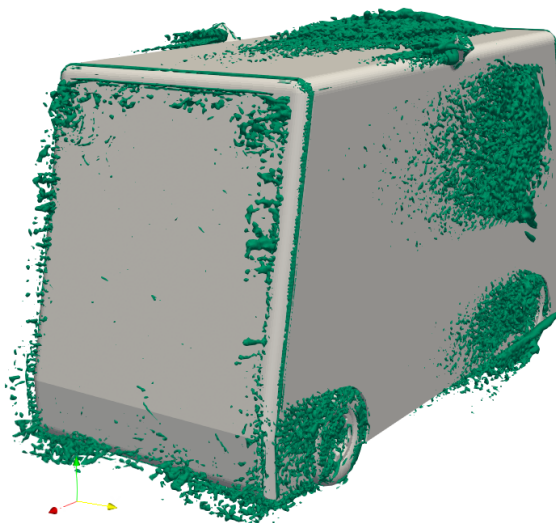


Figure C.194: Rear isometric view of the Q-criteria (value $q = 2000 \text{ s}^{-2}$) of sensor position / and type big puck

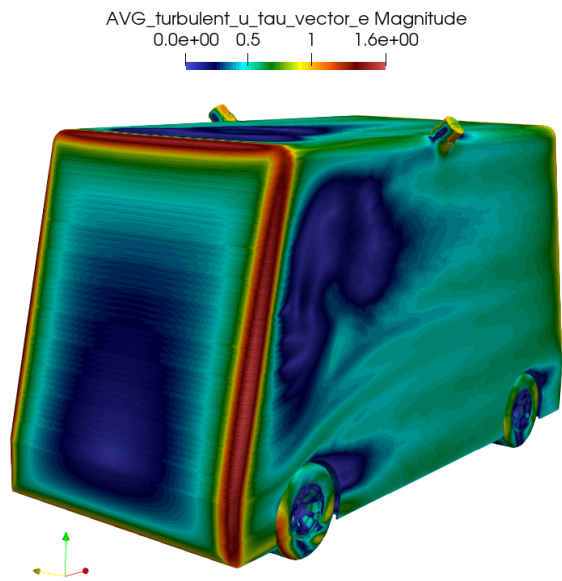


Figure C.195: Front isometric view of the u_τ of sensor position I and type big puck

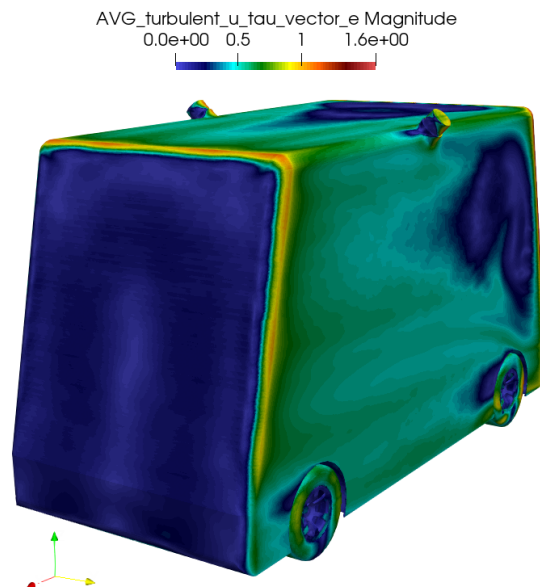


Figure C.196: Rear isometric view of the u_τ of sensor position I and type big puck



Figure C.197: Side view of the vorticity (value $|\omega| = 10 \text{ s}^{-1}$) of sensor position I and type big puck

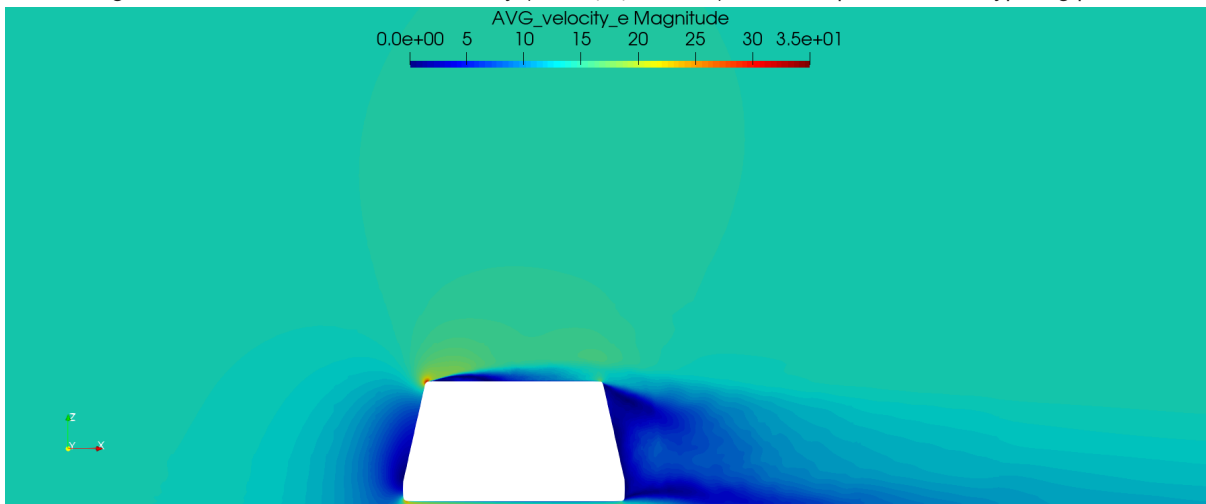


Figure C.198: Side view symmetry plane of the velocity magnitude of sensor position I and type big puck

D Appendix 4: Aerodynamic report of sensor layouts

The structure of the aerodynamic report is the same as in the design iterations and single sensor positions (Figure B.1). The included simulations are:

- Sensor layout coded: b_S_d_B.
- Sensor layout coded: c_S_i_S.
- Sensor layout coded: a_S_b_S_k_S.
- Sensor layout coded: a_S_g_S_i_S.
- Sensor layout coded: b_B_c_S_l_S.
- Sensor layout coded: a_S_c_S_h_S_i_S.
- Sensor layout coded: a_boxB_c_B_g_S_i_S.

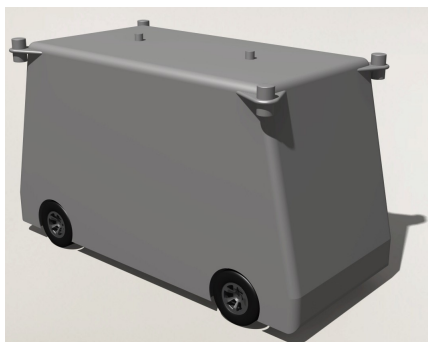


Figure D.1: Render of sensor layout coded: b_S_d_B

Sensor layout coded: **b_S_d_B**

Table D.1: Data table of sensor layout coded: b_S_d_B

| Sensor position | <i>b</i> | <i>d</i> |
|-----------------|----------|----------|
| Sensor shape | puck | puck |
| Sensor size | small | big |
| ΔC_d | 16 | |

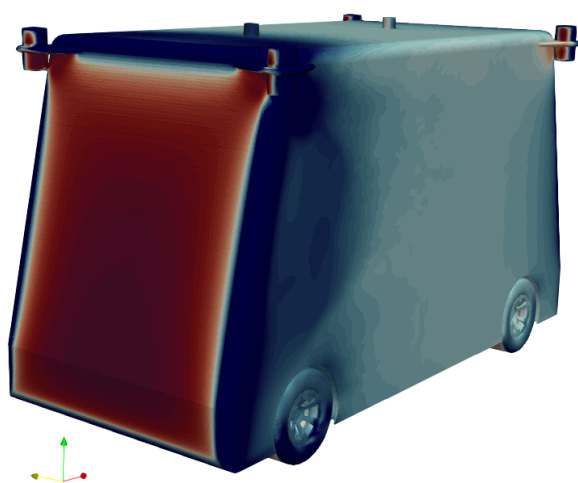


Figure D.2: Front isometric view of the C_p of sensor layout coded: b_S_d_B

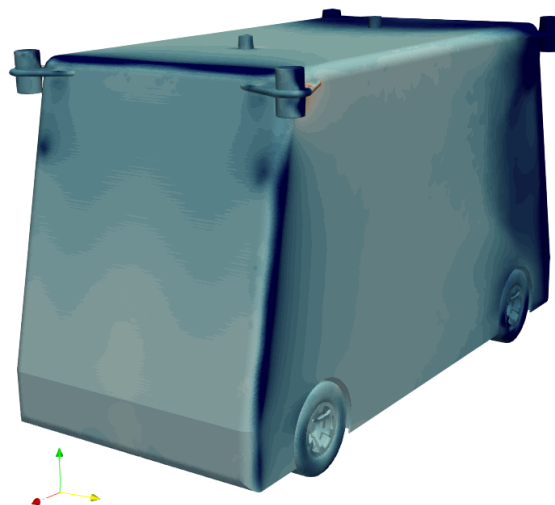


Figure D.3: Rear isometric view of the C_p of sensor layout coded: b_S_d_B

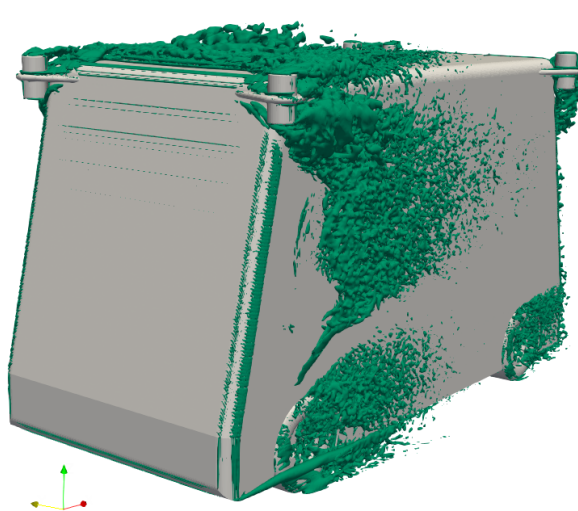


Figure D.4: Front isometric view of the Q-criteria (value $q = 2000 \text{ s}^{-2}$) of sensor layout coded: b_S_d_B

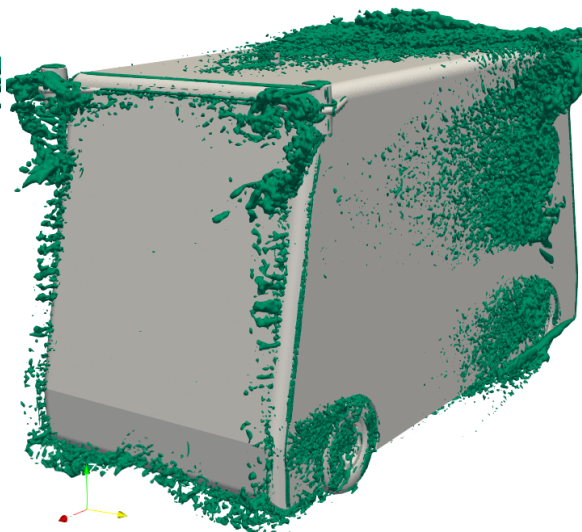


Figure D.5: Rear isometric view of the Q-criteria (value $q = 2000 \text{ s}^{-2}$) of sensor layout coded: b_S_d_B

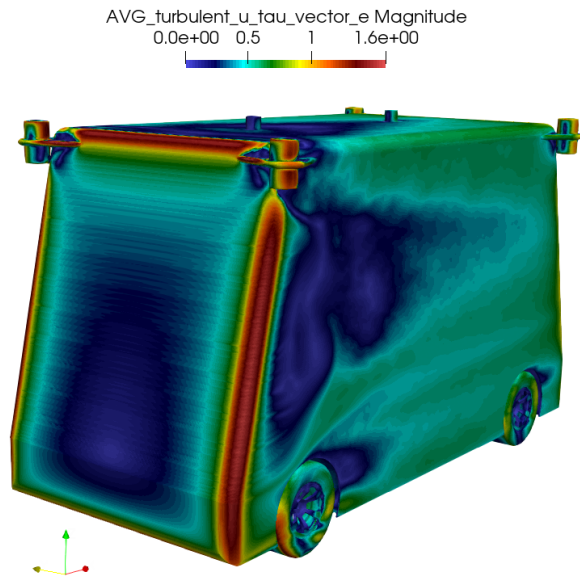


Figure D.6: Front isometric view of the u_τ of sensor layout coded: b_S_d_B

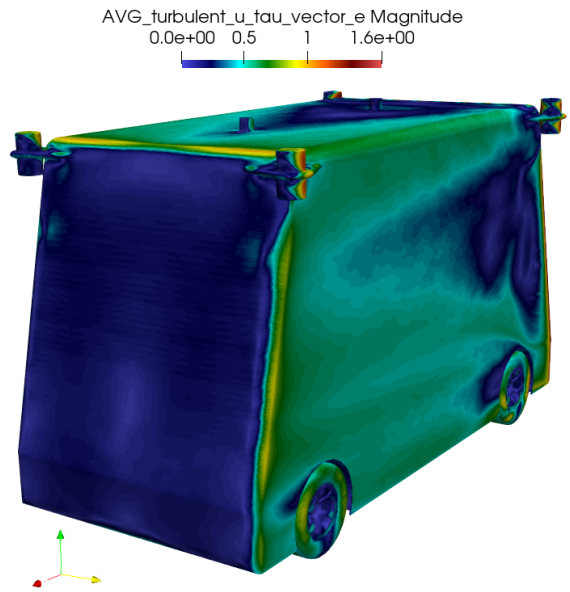


Figure D.7: Rear isometric view of the u_τ of sensor layout coded: b_S_d_B

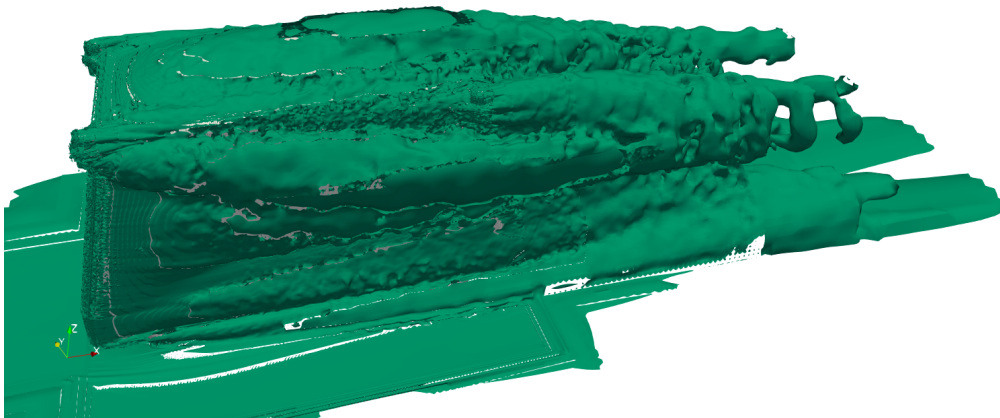


Figure D.8: Side view of the vorticity (value $|\omega| = 10 \text{ s}^{-1}$) of sensor layout coded: b_S_d_B

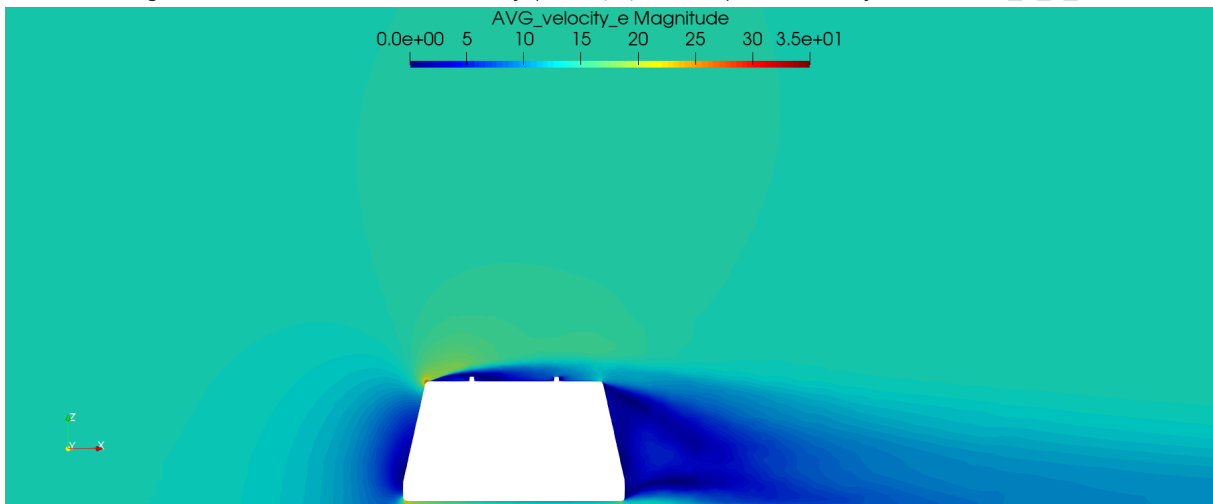


Figure D.9: Side view symmetry plane of the velocity magnitude of sensor layout coded: b_S_d_B

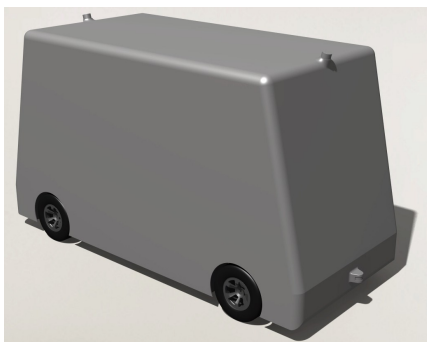


Figure D.10: Render of sensor layout coded: c_S_i_S

Sensor layout coded: **c_S_i_S**

Table D.2: Data table of sensor layout coded: c_S_i_S

| Sensor position | c | i |
|-----------------|-------|-------|
| Sensor shape | puck | puck |
| Sensor size | small | small |
| ΔC_d | -12 | |

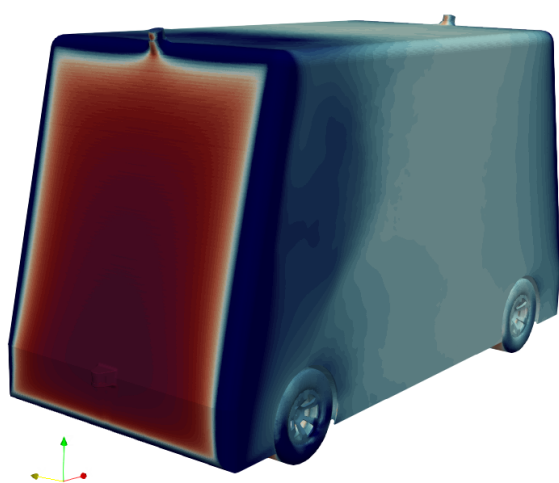


Figure D.11: Front isometric view of the C_p of sensor layout coded: c_S_i_S

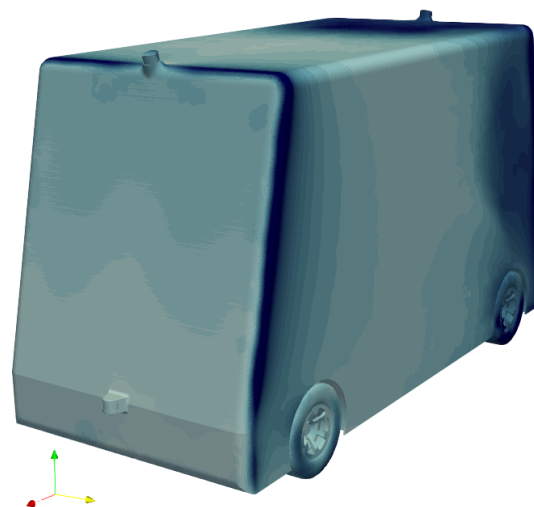


Figure D.12: Rear isometric view of the C_p of sensor layout coded: c_S_i_S

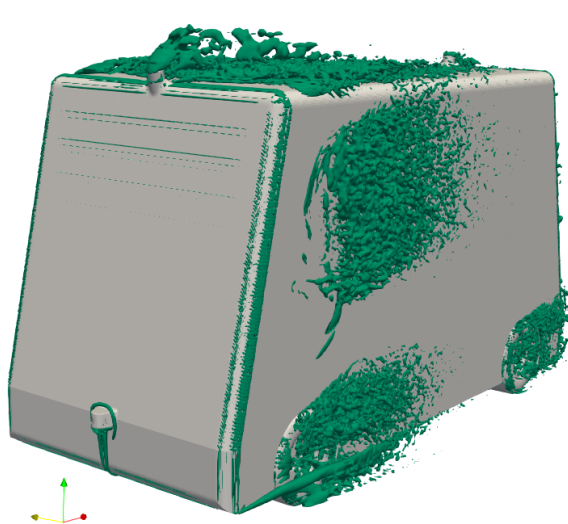


Figure D.13: Front isometric view of the Q-criteria (value $q = 2000 \text{ s}^{-2}$) of sensor layout coded: c_S_i_S

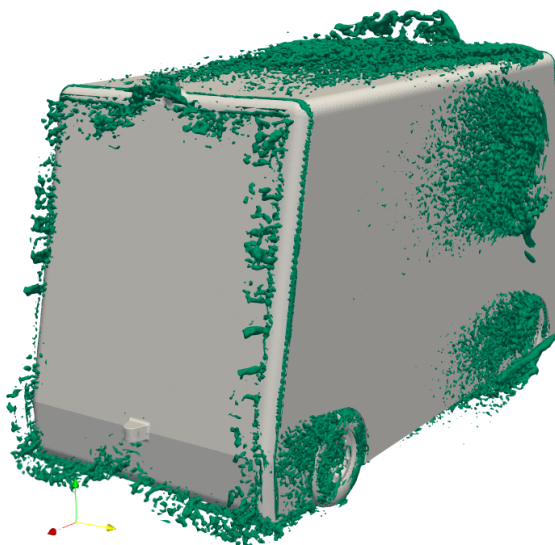


Figure D.14: Rear isometric view of the Q-criteria (value $q = 2000 \text{ s}^{-2}$) of sensor layout coded: c_S_i_S

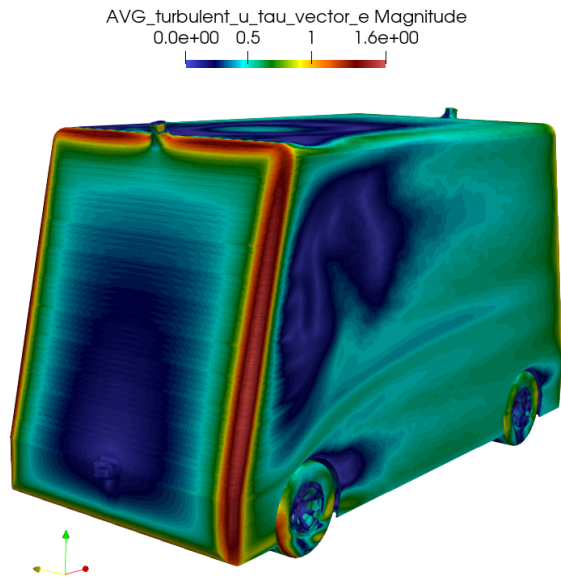


Figure D.15: Front isometric view of the u_τ of sensor layout coded: c_S_i_S

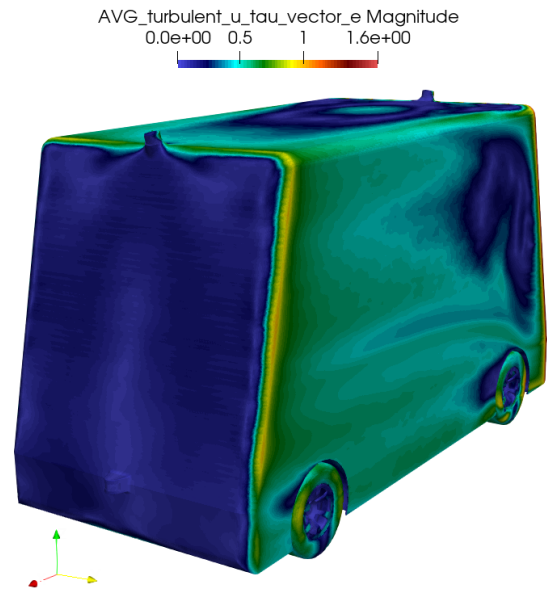


Figure D.16: Rear isometric view of the u_τ of sensor layout coded: c_S_i_S

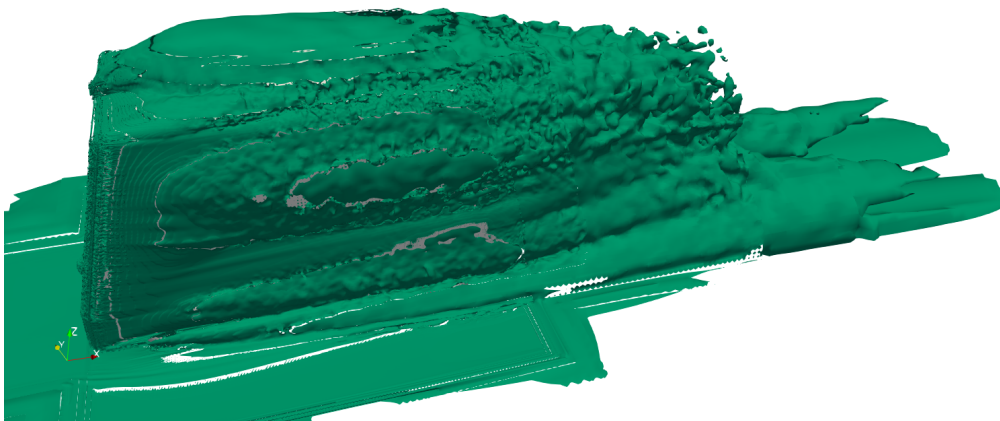


Figure D.17: Side view of the vorticity (value $|\omega| = 10 \text{ s}^{-1}$) of sensor layout coded: c_S_i_S

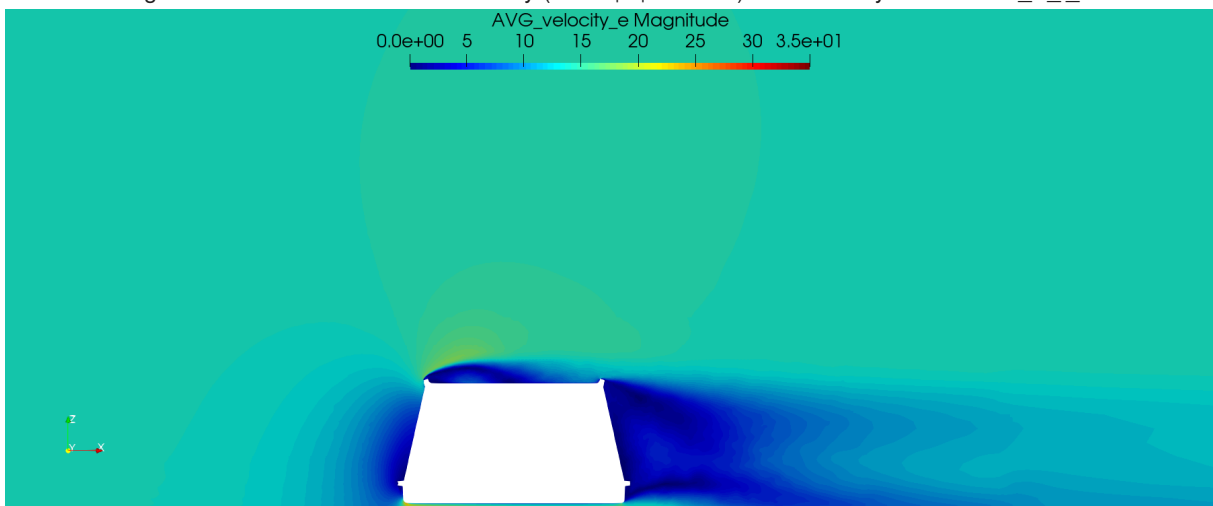


Figure D.18: Side view symmetry plane of the velocity magnitude of sensor layout coded: c_S_i_S

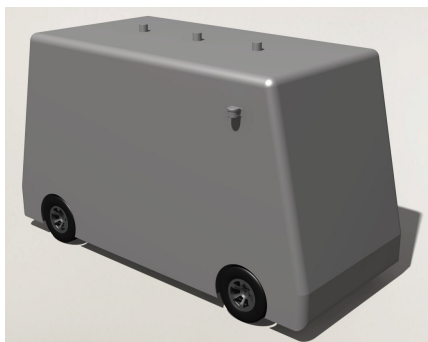


Figure D.19: Render of sensor layout coded: a_S_b_S_k_S

Sensor layout coded: **a_S_b_S_k_S**

Table D.3: Data table of sensor layout coded: a_S_b_S_k_S

| Sensor position | <i>a</i> | <i>b</i> | <i>k</i> |
|-----------------|----------|----------|----------|
| Sensor shape | puck | puck | puck |
| Sensor size | small | small | small |
| ΔC_d | | -25 | |

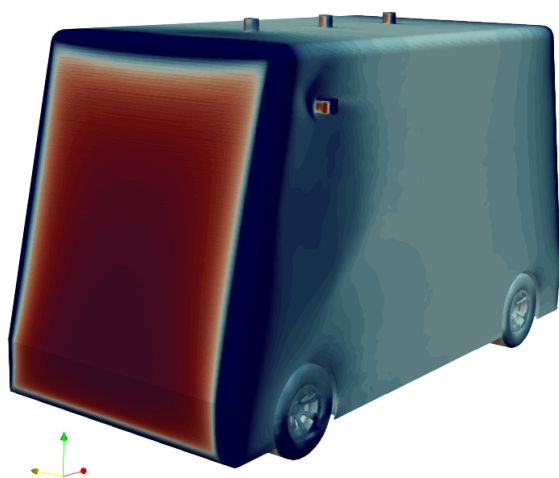


Figure D.20: Front isometric view of the C_p of sensor layout coded: a_S_b_S_k_S

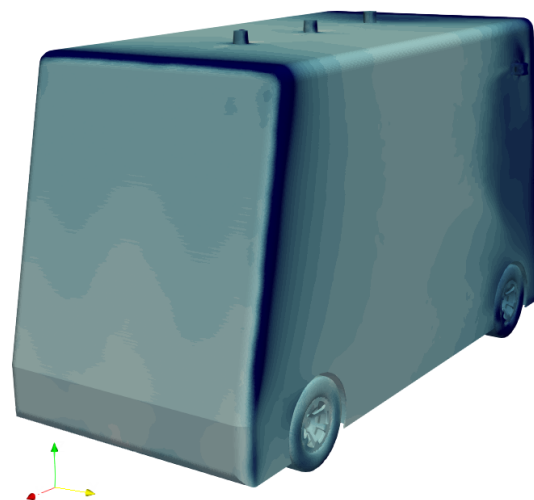


Figure D.21: Rear isometric view of the C_p of sensor layout coded: a_S_b_S_k_S

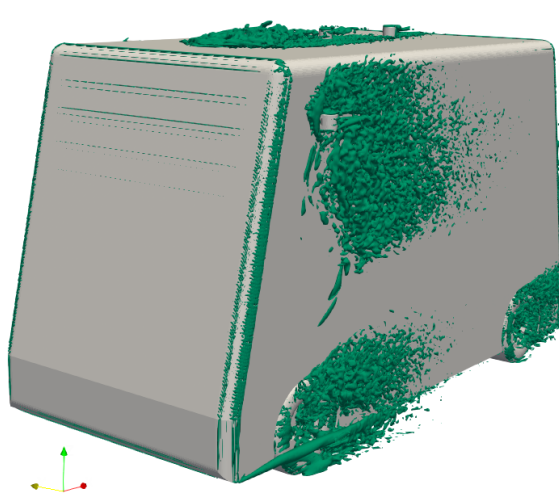


Figure D.22: Front isometric view of the Q-criteria (value $q = 2000 \text{ s}^{-2}$) of sensor layout coded: a_S_b_S_k_S



Figure D.23: Rear isometric view of the Q-criteria (value $q = 2000 \text{ s}^{-2}$) of sensor layout coded: a_S_b_S_k_S

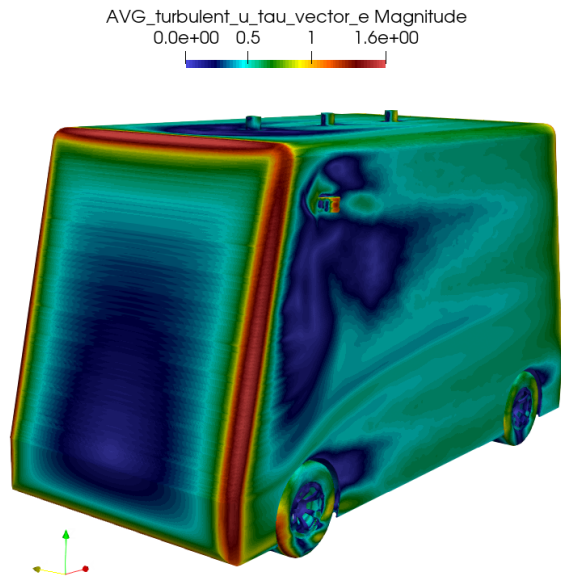


Figure D.24: Front isometric view of the u_τ of sensor layout coded: a_S_b_S_k_S

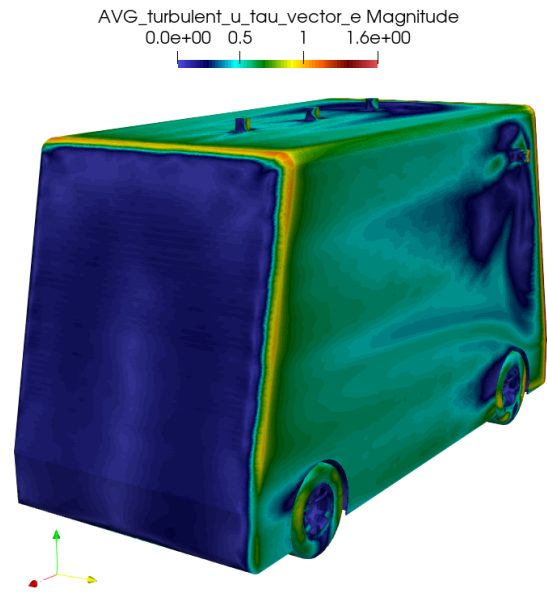


Figure D.25: Rear isometric view of the u_τ of sensor layout coded: a_S_b_S_k_S

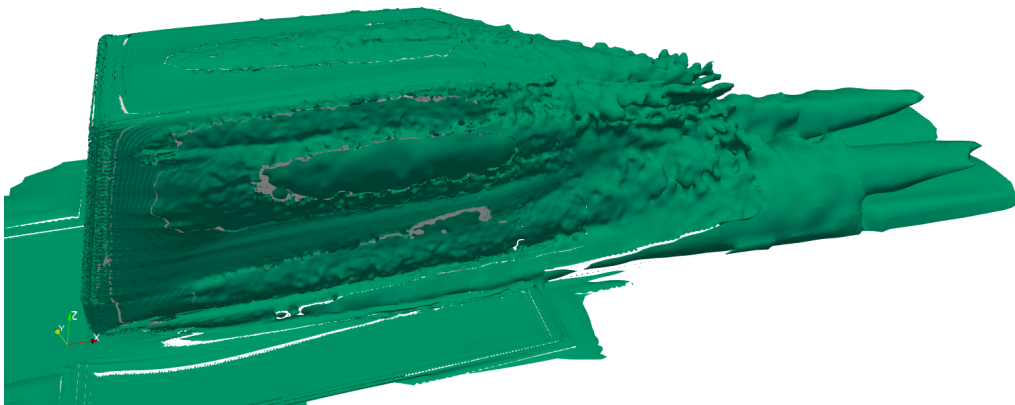


Figure D.26: Side view of the vorticity (value $|\omega| = 10 \text{ s}^{-1}$) of sensor layout coded: a_S_b_S_k_S

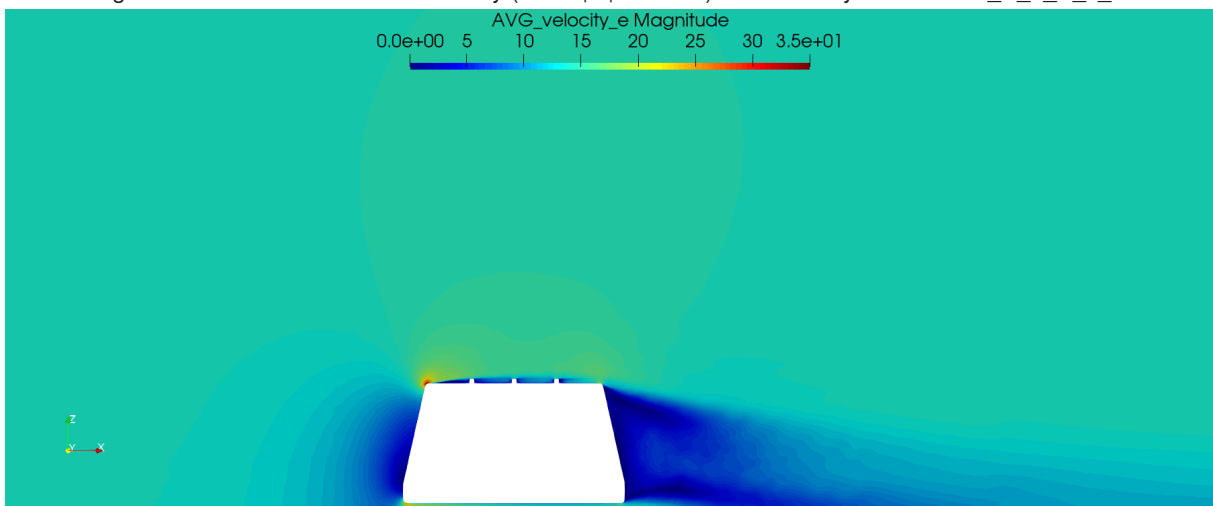


Figure D.27: Side view symmetry plane of the velocity magnitude of sensor layout coded: a_S_b_S_k_S

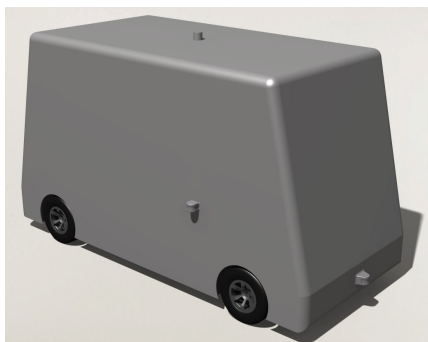


Figure D.28: Render of sensor layout coded: a_S_g_S_i_S

Sensor layout coded: a_S_g_S_i_S

Table D.4: Data table of sensor layout coded: a_S_g_S_i_S

| Sensor position | a | g | i |
|-----------------|-------|-------|-------|
| Sensor shape | puck | puck | puck |
| Sensor size | small | small | small |
| ΔC_d | | -22 | |

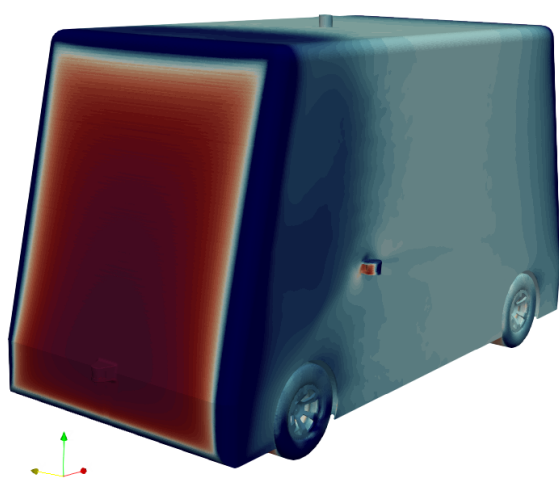
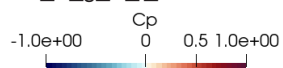


Figure D.29: Front isometric view of the C_p of sensor layout coded: a_S_g_S_i_S

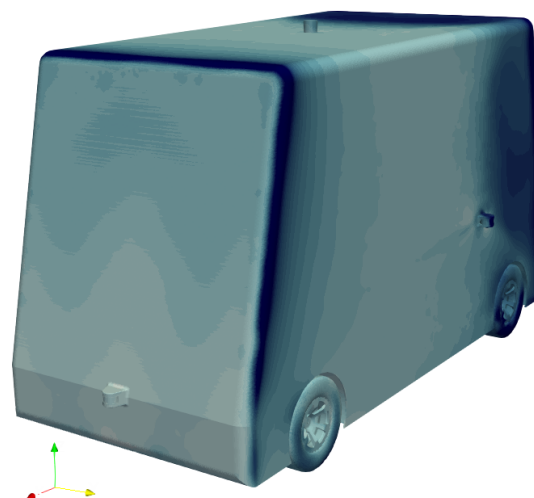


Figure D.30: Rear isometric view of the C_p of sensor layout coded: a_S_g_S_i_S

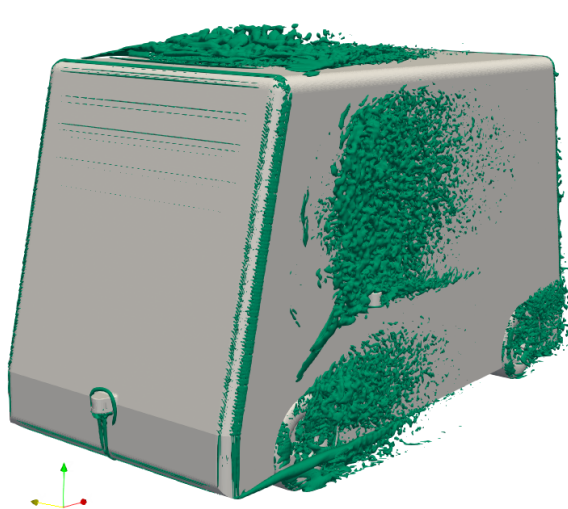


Figure D.31: Front isometric view of the Q-criteria (value $q = 2000 \text{ s}^{-2}$) of sensor layout coded: a_S_g_S_i_S



Figure D.32: Rear isometric view of the Q-criteria (value $q = 2000 \text{ s}^{-2}$) of sensor layout coded: a_S_g_S_i_S

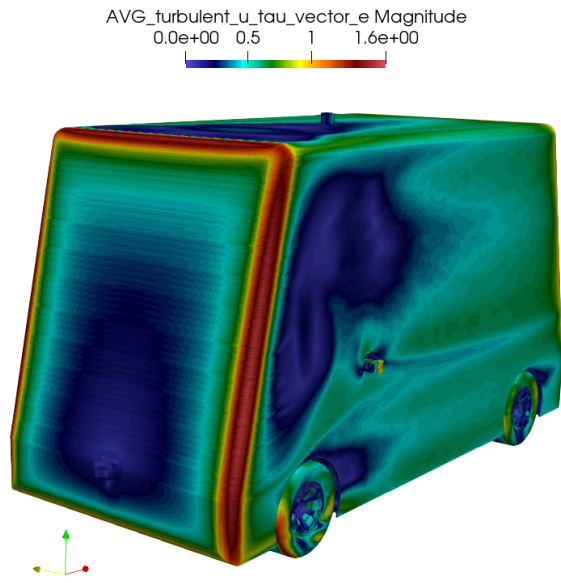


Figure D.33: Front isometric view of the u_τ of sensor layout coded: a_S_g_S_i_S

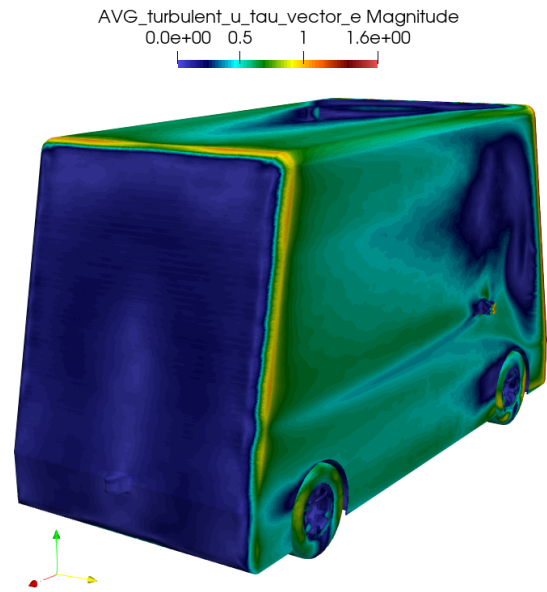


Figure D.34: Rear isometric view of the u_τ of sensor layout coded: a_S_g_S_i_S

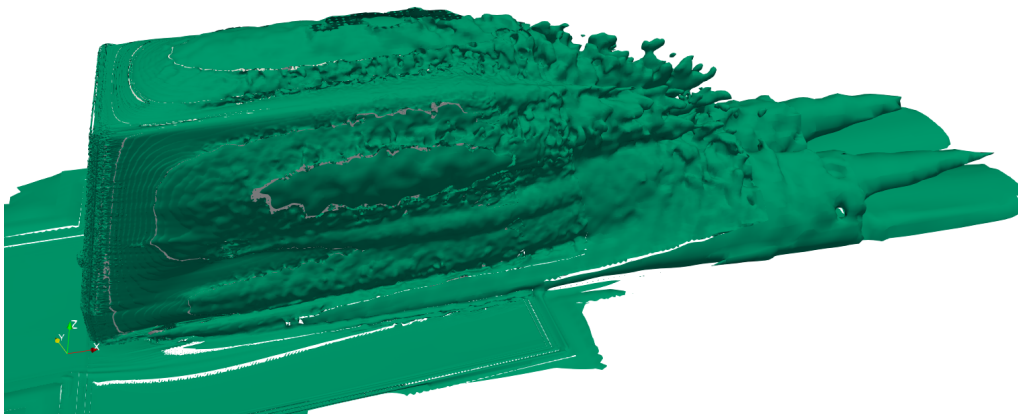


Figure D.35: Side view of the vorticity (value $|\omega| = 10 \text{ s}^{-1}$) of sensor layout coded: a_S_g_S_i_S

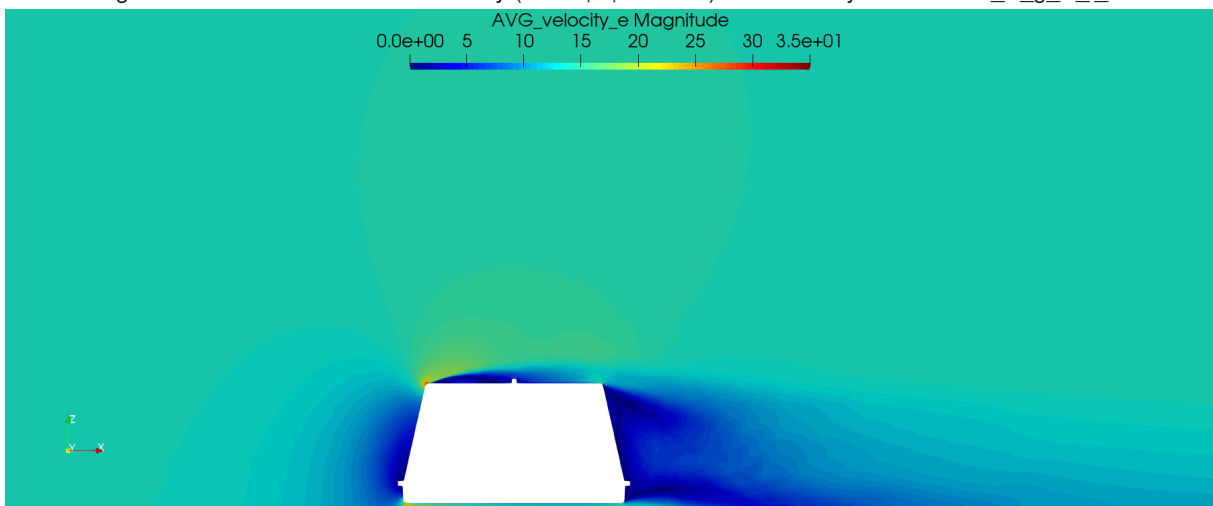


Figure D.36: Side view symmetry plane of the velocity magnitude of sensor layout coded: a_S_g_S_i_S

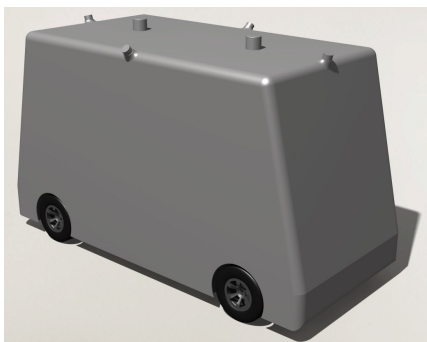


Figure D.37: Render of sensor layout coded: `b_B_c_S_I_S`

Sensor layout coded: `b_B_c_S_I_S`

Table D.5: Data table of sensor layout coded: `b_B_c_S_I_S`

| Sensor position | <i>b</i> | <i>c</i> | <i>l</i> |
|-----------------|----------|----------|----------|
| Sensor shape | puck | puck | puck |
| Sensor size | big | small | small |
| ΔC_d | | -8 | |

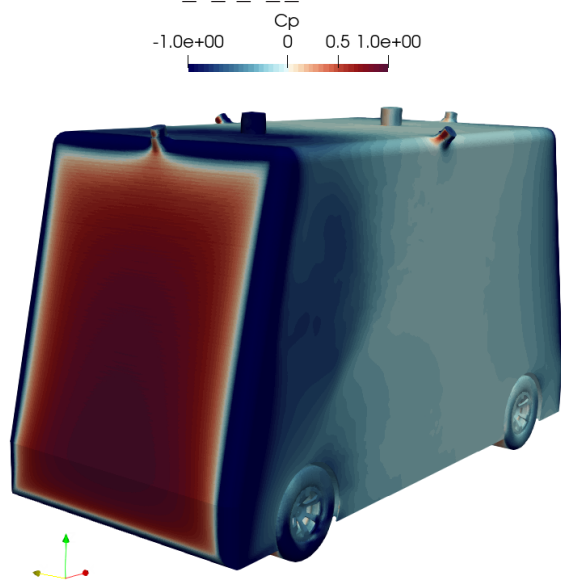


Figure D.38: Front isometric view of the C_p of sensor layout coded: `b_B_c_S_I_S`

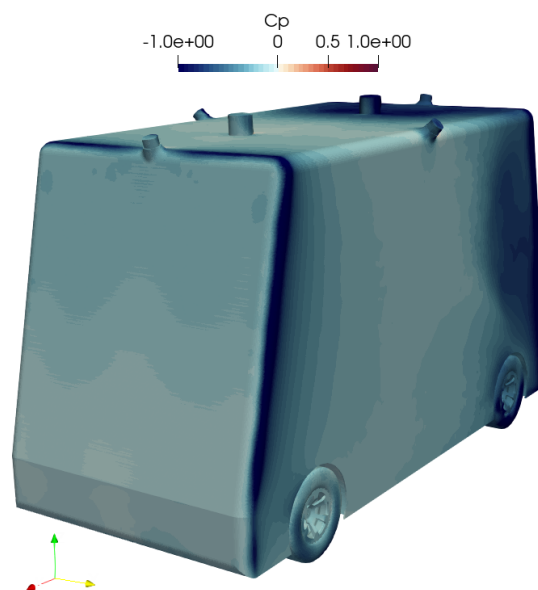


Figure D.39: Rear isometric view of the C_p of sensor layout coded: `b_B_c_S_I_S`

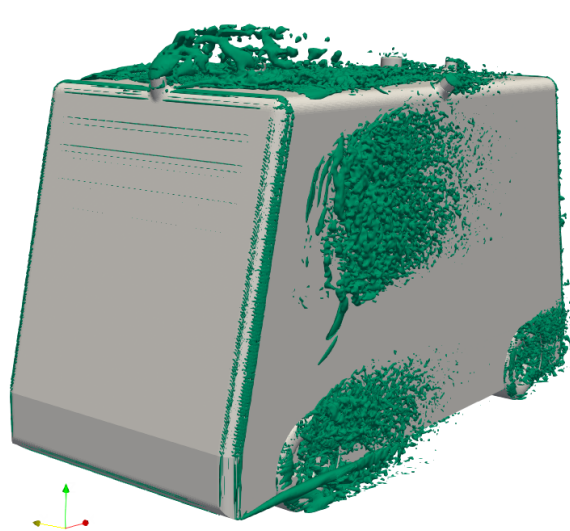


Figure D.40: Front isometric view of the Q-criteria (value $q = 2000 \text{ s}^{-2}$) of sensor layout coded: `b_B_c_S_I_S`



Figure D.41: Rear isometric view of the Q-criteria (value $q = 2000 \text{ s}^{-2}$) of sensor layout coded: `b_B_c_S_I_S`

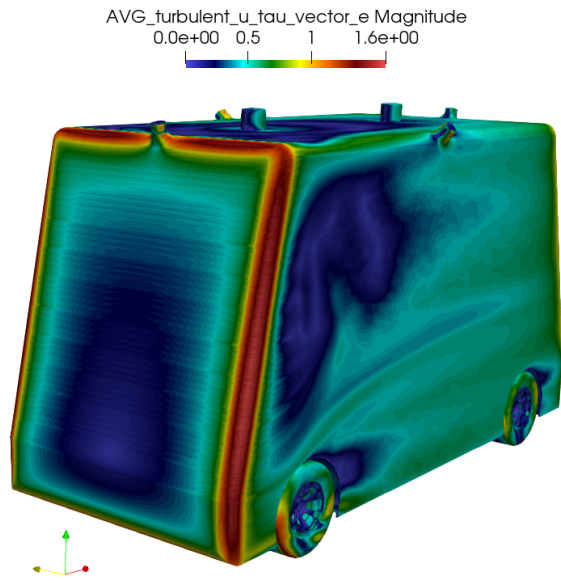


Figure D.42: Front isometric view of the u_τ of sensor layout coded: b_B_c_S_I_S

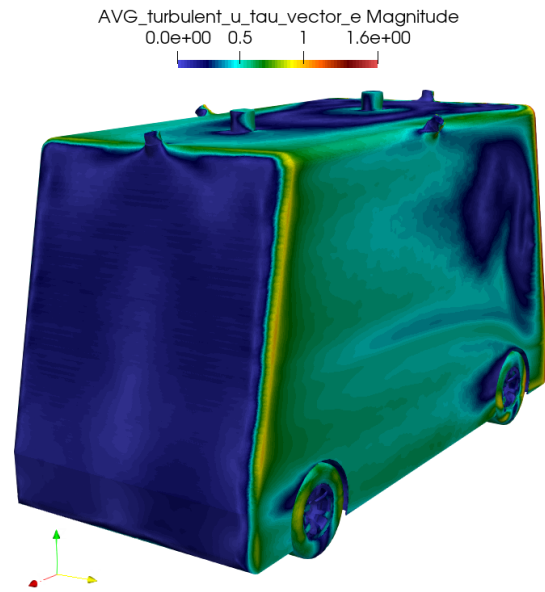


Figure D.43: Rear isometric view of the u_τ of sensor layout coded: b_B_c_S_I_S

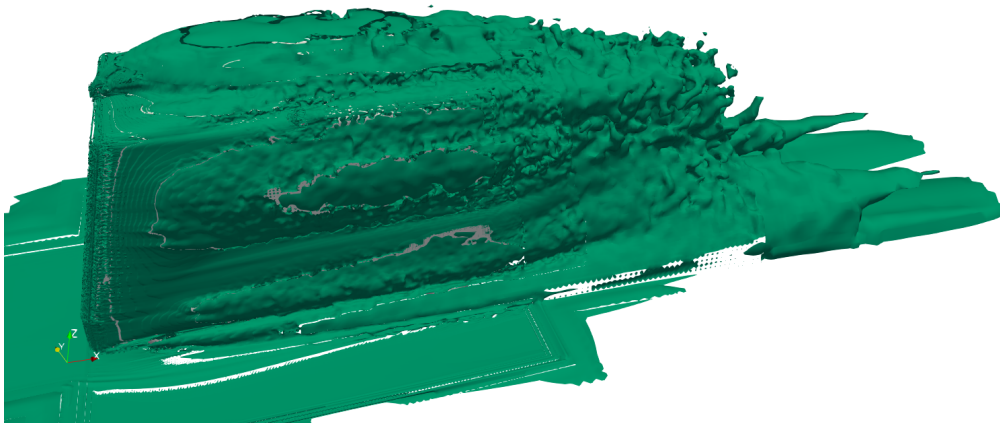


Figure D.44: Side view of the vorticity (value $|\omega| = 10 \text{ s}^{-1}$) of sensor layout coded: b_B_c_S_I_S

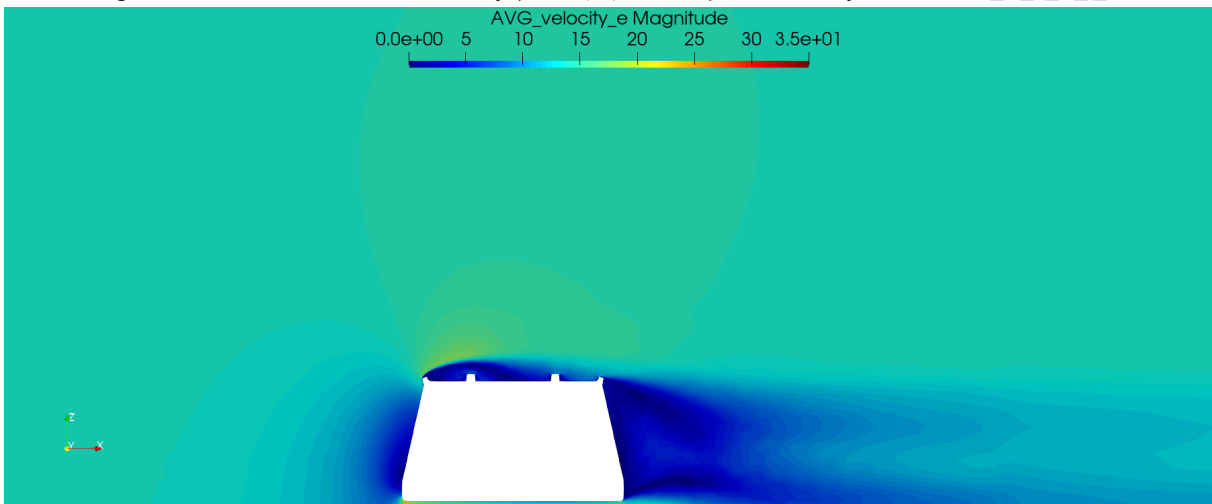


Figure D.45: Side view symmetry plane of the velocity magnitude of sensor layout coded: b_B_c_S_I_S



Sensor layout coded: `a_S_c_S_h_S_i_S`

Table D.6: Data table of sensor layout coded: `a_S_c_S_h_S_i_S`

| Sensor position | <i>a</i> | <i>c</i> | <i>h</i> | <i>i</i> |
|-----------------|----------|----------|----------|----------|
| Sensor shape | puck | puck | puck | puck |
| Sensor size | small | small | small | small |
| ΔC_d | -3 | | | |

Figure D.46: Render of sensor layout coded: `a_S_c_S_h_S_i_S`

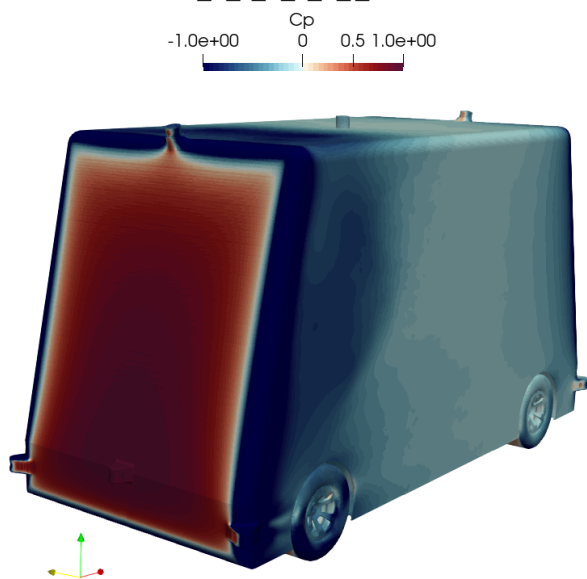


Figure D.47: Front isometric view of the C_p of sensor layout coded: `a_S_c_S_h_S_i_S`

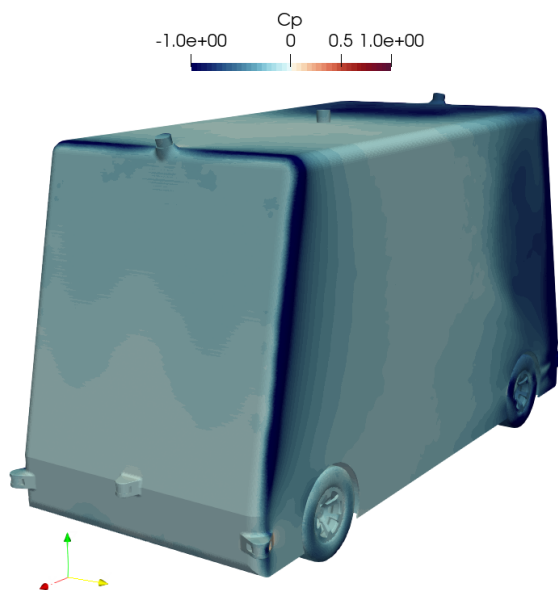


Figure D.48: Rear isometric view of the C_p of sensor layout coded: `a_S_c_S_h_S_i_S`



Figure D.49: Front isometric view of the Q-criteria (value $q = 2000 \text{ s}^{-2}$) of sensor layout coded: `a_S_c_S_h_S_i_S`

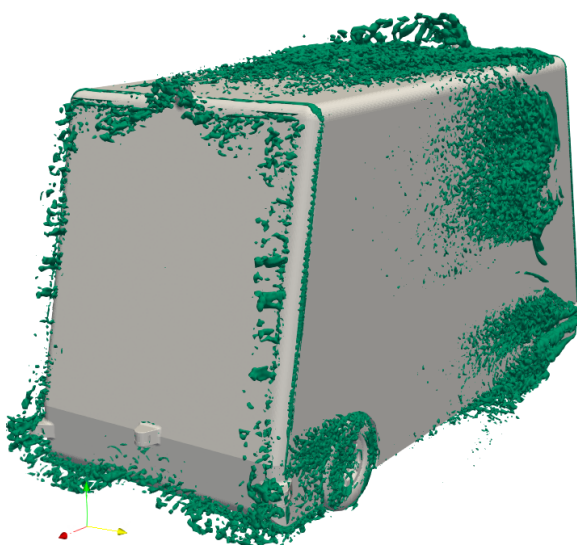


Figure D.50: Rear isometric view of the Q-criteria (value $q = 2000 \text{ s}^{-2}$) of sensor layout coded: `a_S_c_S_h_S_i_S`

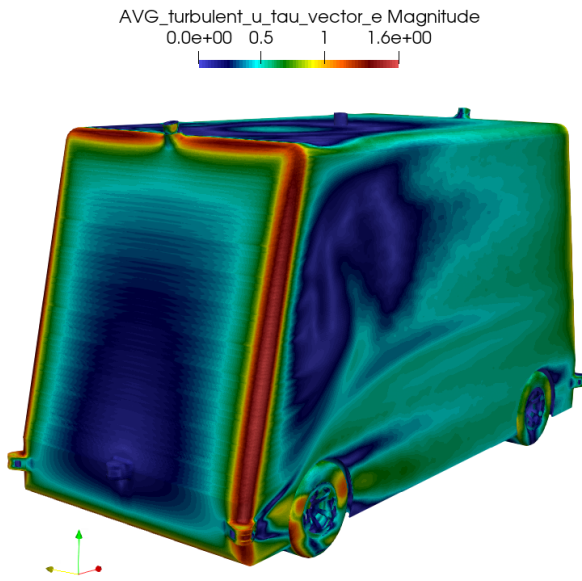


Figure D.51: Front isometric view of the u_τ of sensor layout coded: a_S_c_S_h_S_i_S

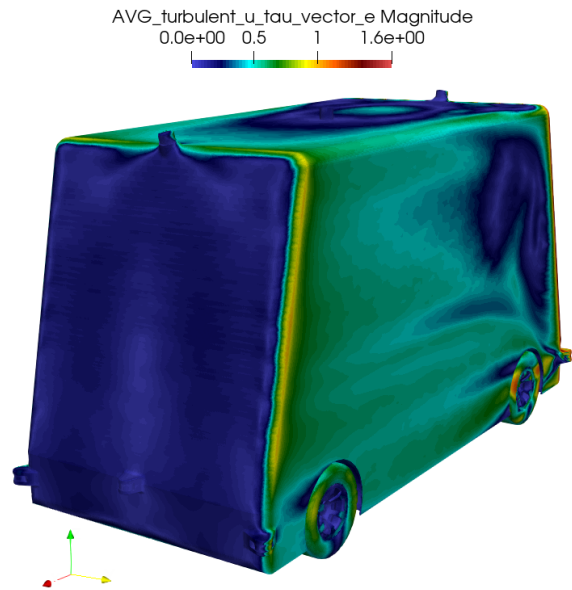


Figure D.52: Rear isometric view of the u_τ of sensor layout coded: a_S_c_S_h_S_i_S

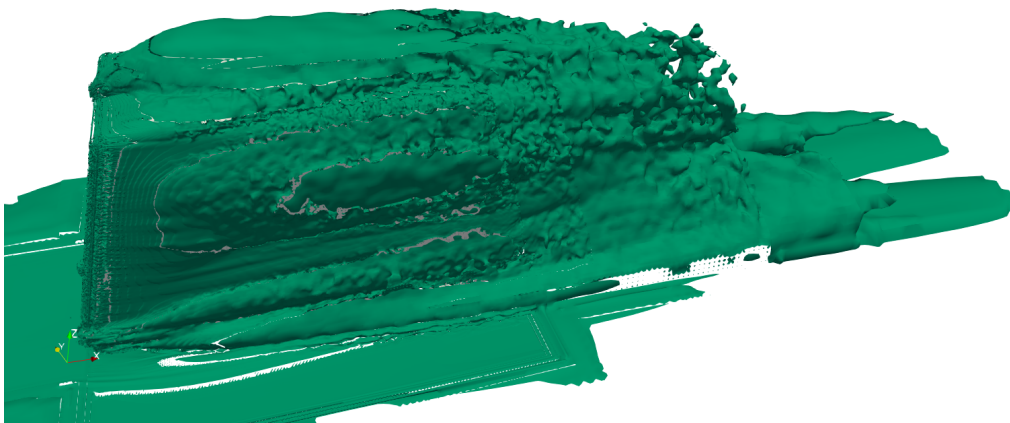


Figure D.53: Side view of the vorticity (value $|\omega| = 10 \text{ s}^{-1}$) of sensor layout coded: a_S_c_S_h_S_i_S

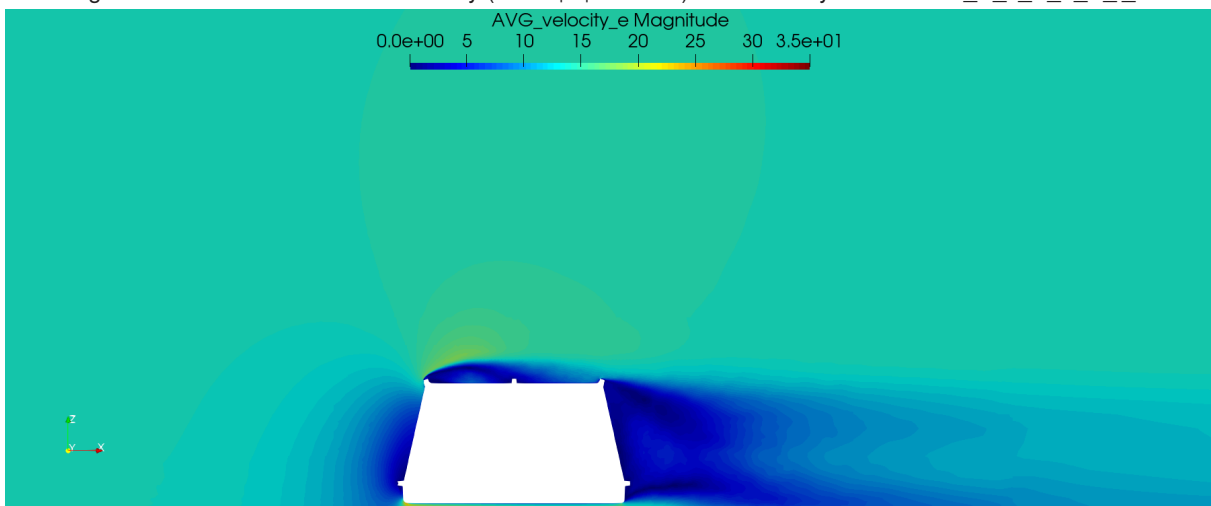


Figure D.54: Side view symmetry plane of the velocity magnitude of sensor layout coded: a_S_c_S_h_S_i_S

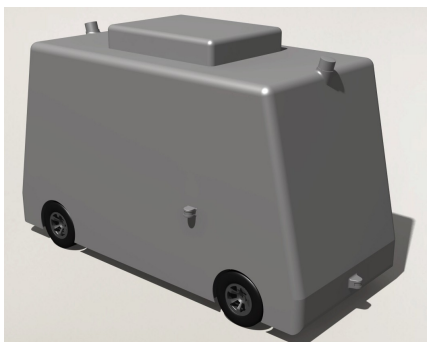


Figure D.55: Render of sensor layout coded: a_boxB_c_B_g_S_i_S

Sensor layout coded: **a_boxB_c_B_g_S_i_S**

Table D.7: Data table of sensor layout coded: a_boxB_c_B_g_S_i_S

| Sensor position | <i>a</i> | <i>c</i> | <i>g</i> | <i>i</i> |
|-----------------|----------|----------|----------|----------|
| Sensor shape | box | puck | puck | puck |
| Sensor size | big | big | small | small |
| ΔC_d | -54 | | | |

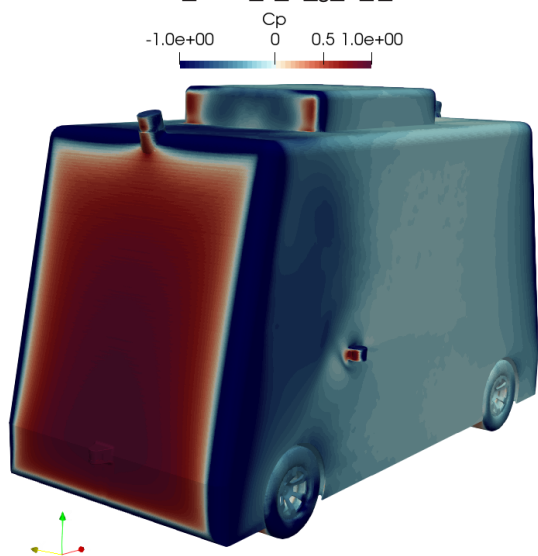


Figure D.56: Front isometric view of the C_p of sensor layout coded: a_boxB_c_B_g_S_i_S

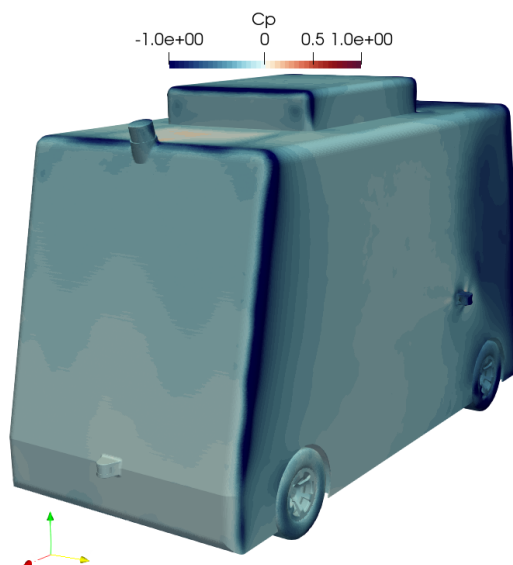


Figure D.57: Rear isometric view of the C_p of sensor layout coded: a_boxB_c_B_g_S_i_S

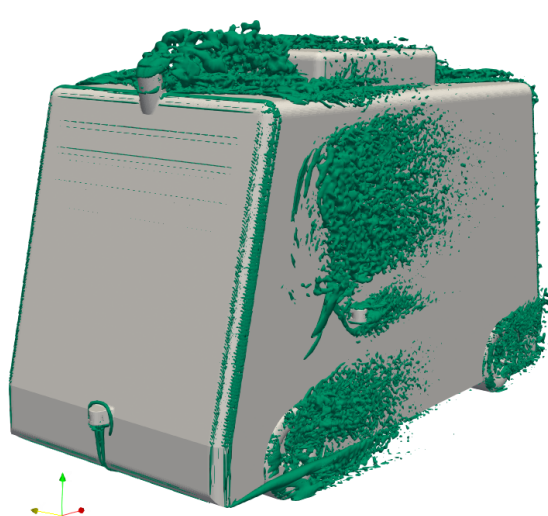


Figure D.58: Front isometric view of the Q-criteria (value $q = 2000 \text{ s}^{-2}$) of sensor layout coded: a_boxB_c_B_g_S_i_S

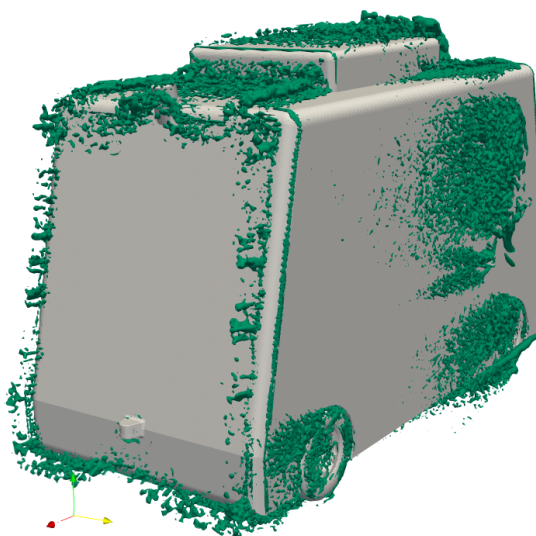


Figure D.59: Rear isometric view of the Q-criteria (value $q = 2000 \text{ s}^{-2}$) of sensor layout coded: a_boxB_c_B_g_S_i_S

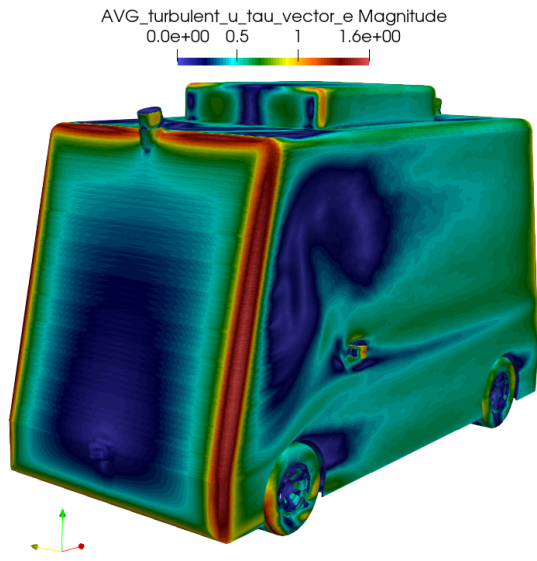


Figure D.60: Front isometric view of the u_τ of sensor layout coded: a_boxB_c_B_g_S_i_S

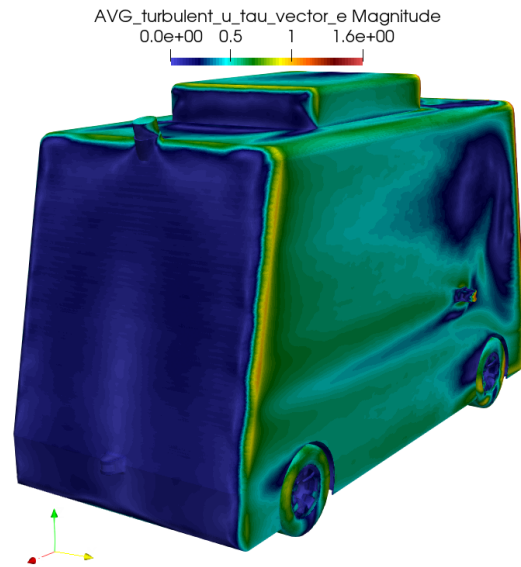


Figure D.61: Rear isometric view of the u_τ of sensor layout coded: a_boxB_c_B_g_S_i_S

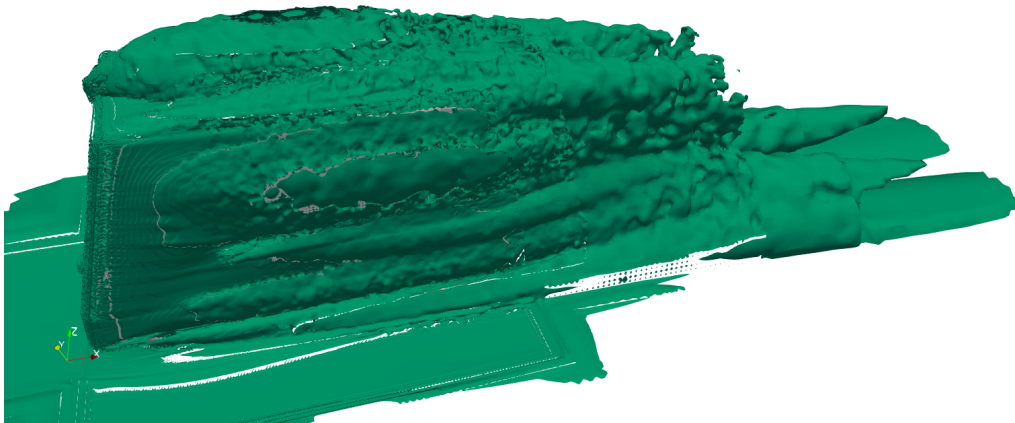


Figure D.62: Side view of the vorticity (value $|\omega| = 10 \text{ s}^{-1}$) of sensor layout coded: a_boxB_c_B_g_S_i_S

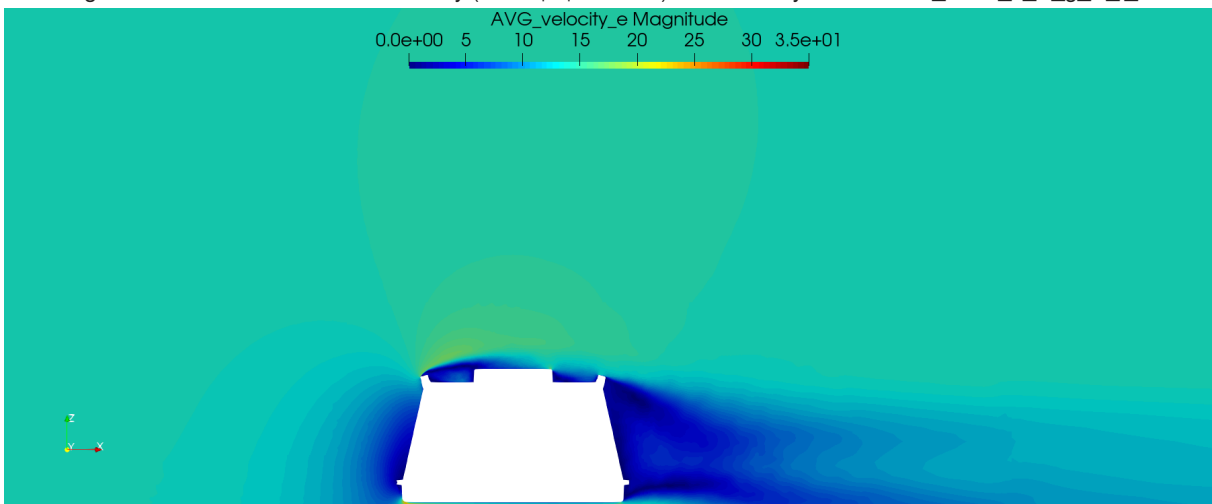


Figure D.63: Side view symmetry plane of the velocity magnitude of sensor layout coded: a_boxB_c_B_g_S_i_S

E Appendix 5: Content of the attached SD card

- 01_Writing
 - Figures
 - Latex_files
- 02_Literature
- 03_Simulation_Setups
 - DrivAer
 - Generic_Shuttle
 - Design_variables
 - Single_sensor
 - Sensor_setup
- 04_Macros_Postprocessing
- 05_CAD_Files